Fakultät für Luftfahrt, Raumfahrt und Geodäsie
Technische Universität München

Leading-Edge Vortex Control by Unsteady Blowing

Andrei Buzica

Vollständiger Abdruck der von der Fakultät für Luftfahrt, Raumfahrt und Geodäsie der Technischen Universität München zur Erlangung des akademischen Grades eines

Doktor-Ingenieurs (Dr.-Ing.)

genehmigten Dissertation.

Vorsitzender:
Prof. Dr.-Ing. Florian Holzapfel

Prüfende der Dissertation:
1. apl. Prof. Dr.-Ing. Christian W. M. Breitsamter
2. Prof. Dr. rer. nat. habil. Christian Kähler

Die Dissertation wurde am 12.10.2020 bei der Technischen Universität München eingereicht und durch die Fakultät für Luftfahrt, Raumfahrt und Geodäsie am 01.07.2021 angenommen.

Abstract

The flow field around an incidenced delta-wing is dominated by a complex vortex system. The boundary layer separating at the sharp leading edge becomes a shear layer and rolls up forming the leading-edge vortex above the wing. High suction is the result of the vortex inducing high near-wall velocities on the wing's upper surface. With increasing angle of attack, the pressure on the upper wing surface decreases at a higher rate compared to conventional high-aspect-ratio wing configurations. The non-linear lift increase contributes to the characteristic manoeuvering agility of delta-wing configuration.

At high incidences, the vortex becomes unstable and breaks down. Thus, periodic flow phenomena (instabilities) dominate the flow field. By increasing the angle of attack up to post-stall, the leading-edge vortex collapses leading to an abrupt lift loss. These flow processes generate unsteady loads on the wing structure and flight control loss. Flow control offers a great perspective for extending the flight envelope. Frequency conditioned blowing addresses flow instabilities in order to achieve a global effect, as vortex stabilisation or sustaining the reattached shear layer around stall. This enhances wing performance, stability, controllability and stall margins.

This thesis investigates the unsteady vortex system above a delta-wing model at three high-angle-of-attack flight regimes: prior to, near and beyond stall. Extensive stereoscopic PIV and transient CFD determine the three dimensional flow field structure. The applied active flow control method relies on unsteady jets distributed along the leading edge. Synchronising the jets results in increased flowfield alteration with higher increase in performance compared to frequency/phase variation. The biggest effect is achieved at post-stall, at which the otherwise separated shear-layer gets reattached on the upper surface, increasing lift by more than 50%. At lower incidences, the mean vortex breakdown position is delayed, however with no significant increase in aerodynamic coefficients. The mechanisms leading to the flow manipulation are investigated here contributing to a better understanding of the leading-edge vortex response to pulsed blowing.

Zusammenfassung

Das Strömungsfeld um einem angestellten Deltaflügel ist dominiert von einem komplexen Wirbelsystem. Ein Vorderkantenwirbelsystem entsteht dadurch, dass die Grenzschicht an der scharfen Vorderkante ablöst und sich zu einem Vorderkantenwirbel aufrollt. Hoher Unterdruck entsteht durch den Wirbel, der hohe Geschwindigkeiten an der Flügeloberfläche induziert. Mit steigendem Anstellwinkel sinkt der Druck überproportional verglichen mit konventionellen Flügeln mit hoher Streckung. Die dadurch entstehende nichtlineare Auftriebsänderung ist ausschlaggebend für die hohe Manövrierbarkeit der Deltaflügelkonfigurationen.

Im hohen Anstellwinkelbereich wird der Wirbel instabil und platzt auf. Dabei treten anfachende periodische Strömungsphänomene (Instabilitäten) auf. Erhöht man den Anstellwinkel weiter bis zum Post-Stall, so kollabiert der Wirbel und erzeugt einen sprunghaften Auftriebseinbruch. Diese Phänomene können den Anstellwinkelbereich von Deltaflügelkonfigurationen limitieren. Die Beeinflussung des Wirbelsystems durch instationäre Aktuatoren ermöglicht eine effizient Erweiterung des Flugbereichs. Die Methode beruht auf der frequenzkonditionierten Manipulation der Strömungsinstabilitäten, mit dem Ziel eine Wirbelstabilisierung oder Wiederanlegen der Scherschicht zu erzielen. Dadurch wird bei hohen bis sehr hohen Anstellwinkeln die flugmechanische Leistung verbessert, beispielsweise durch Erhöhung der Flugstabilität (Rollstabilität), Verbesserung der Steuerung wie auch Erhöhung des Stall-Anstellwinkels.

Gegenstand dieser Arbeit ist die detaillierte Analyse des Strömungsfeldes, welches bei einem Deltaflügelmodell bei drei hohen Anstellwinkeln zu beobachten ist: im Pre-Stall, Stall und Post-Stall. Zur Erfassung der dreidimensionalen Strömungsstruktur dienen PIV und transiente CFD Simulationen. Die Untersuchung umfasst dabei unbeinflusste (Basis Fall) wie auch beeinflusste Vorderkantenwirbel (Aktuierter Fall). Die Strömungsbeeinflussung beruht auf pulsierenden Jets, welche entlang der Flügelvorderkante verteilt sind und die Scherschicht anregen. Werden die Jets synchronisiert, ergibt sich eine signifikante Beeinflussung des Strömungsfeldes mit Steigerung der aerodynamischen Effizienz im Vergleich zu Pulsieren mit räumlicher Frequenz- oder Phasenvariation. Das Wiederanlegen der Scherschicht an der Flügeloberseite im Post-Stall erhöht den Auftrieb um über 50%. Bei kleineren Anstellwinkeln verzögert das instationäre Ausblasen das Wirbelaufplatzen, jedoch ohne signifikante Änderung der aerodynamischen Koeffizienten. Die Analyse der Mechanismen, welche zur Manipulation der Wirbelströmung führen, ist ein wichtiger Bestandteil dieser Arbeit. Diese vermitteln ein besseres Verständnis der Strömungsantwort bei pulsierendem Ausblasen.

Contents

List of Figures

List of Tables

Acronyms

ACE	**A**ctive **C**ore **E**xhaust
AFC	**A**ctive **F**low **C**ontrol
avg	**av**era**g**e
BD	**B**reakdown **D**elay
CFD	**C**omputational **F**luid **D**ynamics
CFL	**C**ourant **F**riedrich **L**evy
CPU	**C**entral **P**rocessing **U**nit
DARPA	**D**efence **A**dvanced **R**esearch **P**rojects **A**gency
DDES	**D**elayed **D**etached-**E**ddy **S**imulation
DES	**D**etached-**E**ddy **S**imulation
DMD	**D**ynamic **M**ode **D**ecomposition
DNS	**D**irect **N**umerical **S**imulation
FV	**F**requency **V**ariation (actuation mode)
HPC	**H**igh **P**erformance **C**omputing
KH	**K**elvin **H**elmholtz
LES	**L**arge **E**ddy **S**imulation
LDV	**L**aser **D**oppler **V**elocimetry
MEMS	**M**icrofabricated **E**lectro**m**echanical **S**ystem
NASA	The **N**ational **A**eronautics and **S**pace **A**dministration
NTF	**N**ational **T**ransonic **F**acility
ONERA	**O**ffice **N**ationale d'**E**tudes et de **R**echerches **A**érospatiale
PDF	**P**robability **D**ensity **F**unction
PIV	**P**article **I**mage **V**elocimetry
POD	**P**roper **O**rthogonal **D**ecomposition
PSD	**P**ower **S**pectral **D**ensity
PTU	**P**ortable **T**iming **U**nit
PV	**P**hase **V**ariation (actuation mode)
px	**pix**el (used as unit)
RANS	**R**eynolds **A**veraged **N**avier **S**tokes
rms	**r**oot **m**ean **s**quare
SGS	**S**ub **G**rid **S**cale
SR	**S**eparation **R**eduction
SST	**S**hear **S**tress **T**ransport
TED	**T**railing-**E**dge **D**evice
TKE	**T**urbulent **K**inetic **E**nergy
TRL	**T**echnology **R**eadiness **L**evel

TUM-AER	**T**echnical **U**niversity of **M**unich- Chair of **Aer**odynamics and Fluid Mechanics
URANS	**U**nsteady **RANS**
VFE-2	**V**ortex **F**low **E**xperiment **2**
VG	**V**ortex **G**enerator
WR	**W**ake **R**eduction
ZNMF	**Z**ero-**N**et-**M**ass **F**lux

Symbols

$\boldsymbol{A}$	Linear mapping matrix
a_i	Linear coefficients
A_j	Jet exit cross area [m^2]
A_I	Interrogation window size [px^2]
A_{ref}	Reference area [m^2]
A_w	Wing planform area [m^2]
$\boldsymbol{b}$	DMD coefficient vector scaled on initial snapshot
C_L, C_D	Lift, drag coefficients [-]
C_{DES}	DES constant [-]
ΔC_L	Lift increase due to actuation [-]
$C_{L,\text{Baseline}}$	Lift of baseline flow [-]
C_{MX}, C_{MY}	Rolling and pitching moment coefficients [-]
c_p	Surface pressure coefficient [-]
$c_{p,\text{avg}}, c_{p,\text{rms}}$	Average and rms of pressure coefficient [-]
c_r	Root chord length [m]
c_μ	Momentum coefficient [-]
C_X, C_Z	Longitudinal and normal force coefficient [-]
D	Drag force [N]
f	Frequency [Hz]
F^+	Reduced actuation frequency (equivalent to St) [-]
F_1, F_2	SST blending functions [-]
f_a	Actuation frequency [Hz]
F_{DES}	DES blending function [-]
f_{dom}	Dominant frequency [Hz]
f_s	Sampling frequency [Hz]
F_X, F_Z	Longitudinal and normal force [N]
H	Helicity [m/s^2]
h_{pen}	Péniche height [m]
k	Turbulent kinetic energy [m^2/s^2]
k_{red}	Reduced frequency [-]
L	Lift force [N]
l_f	Lens focal length [mm]
l_{ref}	Reference length [m]
l_S	Smagorinsky mixing length [m]
l_t	Turbulent length scale [m]
l_μ	Mean aerodynamic chord length [m]

M_X, M_Y	Rolling and pitching moment [Nm]
N	Number of snapshots for DMD [-]
N_P	Number of correlation passes [-]
$N_{v,\mathrm{pos}}$	Cumulated number of vortex events with positive vorticity [-]
OV	Window overlap for the cross-correlation algorithm [%]
p	Pressure [Pa]
p'	Pressure fluctuation [Pa]
p_{in}	Actuation inlet pressure [bar]
$p_t, p_{t,\infty}$	Local and freestream total pressure [Pa]
Q	Q-criterion [1/s^2]
r	Reverse flow radius [m]
r_c	Discrete vortex core radius [mm]
Re	Reynolds number [-]
s	Wing half span [m]
$S, \boldsymbol{S}$	Integration surface [m^2]
$\boldsymbol{S}$	Companion type matrix
$\tilde{\boldsymbol{S}}$	Similarity matrix of $\boldsymbol{S}$
$S_{ij}, \boldsymbol{S}$	Strain-rate tensor [1/s]
$\overline{S}_{ij}$	LES filtered strain-rate tensor [1/s]
St	Strouhal number [-]
t	Time [s]
t_i	Indexed time step with i = 1,..., N [s]
T	Periodic cycle duration $1/f$ [s]
T	Temperature [K]
Δt_P	Time between laser pulses [μs]
Tu	Freestream turbulence level [%]
$\boldsymbol{U}$	Left singularity vectors (topos)
u, v, w	Body-fixed local velocity components [m/s]
$\boldsymbol{u}$	Velocity vector [m/s]
u', v', w'	Velocity fluctuation [m/s]
u_{avg}	Average axial velocity [m/s]
u_∞, w_∞	Longitudinal and vertical freestream velocity [m/s]
$u_{\mathrm{meas}}, u_{\mathrm{true}}$	Measured and true velocity [m/s]
U_i	Uncertainty in each window [m/s]
$\overline{U}_i$	Low-pass filtered velocity component [m/s]
u'_j	Jet velocity magnitude fluctuation [m/s]
$u_{\mathrm{rms}}, v_{\mathrm{rms}}, w_{\mathrm{rms}}$	Rms of the local velocity components [m/s]
u_θ	Azimuthal velocity component [m/s]
U_∞	Freestream velocity magnitude [m/s]
$\boldsymbol{v}_i$	Snapshot vector
$\boldsymbol{V}_i^N$	Snapshot matrix (from i to N)
v_j, w_j	Jet velocity components in leading-edge system [m/s]
$\boldsymbol{W}$	Right singularity vectors (chronos)

x_{bd}	Longitudinal breakdown location [m]
Δx_{bd}	Downstream breakdown displacement [m]
X_u	Fourier transform of the relative axial velocity [s]
x, y, z	Longitudinal, lateral and vertical coordinates [m/s]
$\boldsymbol{y}_i$	DMD eigenvector
y_p	Spanwise location of the force application point [m]
α	Angle of attack [° (deg)]
α_{Bursting}	α with bursting at trailing edge [° (deg)]
$\alpha_{\max}$	Angle of attack at maximum lift [° (deg)]
β	Angle of sideslip [° (deg)]
Γ_x	Circulation in x-direction [m^2/s]
$\Gamma_{x,\max}$	Maximum vortex circulation in x-direction [m^2/s]
$\Gamma_{x,\text{pos}}$	Average vortex circulation with positive vorticity [m^2/s]
δ	Wing thickness [m]
δ_{ij}	Kronecker delta [-]
Δ	Grid spacing [mm]
Δ_{PIV}	PIV grid spacing [mm]
$\Delta_x, \Delta_y, \Delta_z$	Grid spacing [mm]
$\Delta_{\max}$	Maximum cell edge length [m]
ϵ	Measurement error [m/s]
θ	Phase-angle of blowing cycle / phase delay [° (deg) / %]
Λ	Wing aspect ratio [-]
λ_2	Vortex identification criterion [$1/s^2$]
λ_i	Logarithmic mapping of DMD eigenvalues μ_i
μ	Laminar dynamic viscosity [kg/(m s)]
μ_t	Turbulent dynamic viscosity [kg/(m s)]
μ_i	DMD eigenvalue
ν	Laminar kinematic viscosity [m^2/s]
ν_r	SGS kinematic viscosity [m^2/s]
ν_t	Turbulent kinematic viscosity [m^2/s]
ρ_j	Jet exit density [kg/m^3]
ρ_∞	Freestream density [kg/m^3]
$\boldsymbol{\Sigma}$	Singular value matrix
τ	Dimensionless time [-]
τ_{ij}	Shear-stress tensor [N/m^2]
τ_{ij}^R	SGS tensor [N/m^2]
τ_{ij}^r	Residual stress tensor [N/m^2]
ϕ	SST constant blending between ϕ_1 and ϕ_2 [-]
ϕ_1	SST constants in $k-\epsilon$ region [-]
ϕ_2	SST constants in $k-\omega$ region [-]
ϕ_i	DMD mode
φ	Leading-edge sweep angle [° (deg)]

ω	Specific turbulent dissipation rate [m^2/s^3]
ω	Angular frequency [1/s]
$\boldsymbol{\omega}$	Vorticity vector [1/s]
Ω	Absolute vorticity [1/s]
$\Omega_{ij}, \boldsymbol{\Omega}$	Vorticity tensor [1/s]
$\omega_x, \omega_y, \omega_z$	Vorticity [1/s]

Constants

Sutherland's law:
$T_0 = 273.15\,\mathrm{K}$
$\mu_0 = 1.716 \cdot 10^{-5}\ \frac{\mathrm{m}^2}{\mathrm{s}}$

SST constants:
$\beta^* = 0.09$
$\kappa = 0.41$

Inner SST constants $(k-\omega)$:
$a_1 = 0.31$
$\beta_1 = 0.075$
$\sigma_{k1} = 0.85$
$\sigma_{\omega 1} = 0.5$
$\gamma_1 = \beta_1/\beta^* - \sigma_{\omega 1}\kappa^2/\sqrt{\beta^*}$

Outer SST constants $(k-\epsilon)$:
$\beta_2 = 0.0828$
$\sigma_{k2} = 1.0$
$\sigma_{\omega 2} = 0.856$
$\gamma_2 = \beta_2/\beta^* - \sigma_{\omega 2}\kappa^2/\sqrt{\beta^*}$

DES Constant:
$C_{\mathrm{DES}} = 0.61$

Discrete vortex detection filters:
$\lambda_{2,\mathrm{rms,Filter}} = 4 \cdot 10^4\ 1/\mathrm{s}^2$
$\lambda_{2,\mathrm{avg,Filter}} = -2 \cdot 10^4\ 1/\mathrm{s}^2$
$\lambda_{2,\mathrm{Peak,Filter}} = -1 \cdot 10^5\ 1/\mathrm{s}^2$

1 Introduction

To better understand the benefits and challenges associated with leading-edge vortex control, this chapter provides a historical overview of relevant technologies. Additionally, applications of flow control on transport aircraft and delta-wing configurations are presented. As well as recent research on leading-edge vortex manipulation, flow control approaches applied on the "Vortex Flow Experiment 2" (VFE-2) configuration are highlighted. In the final subsection, the motivation for conducting the present investigation is summarised. The unique design of slot geometry investigated in this work simulates unsteady vortex generators (VGs), offers a new perspective on vortex interaction and complements with detailed analysis current research on unsteady vortex-flow manipulation.

1.1 State of the Art in Flow Control

1.1.1 Historical Perspective

Gad-El-Hak [36] introduces *Flow Control* as a multi-disciplinary field of a very high technological importance, through which flow states are altered to achieve beneficial outcomes (e.g. transition delay/triggering, separation postponement, lift enhancement, drag reduction, turbulence augmentation/reduction or noise suppression). The author separates the history of flow control into five eras. In the empirical era (before 1900), mankind develops mechanisms for controlling the flow of rivers and irrigation systems. With the postulation of Prandtl's boundary layer theory presented in 1904 [117], the scientific era of flow control begins, in which its theoretical foundations are developed (1900–1940). The World War II era is represented by development of flow control in military applications in search of better aircraft performance, speed and manoeuvrability (1940–1970). An overview of military applications is presented e.g. in [77]. During the energy crisis (1970-1990), the main research focus, assisted by the application of CFD, was to increase efficiency by reduction of skin friction drag. In the following era ($\geq$1990), advancements in microelectronics enabled the development of reactive flow control systems, manipulating coherent flow structures and flow instabilities.

1.1.2 Present and Future Trends

The field of flow control is vast, incorporating a considerable number of technologies [32]. Therefore, two classification schemes for devices are discussed here. The methods can be categorised as passive or active means for flow manipulation. The passive mechanisms, which are deployed throughout the entire operation, have the advantage over active

mechanisms that no external energy input is required for operation. This means that they extract energy from the local flow even in situations when no control is needed. For example, at the cost of parasitic drag during design conditions, vortex generators (VGs) produce streamwise vortices that enhance the energy transport towards the boundary layer, making it more resistant to separation at high flow incidences (e.g. stalled airfoil) [24, 31]. The same effect can be achieved with skewed and pitched pulsed jets as an Active Flow Control (AFC) system and are available on demand without detrimental effects at design conditions (apart from additional weight).

Another classification of flow control systems distinguishes between steady and unsteady flow disturbance generation. Passive control devices are generally steady (e.g. VGs, bleed air, Gurney flaps or turbulators) whereas active flow control is mainly unsteady (adaptable or periodic). Unsteady passive devices find application in flow induced excitation of a surface, e.g. delta wing [141], or fluidic oscillators [80]. For better efficiency, periodic disruption of the flow field is more appealing because flow instabilities can be addressed in order to achieve the manipulation of the mean flow field [44].

Colis et al. give a wide and very interesting perspective of current directions of AFC technology development, highlight important theoretical and numerical issues and propose a generic roadmap for oscillatory AFC applications in separation control [30]. The authors also highlight the importance of cooperation between the fields of flow instability and flow control. A good understanding of inherent flow instabilities is required for an efficient manipulation thereof, which leads to an alteration of the mean flow field [145]. The main control theories comprise: open-loop, closed-loop, optimal control and reduced-order modelling. Machine learning and current computational power has also unlocked model-based approaches that offer robust control strategies. Because they offer great potential for aiding the AFC research community, important aspects on numerical approaches of baseline and disrupted flow field are discussed for RANS, LES and DNS. The suggested roadmap includes the definition of a target in flow physical variables, mechanisms to achieve the targeted process, applied methods, needed tools along the routes and technology readiness level (TRL) indication for each route [30].

1.1.3 Separation Control

Greenblatt and Wygnanski review periodic actuation flow separation control devices [44]. The two-dimensional (2D) separation scenario is of supreme technological interest, as it leads to a significant loss in aerodynamic performance (lift decrease, drag increase). The authors offer a historical perspective on research efforts to understand and control different relevant types of 2D (from flap, aerofoil, backward-facing step, convex/concave surfaces, etc.) and 3D flow separation (swept leading edges, separation behind blunt geometries, etc.). The separation process constitutes of periodic shedding of coherent structures. The review article proves that periodic hydrodynamic excitation promotes the generation of these structures, which are responsible for momentum transport across the mixing layer. As a result, excitation of the shear layer reduces the mean separation bubble or even reattaches the flow to the surface of a deflected flap [109], flat plate [42] or an airfoil [129, 130] by energising the bubble.

There are two key actuator parameters expressed in flow physical terms: reduced frequency F^+ (equivalent to the Strouhal number St) and momentum coefficient c_μ (amplitude), both of which have been explored in extensive parametric studies. The mathematical definitions of both parameters are expressed as:

$$F^+ = f_a \cdot \frac{l_{\text{ref}}}{U_\infty}, \tag{1.1}$$

$$c_\mu = \frac{\rho_j \overline{u_j'^2} A_j}{0.5 \rho_\infty U_\infty^2 A_{\text{ref}}}. \tag{1.2}$$

The actuation frequency f_a is non-dimensionalised by the convective time scale, which is the ratio of a typical reference length l_{ref} (wing root c_r or flap chord length l_f) to freestream velocity U_∞. The momentum coefficient c_μ relates the unsteady jet momentum (the product of density ρ_j, mean square of the jet velocity fluctuation u_j' and the slot exit area A_j) to the freestream momentum based on a reference area (dynamic pressure $\times$ area) $0.5\rho_\infty U_\infty^2 A_{\text{ref}}$. In most cases, the reference area is equal to the wing area, $A_{\text{ref}} = A_w$. With the assumption of incompressibility and with the jets operated with same medium as the outflow, the density terms are equal, $\rho_j = \rho_\infty$, and can be removed from (1.2).

Figure 1.1 shows the effect of excitation frequency on the coherent structures of a mixing layer [112]. Because a shear layer is naturally unstable, the KH instability generates discrete vortices along the mixing layer. The vortex generation can be controlled/ordered by disturbing the shear layer with a constant frequency. Doubling the excitation frequency increases the number of vortices in the shear layer (or vortex sheet) and reduces their diameter. According to a mathematical deduction presented in [44], the reduced frequency for maximum mass transfer across the mixing layer is achieved with F^+ in the order of magnitude of $\mathcal{O}(1)$. This has been validated by numerous experiments presented in the review article.

Figure 1.2 presents the results of one of the aforementioned experimental investigations [109]. The paper concerns itself with the isolation of parameters amplitude c_μ and frequency F^+ and the understanding of the underlying physical mechanisms based on excitation at the shoulder of a deflected flap. The momentum coefficient has a minimum at $F^+ \approx 1$, for reattachment, and $2 \lesssim F^+ \lesssim 4$, for separation prevention [44].

Periodically exciting the flow in the vicinity of separation above airfoils, which generally occurs at the leading edge, mitigates separation and increases performance at stall and post-stall. In the latter flow regime, the lift gain is one order of magnitude higher than the former (cf. Figure 1.3). At post-stall, periodic excitation of the separated shear-layer with a defined frequency alters the "bluff body" shedding frequency, which is typically found around a Strouhal number of $St = 0.2$. Increasing the momentum transport across the separated shear layer by frequency conditioned AFC reduces the separation region and can even lead to flow reattachment [44].

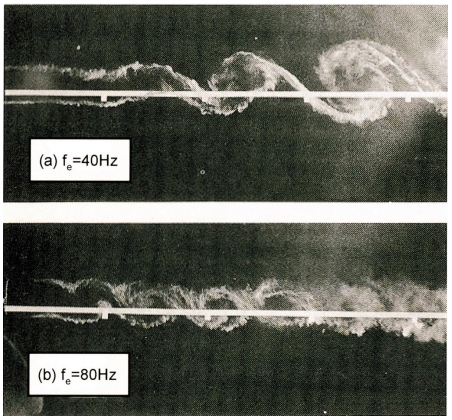

Figure 1.1: Frequency dependent coherent structures in a shear layer [112].

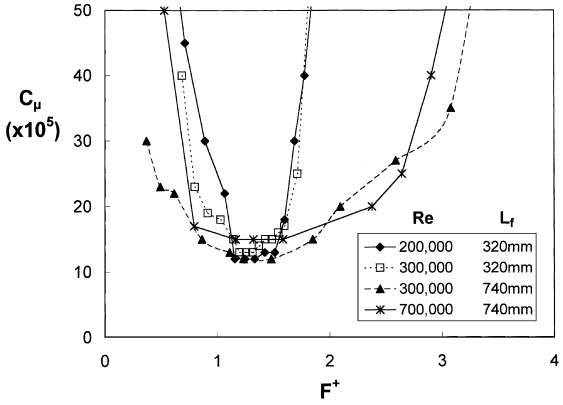

Figure 1.2: Minimum momentum coefficient vs.
reduced frequency of periodic flow excitation [109].

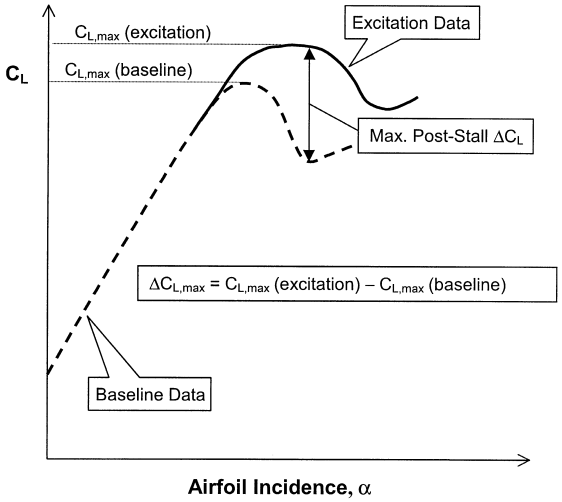

Figure 1.3: Lift gain by separation mitigation through periodic excitation [44].

In an attempt to assess the effect of disturbance injection on separation control applied on an airfoil with spanwise piezoelectric cantilever-type actuators distributed applied either 2D (synchronised) or 3D (desynchronised), Seifert showed that the former provided a greater performance increase [130]. Additionally, better lift was achieved on a delta wing when the actuators were synchronised (2D) as opposed to being operated with phase delay (3D) [95]. 2D disturbances are also more easily introduced in the flow [44]. A parallel can be made with the natural laminar–turbulent transition process, which is initiated by 2D Tollmien–Schlichting instability, demonstrating the more dangerous nature of planar disturbances [138]. At this point, it is worth restating that the instability theory is a key element in efficient flow control.

1.1.4 State-of-the-Art Actuators

In AFC applications, the actuator is the component that interacts directly with the flow. Cattafesta and Sheplak present a review of current actuators [24], in which their specifications, characteristics, selection, design and classification are discussed. Historically, actuators evolved in two directions: either applying the brute-force or the small-disturbance method. Recent research focuses more on the latter method, as it promises an increase in efficiency. Targeting flow inherent instabilities with small localised amplitudes can alter the mean flow with minimum energy input (see Section 1.1.3). After highlighting the opposed requirements of actuators and sensors and the issues of dimensional analysis, the authors offer a review of state-of-the-art actuators. Classification of AFC actuators can be separated into a number of key dimensions: open/closed-loop control, application and flow regime. Three main types of actuators are assessed: fluidic, moving-surface and plasma actuators (Figure 1.4). Here we will briefly discuss State-of-the-art actuator types and their characteristics.

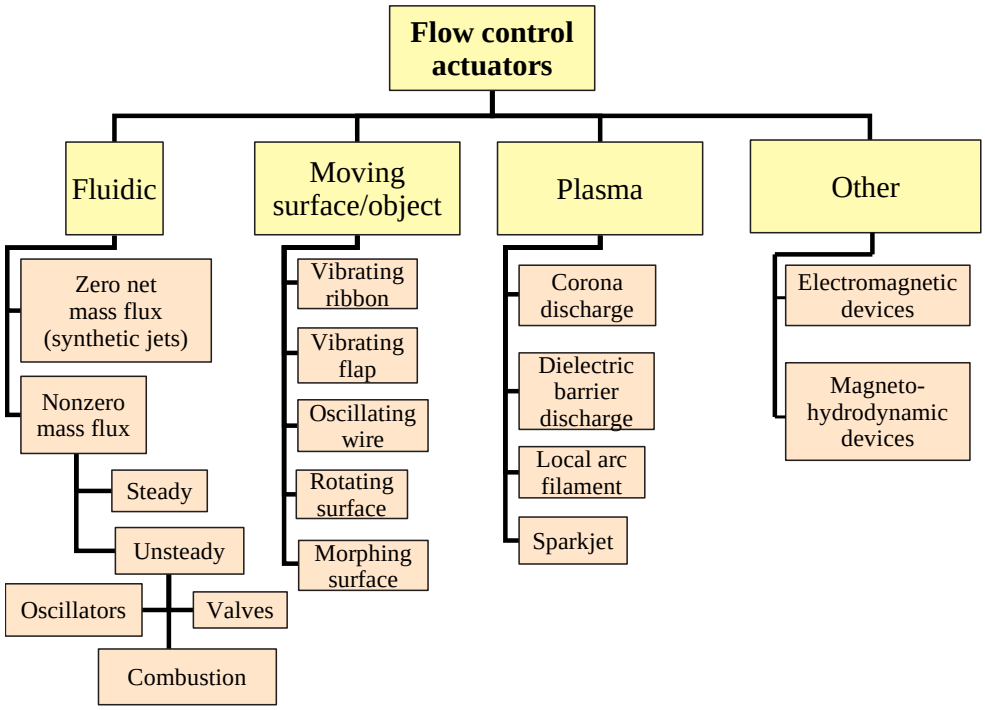

Figure 1.4: Actuator types, based on [24].

Zero-net-mass-flux (ZNMF) actuators are composed of a moving surface inside a cavity connected by an orifice with the outer region. Using the inverse piezoelectric effect or electromagnetic devices, the membrane oscillates, generating periodic suction/blowing of fluid at the slot location. Hence, periodical vortex rings are injected into the flow and develop a time-averaged jet (synthetic jet) [86, 97] (cf. Figure 1.5). The advantages of such devices are low-power requirement, broadband output and no necessity of external fluid. However, limited maximum velocity amplitude, mechanical fatigue of the

resonating membrane, acoustic pollution and slot contamination restrict the application of ZNMF actuators [24]. In [43] and [46], synthetic jet actuators successfully reduce separation over a generic hump and a rotor aerofoil, respectively.

The limitations in disturbance amplitude of synthetic jets can be overcome by **pulsed jets** at the cost of the requirement for external fluid. A pulsed jet is generated by a steady jet system with an additional valve that blocks or allows flow. Regarding efficiency, pulsed jets are superior to steady jets, as the average injected momentum and consequently the input power is significantly lower [44]. Variations of the nozzle geometry and direction extend the application range of pulsed jet actuators (e.g. microjets and vortex generator jets).

Pulsed or sweeping jets can also be generated by **fluidic oscillators** instead of valves. This technology, first reported in [80], has no moving parts and relies instead on alternating separation from a diverging nozzle using the Coandă effect, cf. Figure 1.6. The major drawbacks of this technology include the lack of design tools and the coupling of mass flow rate with frequency, which poses challenges in their integration into feedback-loop control systems.

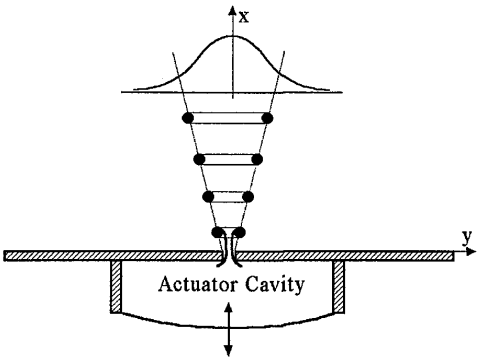

Figure 1.5: Synthetic jet actuator [86].

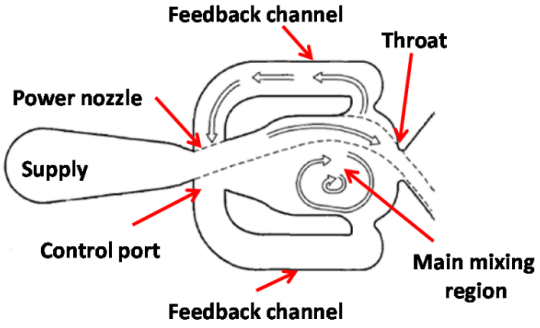

Figure 1.6: Fluidic oscillator [63].

Of the vast number of devices with **moving-surface** technologies, recent research focuses on piezoelectric driven miniature flaps or dimples, e.g. in [130]. Their very fast response time makes feedback control more responsive. In addition, their compactness and low energy usage make them a suitable candidate for active transition and separation control [24].

The third category of flow control represent the **plasma** actuators. A plasma actuator is composed of minimum two electrodes separated by a dielectric material. Under voltage, an electric field is generated between the electrodes, ionizing the fluid in between. Due to the potential difference, a force drives the charged particles (ions) towards the lower potential, which entrains neutral particles leading to mass flow between the electrodes. These systems have no moving parts, are compact and respond quickly - an advantage for feedback-loop control. However, they have a limited velocity amplitude require significant energy input [24].

Overviews of recent developments regarding actuators for wind-tunnel and in-flight tests are presented in [113, 122] at the NASA (The National Aeronautics and Space Administration) Langley Research Centre and in [144] at the French Research Centre (ONERA – Office National d'Etudes et de Recherches Aérospatiales).

1.1.5 Applications in the Aviation Industry

The technological relevance of AFC has lead to an exponentially increasing rate of publication in the field in the last 50 years [32]. Still, relatively few of these concepts mature to a market-ripe technology. This is largely due to the still too small benefit of most AFC devices, the technological complexity, costly manufacturing and mantaince, and the necessity of a fallbacksystem. In this subsection, flow control devices and current research trends are described for successfully tested aeronautical applications.

Current research conducted at the NASA Langley Research Centre includes noise reduction in cavity flows by shear-layer excitation, unsteady circulation control by Coandă blowing, characterization of ZNMF actuators and computational tools for flow control modelling [113, 122].

Wlezien describes successful implementations of micro adaptive flow control investigated at DARPA (Defence Advanced Research Projects Agency) [155]. By removing the low-energy boundary layer above a compressor blade, separation is delayed, which allows for more aggressive blades that achieve higher pressure ratios. This design results in fewer compressor stages, which reduces weight and cost. The Active Core Exhaust (ACE) control developed by Boeing for the C-17 includes compressor bled air injected through fluidic oscillators into the engine exhaust jet [28]. The manipulation of component flow in jet-engine applications is reviewed in [92].

Instead of conventional moving control surfaces, synthetic jet actuators [4, 152, 155] and sweeping jets [75] can alter the pressure distribution around wings and unmanned aerial vehicles (UAVs) contributing to weight reduction and performance increase. Both synthetic jets and vibrating surfaces inducing disturbances at the flapperon's shoulder reduce local flow separation during the hover flight of a V-22 Osprey. The performance increase translates to a 1000 lbs higher payload [155]. The same review paper reports a reduction in shock induced separation at supersonic air intakes. This concept was dubbed Mesoflaps for Aeroelastic Transpiration (MAT)[156].

Shmilovich and Yadlin present three approaches to flow control investigation for the increase of high-lift performance and alleviation of wake/ground vortex in transport aircraft applications [134]. These approaches are based on unsteady RANS simulations and are economical approaches for modelling large parameter variations. Thus, the effect of AFC parameters (e.g. jet location, direction, frequency and phase) on the flow field can be investigated numerically. Promising performance increases have been reported for single/multi-element high-lift wing configurations when distributed ZNMF actuators are employed [78, 79, 133, 159]. Destabilising the wing tip vortex on transport aircraft is of great economical significance as it reduces the limiting minimum staggering during approach. The actuation composes of pressurized bleed air from the engine compressor supplying lateral directed air jets at the wing tip. Periodic excitation is achieved by

harmonic swivelling of the jet nozzles. Frequency-modulated control leads to accelerated trailing vortex decay [132].

Current experimental investigations at ONERA target TRL enhanvement of mechanical and fluidic devices for flow manipulation. In [144], Ternoy et al. report on progress in actuator manufacturing, testing and qualification. Both mechanical and fluidic actuators inject periodic momentum into the flow, altering its state for performance increase (i.e. lift increase, drag decrease). The investigation targets realistic flow conditions (transonic) for technology validation. In this regard, the performance increase resulting from mechanical/fluidic miniature unsteady trailing edge devices (TEDs) was tested for transport aircraft wings at cruise flight. These devices increase the aerofoil's back loading, thus increasing lift and shifting the shock position downstream. Other novel AFC devices investigated at ONERA include "on-demand" VGs [144]. Application examples include separation reduction over retreating rotor blades with the unsteady deployment of metal plates and buffeting alleviation with pulsed jets.

1.1.6 Civil Aircraft

An overview of recent applications of flow control on civil transport aircraft and their corresponding issues is given in [8]. The authors point out that further research is required to safely operate flow control devices. Therefore, realistic conditions, integration and redundancy are important aspects to be considered for aeronautical compliance. Breakthroughs in AFC applications can be achieved by incorporating AFC integration in the early aircraft design phase. The devices bring additional weight and complexity, which has to be compensated for by a net performance increase. The paper presents examples of increased aircraft component performance with modern AFC devices. The flow region to be manipulated is the wing and the high-lift systems. The potential of AFC lies in flow amelioration at off-design conditions. One such example is given by the separation mitigation in the pylon-wing junction during take-off [89]. Another component flow that can be improved for better performances is the flow around the vertical stabilizer [90]. AFC also compensates the detrimental effect of sharklets at high-angle-of-attack regimes [9].

A sensitivity analysis of AFC system operational parameters on overall mass and power consumption of an Airbus A320 is provided in [74]. The conducted study assesses power distribution, compressor scaling (centralised/decentralised) and actuator parameters (amplitude, frequency, velocity ratio) in terms of overall efficiency and identifies limitations. The authors predict that first aircraft applications of AFC devices will be fluidic and piezoelectric, which are suitable for off-design performance increase. Only after further research into alternative power supplies, can plasma actuators be integrated.

1.2 Leading-Edge Vortex Control

1.2.1 Controlled Flow Features

Vortex control is quite a versatile process and is therefore broken down by Gursul into three technologically relevant vortex types: leading-edge vortex (delta wing), tip vortex (rectangular wing) and wake vortex (bluff body) [53]. In order to efficiently control these types of vortices, knowledge of the flow physics and the corresponding influential parameters is required. Table 1.1 identifies the main control parameters for each flow feature.

Table 1.1: Vortex physics and parameters, based on [53].

Flow features	Control parameters
Separation and vortex formation	Angle of attack and sweep angle
Vortex growth	Swirl angle and circulation
Vortex breakdown	Swirl angle and adverse pressure gradient
Vortex instabilities and unsteadiness	Periodic excitation
Vortex-vortex interaction	Radius–distance ratio
Vortex-jet interaction	Jet momentum, distance and orientation

Initial flow separation leading to vortex formation is an important flow feature and can be manipulated by changing its location. While separation coincides with the sharp edges, blunt/rounded edges lead to variations in the separation region, which are dependent on edge curvature, roughness and freestream conditions [23]. The edge direction relative to the inflow vector is given by the incidence α and sweep angle φ. These parameters directly influence the vortex strength, structure and position [53].

The downstream vortex development is dependent on the swirl (ratio of azimuthal to streamwise velocity), which in turn affects the streamwise pressure gradient. The vortex layer detaching from the surface and feeding the vortex contributes to a downstream monotonic circulation increase. Vortex breakdown is mainly influenced by the swirl angle and streamwise pressure gradient. It has been demonstrated that reaching a swirl angle of 50° leads to vortex breakdown [57] (see also Section 2.5).

In a shear layer, the KH instability promotes the generation of discrete vortices that interact with each other, contributing to vortex roll-up. Vortex generation can be manipulated in order to affect the shear layer's curvature (see Section 1.1.3). Injecting periodic disturbances in the flow influences the flow inherent instabilities and unsteadiness.

The helical-mode instability downstream of breakdown causes unwanted quasi-periodic pressure fluctuations [12, 48]. Exciting this instability leads to an increased spreading of the swirling flow, as demonstrated in [47].

The vortex–vortex or vortex–jet interaction are influenced mainly by the relative distance, vortex strength and orientation. These interactions may include vortex merging, vortex destabilisation or turbulence injection, depending on the volitional effect [53].

1.2.2 Passive Control

As discussed in Section 1.1.2, passive control implies disturbance injection by steady (surfaces, bumps, strakes, VGs and bleed) or unsteady means (flexible wing and fluidic oscillators) without any external energy input. The energy required for disturbance generation (i.e. discrete vortex) is extracted from the baseline flow. The double-delta [93, 148] and canard-delta configurations demonstrate [69, 110] increased maximum lift and stall angle as a result of interaction between multiple vortices. Based on CFD simulations, Hitzel demonstrates the improvement in high-angle-of-attack rolling stability, when leading-edge root extensions are mounted on a modern fighter jet [62].

Passive vortex excitation by flow induced oscillations of a flexible non-slender delta wing proved a significant enhancement in maximum lift compared to that of a rigid wing [141]. The flow unsteadiness increases with the angle of attack, exciting the asymmetric structural bending mode of the flexible wing. The fluid/structure interaction is self sustained and represents a passive feedback actuation. The structural Strouhal number is in the same order of magnitude as the shear-layer instability ($St = \mathcal{O}(1)$).

1.2.3 Active Flow Control

The delay of vortex breakdown is successful if the swirl angle is reduced by axial momentum injection in or along the vortex core, as investigated on a 70° delta wing by [105, 126]. In practical terms, breakdown is "blown away" by the additional axial momentum. However, steady blowing requires a many-fold increase in energy input and a continuous fluid supply when compared with unsteady (periodic) fluid injection. On the same delta-wing platform (70°), researchers conducted experimental [55, 135] and complementary numerical investigations [33, 105] on breakdown control by periodic sinusoidal blowing/suction at the leading edge.

The main two dimensionless control parameters, the momentum coefficient c_μ and the reduced actuation frequency (disturbance Strouhal number) F^+, were varied to observe maximum breakdown delay [55]. Smoke visualisations reveal maximum downstream shift of the breakdown point at actuation parameters set at $c_\mu = 0.45\%$ and $F^+ = 1.2 - 1.4$, at a Reynolds number of $Re = 1 - 5.5 \cdot 10^5$. However, according to transient water-tunnel particle image velocimetry (PIV) investigations (at a lower Reynolds number $Re = 2.5 \cdot 10^4$), vortex breakdown is in fact not delayed, but breakdown wake is reduced due to local axial momentum increase [135].

A major pitfall in investigating breakdown delay is the large fluctuations in the the breakdown (stagnation) point, which make its determination by measurements more difficult. CFD modelling of the unforced and forced flowfield is an alternative. In [105], the simulations of the flow past a 70° swept delta wing angled at $\alpha = 35°$ demonstrated a breakdown downstream shift of 25% root chord length and a relative normal force increase of 27% when periodic blowing/suction was applied ($c_\mu = 0.7\%$, $F^+ = 2.2$).

According to phase-averaged PIV investigations, the blowing phase generates a strong shear-layer vortex that enhances the momentum transport into the primary vortex core (cf. Figure 1.7). While the breakdown location remains mostly unaffected, axial velocity

increases near the surface, increasing suction and, thus, the normal force. The phase-averaged lateral motion of the vortex core due to periodic forcing is elliptical.

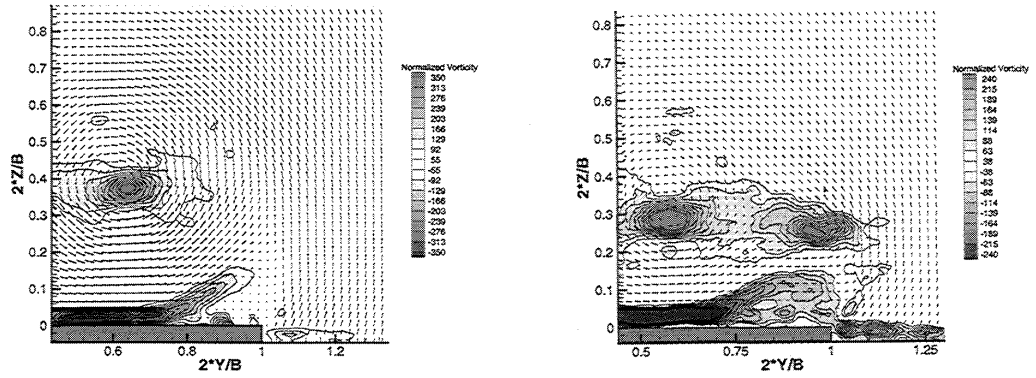

(a) Unforced flow. **(b)** During blowing (phase 120° of sinus).

Figure 1.7: Axial vorticity distribution in the crossflow plane $x/c_r = 0.4$ above a $\varphi = 70°$ delta wing [135].

Alternating blowing and suction tangential to the rounded leading edge of a 75°-swept delta wing proved a farther downstream shift of the breakdown point, $\Delta x/c_r = 0.46$ (cf. Figure 1.8), than the steady counterpart [45] (0.26 and 0.35 for steady blowing and suction, respectively). The angle of attack investigated, $\alpha = 54°$, corresponds to a breakdown occurring near the apex. The optimal control parameters for periodic disruption are $c_\mu = 0.36\%$, $F^+ = 1.3$. The same smoke visualisation technique used in the investigation showed a long-time lag of the breakdown location in response to removing the applied actuation. This high hysteresis of breakdown in response to delta wing maneuvers (e.g. pitching) is reported also in [121, 157].

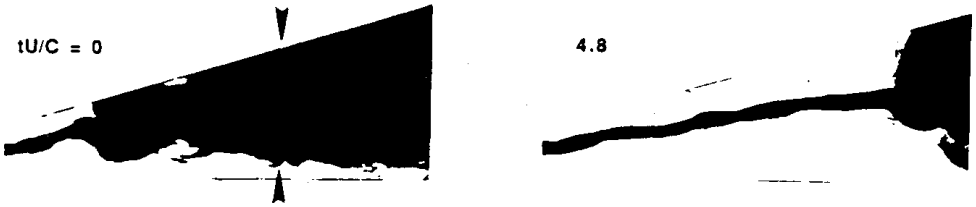

Figure 1.8: Dye visualising the vortex core and the breakdown point at the start (left) of blowing/suction and farthest downstream breakdown displacement, $t \cdot U_\infty/c_r = 0.9$ after actuation interruption, $Re = 1.7 \cdot 10^4$ [45].

Oscillating piezoelectric membranes generate sinusoidal blowing/suction through slots located in five segments along the leading edge of a 60° delta wing [95]. A study of the lift gain in relation to the actuation signal concluded that a low frequency burst mode actuation ($c_\mu = 0.03\%$, $F^+ = 1.0$) generates almost 25% more normal force compared to a sinusoidal low-frequency modulated signal ($c_\mu = 0.4\%$, $F^+ = 2.0$) at ten

times less input momentum. Conclusively, the shear layer receptivity of disturbances is strongly dependent on the actuation mode signal. The dynamics involving the shear-layer manipulation over a delta wing is analogue to 2D separation control, discussed in Section 1.1.3.

The KH instability generates downstream amplified discrete vortices that induce the inboard bending of the shear layer [37]. Periodic wing rolling at optimum frequency reorders and strengthens the shear-layer vortices and the curvature of the vortex sheet (cf. Figure 1.9), leading to reduction of the separation region or even to flow reattachment [38, 54, 103]. Analogue to the planar (2D) separation scenario discussed in Section 1.1.3, lowest disturbance amplitudes c_μ are required if the reduced actuation frequency is adjusted to $F^+ = \mathcal{O}(1)$.

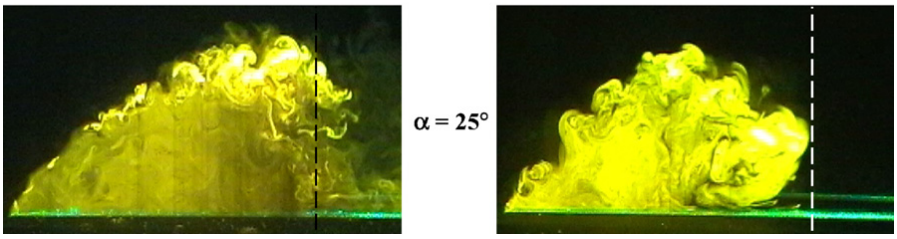

Figure 1.9: Flow visualisation of a stationary (left) and rolling wing with a reduced frequency of $F^+ = 1$ (right) [54].

Table 1.2 sums up the investigations discussed above. The first columns show the actuation mode and the sweep angle. The list's order corresponds to downwards increasing sweep angle. Comparative to the fluidic AFC devices, the first four rows represent oscillatory surface movements, either through passive fluid–structure interaction [141] or rigid wing motion [52, 147, 158]. For optimal periodic flow control on leading edge vortices, the actuation frequency is adjusted for achieving maximum axial momentum transport, at $F^+ = \mathcal{O}(1)$. Frequency tuning allows minimum momentum coefficients ($c_\mu = 0.03\% - 0.80\%$), at which the flow is greatly altered. The effects of actuation are: breakdown delay (BD), separation reduction (SR), breakdown wake reduction (WR) and KH instability alteration. With these parameters, the flow control devices improve considerably the lift on the investigated delta wings. By shear-layer reattachment on a non-slender wing even a relative normal force coefficient increase of $\Delta C_Z = 64\%$ is possible [154].

Table 1.2: Optimal control parameters from several publications.
BD – breakdown delay, SR – separation reduction and
WR – wake-type-region reduction (without necessarily delaying breakdown).

Mode	Sweep angle	c_μ	F^+	Effect	Reference
Flexible structure	40°		$\mathcal{O}(1)$	SR	[141]
Pitching oscillation	38.7°		2.06	SR	[158]
Oscillating wing	$30° - 50°$	$\Delta\phi = 5°$	1–2	BD, SR	[52]
Rolling wing	50°	$\Delta\phi = 1°$	1.00	SR	[147]
Pulsed blowing	45°	0.25%	0.70	SR	[25]
Oscillatory blowing	50°	0.80%	1–2	BD, SR $\Delta C_Z = 64\%$	[154]
Periodic blowing	60°		5.50	KH alteration	[38]
Burst mode ZNMF	60°	0.03%	1.00	$\Delta C_Z = 20\%$	[95]
Sine mode ZNMF	60°	0.40%	2.00	$\Delta C_Z = 15\%$	[95]
Sine ZNMF	70°	0.45%	1.2–1.4	$\Delta x_{bd}/c_r = 20\%$	[55]
Sine ZNMF	70°	0.40%	1.75	WR	[33, 135]
Sine ZNMF	70°	0.70%	2.20	$\Delta C_Z = 27\%$ $\Delta x_{bd}/c_r = 25\%$	[103]
Tangential ZNMF	75°	0.36%	1.30	$\Delta x_{bd}/c_r = 46\%$	[45]

1.2.4 Feedback Flow Control

The integration of AFC devices in closed-loop feedback systems brings advantages with respect to open-loop systems in terms of pilot input. Therefore, the right correlation between a sensing variable and a suitable flow control parameter is essential for designing the feedback chain. This has been achieved in [51] using a single unsteady surface pressure measurement point. The pressure rms is nearly linearly correlated (within a certain range) with the incidence angle α. The pressure fluctuation $p'(t)$ is used as input of the feedback loop, which is sketched in Figure 1.10. At a constant angle of attack, the breakdown location is a linear function of the leading-edge sweep. When breakdown approaches the aft pressure port, the fluctuations increases. Breakdown delay is then achieved by increasing the sweep angle. In a flow sense, this translates into reduction of the swirl angle upstream of breakdown.

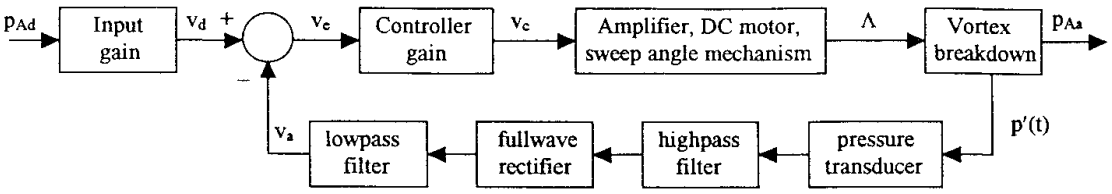

Figure 1.10: Closed-loop feedback block diagram for of active breakdown control [51].

Surface pressure measurements were also used for feeding the closed loop system in [91]. In this investigation, the authors propose a reactive flow controller based on an AFC dynamic model of vortex breakdown location. The actuator is a modulated jet along the core. The method was validated in wind tunnel tests.

The use of microfabricated electromechanical systems (MEMS) have reached popularity recently and show great potential in the sensing part of closed-loop flow control [98]. In addition, this technology can be used also as moving-surface actuators, which can be easily integrated on a delta-wing's leading edges [67]. The generated rolling moment is significant and can be applicable to UAV flight control.

1.3 Motivation

1.3.1 Vortex Flow Experiment 2

The delta wing geometry investigated in the current thesis represents the geometry of the "Vortex Flow Experiment 2" (VFE-2), which is defined in [29]. The objectives of this project was the generation of a vast aerodynamic and flow data set for the generic 65° swept delta wing [70, 71]. The influence of leading-edge radius, Reynolds number, Mach number and angle of attack on the flow field and aerodynamic characteristics of the VFE-2 model was investigated both experimentally and numerically by several participating institutions from different countries. Independently obtained experimental results on the wing model with sharp edges are presented in [29, 35]. Complementary numerical investigations are conducted in [3, 85, 140, 160]. The vast aeronautical data set obtained for the baseline geometry offers a reference case for comparing retrofitted flow control devices. This section reports on some passive and active flow control devices applied on the VFE-2 configuration, including the investigations preceding the current thesis at the Chair of Aerodynamics and Fluid Mechanics of the Technical University of Munich (TUM-AER). Section 3.2 details geometric parameters of the VFE-2 delta wing.

1.3.2 Flow Control on VFE-2

Based on the VFE-2 generic delta-wing geometry, Chen and Wang manufactured sinusoidal leading edges and investigated by means of PIV the flow field at $\alpha = 10°$ around the unmodified and modified geometry [27]. The sinusoidal leading edge represents a biomimetic approach for passive flow control, as observed for example on the fins of humpback whales. By locally varying the sweep angle, a multiple leading-edge vortex system is generated above the wing, instead of the two vortex system of the baseline case at same flow conditions (cf. Figure 1.11). Both investigated geometries generate an equal amount of suction at low angles of attack, however, locally varying sweep angle pushes the breakdown occurrence towards higher angles of attack than a constant leading-edge sweep angle of $\varphi = 65°$.

Other applications of flow control to the VFE-2 wing with sharp leading edge conducted at TUM-AER are presented briefly here. Numerical analysis by means of LES demonstrated that bleed air from the pressure side and injected into the core delays breakdown as demonstrated in Figure 1.12, which compares the leading-edge vortices visualised by the Q-criterion for the baseline and the slotted geometry [162]. This passive method shows great perspective for delta wing performance increase.

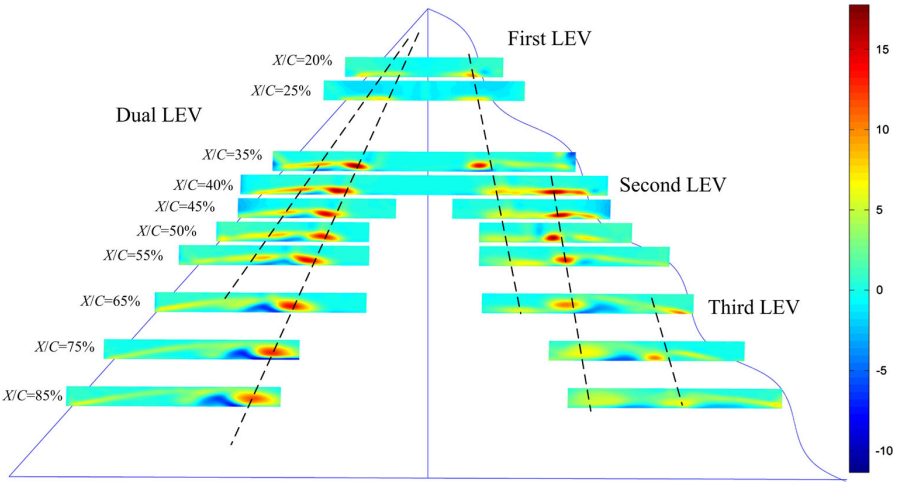

Figure 1.11: Leading-edge vortices above a VFE-2 model. left – straight leading edge, right – sinusoidal leading edge [27].

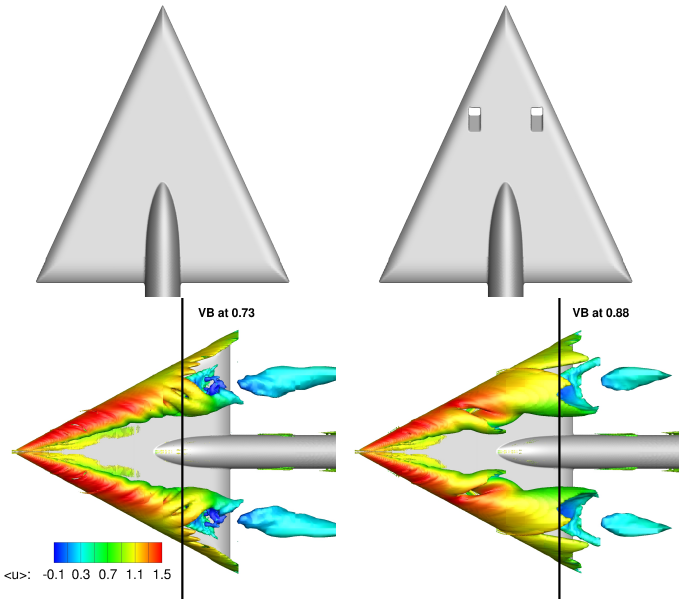

Figure 1.12: Vortex system above the VFE-2 configuration at $\alpha = 28°$ with designated vortex breakdown location. Left – baseline, right – pressure side slots. [162].

1.3.3 Preliminary Investigations

Preceding the current investigations, Kölzsch conducted experiments at TUM-AER with two unsteady active flow control mechanisms integrated along each leading edge of the two manufactured delta wing half models, representing the VFE-2 configuration [82] (cf. Figure 1.13).

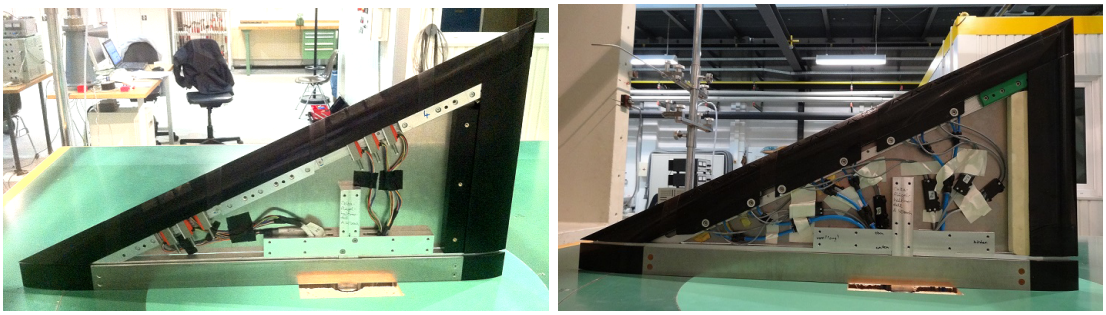

Figure 1.13: VFE-2 half delta-wing models with unsteady AFC actuators distributed along the leading edge: Oscillating flaps (left) and pulsed jets (right) [82].

First, the unforced flow field was investigated by means of balance, surface pressure and flow field measurements with the scope of identifying relevant flight regimes. Consequently, three cases were defined corresponding to moderate to very high angle of attack flow conditions, at which the flow demonstrates increased unsteadiness. Hot-wire and unsteady surface pressure measurements with consequent spectral analysis (cf. Figure 1.14) revealed dominant periodic oscillations corresponding to inherent flow instabilities, like the helical-mode and shear-layer instability (detailed in Section 2.6).

Second, frequency-conditioned AFC is applied at the leading-edge. Therefore two half-wing models were manufactured integrating the AFC mechanisms. The commonality of these devices lies in the process of injecting periodic disturbances in form of discrete miniature vortices into the shear layer with the scope of manipulating the natural instabilities for an increase of aerodynamic performance.

Third, an extensive parametric study confirmed that actuating with frequencies close to values measured in the natural flow corresponding to inherent instabilities offers highest alteration of the flow field and aerodynamic characteristics. However, due to the additional momentum injection compared to the oscillating flaps, pulsed blowing has a greater effect on the flow field and aerodynamic coefficients on a wider angle of attack range. In Figure 1.14, the crossflow distribution of x-velocity root mean square (rms) reveals the breakdown wake with local periodic motion. The red PSD curve is the response to $F^+ = 2.6$ pulsed blowing and shows that instabilities are manipulated by shifting the dominant frequencies.

The above investigation concludes that actuating with frequencies of natural flow oscillations stabilises the flow field by reattaching the shear layer. Pulsed jets are superior to leading-edge oscillators because the additional momentum extends the effectiveness over a wider angle-of-attack range beyond stall. At stall, the fluidic actuators even generate additional lift with the expense of additional drag compared to shear layer disturbance without momentum insertion.

Continued research efforts are necessary to answer some still open questions to this promising type of flow control which opens the scene for the current research effort. Therefore, additional PIV investigation by increased longitudinal resolution of crossflow planes, phase-locked sampling and measurements along the core are conducted. Also high-fidelity detached eddy simulations (DES) complement the analysis with transient flow data.

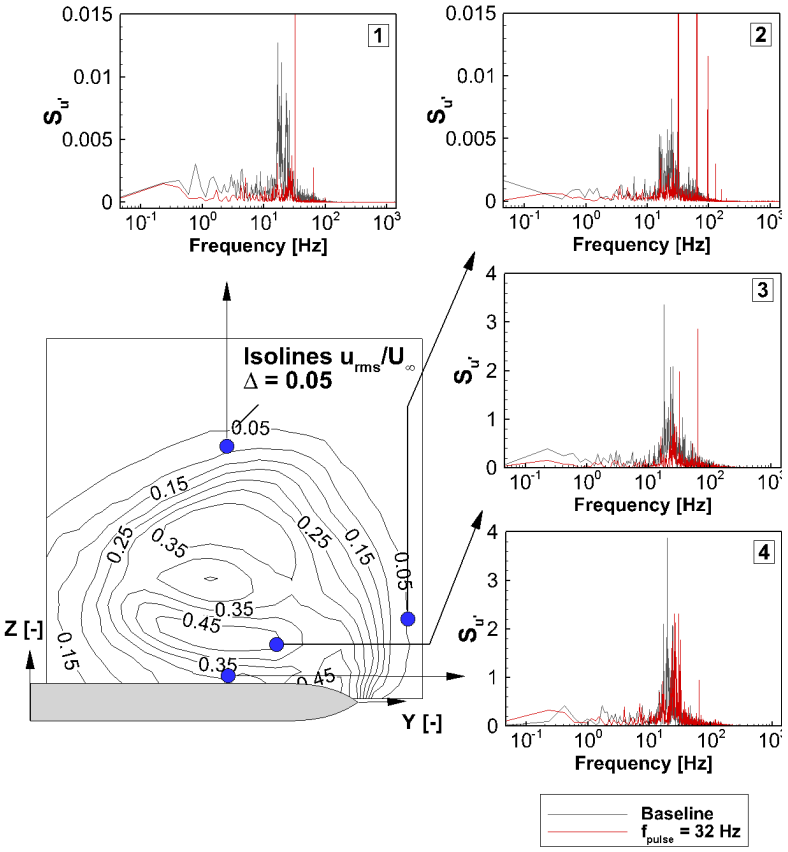

Figure 1.14: Power spectral density distribution in the stalled flow field at $x/c_r = 0.6$ without and with pulsed blowing at $F^+ = 2.6$ [82].

1.3.4 Research Questions

Despite of numerous research investigations on vortex dominated flows and its control, there is still little research on active flow control at very high angles of attack extending beyond the flight envelope borders. Special focus here is on the flight regimes around stall for the VFE-2 model with pulsed blowing. Concerning the delta-wing flow field, the following research questions are answered in this thesis:

- How does the time-averaged 3D flow structure above the wing at high angles of attack respond to pulsed blowing?
- What is the effect of frequency modulation on the flow field?
- How does desynchronised jets affect the flow field and the aerodynamic characteristics?
- What is the fundamental interaction of the periodic jets with the shear layer?
- What are the mechanisms that lead to breakdown delay and shear-layer reattachment at optimal actuation parameters?
- What kind of instabilities are manipulated?

1.4 Outline

This thesis is structured into six chapters. After the introduction, chapter two covers fundamentals in leading-edge vortex flows, followed by the presentation of the experimental and numerical methods in chapters three and four, respectively. Chapter five is the core of the thesis and contains the presentation of experimental and numerical results and their interpretation. The synergy of wind-tunnel measurements with several techniques and numerical simulations brings forth the advantages of each investigative method and offers a holistic view on the natural but also on the manipulated vortex dominated field. A summary of concluding remarks and way-forward recommendations constitute the final chapter.

2 Fundamentals of Leading-Edge Vortices

This chapter covers the physics of leading-edge vortex flow. Particularly, a general description of the vortex is provided. Then the vortex behaviour with respect to some parameters, such as angle of attack and leading-edge sweep angle, is analysed. Finally, the unsteady behaviour is documented including the flow inherent instabilities.

2.1 Leading-Edge Vortex System

Moving a delta wing at incidence through a fluid generates a pair of counter-rotating leading-edge vortices on the suction (upper) side, as sketched in Figure 2.1. The pressure side attached boundary layer separates at the leading-edge becoming a free shear layer. To satisfy the swirl equilibrium, the fluid detaching from an angled edge begins to spiral downstream. The high axial component of the freestream momentum in combination with the vorticity detached from the surface sustains the typical spiralling fluid motion. Thus, the leading-edge vortex is the product of the shear-layer roll-up. With this process, the boundary-layer vorticity detaches from the lower surface and is transported along the shear-layer (feeding-sheet) into the primary vortex core. The linearly increasing feeding of vorticity leads to a conical-flow development along the entire leading edge, as in the sketch of a typicall developed leading-edge vortex system, presented in Figure 2.1.

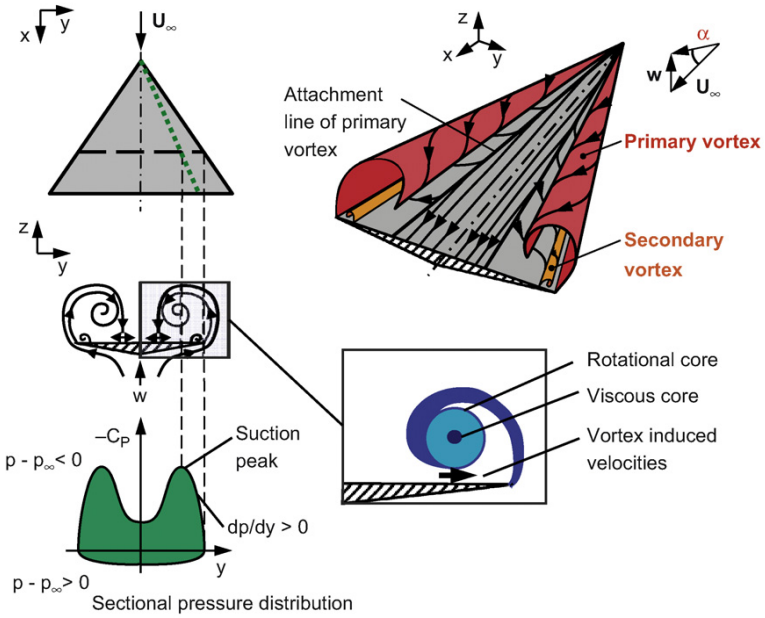

Figure 2.1: Leading-edge vortex system [12].

The red surface in the upper right corner of Figure 2.1 represents the separated shear layer supplemented by swirling streamlines. On the suction side, the vortex system generates a complex pattern of skin friction lines, designating separation and reattachment regions. The primary vortex extends between the leading edge, which coincides with the primary separation line, and the primary (most inboard) reattachment line.

The primary vortex induces high near-wall outboard-directed momentum, generating high suction with maximum below the vortex core. Departing farther in spanwise direction from the suction maximum, the flow encounters an adverse pressure gradient and separates from the surface generating the secondary vortex (orange surface in Figure 2.1). The secondary structure is much smaller, closer to the surface and rotates in the oposite direction compared to the primary vortex. It contributes insignificantly to the integral aerodynamic coefficients, however, it demonstrates a significant displacement effect on the primary structure [68].

2.2 Incidence Dependency

The vortex evolution with increasing angle of attack is presented in Figure 2.2 accompanied by the typical lift polar, as reported also in [12]. At moderate angles of attack, the vortex develops along the entire leading-edge. While increasing the incidence, the leading-edge vortex intensifies and its cross section expands. The core shifts inboard and upwards, aligning with the freestream direction. The leading-edge vortex generates additional lift compared to potential flow theory, also known as the vortex lift. This lift portion increases in a non-linear manner with the angle of attack.

The lift coefficient increases continuously up to the first occurrence of vortex breakdown (or vortex bursting) at the trailing edge. The breakdown phenomenon is a dominant vortex instability that limits the flight envelope. It leads to abrupt core flow deceleration and lateral expansion of the vortex. Downstream, the flow transitions from jet to wake-type and initiates dissipation into turbulence. This important phenomenon is discussed in Section 2.5. The breakdown location moves upstream with further increasing α, until it reaches the apex. Breakdown at the apex signals the onset of stalled flow and reaching maximum lift. Beyond $\alpha_{\max}$, lift decreases with α and the vortex collapses generating complete separation on the suction side, similar to bluff-body wake flow.

2.3 Sweep Effect

In a review paper on the leading-edge flow, Gursul categorizes the delta-wing configurations in slender and non-slender wings based on φ [49]. Non-slender wings have a leading edge sweep angle of up to $\varphi = 55°$. For $\varphi \geq 65°$, the wing is defined as slender. Consequently, wing configurations with sweep angle in between both categories ($55° \leq \varphi \leq 65°$) can be considered as semi-slender. The sweep classification in Table 2.1 is based on sweep angle ranges that are approximated and do not represent universally defined bounds. The vortex system is the common flow feature for both non-slender and slender delta wings. Yet, differences are observed in the flow field topology and highlighted subsequently.

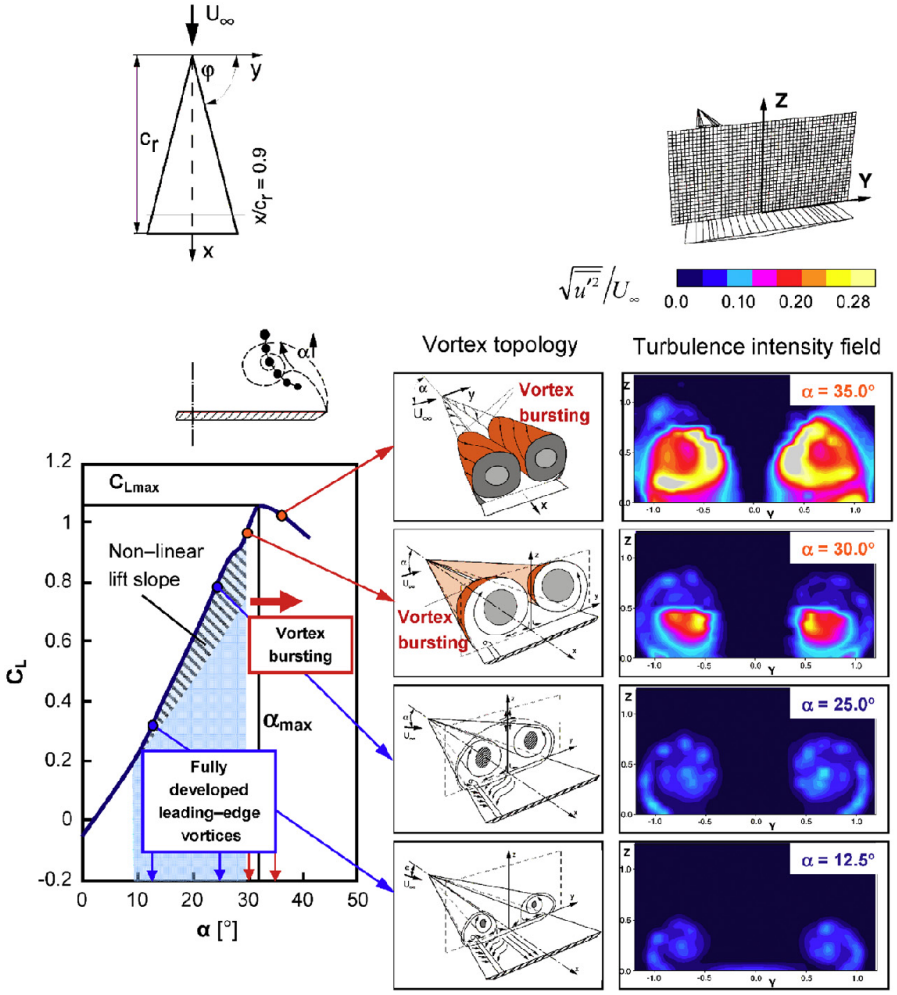

Figure 2.2: Delta-wing polar and corresponding flow field [12].

Table 2.1: Delta wings classification based on sweep angle.

Delta wing	φ
Non-slender	$\geq 55°$
Semi-slender	$55° - 65°$
Slender	$\leq 65°$

Earnshaw and Lawford [34] conducted measurements determining the aerodynamic loads, the vortex breakdown position and the surface flow patterns in low-speed wind-tunnel experiments. The authors investigated six sharp-edged cambered delta-wing models with leading-edge sweep angles ranging from 45° to 76°. The lift characteristics change with increasing sweep angle as depicted in Figure 2.3. At a fixed angle of attack, the wing with higher leading-edge sweep angle generates less normal force. However, more sweep translates to higher axial momentum within

the primary vortex and the resistance to breakdown increases. The angle of attack, at which the vortex departs from the surface (around $\alpha_{\max}$) increases with higher sweep angle. Additionally, Up to a sweep angle of $\varphi = 65°$, the unsteady loading measured above a fixed point on the wing's upper surface increased rapidly with α and the determination of the breakdown location with tuft measurements was problematic. In contrast, the increase of force fluctuations with the angle of attack is milder for the investigated slender wings.

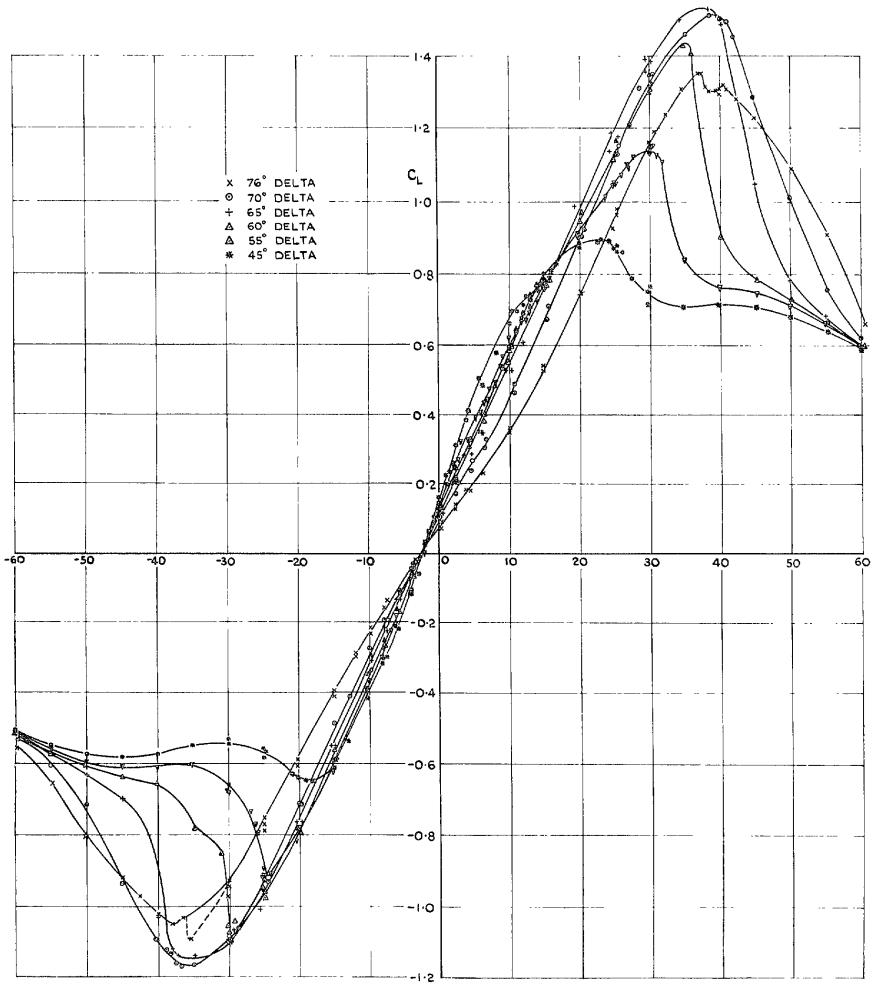

Figure 2.3: Lift coefficient polar for a series of cambered delta wings with variating leading-edge sweep angles [34].

At a fixed angle of attack, increasing the leading-edge sweep leads to a reduction of the leading-edge vortex strength and, consequently, of the vortex lift [61]. In [13], Reynolds-Averaged Navier–Stokes (RANS) computations demonstrated that the aerodynamic coefficients of longitudinal motion (lift, drag and pitching moment) increase with the reduction of φ.

Figure 2.4 shows five distinct regions of the leading-edge evolution stages in a plane spanned by the sweep (x-axis) and incidence angle (y-axis), as reported in [12]. At low angles of attack (region 1), the primary vortex is partly developed. Due to the downstream increasing boundary-

layer thinckness, the flow separates first at the wing tip, which is the onset of the leading-edge vortex. The vortex develops upstream with increasing angle of attack. Region 2 represents the fully developed vortex. Its core moves inboard and upward, as α increases. At high angles of attack, the vortex pair on the suction side of slender delta wings with $\varphi \geq 70°$ reach a common reattachment line in the wing's symmetry plane ($y = 0$), designated as region 3.

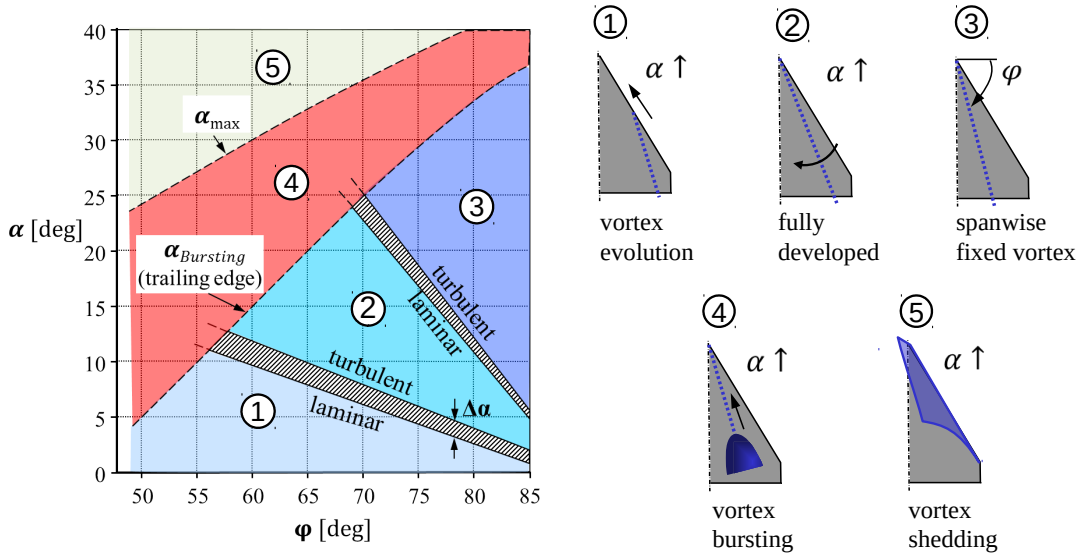

Figure 2.4: Leading-edge vortex stages in the parameter space spanned by angle of attack and sweep angle, based on [12].

The borders between regions 1, 2 and 3 are dependent on the flow state. A turbulent flow delays the transition between regions to higher angles of attack, when compared to laminar flow. The boundary layer state influences the secondary separation line. The laminar separation occurs farther upstream than the turbulent one, leading to a larger secondary vortex, displacing the primary vortex farther inboard and upwards [68].

Vortex breakdown occurs in region 4, in which the breakdown moves upstream as the angle of attack increases. At $\alpha_{\max}$, the primary structure bursts near the apex. Downstream, the flow field constitutes of a wake flow. The post-stall region is designated as region 5 in Figure 2.4. Under these freestream conditions, the vortex is highly unstable and collapses eventually due to the very high adverse pressure gradient. The shear layer does not reattach on the upper surface. The wing stalls as the flow above is completey separated. Within the non-reattaching shear layer, periodic motion generated by shedding of coherent structures along the leading edge was observed [118, 119].

The α_{Bursting} and $\alpha_{\max}$ curves of Figure 2.4 are strongly dependent on the sweep angle. Therefore, it is common for non-slender delta wings that the partly developed vortex breaks down at moderate angles of attack with a smoother transition from a jet type to wake type as for slender wings. Flow field investigations on a 50° swept delta wing are reported in [41, 142, 143]. Investigations on a 53° diamond wing conducted at TUM-AER are referred in [18, 20, 65, 66].

Figure 2.5 compares the flow field between wings of different sweep angles, $\alpha = 50°$ (a) and 65° (b), at $\alpha = 20°$ [111]. The investigation plane is located at a relative root chord section of $x/c_r = 0.3$ and shows the distribution of the mean axial velocity relative to the freestream

velocity supplemented by tangential vectors (left) and the instantaneous axial vorticity. The reduced velocities on the suctions side of the non-slender describe the typical wake type flow.

The shear layer designated by moderate positive vorticity spirals around the wake region without rolling up. At similar conditions, a primary vortex develops above the semi-slender wing, as demonstrated by high axial velocity/vorticity concentrated in the core.

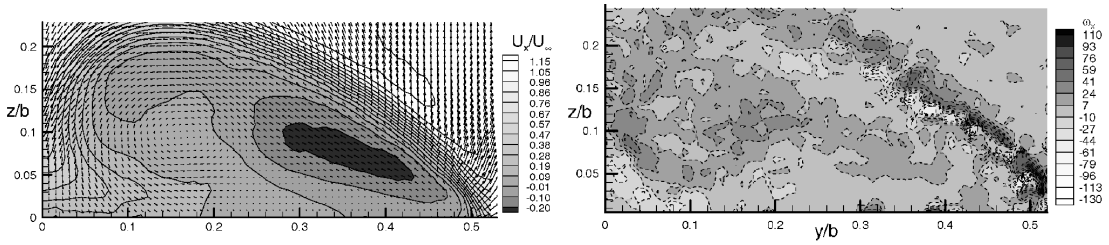

(a) $\varphi = 50°$, $Re = 8.5 \cdot 10^3$.

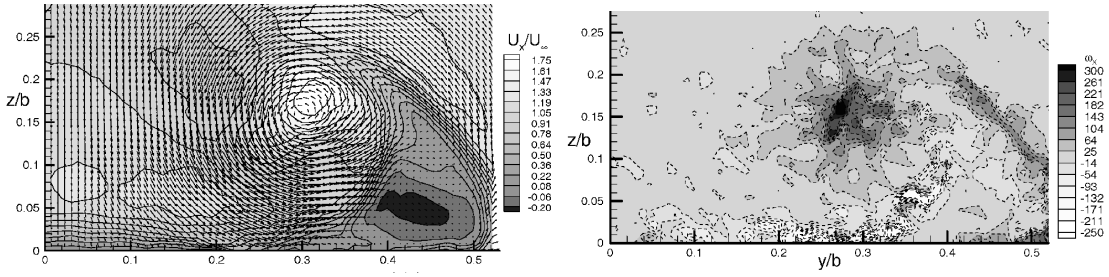

(b) $\varphi = 65°$, $Re = 1.5 \cdot 10^4$.

Figure 2.5: Distribution of mean relative axial velocity (left) and instantaneous axial vorticity (right) from PIV measurements at $x/c_r = 0.3$, $\alpha = 20°$ [111].

2.4 Features of a Stable Vortex

With a good approximation, the flow of a stable vortex (prior to breakdown) is conical, meaning that flow variables above the wing are constant along rays with origin at the apex. This hypothesis is validated by hot-wire investigations above a 75° swept wing in [150]. Figure 2.6 presents an extract of the results. The graphs describe the distribution of axial (a) and circumferential velocity (b) across the vortex core at six chord stations ($x/c_r = 0.3$–0.8). The curves are self similar and axis-symmetric relative to the vortex core, within the bounds of the measurement grid resolution. The resolution of the sampling grid affects the vorticity in the core, which increases with grid refinement [107].

In physical terms, the vortex' intensity grows downstream. Owed to the constant vorticity feeding of the shear layer, circulation increases linearly, excluding leading/trailing edges and breakdown region. The vortex cross section increases also as a linear function of the chordwise position. Besides vorticity, mass and momentum are convected through the shear layer into the vortex core. The fluid in the core has high axial velocity that can reach up to three times the freestream velocity. The core is also dominated by high fluctuations leading to increased turbulent viscosity. Hence, two concentric regions across the leading-edge vortex core are identified: the viscous center with rigid body rotation and the inviscid rotational core.

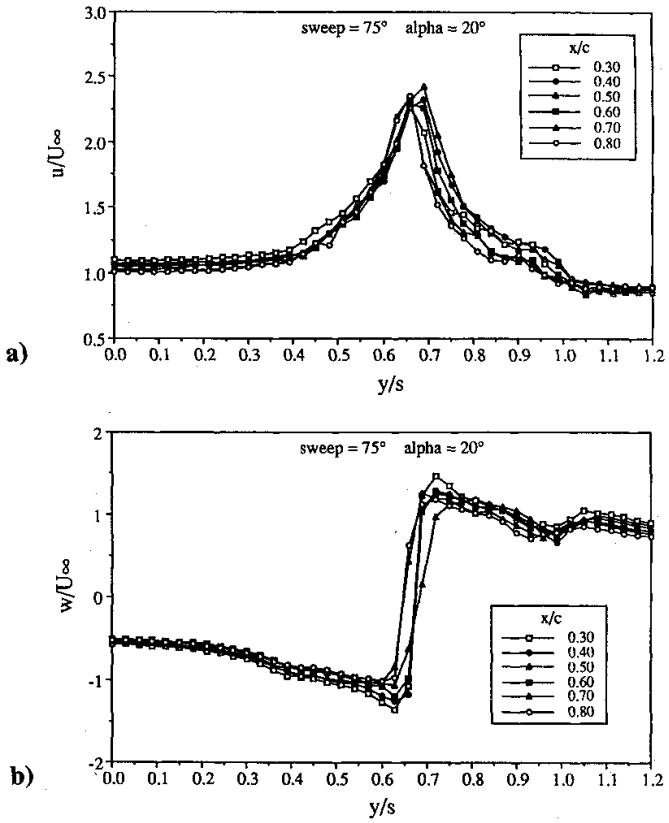

Figure 2.6: Selfsimilar distribution of relative axial (a) and circumferential velocity (b) measured above a $\varphi = 75°$ swept delta wing at $\alpha = 20°$ [150].

Theoretical approaches to compute the vortex dominated flow field have been proposed and are discussed briefly. One method is based on potential flow theory and implies modeling the wing as infinitesimal lifting surfaces with downstream shed vortices [40]. Another approach models the vortex flow field as two line vortices (primary core) connected via a vortex sheet (shear layer) to each leading edge [14, 94]. The lift predictions on sharp-edge delta wings have been improved compared to the previously discussed methods by introducing the "leading-edge suction analogy" [114]. Hall solved the Navier-Stokes equations in the vortex flow core by separating it into a outer inviscid but rotational region and a diffusion-dominated inner region [56].

Lee and Ho described a stationary leading edge vortex, when the vorticity generated at the leading edge equals the vorticity convected along the vortex core [88]. By violating this equilibrium at sufficiently high angles of attack, the vortex transitions between states (stable/burst vortex). While increasing the angle of attack, the generation rate of leading-edge vorticity increases up to a critical value [108]. Above this value, aerodynamic forces fail to generate a stable vortex, resulting in divergence and redistribution of vorticity, as observed in post-breakdown regions. Another physical interpretation of vortex breakdown is given in [15]. The breakdown is the result of the tilting and stretching of the vortex core in response to stagnation. Therefore, the dominating longitudinal vorticity vector rotates in tangential direction generating azimuthal vorticity.

2.5 Vortex Breakdown

As reported in Section 2.2, breakdown occurs, when the angle of attack reaches a certain threshold. With increasing angle of attack, both the flow swirl angle (ratio of the tangential and axial velocity u_θ/u) and the adverse pressure gradient $\partial p/\partial x$ increase. Both parameters are the main crossdependent control parameters for breakdown (including divergence of the stream tubes) [57]. Breakdown leads to an abrupt change of flow states: from a jet-type to a wake-type swirling flow. During this process, the core flow decelerates, stagnates and changes sign connected with increasing pressure downstream. The same flow feature is obtained in a swirling flow when a body is introduced in the core. Figure 2.7 sketches the statistically steady vortex core with breakdown occurring at a longitudinal position of x_{bd} and the qualitative distribution of the average and root mean square (rms) of the axial velocity component across the core.

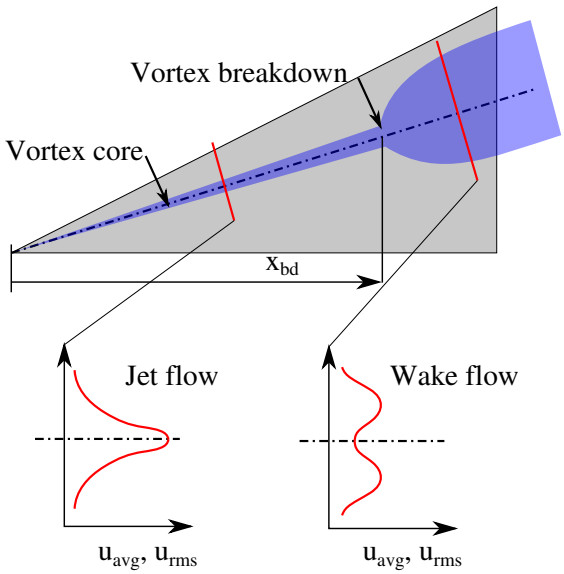

Figure 2.7: Sketch of the vortex core with breakdown and qualitative cross-core axial velocity profiles up- and downstream of the breakdown position.

There are two types of vortex breakdown patterns: the spiral (asymmetric) and bubble (axissymmetric) type, sketched in Figure 2.8. Both breakdown types occur even in alternating sequence and mixed forms above delta wings. However, at relevant Reynolds numbers, the spiral type breakdown is the common form for leading-edge vortices [57].

Hall assesses three theories describing the breakdown phenomenon, based on [57]:

1. Analogy to 2D-separation,
2. Hydrodynamic instability,
3. Critical state.

Both experiments and mathematical modelling demonstrate that the third theory offers the most complete description of the flow feature [57]. Analogue to shocks in gas dynamics, the critical state theory suggests that breakdown occurs when the flow transitions from a supercritical to a subcritical state, therefore, crossing a critical point—onset of breakdown. Breakdown appears as the incapability of the supercritical flow to suport standing waves, which leads abruptly (hydraulic jump) to an equilibrium state (subcritical) that can support these waves. The information

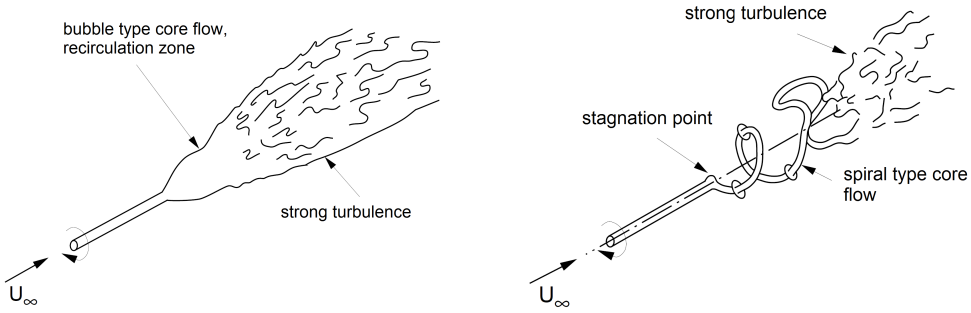

Figure 2.8: Types of vortex breakdown [12].

propagation in the supercritical flow occurs only in downstream direction. The consequence of sudden expansion of the vortex core tube is the information passing in downstream direction and the flow not "expecting" breakdown [50].

2.6 Vortex Flow Instabilities

In Figure 2.9, Rockwell sketches the instabilities, which evolve at different relative short time scales $t \ll c_r/U_\infty$ in the vortex flow system above a delta wing [121]. The unsteady events of short time scales are the feeding-sheet (KH), vortex breakdown and wake (trailing edge) instabilities. Long time scale events $t \gg c_r/U_\infty$ are boundary layer separation and stall (unordered chaotic motion of fluid) caused by upstream motion vortex bursting and/or inboard separation of attached flow. The frequency spread leads to no influence between these two instabilities groups. In addition, the paper author reviews successful flow manipulation by frequency-conditioned flow control when (sub)harmonics of inherent instabilities were triggered.

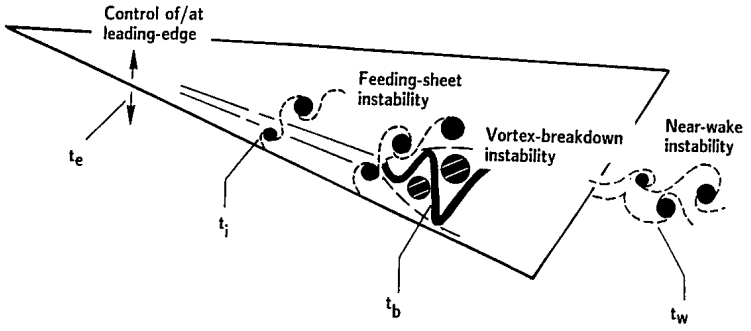

Figure 2.9: Typical leading-edge vortex flow instabilities occuring over a relatively short time span [121].

Gursul describes the unsteady flows that coexist above steady wings at high angles of attack, which have crucial importance in the controllability and stability of aircraft [50]. This include shear layer instabilities, vortex wandering, vortex breakdown and vortex shedding. These flow

phenomena are equally relevant to the dynamic of the vortex flow and might cause severe deterioration, both to structure as well as to flight stability/controllability (e.g. wing/fin buffeting and wing rock), also reported in [12, 118, 119].

Most instabilities occupy a certain frequency range as showed in Figure 2.10. The borders are continuous, e.g. the dominant frequency of the helical mode converges to the frequency of vortex shedding, when the angle of attack increases. The dynamics of vortex unsteady events need to be thoroughly analysed to account for certain manoeuvres and the vortex response. The response of the vortex bursting to pitching is a long transition time to reach an equilibrium state (a couple of convective times). The stationary wing at high incidences produces low-frequent transversal oscillations of the breakdown location, $f \cdot c_r/U_\infty \approx 0.03$.

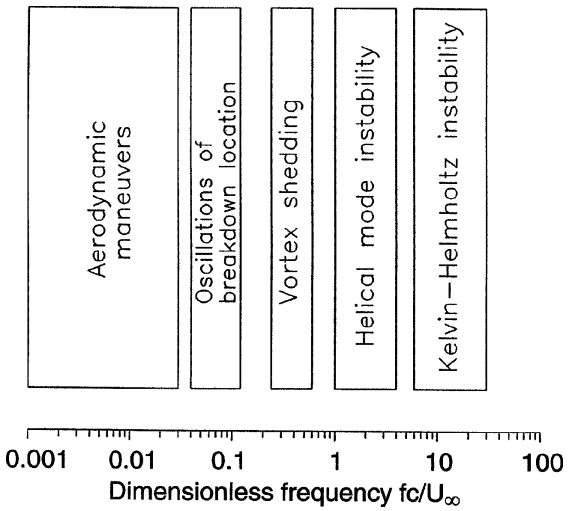

Figure 2.10: Instabilities spectrum [50].

URANS and DES computations reveal that the instability frequencies are sensitive to the computational grid resolution [123]. Nevertheless, they predicted well the dominant peak in the velocity power spectral density (PSD). Breitsamter discovers a constant relating the dominant frequency of the helical mode instability f_{dom}, the chord station x, the sweep angle φ and the angle of attack α, based on exhaustive hot-wire experiments:

$$\frac{f_{\mathrm{dom}} \cdot x}{U_\infty} \cdot \cot(\varphi) \cdot \sin(\alpha) = 0.28 \pm 0.025. \tag{2.1}$$

Mitchell et al. showed in both numerical results, as well as scanned planes by laser doppler velocimetry (LDV), the existence of stationary but also periodic shear layer vortices [103, 104]. These structures have their origin at the leading edge and spiral around the primary vortex. The grid resolution affected the resolved structures in LES regions, but even a coarse grid predicted well the low-frequent energy containing flow motion.

Experimental investigation of the instantaneous vortex field revealed the existence of ordered structures in the shear layer wrapping around the primary vortex core, Figure 2.11. Visbal and Gordnier isolate the shear layer instabilities and postulate the origin of the substructures being in the periodic boundary layer separation on the wing's upper surface [149]. The downstream convection and development of secondary instabilities lead to concentrations of vorticity that in turn may trigger upstream separation. The numerical method predicted a flow field similar to experimental visualisation, e.g. when comparing Figure 2.12 to Figure 2.11.

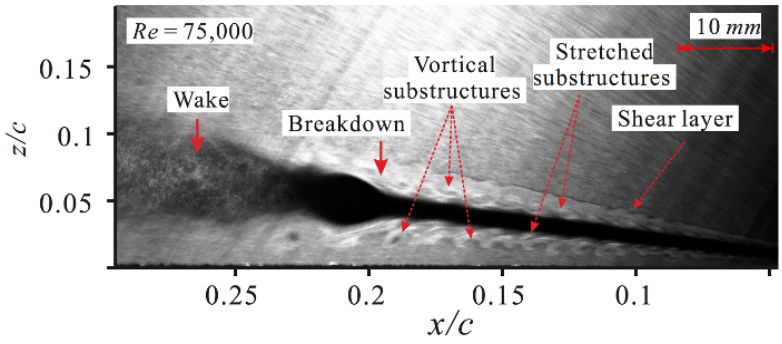

Figure 2.11: Flow visualisation through the vortex core detecting the inherent instabilities [131].

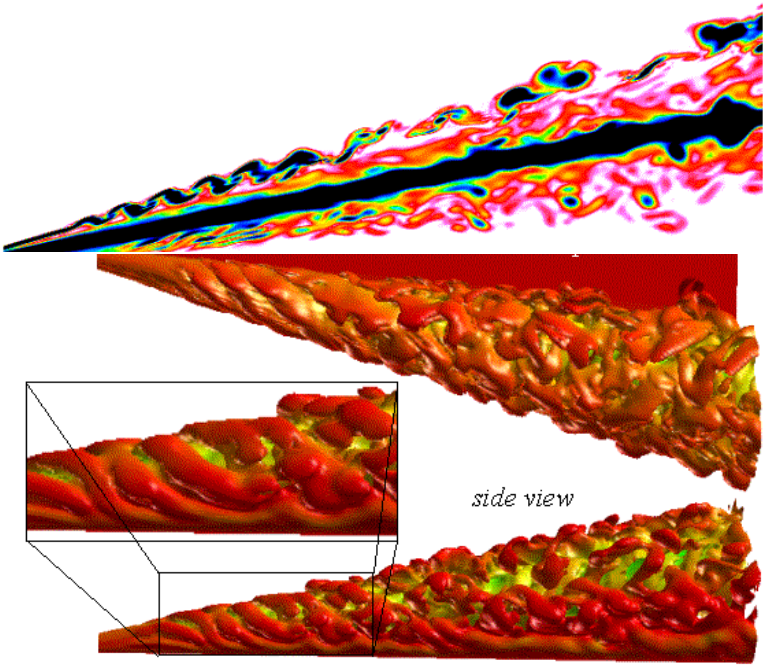

Figure 2.12: Computed instantaneous vorticity distribution above a 75° delta wing in absence of breakdown [149].

Vortex shedding was observed by dye visualisation along the leading edge of water tunnel delta-wing models of $\varphi = 45°$ and $60°$ at $Re = 1.3 \cdot 10^4 - 3.5 \cdot 10^5$ [37]. After separation, dye concentrated in regions almost parallel to the leading edge, which diameter grow as these are transported downstream. The pairing process is the consequence of mutual vortex interaction and induction on each other. The authors observed that, while the sweep angle has no influence on the vortex shedding frequency, the frequency decreases as the angle of attack increases. The freestream velocity is inverse proportional to the number of shed vortices per unit time. The following relationship has been found for $\alpha = 15°$:

$$\frac{f \cdot c_r}{U_\infty} = \frac{1625}{\sqrt{Re}}. \tag{2.2}$$

The periodic departure of vorticity from the surface is investigated at very high angles of attack ($\alpha = 35° - 80°$ for $\varphi = 76°$) in [118, 119]. The authors discovered that the dominant frequency decreases non-linearly with increasing angle of attack independent of the Reynolds number, as presented in Figure 2.13. As the flow field transitions from attached vortices ($\alpha < 35°$) to breakdown creeping upstream and finally to periodic symmetric vortex shedding ($35° < \alpha < 70°$), the frequency related to different instabilities follow a universal curve. The asymmetric shedding mode occurs at $\alpha > 70°$, representing a secondary higher frequency peak in the velocity PSD in the wake. Increasing α further leads to increased dominance of the asymmetric shedding mode with respect to the symmetric one.

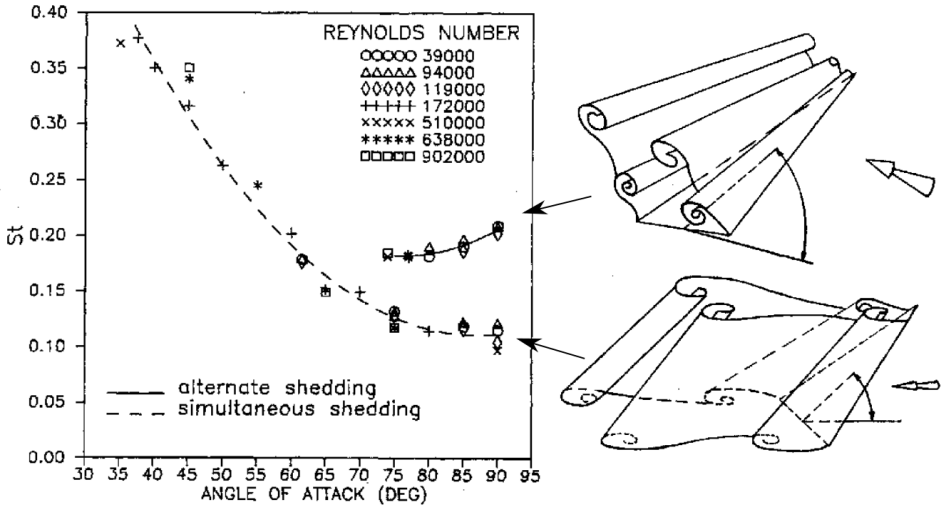

Figure 2.13: Dominant Strouhal number measured in the wake of a 76° delta wing as function of angle of attack[119]. The secondary higher frequency peak represents the asymmetric shedding type that gains more dominance with increasing α.

3 Experimental Methodology

The experimental apparatus is presented in this chapter, including low-speed wind-tunnel facility, wind-tunnel model with actuators, the measurement techniques and a summary of the test-case matrix.

3.1 Wind Tunnel Facilities

All experiments were conducted in the atmospheric low-speed wind tunnel facilities of the Chair of Aerodynamic and Fluid Mechanics, Technical University of Munich (TUM-AER). Figure 3.1 sketches the outline of the return-type wind tunnel A located at the Faculty of Mechanical Engineering in Garching by Munich [1].

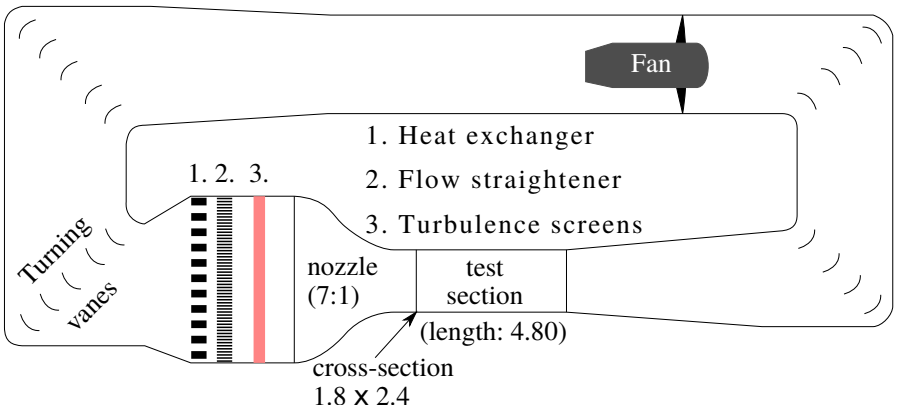

Figure 3.1: Sketch of TUM-AER wind tunnel A (dimensions in m).

An axial fan is driven by a 420 kW motor generating the air mass flow through the tunnel. Before reaching the nozzle with a 7:1 cross-sectional contraction, the air flow is directed by turning vanes at the tunnel's corners. The air flow passes through a heat exchanger (1.), a flow straightener (2.) and turbulence screens (3.). The 4.8 m long test section can be operated as closed or open type and maximum inlet velocities of 65 m/s and 75 m/s can be reached, respectively. Due to practical reason and because the streamlines adapt similarly to the free-flight conditions, the test section with the open configuration is opted in all experiments. The nozzle exit plane has a 1.8 m × 2.4 m (height × width) rectangular cross section. In the open-type test section, the freestream turbulence level, angular and velocity deviations are within $Tu < 0.4\%$, $\Delta\alpha = \Delta\beta < 0.2°$ and $\Delta U_\infty < 0.12\,\mathrm{m/s}$, all decreasing with increasing air flow. At the end of the test section is a collector with adjustable inlet walls.

[1] `http://www.aer.mw.tum.de/windkanaele/windkanal-a/`, accessed Feb. 2020

3.2 Wind Tunnel Model

3.2.1 Baseline Geometry

The delta-wing half model investigated represents the wing geometry with the sharp leading edge established within the "Vortex Flow Experiment 2" (VFE-2) project [70]. Within the second phase of the international project, partnering research institutes collected experimental and numerical investigations in an extensive database. From these findings, a better understanding of leading-edge vortex flows and validation of corresponding CFD methods was achieved [72].

The geometry with different leading edge radii, measured initially in the the Langley National Transonic Facility (NTF) [29], has been investigated also at TUM-AER [35]. Kölzsch designed a half-model of the sharp edged VFE-2 delta wing that incorporates two actuation systems [82], moving-surface (oscillating miniature flaps) and fluidic actuation (pulsed blowing). In terms of flow field manipulation, the latter system is superior to the former [82] and, for this reason, pulsed blowing is the AFC type investigated here.

Figure 3.2 shows the delta-wing half modell and Table 3.1 sums up its geometric parameters. The delta wing has a leading-edge sweep angle of $\varphi = 65°$ (semi-slender delta wing). The root chord measures $c_r = 0.977\,\mathrm{m}$, resulting in a half span of $s = 0.456\,\mathrm{m}$ and an aspect ratio of $\Lambda = 1.867$. Two metal plates (light grey), upper and lower skin, are connected to the symmetric leading/trailing-edge parts (in dark colour), fabricated from glasfiber reinforced plastic [82, 84]. The wing thickness is constant, $\delta/c_r = 3.4\%$, but decreases towards zero at the leading/trailing edges.

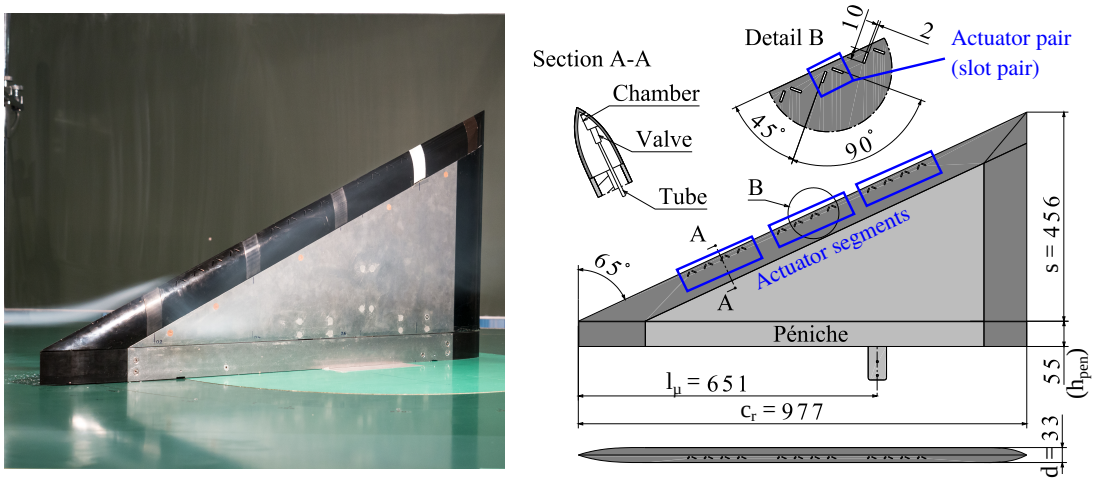

Figure 3.2: Wind-tunnel model with dimensions in mm.

Table 3.1: Geometric parameters of the delta-wing half model.

φ	Λ	c_r	s	A_w	l_μ	δ/c_r
65°	1.867	0.977 m	0.456 m	0.223 m^2	0.651 m	3.4%

3.2.2 Fluidic Actuation System

The actuation system generates pulsating air jets through slots distributed in V-shaped pairs and in three segments along the leading edge, between relative root chord positions of $x/c_r = 0.4$, 0.6 and 0.8. As shown in the detail view B in Figure 3.2, the high-aspect-ratio rectangular orifices (2 mm × 10 mm) are arranged pairwise at a right angle to each other and at 45° with respect to the leading edge.

From each of the 12 plenum chambers laminated inside the leading edge, air exits through one slot pair. The chambers are supplied by a tubing system connecting each segment (of 4 actuator pairs) to independent high-pressure air supply ($4 - 5$ bar). The fast-switching *FESTO MHJ9* valves ($f_a \leq 1$ kHz) are located between the high pressure air supply and the plenum chambers (see detail cut A–A in Figure 3.2) and generate the jet pulsation. Each valve can be operated individually. However, only periodic signals have been investigated in this work.

Figure 3.3 shows the periodic signal measured by an X-type hotwire probe placed 6 mm above the midsection of one slot at quiescent air condition ("ground test"). The measurement plane, spanned by the axial and cross component is orthogonal to the leading edge. Thus, the jet velocity components normal to the wing w_j and spanwise, normal to the leading edge are measured (see included sketches in Figure 3.3).

The slot exit velocity signal is a step signal, reproducing the most effective actuation mode, the burst mode [95]. The velocity response to the actuation at three actuation frequencies, in decreasing order $f_a = 65$ Hz, 32 Hz and 12 Hz and two inlet pressures , $p_{in} = 4$ and 5 bar. These actuation parameters had the most effect on the flow field and on the aerodynamic coefficients [82–84]. As seen in the power spectral density distributions (right), the flow responds also with higher harmonics oscillations.

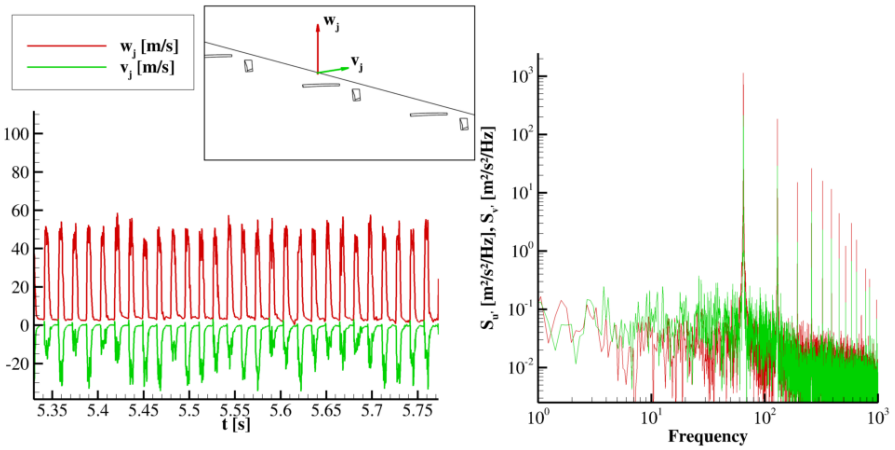

(a) $f_a = 65\,\text{Hz}$, p_{in} =4 bar ($\alpha = 23°$).

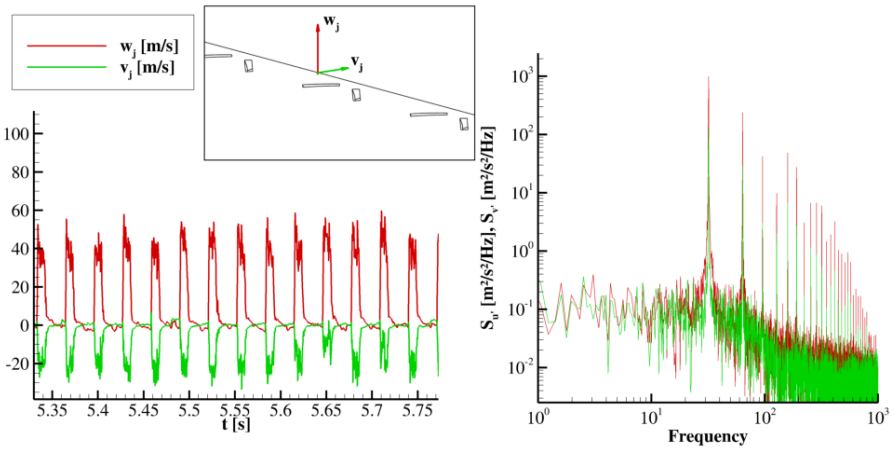

(b) $f_a = 32\,\text{Hz}$, p_{in} =4 bar ($\alpha = 35°$).

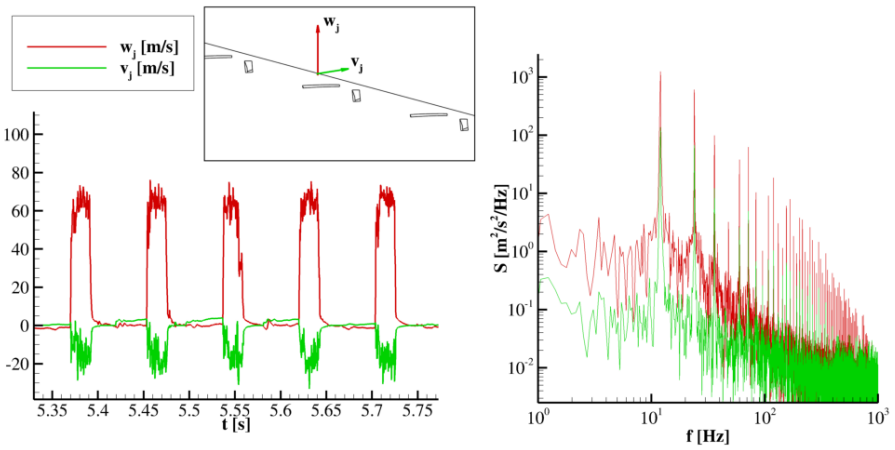

(c) $f_a = 12\,\text{Hz}$, p_{in} =5 bar ($\alpha = 45°$).

Figure 3.3: Velocity signal above one slot during actuation under quiescent air conditions.

3.3 Measurement Techniques

3.3.1 Balance Measurements

Throughout all the measurement campaigns, the model was placed in the test section as shown in Figure 3.4a. The model is connected at $2/3c_r$ distance from the apex (reference point for the pitching moment) via an inner vertical bar (Figure 3.2) to an external piezo-electric stain-gauge balance located underneath the test section (Figure 3.4b). The angle of attack is adjusted by turning the balance with its own mechanism. The rotation axis is 1.5 m downstream of the nozzle exit plane.

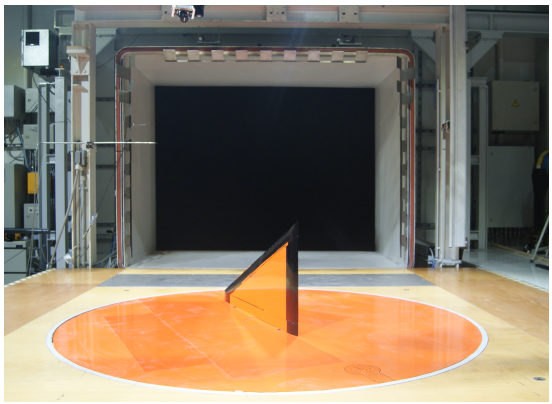

(a) Test section with wing model.

(b) Balance with adjustable incidence angle beneath the test section.

Figure 3.4: Wind-tunnel setup and balance.

Prior to the actual measurements under selected freestream conditions, the gravitational forces and moments were measured in a α-sweep and saved in a "zero polar" ($U_\infty = 0$). The gravitational part is substracted from the measured values. Also during the balance measurements, no contact was assured between the péniche and the wing. Therefore, only the aerodynamic forces are considered during the measurement.

In total, all six aerodynamic force/moment components were measured in the body fixed system, but only four are considered in this work:

- Tangential F_X and normal force F_Z,
- Rolling moment M_X and pitching moment M_Y.

The pitching moment reference point is located at the connection of the wing with the balance, at $x/c_r = 2/3$. The rolling moment is relative to the x-axis. The dimensionless aerodynamic coefficients relate the forces to the inflow dynamic pressure $0.5\rho U_\infty^2$, and the wing area A_w. Additionally, the aerodynamic moment coefficients are related to a reference length, l_μ (mean aerodynamic chord) or s (half span). Only the expressed coefficients are investigated here:

$$C_{X/Z} = \frac{F_{X/Z}}{0.5\rho U_\infty^2 A_w}, \tag{3.1}$$

$$C_{MX} = \frac{M_X}{0.5\rho U_\infty^2 A_w s} \text{ and} \tag{3.2}$$

$$C_{MY} = \frac{M_Y}{0.5\rho U_\infty^2 A_w l_\mu}. \tag{3.3}$$

As seen in Figure 3.5, the coordinate system of the moments is rotated by 180° around the y-axis (e.g. C_X is positive with increasing chord, but C_{MX} points in the opposite direction). To obtain the lift L and drag forces D from the force components, a coordinate system transformation is required from the body-fixed system to the aerodynamic system. The coefficient transformation is expressed as a rotation by α around the pitch axis (y-axis):

$$\begin{pmatrix} C_D \\ C_L \end{pmatrix} = \begin{pmatrix} \cos(\alpha) & \sin(\alpha) \\ -\sin(\alpha) & \cos(\alpha) \end{pmatrix} \cdot \begin{pmatrix} C_X \\ C_Z \end{pmatrix} = \begin{pmatrix} D \\ L \end{pmatrix} \cdot \frac{1}{0.5\rho U_\infty^2 A_w}. \tag{3.4}$$

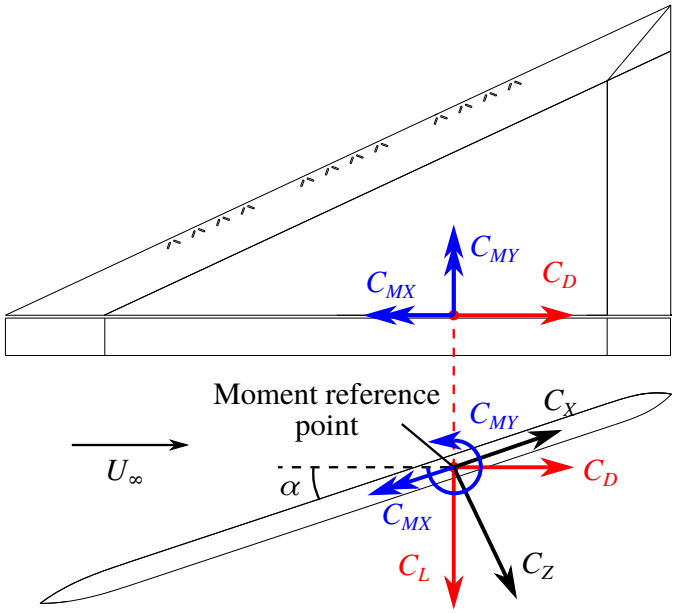

Figure 3.5: Body-fixed force and moment components.

The angle of attack considered are in the range $0° \leq \alpha \leq 50°$. For the high angle range of $40° \leq \alpha \leq 50°$, balance measurements were conducted at $\Delta\alpha = 1°$. For $10° \leq \alpha \leq 40°$, the spacing of the measurement points read $\Delta\alpha = 2$ and $3°$. In order to assess the total measurement accuracy, a complete polar has been repeated three times and the standard deviation calculated. Largest deviations are registered around stall, at which the flow field is highly unsteady. Based on this, the measurement accuracy in the entire α-range resulted to be within 0.02 for $C_{L/D}$ and within 0.01 for $C_{MX/MY}$.

The measured polar contains 22 measurement points / angles of attack:

$$\begin{aligned} \alpha \in \{&0°;\ 5°;\ 10°;\ 13°;\ 15°;\ 18°;\ 20°;\ldots \\ &23°;\ 25°;\ 28°;\ 30°;\ 33°;\ 35°;\ 38°;\ldots \\ &40°;\ 41°;\ 42°;\ 43°;\ 44°;\ 45°;\ 50°\}. \end{aligned} \tag{3.5}$$

3.3.2 Particle Image Velocimetry

The stereoscopic PIV measurements generated a considerable data base for baseline and actuated flow fields. The measurement technique, the wind-tunnel setup, the test configurations and post-processing steps are described below. Two setups are investigated based on the orientation of the measurement plane: high-speed cameras located above the test section, similar to previous PIV investigations [64, 82] for crossflow scanning and cameras located sideways for scanning longitudinally along the vortex. The current setup is reported also in [6, 7, 16, 17].

3.3.2.1 Setup

For flow visualisation, a high volume liquid seeding generator pulverizes Di-Ethyl-Hexyl-Sebacat (DEHS) droplets of approximately 1 μm in diameter into the collector air stream, behind the test section. The seeding particles are mixed homogeneously along the wind-tunnel's return duct before reaching the test section's inlet. A 325 mJ Nd:YAG double-cavity double-pulsed laser produces a 532 nm laser beam that, expanded by a widening optic, illuminates the seeding particles located in the measurement plane.

For a stereoscopic analysis, two high-speed sCMOS cameras record instant frames from two perspectives. Scheimpflug adapters tilt the *NIKON* lenses (focal lengths of $l_f = 135$ mm or 50 mm) relative to the 2560×2160 pixel camera chip, achieving focused regions along the entire frame.

A portable timing unit (PTU) synchronises the camera recording with the double laser pulses per measurement (double frame technique). The recording parameters are listed in Table 3.2, which includes the sampling frequency f_s, the time between pulses Δt_P, number of passes of the correlation algorithm N_P, Maximum interrogation window size A_I, Interrogation window overlap OV and grid spacing Δ_{PIV}.

Table 3.2: PIV setup parameters. "T" stands for "triggered" and the additional values separated by backslash represent the aft crossflow planes.

α	f_s [Hz]	Δt_P [μs]	N_P	A_I [px^2]	OV	l_f [mm]	Δ_{PIV} [mm]
1. Core flow investigation							
23°	12	40	2	32	0%	135	4.9
35°	12	20	2	32	0%	135	4.9
45°	13	20	2	32	0%	135	4.7
2. Cross flow investigation							
23°	12	40	2	64	50%	135	5.1/4.9
35°	12	20	2	64	50%	135	3.3/4.5
45°	11	20	2	64	50%	135	3.7
45°	11	20	3	48	50%	50	8.9
3. Phase-averaged investigation							
23°	T	40	2	32	0%	135	3.1/5.2
35°	T	20	2/3	48	50%	135/50	3.4/9.0
45°	T	20	2/3	48	50%	135/50	3.4/8.9

Depending on the measurement plane orientation, two different PIV setup configurations are used: parallel to the vortex core and normal to the wing's x-axis. For the measurements along

the core, the cameras are mounted side-ways and the laser above the test section, see Figure 3.6a. Each system is mounted on its own traversing unit. The system can retain the calibration, if the relative position between cameras and laser source is kept. The position of the planes along the core are placed depending on the angle of attack, as sketched in Figure 3.6b, and result from extracting the mean core positions at discrete planes measured in preliminary investigations [82].

For $\alpha = 23°$ the measurement plane (green in Figure 3.6b) forms an angle of 6.8° with the wing's plane with respect to the y-axis at the apex of the wing ($x = 0$). In a cut along the wing symmetry plane (xz), the red line marks the position of the measurement plane at $\alpha = 35°$, at which the vortex expands and the vortex axis departs from the surface. At $\alpha = 45°$ no vortex can exist naturally. Therefore, the rotation axis of the sustained vortex with pulsed blowing at $F^+ = 1.0$ is taken as reference. The average position is located along the blue plane, which is obtained by shifting the red plane along the span by $\Delta z/s = 0.02$.

With the second configuration shown in Figure 3.7a, the velocity field in crossflow planes above the wing are measured as sketched in Figure 3.7b. The cameras are mounted above the test section on the traversing unit, together with the laser. In contrast to the setup described previously, the upstream camera (1) looks on the upstream side of the PIV plane and the downstream camera (2) is oriented on the backside of plane. In total, 19 crossflow planes are measured for all three angles of attack $\alpha = 23°, 35°$ and 45°, at four actuation modes (baseline, synchronised blowing, frequency-modulated and phase-modulated mode). The close stacking of cross flow planes adds information of the downstream development of the vortex.

After recording, the raw sets of images are post-processed by *DAVIS 8.4* provided with the PIV system by *LAVISION* using the cross-correlation technique. After dividing the corrected images in quadratic interrogation windows measured in pixels A_I, the program computes the displacement of particle images in each window using a multi-pass technique (number of passes in Table 3.2). With the optimal time between pulses Δt_P an optimum rms shift of 5 pixels is assured, thus reducing the out-of-plane departure of particles.

A calibration is required after adjusting the cameras and laser, all focusing on the measurement plane. For this, a calibration plate ("target") with a defined pattern of points gives the information of transforming units of the particle displacements from pixels in meters. In each interrogation window $(1, \ldots, N)$ three instantaneous velocity components ($i = x, y, z$) are obtained:

$$u_{iN} = \frac{d_{iN}}{\Delta t_p}. \tag{3.6}$$

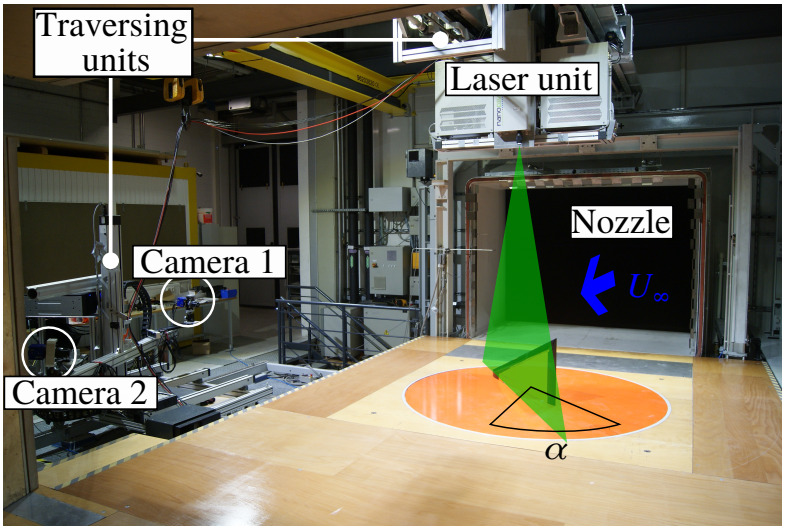

(a) Test section.

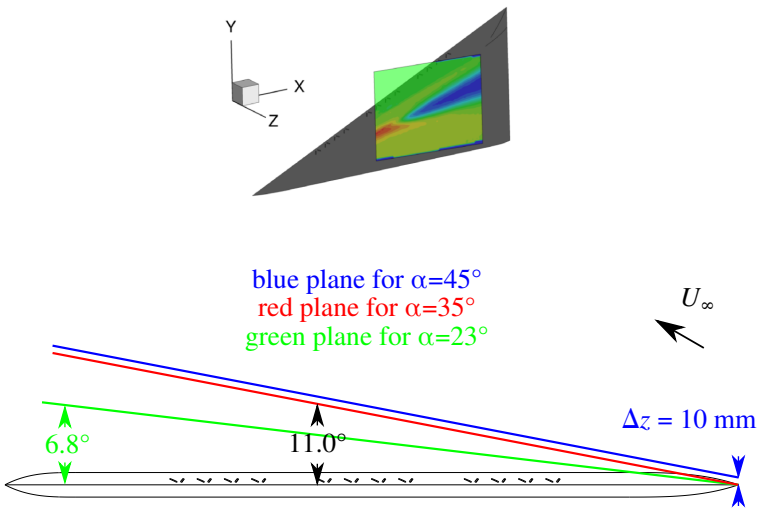

(b) Plane locations.

Figure 3.6: PIV setup for flow measurements along the vortex core.

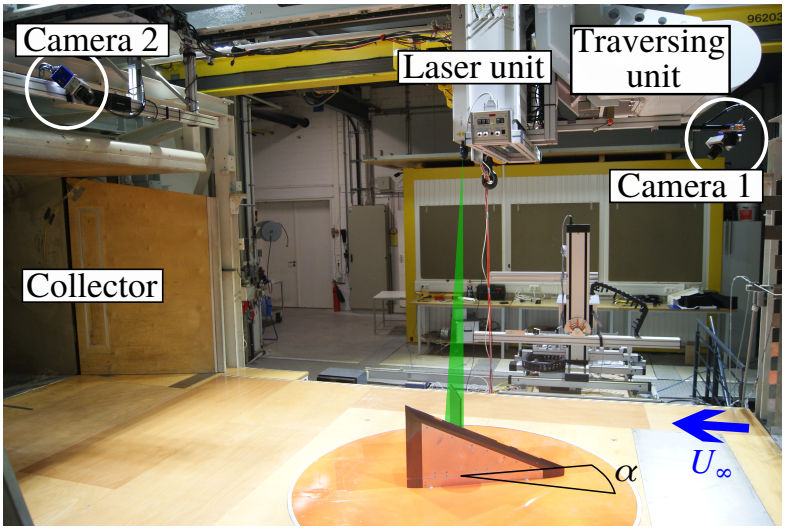

(a) Test section.

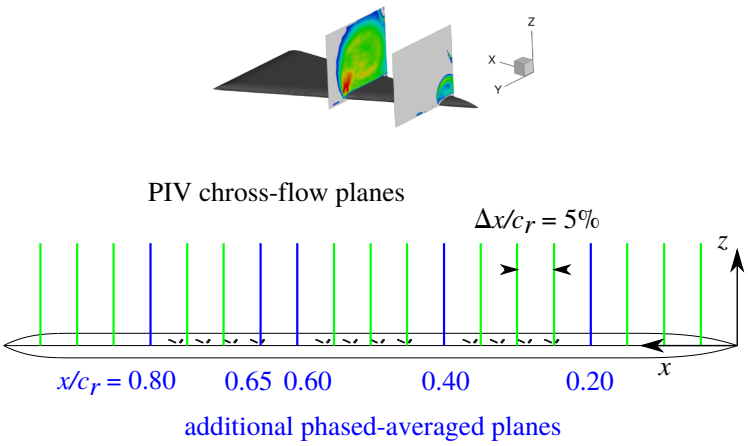

(b) Plane locations.

Figure 3.7: PIV setup measurements across the vortex core.

3.3.2.2 Phase-Averaged Recording

Phase-averaged PIV investigations implies synchronising the recording with the blowing sequence. Therefore, the digital signal sent to the valves is used as trigger signal for the PTU. Preliminary ground tests using a tuft were required to define the jet onset as the start of one blowing cycle. See Figure C.1 for the tuft positions throughout one blowing cycle. In this manner, three cases with synchronised blowing at $\alpha = 23°, 35°$ and $45°$ were investigated, see Table 3.2. Corresponding frequencies ranged at $f_s = 12\,\text{Hz}$–$65\,\text{Hz}$. One blowing cycle is divided by 8 equally distanced phase angles:

$$\theta = 45°, 90°, 135°, 180°, 225°, 270°, 315°, 360°. \tag{3.7}$$

Five crossflow plane sections are scanned during the phase-averaged measurements at 4 chord locations between the blowing segments, and one plane above one blowing slot (x/c_r =0.653). Their location relative to the wing are shown in blue in Figure 3.6b. The phase averaged chord sections are:

$$x/c_r = 0.20, 0.40, 0.60, 0.65, 0.80. \tag{3.8}$$

3.3.2.3 Uncertainty Quantification

Uncertainty quantification is important to evaluate the error from the displacement calculation and further discussed here based on [127]. The measurement error ϵ is the difference between the measured and the true displacement:

$$u_{\text{meas}} = u_{\text{true}} + \epsilon. \tag{3.9}$$

There is a distinction between bias and random error related to the input values. The bias error remains constant while the random error fluctuates for same PIV input parameters. The probability density function (PDF) of the latter has a normal distribution. The error sources are multiple and covering the most of them is preferable for an accurate estimation of measurement uncertainty. Contributing to the overall error are: noise, out-of-plane motion, particle image size (peak locking for sizes $< 1\,\text{px}$), velocity gradients, sub-pixel displacements and particle density. Throughout the entire measurement process, these error sources are influenced by seeding tracers, illumination source, digital recording, image processing and interrogation algorithms. Optimal choice of these reduces the bias error to a minimum, leaving the random error to be estimated. For zero bias and assuming converged PIV displacement calculation, the root-mean-squares (rms) of uncertainty and error are equal:

$$\sqrt{\frac{\sum_{i=1}^{N} U_i^2}{N}} = \sqrt{\frac{\sum_{i=1}^{N} \epsilon_i^2}{N}}. \tag{3.10}$$

Hence, the estimation of uncertainty translates to the measurement error. For uncertainty estimation four methods were proposed recently:

1. uncertainty surface method [146]
2. peak ratio method [26]
3. particle disparity method [128]
4. correlation statistics [153]

Comparative assessment of these methods demonstrated highest accuracy (85%) for uncertainty estimation with the correlation statistics method, even with peak locking or low particle densities (75%)[127]. Therefore the uncertainty of the displacement calculation in this work is based on the fourth method. Highest uncertainty values exist in the vortex core and in the breakdown region. However, the average velocity uncertainty did not exceed $2.5\%U_\infty$ in all three components. Phase-averaged crossflow investigations showed local uncertainty peaks below $3.8\%U_\infty$ above the blowing slots and during the blowing phases.

3.3.3 Hot-Wire Anemometry

Hot-wire investigation of the flow field was conducted with a multi-channel constant-temperature anemometer (*AA Lab*). As in [82], a two-wire X-type miniature probe was used to acquired 19200 digital samples (6.4 s) of the anemometer output voltages with a frequency of 3000 Hz and a 1000 Hz low-pass filtering. The maximum sampled reduced frequency is $k_{\mathrm{red}} = f \cdot c_r/U_\infty = 23.5$. The velocity was calculated from the output voltages based on velocity and directional calibration conducted prior to the measurements. The power spectral density (PSD), the mean and root-mean-square velocity values are estimated within an accuracy of 3.5%, 0.5% and 2%, respectively [82].

3.3.4 Surface Pressure Measurements

The distribution of the mean and fluctuating surface pressure coefficient c_p in three crossflow planes at $x/c_r = 0.4$, 0.6 and 0.8 are obtained from steady and unsteady pressure measurements [82]. A Scanivalve system samples with a frequency of 20 Hz the differential steady pressure in 46 positions on the upper surface and 3 positions on the lower surface for a total time of 30 s. The unsteady pressure is determined by 29 piezoresistive sensors (Kulite XCQ-107-093-5D) with a sampling rate of 3000 Hz and a measurement time of 10 s. The cut-off frequency of the analogue low-pass filter (Butterworth) is set at 1000 Hz. The accuracy of the measured pressure coefficient is estimeted to not exceed 0.7% [82].

3.4 Test Cases

The test case matrix is spanned by number of angles of attack investigated and four actuation modes. As the PIV investigations focussed on three discrete angles of attack, the PIV test case matrix is defined as:

$$\text{Test cases} = \begin{bmatrix} 23° \\ 35° \\ 45° \end{bmatrix} \times \begin{bmatrix} \text{Baseline} \\ \text{Constant frequency} \\ \text{Frequency variation (FV)} \\ \text{Phase variation (PV)} \end{bmatrix}. \tag{3.11}$$

The baseline configuration represents the undisturbed, natural vortex flow and is the reference case for assessing the effect of all three actuation modes on the PIV investigations as well as for balance measurements. The actuation modes distinct from each-other by the timing of the blowing cycles for each of the 12 slot pairs. Therefore, the modes are classified in constant frequency (FV1, FV2) and phase variations (PV1, PV2, PV3, PV4).

Tables 3.3,3.4 and 3.5 list the reduced actuation frequency per slot pair F_i^+ and the time delay with respect tot the first slot pair as division of the cycle period $\Delta t/T$ for each actuation mode and each flow regime. The parameters are chosen based on two hypothesis:

1. The dominant frequencies decrease along the chord $f \backsim 1/x$. Pulsating with the chord-dependent frequency could trigger local instabilities.

2. Assuming a nearly constant downstream transport of discrete disturbances injected at the leading edge, a phase delayed pulsation correlated with the convection could amplify the effect of the disturbance.

Two frequency variation modes were investigated for all three flow regimes: quasi-continuous (FV1) and segment-wise frequency decrease (FV2). Figures 3.8, 3.9 and 3.10 show graphically the variations of frequency (a) and phase (b). The dotted line represents the dominant frequency along the chord length of the breakdown location as observed in [12]:

$$f = \frac{U\infty}{x \cdot \cot(\varphi) \cdot \sin(\alpha)} \cdot 0.28. \tag{3.12}$$

In non-dimensional formulation:

$$F^+ = \frac{f \cdot c_r}{U\infty} = \frac{0.28}{x/c_r \cdot \cot(\varphi) \cdot \sin(\alpha)} \cdot 0.28. \tag{3.13}$$

For the phase variations, linearly increasing phases are implemented and ordered by increasing slope in PV1, PV2 and PV3, see Figures 3.8b, 3.9b and 3.10b. PV4 represents a segment-wise increase of phase. The greyed columns are actuation modes investigated also via PIV.

Table 3.3: Parameters for different actuation modes at $\alpha = 23°$.

Slot nr.	Chord pos.	$F^+ = 2.6$	FV1	FV2	PV1	PV2	PV3	PV4
	x/c_r	F_i^+			$\Delta t/T$ [%]			
1	0.25	2.6	3.3	7.5	0	0	0	0
2	0.29	2.6	3.3	5.0	9	10	12	0
3	0.32	2.6	3.3	5.0	18	20	24	0
4	0.36	2.6	3.3	5.0	28	30	36	0
5	0.45	2.6	2.4	2.5	50	53	65	65
6	0.48	2.6	2.4	2.5	58	62	76	65
7	0.52	2.6	2.4	2.5	68	72	88	65
8	0.56	2.6	2.4	2.5	77	82	100	65
9	0.65	2.6	2.4	2.5	0	6	130	130
10	0.69	2.6	2.4	2.5	9	16	142	130
11	0.72	2.6	2.4	2.5	18	26	154	130
12	0.76	2.6	2.4	2.5	27	36	166	130

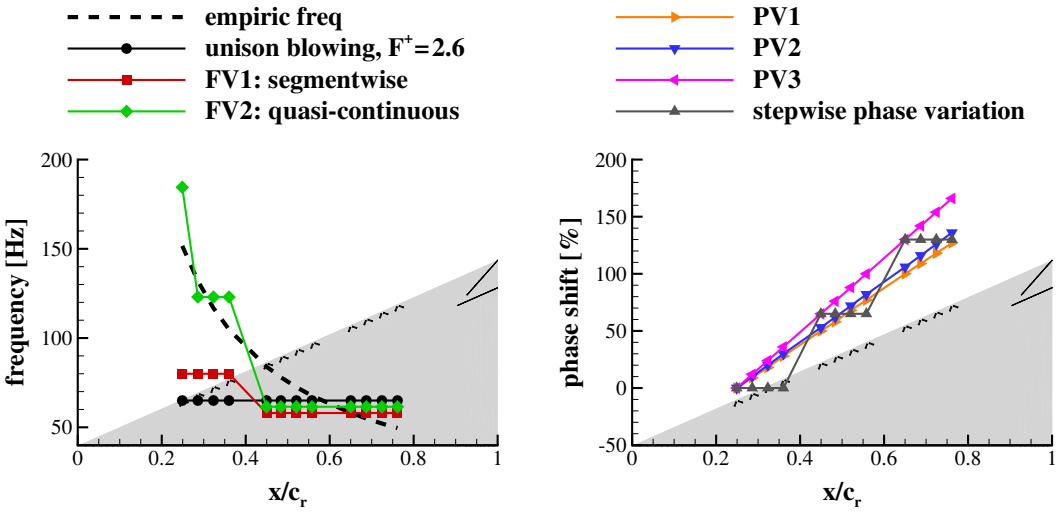

(a) Frequency variations. **(b)** Phase variations.

Figure 3.8: Variation of frequency and phase along the chord at $\alpha = 23°$.

Table 3.4: Parameters for different actuation modes at $\alpha = 35°$.

Slot nr.	Chord pos.	$F^+ = 2.6$	FV1	FV2	PV3	PV4
	x/c_r	F_i^+			$\Delta t/T$ [%]	
1	0.25	2.6	2.7	5.0	0	0
2	0.29	2.6	2.7	3.3	10	0
3	0.32	2.6	2.7	3.3	20	0
4	0.36	2.6	2.7	3.3	30	0
5	0.45	2.6	1.8	1.7	54	54
6	0.48	2.6	1.8	1.7	64	54
7	0.52	2.6	1.8	1.7	74	54
8	0.56	2.6	1.8	1.7	84	54
9	0.65	2.6	1.8	1.7	109	109
10	0.69	2.6	1.8	1.7	119	109
11	0.72	2.6	1.8	1.7	129	109
12	0.76	2.6	1.8	1.7	139	109

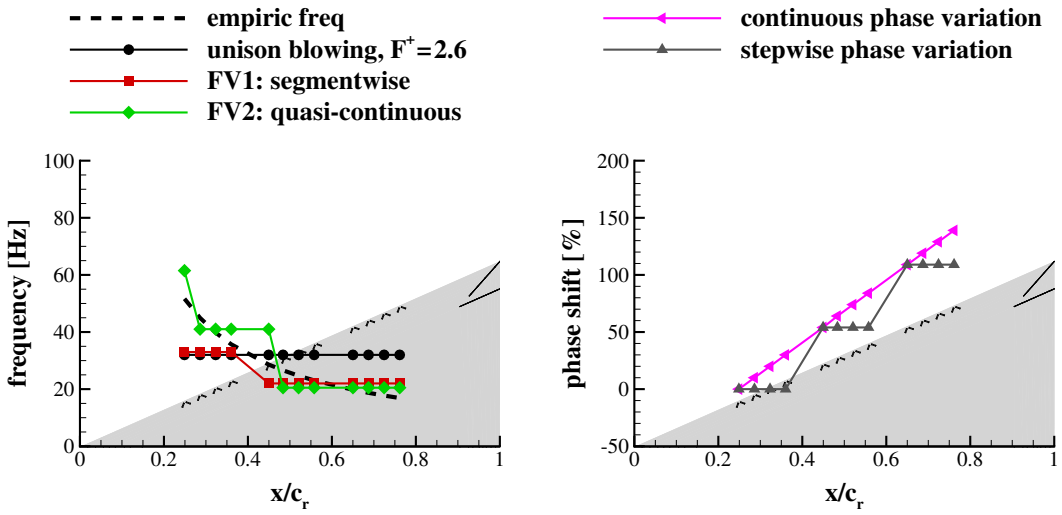

(a) Frequency variations.

(b) Phase variations.

Figure 3.9: Variation of frequency and phase along the chord at $\alpha = 35°$.

Table 3.5: Parameters for different actuation modes at $\alpha = 45°$.

Slot nr.	Chord pos.	$F^+ = 1.0$	FV1	FV2	PV1	PV2	PV3	PV4
	x/c_r	F_i^+			$\Delta t/T$ [%]			
1	0.25	1.0	1.3	4.2	0	0	0	0
2	0.29	1.0	1.3	3.3	4	5	8	0
3	0.32	1.0	1.3	2.5	9	10	16	0
4	0.36	1.0	1.3	2.5	13	15	23	0
5	0.45	1.0	0.8	1.7	24	28	42	42
6	0.48	1.0	0.8	1.7	28	32	49	42
7	0.52	1.0	0.8	1.7	32	38	57	42
8	0.56	1.0	0.8	1.7	36	43	65	42
9	0.65	1.0	0.8	1.7	47	55	84	84
10	0.69	1.0	0.8	1.7	52	61	92	84
11	0.72	1.0	0.8	1.7	56	66	100	84
12	0.76	1.0	0.8	0.8	60	71	107	84

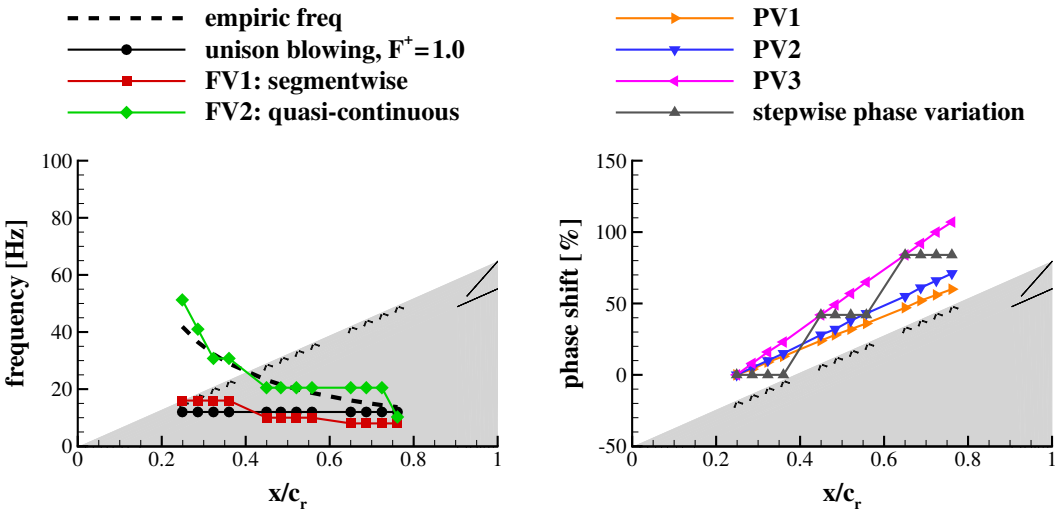

(a) Frequency variations.

(b) Phase variations.

Figure 3.10: Variation of frequency and phase along the chord at $\alpha = 45°$.

4 Numerical Methodology

This chapter covers the numerical methods employed to simulate the wind-tunnel conditions with the purpose of retrieving additional valuable transient information from all three angles of attack. Both actuation conditions are simulated: Baseline and pulsed blowing. Subsequent to the brief description of the flow solver and computational resources, this chapter reports on the computational mesh and the numerical setup. Finally, the numerical tools used for post-processing are described.

4.1 Flow Solver

All computations were conducted with the pressure-based flow solver implemented in *ANSYS Fluent 19.2* on 140 parallel CPU cores. For this purpose the high-performance-computing (HPC) cluster SuperMUC of the Leibniz Rechenzentrum was used, which has been decommissioned in favour for SuperMUC-NG[1]. Table 4.1 summarises the case-dependent flow phenomena simulated with the corresponding freestream conditions and actuation modes. The numerical setup is also reported in [10, 11, 18, 21].

Table 4.1: Six investigated DES cases: two actuation modes at three flight regimes.

Flow typology	$\boldsymbol{\alpha}$	$\boldsymbol{Re}$	**Actuation**	
Breakdown aft above the wing	23°	$1.0 \cdot 10^6$	Baseline	$F^+ = 2.6$
Breakdown at the apex	35°	$0.5 \cdot 10^6$	Baseline	$F^+ = 2.6$
Massive wake / Sustained vortex	45°	$0.5 \cdot 10^6$	Baseline	$F^+ = 1.0$

4.1.1 Governing Equations

Mass and momentum conservation are expressed in Equations 4.1 and 4.2, respectively. The reader is reffered, e.g. to the work of Pope [116].

$$\frac{\partial \rho}{\partial t} + \frac{\partial (\rho u_i)}{\partial x_i} = 0 \tag{4.1}$$

$$\begin{aligned} \frac{\partial (\rho u_i)}{\partial t} + \frac{\partial (\rho u_i u_j)}{\partial x_j} &= -\frac{\partial p}{\partial x_i} + \frac{\partial \tau_{ij}}{\partial x_j}, \\ \tau_{ij} &= \mu \cdot \left(\frac{\partial u_i}{\partial x_j} + \frac{\partial u_j}{\partial x_i} - \frac{2}{3} \delta_{ij} \frac{\partial u_k}{\partial x_k} \right). \end{aligned} \tag{4.2}$$

The laminar dynamic viscosity $\mu = \nu\rho$ is temperature dependent according to Sutherland's law:

$$\mu = \mu_0 \left(\frac{T}{T_0} \right)^{3/2} \frac{T_0 + 110.4\,\mathrm{K}}{T + 110.4\,\mathrm{K}}, \mu_0 = 1.716 \cdot 10^{-5}\,\frac{\mathrm{m}^2}{\mathrm{s}}, T_0 = 273.15\,\mathrm{K} \tag{4.3}$$

[1] `https://www.lrz.de/services/compute/supermuc/`

4.1.2 Reynolds Averaged Navier–Stokes Equations

The Reynolds decomposition applies to the conservative variables, which then consists of the mean and the fluctuating parts:

$$u = \overline{u} + u', p = \overline{p} + p'. \tag{4.4}$$

Assuming incompressibility ($\rho = const$) and applying the Reynolds decomposition, the equations 4.1 and 4.2 reduce to:

$$\frac{\partial u_i}{\partial x_i} = 0, \tag{4.5}$$

$$\frac{\partial u_i}{\partial t} + \frac{\partial \overline{u_i u_j}}{\partial x_j} = -\frac{1}{\rho}\frac{\partial \overline{p}}{\partial x_i} + \frac{1}{\rho}\frac{\partial \overline{\tau_{ij}}}{\partial x_j} - \frac{\partial \overline{u_i' u_j'}}{\partial x_j}. \tag{4.6}$$

The additional Reynolds stress tensor $\overline{u_i' u_j'}$ appears in the momentum equations as a result of the Reynolds decomposition. This additional term acts as a viscous term. Assuming anisotropy, the turbulent-viscosity hypothesis states that

$$-\overline{u_i' u_j'} = \nu_t \left(\frac{\partial u_i}{\partial x_j} + \frac{\partial u_j}{\partial x_i} \right) - \frac{2}{3} k \delta_{ij} \tag{4.7}$$

with ν_t as the turbulent kinematic viscosity. Because the number of unknown terms increases as a consequence of the decomposition, the mass and flux equations need to be closed by a suitable turbulence model.

4.1.3 Shear Stress Transport

Proposed by Menter [99], the shear stress transport (SST) model adds two transport equations, one for the turbulent kinetic energy k and another one for the turbulent dissipation rate ω:

$$\underbrace{\frac{D\rho k}{Dt}}_{\text{Inertia}} = \underbrace{\tau_{ij}\frac{\partial u_i}{\partial x_j}}_{\text{Production}} - \underbrace{\beta^* \rho \omega k}_{\text{Dissipation}} + \underbrace{(\mu + \sigma_k \mu_t)\frac{\partial^2 k}{\partial x_j \partial x_j}}_{\text{Diffusion}}, \tag{4.8}$$

$$\underbrace{\frac{D\rho\omega}{Dt}}_{\text{Inertia}} = \underbrace{\frac{\gamma}{\nu_t}\tau_{ij}\frac{\partial u_i}{\partial x_j}}_{\text{Production}} - \underbrace{\beta\rho\omega^2}_{\text{Dissipation}} + \underbrace{(\mu + \sigma_\omega \mu_t)\frac{\partial^2 \omega}{\partial x_j \partial x_j}}_{\text{Diffusion}} + \underbrace{2\rho(1-F_1)\sigma_{\omega 2}\frac{1}{\omega}\frac{\partial k}{\partial x_j}\frac{\partial \omega}{\partial x_j}}_{\text{Cross diffusion}}. \tag{4.9}$$

The model switches conveniently between a modified $k-\omega$ model in the boundary layer and the $k-\epsilon$ model in the outer region. The model constants ϕ are blended between the models:

$$\phi = F_1 \phi_1 + (1 - F_1)\phi_2. \tag{4.10}$$

The turbulent viscosity is finally computed from Equation 4.11 by using another blending function F_2. The detailed definition of the turbulence model and the coefficients are included in [99].

$$\nu_t = \frac{a_1}{\max(a_1 \omega; \Omega F_2)}. \tag{4.11}$$

4.1.4 Large Eddy Simulations

Large Eddy Simulations (LES) resolve the large-scale geometry dependent turbulence and then model the small-scale turbulence. Generally, 80% of the turbulent kinetic energy (TKE) is solved by the momentum equations. Considering computational accuracy and effort, the method fills the gap between Reynolds-averaged Navier–Stokes (RANS) and Direct Numerical Simulations (DNS) [116].

The method includes a filtering step before solving the unsteady field. The velocity field and each scalar field is filtered similarly to the Reynolds decomposition in a filtered and a sub-grid fluctuating part:

$$\boldsymbol{u}(\boldsymbol{x},t) = \overline{\boldsymbol{U}}(\boldsymbol{x},t) + \boldsymbol{u}''(\boldsymbol{x},t),\ \overline{u_i''} \neq 0. \tag{4.12}$$

In contrast to Reynolds decomposition, the filtered part is random but without the low scale motion, which is modelled. In addition, the filtering of the sub-grid motion does not reduce to zero.

Applying the decomposition (4.12) on the equations of motion (4.5) results in Navier–Stokes equations of the filtered variables with a residual term containing the sub-grid scale (SGS) tensor τ_{ij}^R. In Fluent, the filtering is conducted within the finite-volume discretization. The residual stress is expressed with an eddy-viscosity assumption as:

$$\overline{U_i U_j} = \overline{U}_i \overline{U}_j + \tau_{ij}^R,\ \tau_{ij}^R = \tau_{ij}^r + \frac{2}{3} k_r \delta_{ij}. \tag{4.13}$$

One commonly implemented SGS model is the Smagorinsky model [136]. The residual stress relates the filtered rate of strain scaled by the viscosity of sub-grid scales:

$$\tau_{ij}^r = -2\nu_r \overline{S}_{ij} \tag{4.14}$$

By introducing the mixing length l_s no explicit introduction of a filter is needed:

$$\nu_r = l_S^2 \left|\overline{S}_{ij}\right| \tag{4.15}$$

4.1.5 Detached Eddy Simulations

The expense of LES in wall bounded flows is reduced, when a hybrid RANS/LES approach is used, especially at high Reynolds numbers. Detached Eddy Simulations (DES) switch between unsteady RANS in the boundary layer and LES in the highly unsteady region (vortex, shear layer). For the current investigations, the SST turbulence model is implemented. The DES-SST formulation scales the TKE dissipation term in Equation 4.8 by the TKE-DES-multiplier:

$$F_{\mathrm{DES}} = \max\left(\frac{l_t}{C_{\mathrm{DES}}\Delta_{\max}}(1 - F_2), 1\right). \tag{4.16}$$

with the constant $C_{\mathrm{DES}} = 0.61$ and the maximum cell length $\Delta_{\max}$. The more conservative blending function F_2 from the SST formulation shields the wall-region from the LES region, as in the varian called Delayed Detached Eddy Simulations (DDES) [101]. The governing equations are universal and the switch from RANS to LES is triggered, when the turbulent length scale exceeds the scaled cell length, i.e. when $l_t > C_{\mathrm{DES}}\Delta_{\max}$. Increasing F_{DES} above 1 leads to an increase of the dissipation term in the k transport equation. This then switches to the SGS model, thus, resolving the large scales [139]. Based on the crossflow distribution of F_{DES} in Figure 4.1, the RANS regions in blue are well separated from the LES regions in red.

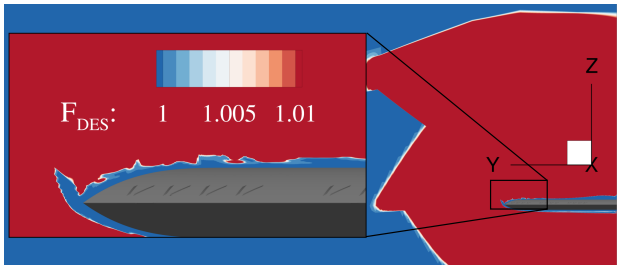

Figure 4.1: The DES switch function takes a value above one in the LES region (red). Blue represents the RANS region.

4.2 Computational Domain

The computational domain depicted in Figure 4.2 measures $15c_r \times 5c_r \times 15c_r$ (length×width×height). The wing is placed with its apex at the origin and closer to the inlet planes in red ($5c_r$) than the downstream opening freestream boundaries in violet ($10c_r$).

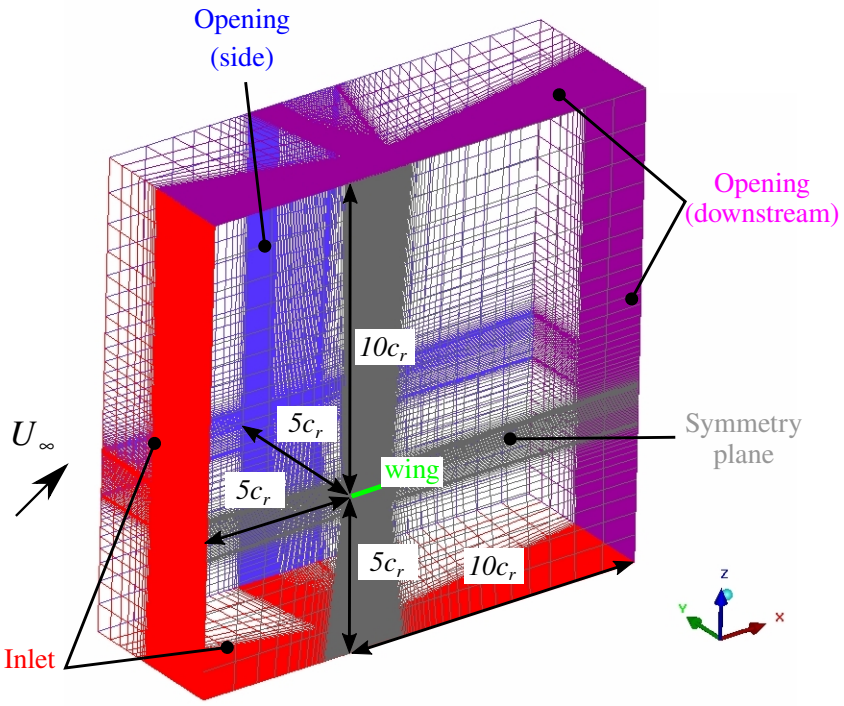

Figure 4.2: Domain boundaries.

At the inlet surface, longitudinal and vertical velocity components are defined by the freestream velocity magnitude U_∞ and the angle of attack α: $u_\infty = U_\infty \cos(\alpha)$, $w_\infty = U_\infty \sin(\alpha)$. The turbulence intensity and the turbulent viscosity ratio are set relatively high at the outer boundaries ($Tu = 5\%$ and $\nu_t/\nu = 10$), such that the turbulence decays downstream towards a value in the vicinity of the wing that corresponds to the wind tunnel values ($Tu \approx 0.3\%$).

Freestream pressure recovery ($p_{avg} = 0$) with backflow boundary conditions are assumed $5c_r$ on the wing starboard side (blue) and $10c_r$ downstream (violet). The outlet planes are located two times farther downstream than the distance between the inlet planes and the wing apex. This allows sufficient convergence of the large high-angle-of-attack wake towards near-freestream flow conditions (see Figure A.1).

The flow is considered to be symmetrical, therefore, a symmetry boundary condition is defined in the xz-plane (grey). This assumption is valid as asymmetric vortex interaction for semi-slender delta-wings with moderate leading-edge sweep angles is negligible [115]. Furthermore, the present investigation comprises of the wind-tunnel setup without péniche with the purpose of analysing the flow manipulation of a singular vortex by pulsed blowing at the leading edge. Hence, a boundary layer modelling of the wind tunnel flow is beyond the scope of this thesis.

4.2.1 Blocking

The domain is discretised in a block-structured manner using the meshing software *ANSYS ICEM CFD 17.0*. Four o-grid layers enclose the wing, as seen in Figure 4.3. This discretization technique permits variable wall-normal element growth corresponding to the requirements for each flow region postulated in [137]. The first layer is located in the boundary-layer region. The volume above the wing within the second and third blocking layer contains the vortex system. In order to minimise the numerical dissipation in LES this region requires a nearly cartesian mesh with high quality. The fourth O-grid layer covers the departure region, where the element spacing increases towards the Euler region. Table 4.2 lists the O-grid parameters and corresponding DES flow regions (dimensions are relative to the half wing span s).

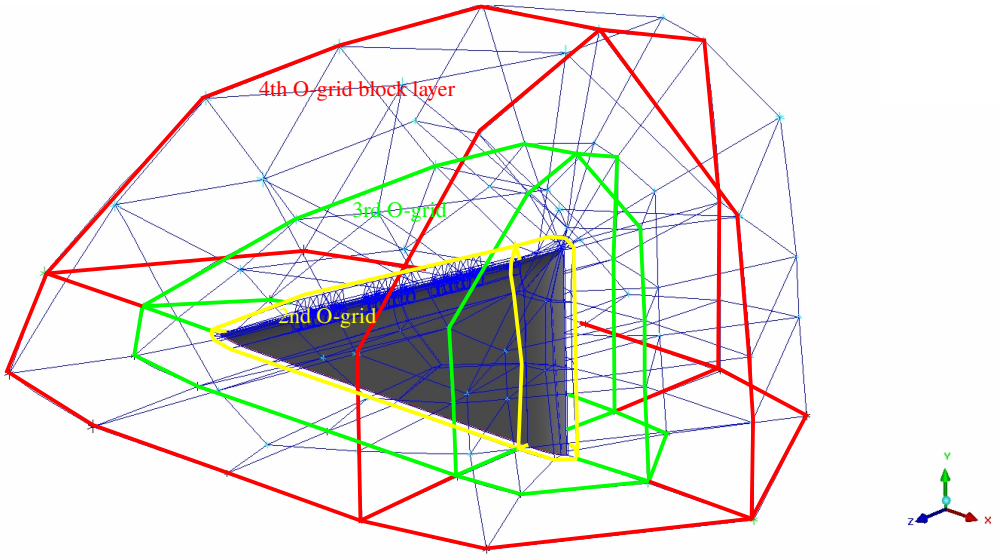

Figure 4.3: Blocking.

Table 4.2: O-grid blocking.

O-Grid	Flow region	Thickness	Initial spacing	Growth rate
1^{st}	Viscous region	$6.5 \cdot 10^{-3} \cdot s$	$2.2 \cdot 10^{-5} \cdot s$	1.13
2^{nd}	Focus region	$5.9 \cdot 10^{-2} \cdot s$	$1.1 \cdot 10^{-3} \cdot s$	1.04
3^{rd}	Focus region	$4.2 \cdot 10^{-1} \cdot s$	$2.9 \cdot 10^{-3} \cdot s$	1.04
4^{th}	Departure region	$6.6 \cdot 10^{-1} \cdot s$	$1.3 \cdot 10^{-2} \cdot s$	1.20

Figure 4.4a shows the blocking above each individual slot pair. This meshing technique enables a structured grid refinement of the local slot exit volume. However, no grid refinement around the slots has been conducted, because the macroscopic effect of blowing is rather the focus of the current investigation and not the detailed slot flow modelling. The surface mesh is adapted around slots marked red in Figure 4.4b. These surfaces have a wall boundary condition for the baseline and a pulsating inlet velocity boundary condition for the actuated cases. Throughout one blowing cycle, the jets are active within the first $T/4$ and inactive during the remaining cycle, $3T/4$. The slot exit velocity components are based on ground testing of the slot exit velocity (see Section 3.2). Table 4.3 lists their definition relative to the freestream velocity magnitude depending on the angle of attack. The dominant component is given by the z-velocity.

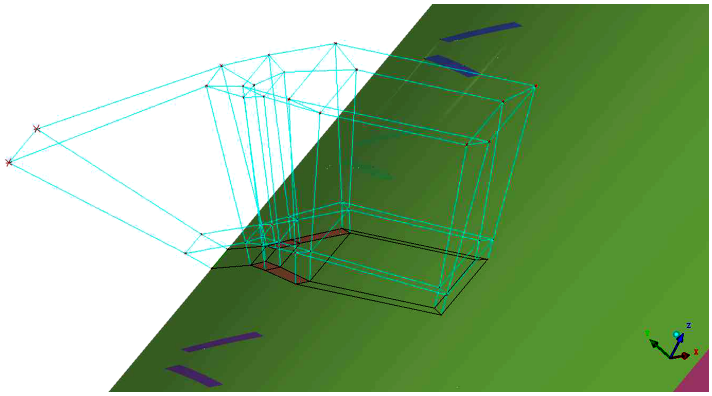

(a) Blocking above a slot pair.

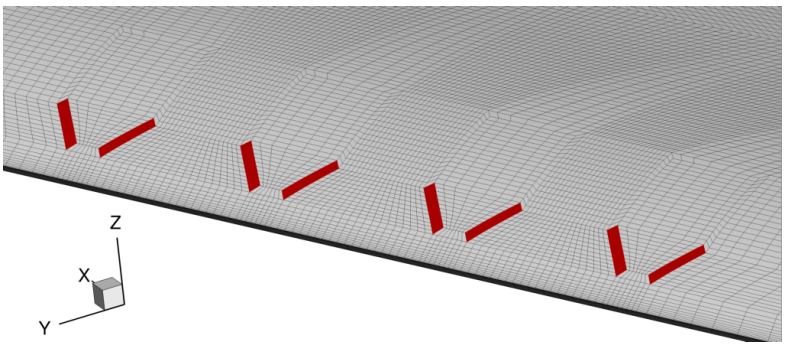

(b) Surface mesh.

Figure 4.4: Slot pair discretisation.

Table 4.3: Jet velocity components.

α	u/U_∞	v/U_∞	w/U_∞
23°	-0.3	-0.7	2.0
35°	-0.7	-1.4	4.1
45°	0.7	-1.5	5.0

4.2.2 Grid Parameters

The Y shaped blocking method divides the wing surface in 411, 408, and 525 elements distributed along the root chord, the trailing edge and leading edge, respectively (Figure 4.5). Excluding the refined leading-edge region (Figure 4.4b), the average element-edge length of the surface mesh is $\Delta_x = 0.0024c_r$ along the root chord and decreases along the span. In comparison, Schiavetta et al. studied the grid resolution affecting the DES solutions of a delta wing flow with element edge length ranging within $0.0035 \leq \Delta/c_r \leq 0.0065$ [123]. In the study, the general grid refinement leads to solutions with even smaller resolved turbulent structures and to a better agreement between CFD and experiments.

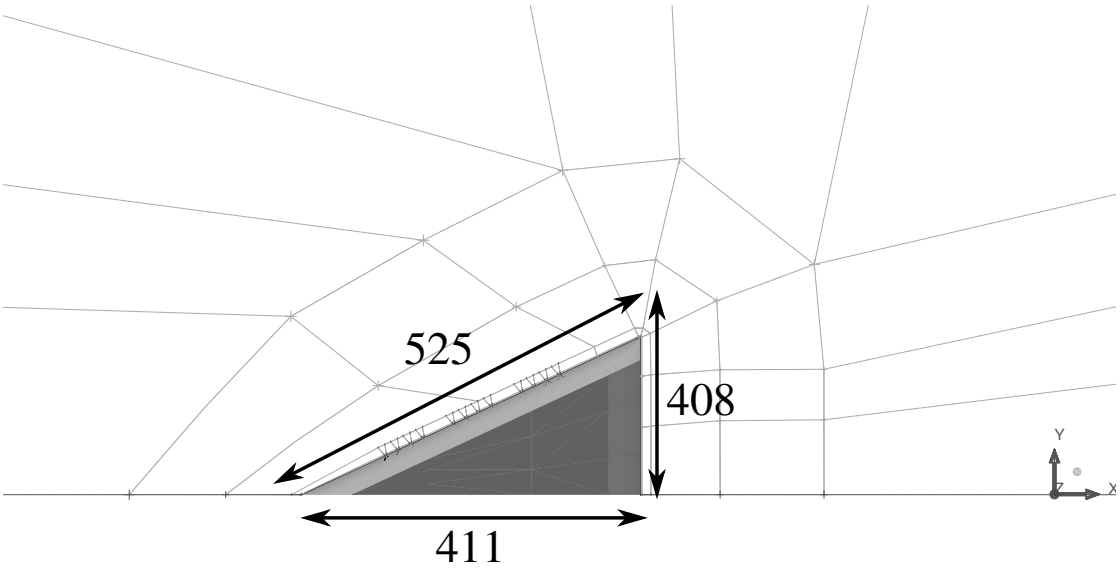

Figure 4.5: Blocking in xy-plane with number of elements.

For the volume mesh inside the block layers shown above, the initial element height and the wall-normal growth ratio are prescribed. The boundary layer is resolved by 27 cell layers (outer boundary marked blue in Figure 4.6). The wall-nearest element has a height within $\Delta_z/s = 2.2 \cdot 10^{-5}$, which translates in wall units to $y^+ < 1$ on the majority of the wing surface (Figure A.2).

In the boundary layer, the elements grow exponentially with a factor of 1.13. In the second (31 layers, yellow) and third blocking layer (59 layers, green) the exponential growth factor of the elements is consistently reduced to 1.04. Hence, the region of the vortex follows the LES-grid quality requirements. The fourth O-grid layer in red connects the LES focus region with the outer flow region (Euler region). Inside this blocking layer, the growth factor is set to 1.2.

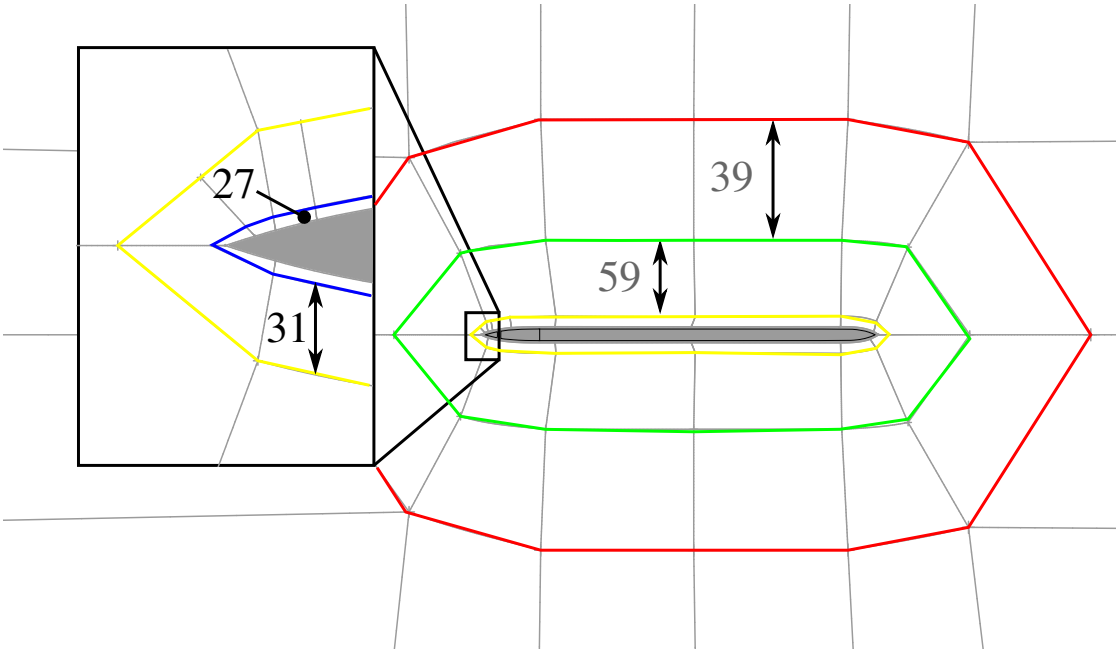

Figure 4.6: Blocking in xz-plane and number of elements.

During a preliminary grid study, the influence of a stepwise grid refinement regarding the O-grids 2–4 was determined. Furthermore, the impact of the apex resolution and the inclusion of a péniche on the vortex flow field was examined. For this purpose the aerodynamic coefficients were evaluated [10, 11]. Besides the filtering of smaller structures, the grid study showed no significant effect on the mean flow when increasing the grid resolution from medium to fine. Therefore, due to computational efficiency, all simulations were conducted on the medium-sized grid, totalling around $49 \cdot 10^6$ hexahedral elements. The mesh has a good quality with a few bad elements in the wing tip region. The grid quality parameters are within the following bounds:

- 3×3×3 determinant > 0.4,
- Equi-angle skewness > 0.1,
- Quality ≥ 0.2.

4.3 Numerical Setup

Table 4.4 lists the flow simulation setup based on [1, 2]. Pressure and velocity are coupled via the SIMPLEC algorithm (Semi-Implicit Method for Pressure Linked Equations–Consistent). The least squares cell-based method evaluates the gradients for the fluxes.

Table 4.4: Numerical setup.

Solver	*ANSYS Fluent 19.2*
Compressibility	Incompressible ($Ma_{\max} < 0.25$)
Pressure-velocity coupling	SIMPLEC
Gradient evaluation	Least Square Cell Based
Turbulence model	DDES-SST
Converged starting solution	RANS $k-\epsilon$ realizable
Transient scheme	Bounded second order implicit
Pressure advection	Second order
Momentum advection	Bounded central differencing
Turbulence advection	First Order Upwind
Pressure under relaxation	0.3
Momentum under relaxation	0.7
k and ω under relaxation	0.8
Turbulent viscosity under relaxation	1.0

Starting from an initial converged flow field, which is obtained by a steady RANS simulations using the k–ϵ turbulence model, the transient flow simulation with the DDES-SST model was initiated. Second order accurate schemes discretise momentum and pressure advection. In case of the turbulence variables k and ω, a first-order scheme is sufficient for an accurate advection modelling (and more stable as the second order scheme), since the source terms in both turbulence transport equations are dominating [100].

A discrete dual time stepping approach with the bounded second-order implicit scheme advances the solution in time. The time-step is 1/800 of one blowing cycle $T = f_a^{-1}$ and depends on the actuation frequency which is in the range of $f_a = 12\,\text{Hz}$–$65\,\text{Hz}$. Consequently, one time-step length varies in the range $\Delta t = 1.0 \cdot 10^{-4} - 1.9 \cdot 10^{-5}\,\text{s}$. The resolved frequencies are in ranges of 2-5 kHz. Applying the Niquist criterion, the investigated spectrum ranges up to 1 kHz, therefore, covering all relevant flow-periodic phenomena.

Table 4.5 presents the three cases investigated: $\alpha = 23°, 35°$ and $45°$ with corresponding unitless parameters. The time is reduced by the convective time scale and expressed as:

$$\tau = \Delta t \frac{U_\infty}{c_r}. \tag{4.17}$$

Table 4.5: Test cases with corresponding control and numerical parameters.

α	Re	F^+	c_μ	τ	CFL	τ_{tot} (Bas. / Act.)
23°	$1.0 \cdot 10^6$	2.6	0.14%	$5 \cdot 10^{-4}$	0.2	40.6 / 30.8
35°	$0.5 \cdot 10^6$	2.6	0.55%	$5 \cdot 10^{-4}$	0.2	44.1 / 45.8
45°	$0.5 \cdot 10^6$	1.0	0.85%	$1 \cdot 10^{-3}$	0.5	51.3 / 30.7

For each angle of attack, simulations cover both, the baseline (without actuation) and synchronised pulsed blowing at case-dependent blowing parameters F^+ and c_μ. The Courant-Friedrich-Levy (CFL) above the wing is expressed in Equation 4.18 and does not exceed 1.

$$CFL = \Delta t \frac{U_\infty}{\Delta_x} \tag{4.18}$$

After the flow field is relaxed, the statistical averaging is initiated. For all test cases, the total simulation time in convective time scales ranges between $\tau_{tot} = 30$ and 51.

4.4 Post-Processing

4.4.1 Dynamic Mode Decomposition

Recently, Dyanmic Mode Decomposition (DMD) was applied and validated for a variety of unsteady flows, e.g. pitching and plunging airfoil, lid-driven cavity flow, flow between two cylinders etc. [96, 106, 125]. In addition, the method showed promising results for reducing significant storage memory for large and streaming datasets to the most relevant flow dynamics [59]. In [151], the breakdown phenomenon of a leading-edge vortex was analysed by extracting DMD modes from volumetric transient flow-field data.

4.4.1.1 Principle

The DMD method, proposed originally by Schmid [124], was applied on the current transient numerical data, following the work flow developed in [120]. In a global stability analysis sense, the method extracts dominant modes with corresponding frequencies, amplitudes and decay/amplification rates. Considering only dominant modes, a reduced order model of the flow dynamics can be obtained. Finally, this reduction helps, on the one hand, to analyse the flow dynamics by detecting the most unstable dominant modes and, on the other hand, to generate a lower dimensional model, e.g. for designing closed-loop flow control.

Snapshots of bundled transient flow field data (or a subdomain thereof) at each constant time interval of Δt are arranged in chronological order as column vectors $\boldsymbol{v}_i$ in the snapshot matrix (each snapshot designated by index $i = 1, \ldots, N$), as in:

$$\boldsymbol{V_1}^N = \{\boldsymbol{v}_1, \boldsymbol{v}_2, \boldsymbol{v}_3, \cdots, \boldsymbol{v}_N\}. \tag{4.19}$$

Matrix ${\boldsymbol{V}_1}^N$ has the dimensions $[n \times N]$, in which n is the total number of local sampled points corresponding to one instance of $i \in [1, \ldots, N]$. The objective of DMD is the generation of a linear mapping matrix $\boldsymbol{A}$ that maps the current snapshot on the subsequent one with

$$\boldsymbol{v}_{i+1} = \boldsymbol{A}\boldsymbol{v}_i. \tag{4.20}$$

Hence, (4.19) can be expressed as

$$\boldsymbol{V}_1{}^N = \{\boldsymbol{v}_1, \boldsymbol{A}\boldsymbol{v_1}, \boldsymbol{A}^2\boldsymbol{v}_1, \cdots, \boldsymbol{A}^{N-1}\boldsymbol{v}_N\}. \tag{4.21}$$

Assuming sufficient number of snapshots, the final snapshot can be expressed as a linear combination of all the previous vectors,

$$\boldsymbol{v}_N = a_1\boldsymbol{v}_1 + a_2\boldsymbol{v}_2 + \cdots + a_{N-1}\boldsymbol{v}_{N-1}. \tag{4.22}$$

The linear mapping of the sequence $[1, \ldots, N-1]$ on to $[2, \ldots, N]$ can be expressed as

$$\boldsymbol{A}\boldsymbol{V}_1{}^{N-1} = \boldsymbol{V}_2{}^N = \boldsymbol{V}_1{}^{N-1}\boldsymbol{S} + \boldsymbol{r}\boldsymbol{e}_{N-1}{}^T, \tag{4.23}$$

with the residual vector $\boldsymbol{r}$, the $(N-1)$th unit vector $\boldsymbol{e}_{N-1}$ and the companion type matrix

$$\boldsymbol{S} = \begin{pmatrix} 0 & & & & a_1 \\ 1 & 0 & & & a_2 \\ & \ddots & \ddots & & \vdots \\ & & 1 & 0 & a_{N-2} \\ & & & 1 & a_{N-1} \end{pmatrix}. \tag{4.24}$$

The eigenvalues of $\boldsymbol{S}$ approximate those of $\boldsymbol{A}$, which describe the system dynamics. However, there is a better alternative and a more robust method compared to the mostly non-practical calculation of $\boldsymbol{S}$. The robust method uses a "full" matrix $\tilde{\boldsymbol{S}}$, relating to $\boldsymbol{S}$ by a similarity transformation. The preparation step includes the singular value decomposition of the snapshot matrix

$$\boldsymbol{V}_1{}^{N-1} = \boldsymbol{U}\boldsymbol{\Sigma}\boldsymbol{W}^H. \tag{4.25}$$

This decomposition extracts the spatial structures (topos) in the singular value matrix containing the proper orthogonal modes $\boldsymbol{U}[n \times n]$ [5, 60]. The temporal structures (chronos) constitute the unitary matrix $\boldsymbol{W}^H[r \times r]$, in which r is the rank of the snapshot matrix $\boldsymbol{V}_1{}^{N-1}$. The diagonal rectangular matrix $\boldsymbol{\Sigma}[n \times r]$ correlates the modes with their energy content.

Substituting the singular value decomposition of $\boldsymbol{V}_1{}^{N-1}$ in (4.23) and rearranging the terms leads to the expression

$$\boldsymbol{U}^H\boldsymbol{A}\boldsymbol{U} = \boldsymbol{U}^H\boldsymbol{V}_2{}^N\boldsymbol{W}\boldsymbol{\Sigma}^{-1} = \tilde{\boldsymbol{S}}, \tag{4.26}$$

which is the projection of the linear operator $\boldsymbol{A}$ onto the proper orthogonal decomposition (POD) basis. The eigenvectors of $\tilde{\boldsymbol{S}}$, expressing $\tilde{\boldsymbol{S}}\boldsymbol{y}_i = \mu_i\boldsymbol{y}_i$ mapped onto the POD-modes defines the ith dynamic (or DMD) mode:

$$\phi_i = \boldsymbol{U}\boldsymbol{y}_i. \tag{4.27}$$

For each DMD mode, dynamic quantities, as the normalized amplitude, reduced frequency, damping/amplification rate are extracted and discussed in this work. Table 4.6 shows the mathematical expressions based on

$$\boldsymbol{b} = \boldsymbol{\Phi}^{-1}\boldsymbol{v}_1 \tag{4.28}$$

and

$$\lambda_i = \frac{\log(\mu_i)}{2\pi\Delta t}. \tag{4.29}$$

Table 4.6: DMD parameters.

Variables	Expression
Normalized Amplitude	$\lvert\boldsymbol{b}_i\rvert/\lVert\boldsymbol{b}_i\rVert_2$
Reduced frequency	$\Re(\lambda_i)\cdot c_r/U_\infty$
Damping rate	$\Im(\lambda_i)$

4.4.1.2 POD vs. DMD

This subsection points out the differences between both popular decomposition methods, dynamic mode (DMD) and proper orthogonal decomposition (POD). DMD orthogonalises the data sequence in time extracting spatio-temporal structures and their corresponding frequencies. In contrast, the POD extracts the structures by spatial orthogonalisations.

Dominant modes resulting from DMD of a lid-driven cavity showed coherent structures near the wall. In contrast, dominant POD structures are located in the center of the cavity, as this decomposition weighs the modes by their energy content and not based on their persistance in the time investigated [125]. Table 4.7 lists the major differences between POD and DMD based on the method, the identified structures, their ranking, eigenvalues of the linear mapping function ($\boldsymbol{A}$ or $\boldsymbol{S}$), description of evolution in time and storage requirements reported in [96, 125].

Despite similar orders of magnitude, the error of flow reconstruction from a few dominant POD modes is lower than the reconstruction from DMD modes. However, if the investigator focusses more on the dynamics of the system and he/she develops optimum control, then DMD is more suitable than POD. For this reason, the transient numerical data of the current investigation is investigated based on the flow decomposed into dynamic modes.

Table 4.7: Comparing both decomposition techniques: POD and DMD.

POD	DMD
Spatial orthogonalisation	Temporal orthogonalisation
Spatial modes	Temporal modes
Energetic structures	Dynamically relevant structures
Decomposition by kinetic energy	Decomposition by oscillation frequency
Real eigenvalues	Complex eigenvalues (Frequency and decay)
Evolution in time by temporal coefficients	Evolution in time by analytical functions
Higher data storage	Lower data storage

4.4.1.3 Reconstruction

The above described DMD method was applied on the transient data bundled from rectangle planes placed in the flow field. As a result, a spectrum of DMD modes was computed from four cases of the delta-wing flow at very high angles of attack. The results are presented and discussed in Section 5.6.

For validating the method the flow field above the delta wing at 35° incidence without flow perturbation (baseline) is reconstructed based on a variable number of dominant modes. The data analysed is the axial velocity sampled from the crossflow plane at 60% relative chord length

($x/c_r = 0.6$) at instances separated by a constant time shift of $10\Delta t = 3.9 \cdot 10^{-4}$ s. In dimensionless representation, the data was sampled at a sufficient small fraction of the convective time scale of $\Delta\tau = 3.2 \cdot 10^{-3}$.

From a total number of 2000 samples, the dynamic modes are extracted and ranked by the normalized amplitude. The normalized amplitudes of the first 50 most dominant modes are plotted in Figure 4.7. The amplitude is high for the first 8 modes, thereafter it decreases below 10%.

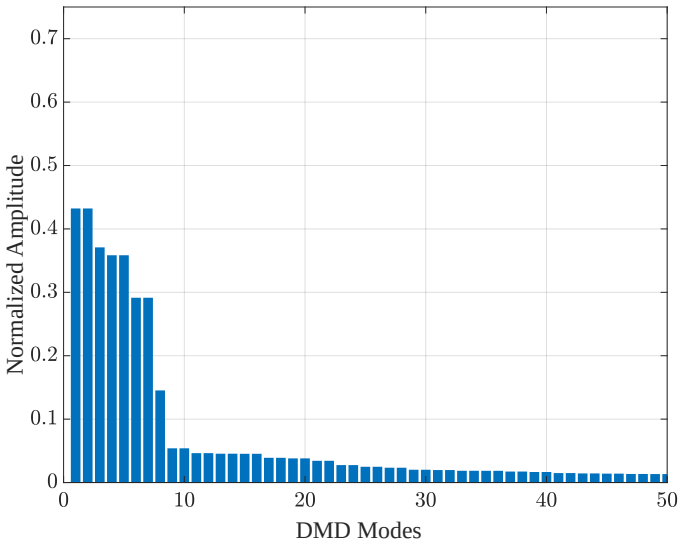

Figure 4.7: DMD modes ranked based on the normalized amplitude. Data from the x-velocity in the crossflow plane at $x/c_r = 0.6$, $\alpha = 35°$, baseline.

The purpose is to represent the dynamics of the flow by a lower dimensional model. Therefore, the question arises, how many modes have to be considered. In the following, the reconstruction from a reduced number of DMD modes is analysed. The reconstruction of a snapshot is expressed by

$$\tilde{\boldsymbol{v}}(t) = \boldsymbol{\Phi} \exp(\boldsymbol{\lambda} t)\boldsymbol{b}, \tag{4.30}$$

with $\boldsymbol{\lambda}$ being the vector of the complex eigenvalues of the matrix $\tilde{\boldsymbol{S}}$ and $\boldsymbol{b}$ the coefficients mapped on the first snapshot, see (4.28).

Figure 4.8a shows the axial velocity distribution of the first snapshot investigated $\boldsymbol{v}_1$. The result of the $\boldsymbol{v}_1$ reconstruction based on the most dominant 20, 100, 400 and 1000 DMD modes is illustrated in Figure4.8b–e. As the number of considered modes increases, the accuracy of the reconstruction is improved. The combination of an unsteady 3D flowfield with a high degree of turbulence leads to multiple dynamic modes constituting the full spectrum of the dynamic system. The modes reach down to the scales that are not filtered by the DES grid.

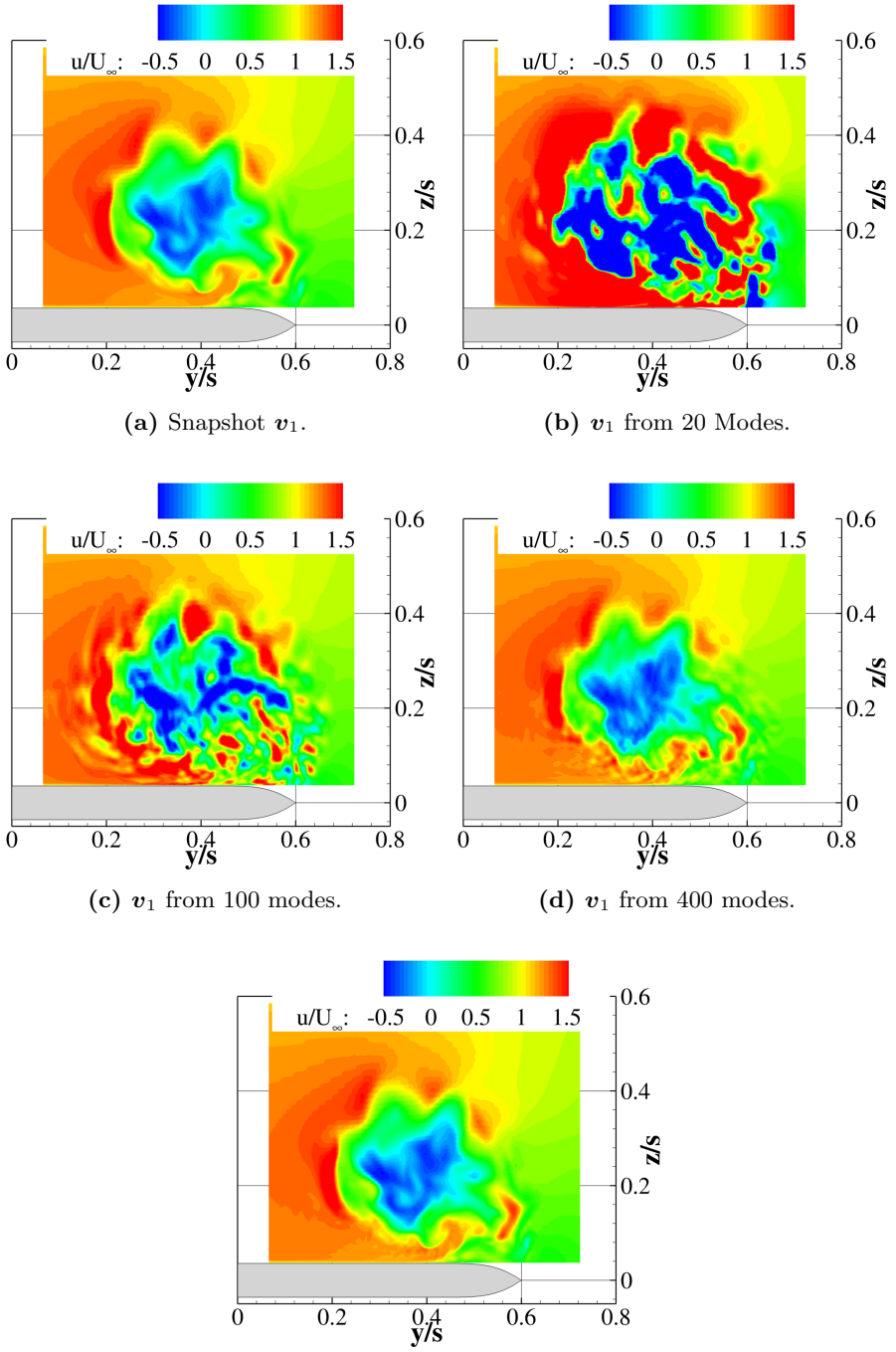

(a) Snapshot $\boldsymbol{v}_1$.

(b) $\boldsymbol{v}_1$ from 20 Modes.

(c) $\boldsymbol{v}_1$ from 100 modes.

(d) $\boldsymbol{v}_1$ from 400 modes.

(e) $\boldsymbol{v}_1$ from 1000 modes.

Figure 4.8: Reconstruction of the axial velocity in the cross flow plane $x/c_r = 0.6$, $\alpha = 35°$, baseline, from increasing number of modes.

4.4.2 Vortex Detection

A post-processing step is introduced to identify relevant vortical structures (discrete vortices) from numerical and experimental data. The applied method is based on the decomposition of the velocity gradient tensor $\nabla \boldsymbol{u}$. The classical Galilei-invariant identification techniques, like the Q-criterion and the λ_2-criterion are used for discrete vortex identification in this thesis. Other techniques are reported in [58, 81].

4.4.2.1 Q-Criterion

The Q-criterion is calculated from the second invariant of $\nabla \boldsymbol{u}$ and it identifies vortices when the vorticity magnitude predominates the strain-rate magnitude [73]:

$$Q = \frac{1}{2}\left(\|\boldsymbol{\Omega}\|^2 - \|\boldsymbol{S}\|^2\right) > 0 \tag{4.31}$$

with the vorticity tensor $\boldsymbol{\Omega}$ as the antisymmetric part of $\nabla \boldsymbol{u}$ and the strain-rate tensor $\boldsymbol{S}$ the symmetric part:

$$\begin{aligned} \boldsymbol{\Omega} &= \frac{1}{2}\left[\nabla \boldsymbol{u} - \nabla \boldsymbol{u}^{\intercal}\right], \\ \boldsymbol{S} &= \frac{1}{2}\left[\nabla \boldsymbol{u} + \nabla \boldsymbol{u}^{\intercal}\right]. \end{aligned} \tag{4.32}$$

4.4.2.2 λ_2-Criterion

Jeong and Hussain first proposed the vortex detection based on the second negative eigenvalue λ_2 of the tensor $\boldsymbol{\Omega}^2 + \boldsymbol{S}^2$ [76]. The pressure minimum condition in the vortex core results from the vorticity transport equation (index notation in 4.33), in which the first two terms are negligible. These terms represent the unsteady irrotational straining term and the viscous term.

$$\underbrace{\frac{\mathrm{D}S_{ij}}{\mathrm{D}t}}^{\to 0}_{\text{Unsteady term}} - \underbrace{\nu S_{ij,kk}}^{\to 0}_{\text{Viscous term}} + \underbrace{\Omega_{ik}\Omega_{kj}}_{\text{Vorticity}} + \underbrace{S_{ik}S_{kj}}_{\text{Strain-rate}} = \underbrace{-\frac{1}{\rho}p_{,ij}}_{\text{Pressure gradient}} \overset{!}{=} 0. \tag{4.33}$$

4.4.2.3 Detection Algorithm in PIV

Similar to the algorithm in [39], the method implemented by Bartasevicius et. al in *MATLAB V2018b* detects discrete vortices from planar stereoscopic PIV data sets. The method filters and splits the λ_2 data field and offers a statistics of detected vortices [7]. The search algorithm constitutes of the following steps:

1. calculate the λ_2-criterion and the statistics over one set of 400 samples,
2. apply three filters: $\lambda_2 = 0$, where
   $\lambda_{2,\mathrm{rms}} < \lambda_{2,\mathrm{rms,Filter}}$,
   $\lambda_2 > 0$,
   $\lambda_2 > \lambda_{2,\mathrm{avg,Filter}}$
3. watershed algorithm [102] for splitting the plane into λ_2 regions (vortex regions),
4. 4^{th} filter: $\lambda_2 = 0$, where $\lambda_2 < \lambda_{2,\mathrm{Peak,Filter}}$ and
5. for each separate region representing the vortex core the circulation, position and radius are calculated.

In the first step, the algorithm (*Matlab* code "calc_L2.m") takes all 400 samples of one measured plane containing the planar information of the instantaneous velocity components (Saved in data files "C00001.dat–C00400.dat"). Subsequently, it calculates the vortex parameters and λ_2 statistics. The vortex parameters are:

1. Swirling strength [161],
2. λ_2 [76] and
3. x-vorticity ω_x

The statistical values include the average $\lambda_{2,\mathrm{avg}}$ and rms $\lambda_{2,\mathrm{rms}}$ values. The search algorithm was applied on the cross flow plane at x/c_r, baseline case, $\alpha = 23°$, and each step documented in Figure 4.9 for the frame 200 out of 400 frames.

The input data is the velocity field, as shown in Figure 4.9a. From this, the vortex field parameters are computed: x-vorticity (b), λ_2-criterion (c) and swirling strength (see Figure A.3).

The subsequent step filters the data based on λ_2 and its statistics. Therefore, steady regions are excluded, if the condition $\lambda_{2,\mathrm{rms}} < \lambda_{2,\mathrm{rms,Filter}}$ is true (Figure A.4). Also the regions with positive λ_2 values are excluded. Here no vortices exist. Finally, the background noise is filtered out: $\lambda_2 > \lambda_{2,\mathrm{avg,Filter}}$ (Figure A.4). The λ_2-criterion after each filtering step is detailed in Figure A.5. Table 4.8 lists the filtering parameters resulting from the study reported in [7].

Table 4.8: λ_2 filters.

$\lambda_{2,\mathrm{rms,Filter}}$	$\lambda_{2,\mathrm{avg,Filter}}$	$\lambda_{2,\mathrm{Peak,Filter}}$
$4 \cdot 10^4\,1/\mathrm{s}^2$	$-2 \cdot 10^4\,1/\mathrm{s}^2$	$-1 \cdot 10^5\,1/\mathrm{s}^2$

The watershed algorithm, as proposed by Meyer [102], detects local minima in the filtered λ_2 field and separates these regions. The result of this field separation is shown in Figure 4.9d. The final filter is applied that extracts only the relatively strong vortices ($\lambda_2 < -1 \cdot 10^5\,1/\mathrm{s}^2$). Figure 4.9e shows the λ_2 distribution after this final filtering step.

In the final step, the cross-sectional surface information obtained from the watershed algorithm $\boldsymbol{S}$ and the vorticity ω_x are used for calculating the circulation for each individual vortex:

$$\Gamma_x = \int\int_S \omega_x \cdot \mathrm{d}\boldsymbol{S}. \tag{4.34}$$

Figure 4.9f shows the final result of the presented detection method: the scatter of the vortices in the instantaneous crossflow plane, with position, radius and strength (circulation) information. This tool complements the analysis of the steady flow field providing additional information from the individual frames. Assessing the flow field based on vortex statistics brings an addition to low-frequency stereo PIV investigations.

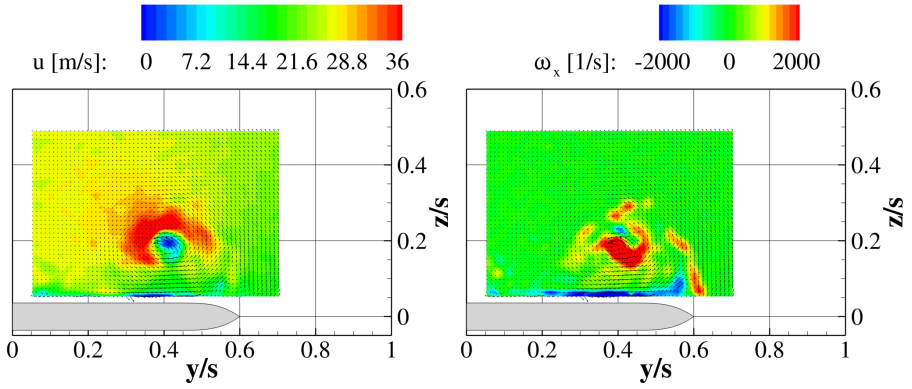

(a) Velocity field from PIV Frame. **(b)** X-vorticity.

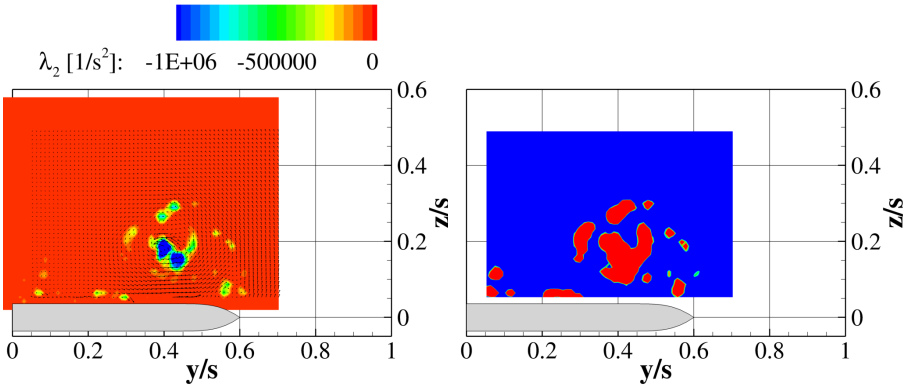

(c) λ_2-criterion. **(d)** Vortex regions.

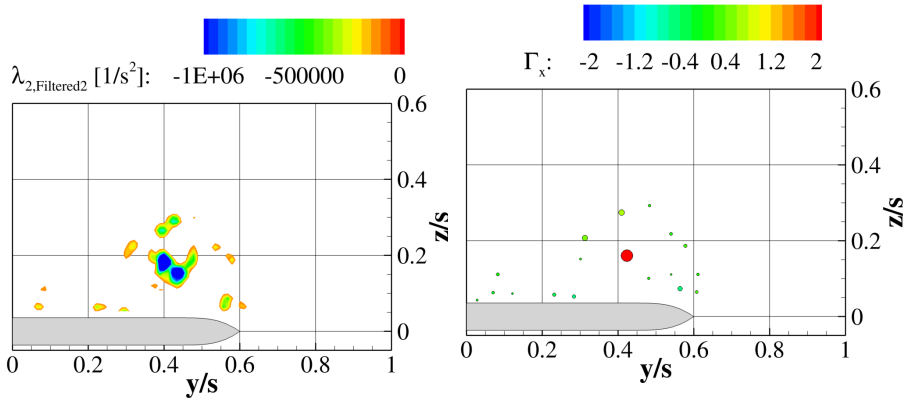

(e) Filtered λ_2-criterion. **(f)** Scatter of vortices with circulation and scaled radius.

Figure 4.9: Results after each step of the search algorithm exemplified on Frame 200. $\alpha = 23°$, $x/c_r = 0.6$, baseline case (vortex bursting).

5 Results and Discussion

The results are presented and discussed based on wind-tunnel measurements and complementary transient numerical simulations. This complementary analysis offers new insights into the mean flow field and the periodic phase-averaged response to pulsed blowing at the leading edge. In the experimental investigation, synchronised and desynchronised actuators (i.e. frequency and phase variation) are assessed based on improvement of aerodynamic coefficients and 3D velocity field alteration. The transient numerical data is analysed regarding the interaction of the injected jets and the flow field alteration resulting in a complex periodic response, which on average delays breakdown and reattaches the shear layer. Significant results and discussions included in this chapter are also published in [16–19, 21, 22].

5.1 Aerodynamic Characteristics

The analysis covers three flight regimes (pre-stall, stall and post-stall) at two freestream Reynolds numbers referenced by the mean aerodynamic chord length ($Re = 0.5 \cdot 10^6$ and $1.0 \cdot 10^6$). Therefore, the Reynolds number independency of the aerodynamic coefficients is analysed before the effect of pulsed blowing and parameter variation on the aerodynamic characteristics.

5.1.1 Reynolds Number Effect

Figure 5.1 presents the measured aerodynamic coefficients of the baseline case as a function of the angle of attack α and the freestream Reynolds number Re. The presented polars include lift, drag, pitching moment and rolling moment coefficients and derived variables, like the lift-to-drag ratio C_L/C_D and the dimensionless spanwise force application point y_p/s.

The lift coefficient C_L increases with the angle of attack in a nonlinear manner up to stall, $\max(C_L) = 1.10$, which is reached at $\alpha_{\max} = 35°$. Prior to stall, the lift slope $\partial C_L/\partial\alpha$ is slightly decreasing. Due to a moderate leading-edge sweep angle of $\varphi = 65°$ and a moderate wing thickness of $\delta/c_r = 3.4\%$ the suction on the upper surface is reduced and the vortical lift contribution is relatively small with respect to more slender and thinner wings (see also [87]). In comparison, a slender thin delta wing generally exhibits an increasing vortex lift slope ($\sim \sin^2(\alpha)$) [114].

At $\alpha = 20°$, the discontinuity in the lift and pitching moment derivative (e.g. $\partial C_{MY}/\partial\alpha$) signals breakdown first occurring above the wing's trailing edge. With increasing α, the breakdown location shifts upstream, reaching the apex at stall. The slope decreases above $\alpha = 20°$, as the high-pressure wake of the vortex breakdown expands upstream. The maximum pitching moment coefficient reads $\max(C_{MY}) = 0.29$ at $\alpha_{\max}$. In contrast, the drag-curve is little influenced by the vortex instability. C_D progresses with a parabolic trend, then continuously departures from this trend in the pre-stall flight regime. Maximum drag ($\max(C_D) = 0.90$) is reached at $\alpha = 41°$, which is considerably higher than $\alpha_{\max}$.

Beyond stall, $\alpha > 35°$, the lift and pitching moment coefficients decrease mildly followed by an abrupt drop between $\alpha = 41° - 42°$. This is caused by the collapse of the vortex system. Above $\alpha = 41°$, the flow field comprises of complete separation without reattachment on the wing's upper surface (see Section 5.2).

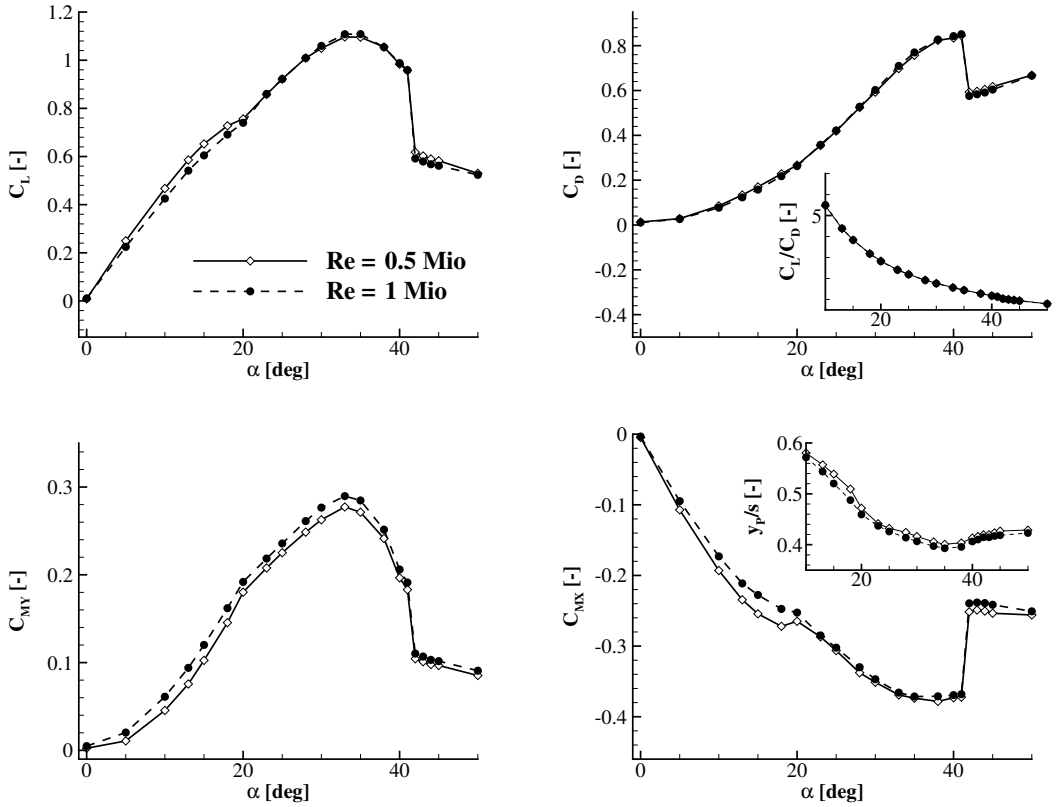

Figure 5.1: Aerodynamic coefficients for two frestream Reynolds numbers: $Re = 0.5 \cdot 10^6$ and $1.0 \cdot 10^6$.

Despite the small Reynolds number effect on the lift coefficient at $\alpha < 20°$, overall, the aerodynamic characteristics are rather insensitive to the increase in Reynolds number from $0.5 \cdot 10^6$ to its double value, as seen in Figure 5.1. In the range $0° \leq \alpha \leq 20°$, the vortex develops over the entire leading-edge. The freestream Reynolds number influences the secondary separation line, which is dependent on the boundary-layer state. A laminar wall separation is located farther upstream and produces a wider secondary vortex than turbulent wall separation. The secondary structure has a displacement effect on the primary structure leading to increased lift and decreased pitching moment [17]. In contrast to the discussed aerodynamic coefficient, the lift-to-drag ratio C_L/C_D is *Re*-independent. The rolling moment coefficient C_{MX} has a similar trend as the lift coefficient. The spanwise force application location of the normal total force is obtained by dividing the rolling moment coefficient by the normal force coefficient, according to the formula:

$$\frac{y_p}{s} = \frac{C_{MX}}{C_Z} \cdot \frac{l_\mu}{s} \tag{5.1}$$

and takes values in the range $0 < y_p/s < 1$ (between the symmetry plane and the wing tip). With increasing angle of attack, the vortex shifts upstream and increases in cross-section. This leads to an inboard shift of the pressure point, decreasing y_p/s. At stall, y_p reaches its minimum value of approximately 0.4 and increases mildly with α towards saturation. The same graph reveals

that the force application point is located slightly more inboard when the freestream Reynolds number is increased. However, a Reynolds number effect at high angles of attack is within the measurement accuracy and can be neglected.

Figure 5.2 compares the flow field at $\alpha = 23°$ for both Reynolds numbers investigated. At both conditions, breakdown occurs at $x/c_r = 0.65$. Therefore, this cannot be the reason for the little difference in pitching moment coefficient. Therefore, the mildly increased axial relative velocity at $Re = 0.5 \cdot 10^6$ within in the vortex flow excluding the breakdown wake region is responsible for an increase by a small amount the pitching moment coefficient compared to the higher Reynolds number.

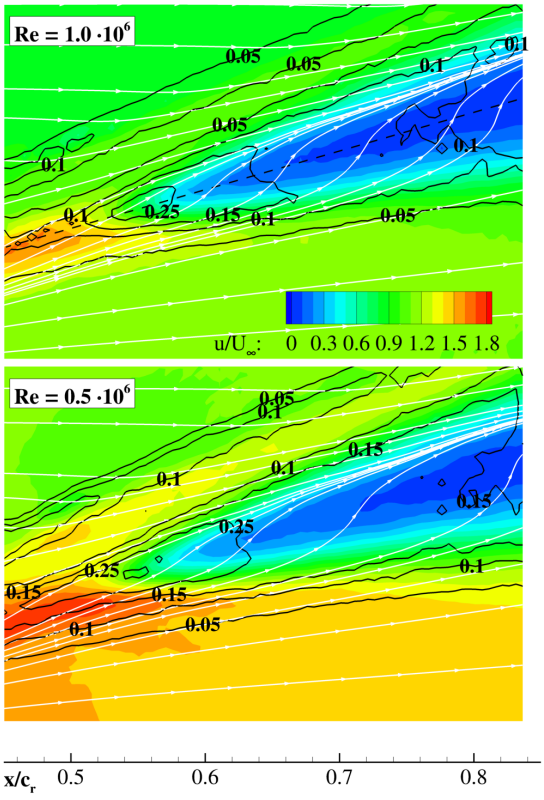

Figure 5.2: Reynolds number effect on the flow field. PIV plane along the vortex core at $\alpha = 23°$, $Re = 0.5 \cdot 10^6$ below and $Re = 1.0 \cdot 10^6$ above with colourmap of the relative axial velocity u/U_∞ and isolines of TKE/U_∞^2.

5.1.2 Actuated Cases

This section provides a complete overview of the pulsed blowing effect on the aerodynamic characteristics at high angles of attack (pre-stall, stall and post-stall flight regimes). In addition, the assessment of different blowing strategies is performed. These strategies include synchronous pulsed blowing at a fixed reduced frequency ($F^+ = 2.6$ for stall and $F^+ = 1.0$ for post-stall) and flight-regime dependent phase/frequency-modulated blowing. The corresponding flow field analysis is conducted in Section 5.2.1.

The actuation parameters are dependent on the freestream conditions as different flow-field instabilities are addressed [12, 82]. Up to $\alpha = 38°$ unison blowing with $F^+ = 2.6$ addresses the helical mode instability. The control of reattachment is best achieved with a reduced actuation frequency at unity. Therefore, a distinction between the stall and post-stall regime is made, as different instabilities are triggered in the respective flow field. As highlighted in Chapter 3, two frequency-dependent (FV1 and FV2) and four phase-dependent modulation techniques (PV1, PV2, PV3 and PV4) are investigated for three cases:

Table 5.1: Considered test cases and corresponding momentum coefficient c_μ.

Flight regime	$\boldsymbol{\alpha}$	$\boldsymbol{Re}$	$\boldsymbol{c_\mu}$
Stall	$23° - 40°$	$1.0 \cdot 10^6$	$1.4 \cdot 10^{-3}$
Stall	$23° - 40°$	$0.5 \cdot 10^6$	$5.5 \cdot 10^{-3}$
Post-stall	$40° - 50°$	$0.5 \cdot 10^6$	$8.7 \cdot 10^{-3}$

5.1.2.1 Phase Modulation

This subsection focuses on phase-modulated blowing. The applied phase-dependent modulation implies that the blowing phase is delayed in downstream direction for each slot individually. It is investigated, if the downstream increasing delay of blowing sequence improves the aerodynamic performance compared to synchronous blowing. This hypothesis is based on the amplification effect of disturbances: when an upstream injected disturbance reaches the current location, blowing is activated by the local slot pair energizing the downstream travelling disturbance package. The phase shift is given as the ratio of time delay and blowing period in Figure 5.3 for all three cases discussed here.

For the stalled condition, two strategies are investigated: continuous/linear and segmentwise phase variation along the leading-edge, which are designated by pink left triangles and gray delta symbols, respectively (Figures 5.3a and b). For the first case (stall at $Re = 1.0 \cdot 10^6$), the phase slope reads $\partial\theta/\partial(x/c_r) = 323\%$. For the following case, with reduced freestream Reynolds number, the phase slope is reduced to a value of 271%. For post-stall, two additional linearly increasing phase shift modes are investigated. Hence, Figure 5.3c shows all considered phase shifted blowing strategies ordered by increasing slope. The objective of this parametric study is to find a correlation between the phase increase $\partial\theta/\partial(x/c_r)$ and the improvement of the aerodynamic coefficients, e.g. lift increase relative to the baseline case. Therefore, post-stall phase delays of $\partial\theta/\partial(x/c_r) = 117\%$, 139% and 208% are subject to the following analysis.

This section addresses the following research questions:

- How does a positive phase delayed blowing affect the aerodynamic characteristics compared to baseline and unison blowing cases?
- How does a segmentwise increase of blowing delay affect the aerodynamic chareacteristics compared to a strictly linear one?
- Does a correlation between phase delay increase and lift coefficient increase exist?

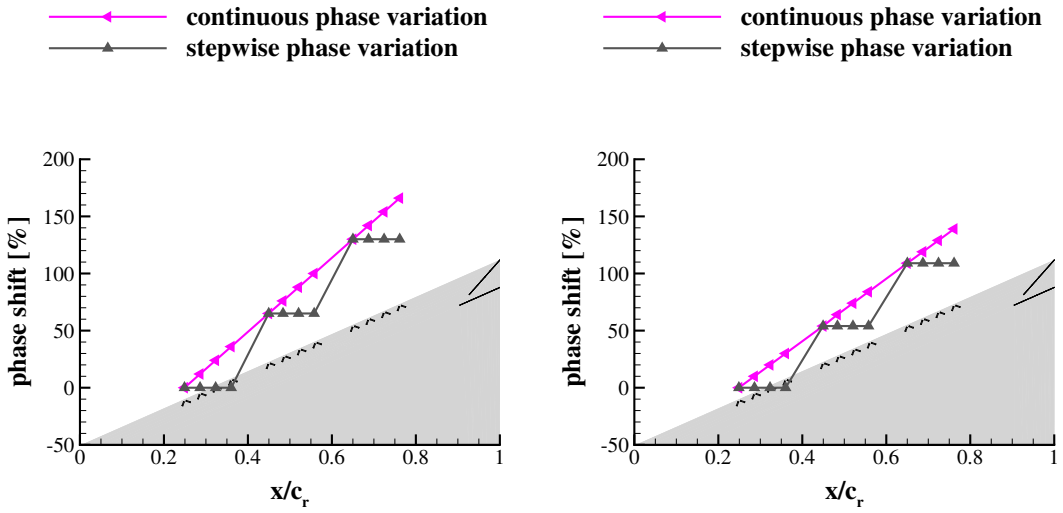

(a) Stall (23°–40°) at $Re = 1.0 \cdot 10^6$.

(b) Stall (23°–40°) at $Re = 0.5 \cdot 10^6$.

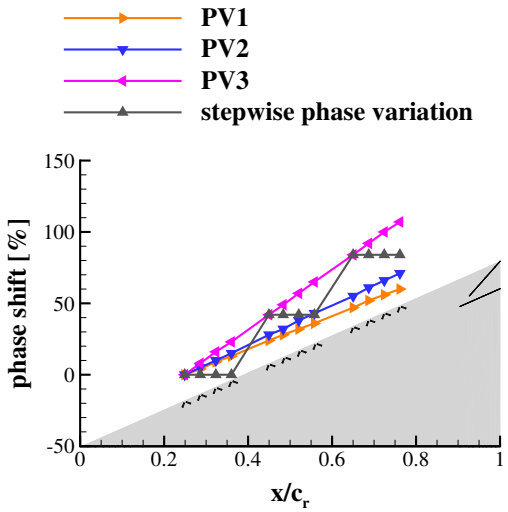

(c) Post-stall (40°–50°) at $Re = 0.5 \cdot 10^6$.

Figure 5.3: Downstream phase shift for different freestream conditions.

Figures 5.4, 5.5 and 5.6 present the aerodynamic coefficients of phase modulated blowing strategies presented in Figure 5.3 compared with the baseline and synchronous blowing case (no phase-shift and constant frequency). Figure 5.4 represents the first case, covering the regime around stall at $Re = 1.0 \cdot 10^6$. Prior to stall, all curves lie on top of each other, evidencing the insensitivity of the integral coefficients and their derived variables towards considered blowing strategies. Beyond stall, at $\alpha = 35° - 40°$, the aerodynamic coefficients diverge from each other, when the angle of attack increases. Lift and drag polars, which are shown in the top part of Figure 5.4, suggest a decrease of the considered coefficients of phase-shifted blowing towards the baseline, while synchronous blowing has no effect on the coefficients.

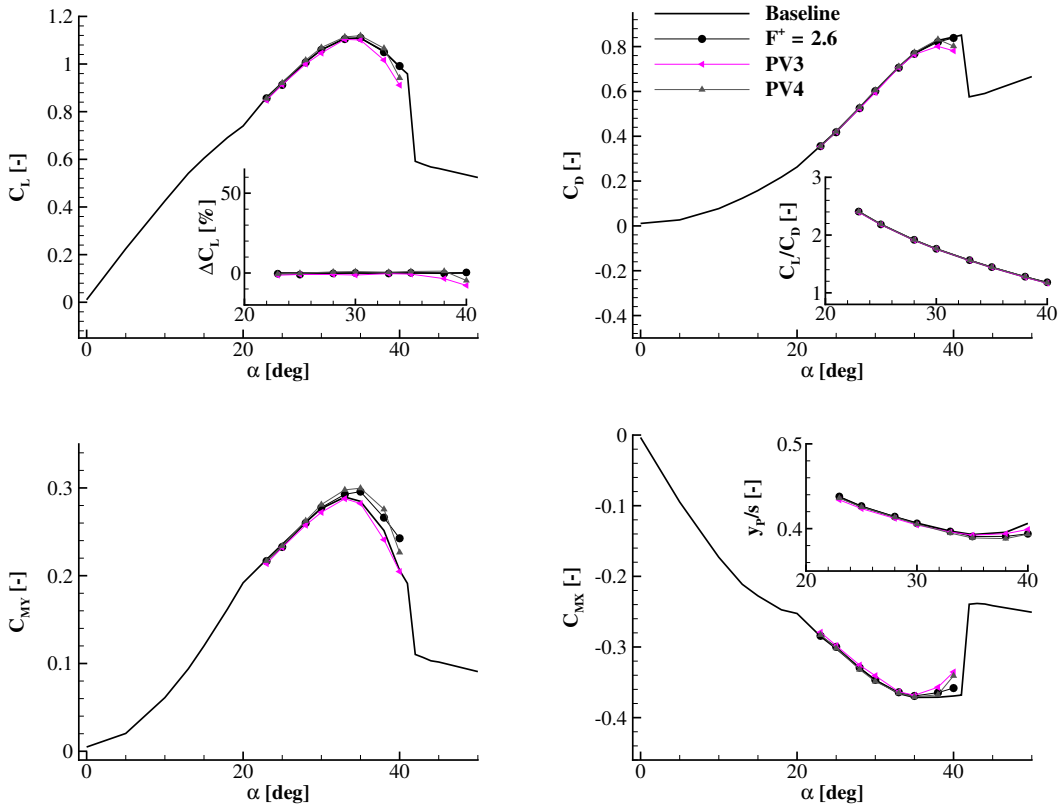

Figure 5.4: Aerodynamic coefficients with phase variation along the leading-edge. Stall (23°–38°) at $Re = 1.0 \cdot 10^6$.

The lift-to-drag ratio, C_L/C_D, is case independent in the considered angle of attack range. The pitching and rolling moment coefficients, displayed at the bottom, reveal an increasing blowing effect at the highest considered angles of attack. The pitching moment is most sensitive to actuation. It increases when pulsed blowing is activated and at least a constant phase delay per segment is set. Linear phase shift of blowing (pink left triangles) produces the same pitching moment coefficients as the baseline case. The rolling moment coefficient is insensitive to pulsed blowing up to stall. Beyond stall, C_{MX} of the actuated cases increase with α, while the baseline coefficient saturates prior to the vortex collapse at $\alpha = 41°$. Based on the polars presented in Figure 5.4, the following observations can be stated:

Synchronous blowing with $F^+ = 2.6$ has no effect on the lift and drag coefficients, while it increases the pitching and rolling moment coefficients in the range $35° < \alpha \leq 40°$. Hence, the resulting force vector does not change in magnitude, but the center of pressure moves slightly upstream and inboard.

Linear phase shift reduces lift and drag at $35° < \alpha \leq 40°$ and does not influence the pitching moment. In this case the resulting aerodynamic force vector decreases in magnitude and its center of pressure is located inboard with respect to the undisturbed case, as revealed by the C_{MX} and y_p/s polars.

Segment-wise phase shift blowing results in aerodynamic coefficients that lie in between the previous cases. This strategy incorporates both locally synchronised actuators and globally downstream segmentwise increasing phase shift.

The subsequent investigation considers the same angle of attack range, but at half of the freestream Reynolds number. As the pressure of air supplied to the actuators is not changed, the momentum coefficient increases relative to the previous case from $c_\mu = 1.4 \cdot 10^{-3}$ to $5.5 \cdot 10^{-3}$ (see Table 5.1). This leads to a more effective manipulation of the aerodynamic coefficients as presented in Figure 5.5. Synchronous blowing with $F^+ = 2.6$ increases the lift/drag and pitching moment coefficient relative to the baseline case in the entire investigated incidence range. Therefore, the increase in c_μ has a beneficial effect on the vortex system and, consequently, on the aerodynamic performance. Phase-modulation has a rather negligible influence on the coefficients. As demonstrated above, blowing with a linear phase delay has a negative effect on the lift increase and a step-wise phase variation results in coefficients of magnitude between synchronised blowing and blowing with downstream linear increasing phase delay.

Figure 5.6 illustrates the manipulation of the post-stall aerodynamic coefficients by different blowing sequences along the leading edge (see also Figure 5.3). All presented pulsed blowing strategies are operated with a reduced frequency of $F^+ = 1.0$ and momentum coefficient of $c_\mu = 8.7 \cdot 10^{-3}$. All applied control strategies eliminate the sudden lift drop by stabilising the burst vortex system, even at the extremely high angle of attack of $\alpha = 50°$. Highest increase of aerodynamic coefficients with respect to the baseline case is achieved with synchronous blowing (no phase delay). This is true for all investigated test cases. Synchronising the blowing jets leads to a lift increase by more than 50% compared to the baseline coefficients with the cost of drag and pitching moment increase. Nonetheless, lift-to-drag ratio improves over the entire investigated angle of attack range ($40° \leq \alpha \leq 50°$). In addition, the center of pressure shifts inboard. This occurs due to the reattachment of the shear-layer on the wing's upper surface, sustaining the burst vortex structure, as discussed in Section 5.2.1.3.

Desynchronising the leading-edge jets attenuates the blowing effect on the flow field and aerodynamic characteristics. Similar investigation at stall is supplemented in Figure B.1 in Appendix B. Hence, an increasing phase gradient $\partial\theta/\partial(x/c_r)$ leads to a decreasing ΔC_L. Unison blowing offers the best actuation strategy. Phase-modulated blowing on delta wing flow is also investigated in [95], from which the same conclusion results: a quasi two-dimensional disturbance injection at the leading-edge leads to the highest lift increase. This hypothesis is consolidated by the results of the segment-wise downstream phase increase, for which disturbances are injected simultaneously per segment. Although on a global scale, the slot ejection delay increases with the same slope as the linear phase delay, the segment-wise 2D disturbance outperforms the purely 3D disturbance injection [17].

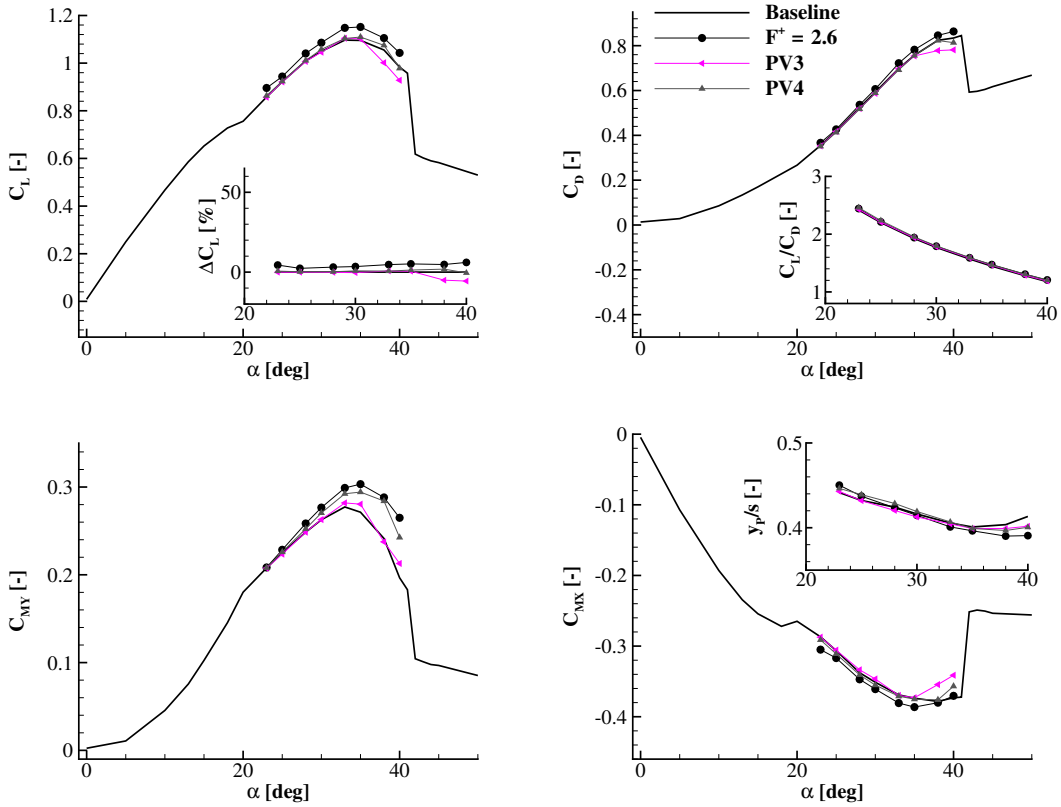

Figure 5.5: Aerodynamic coefficients with phase variation along the leading-edge. Stall (23°–38°) at $Re = 0.5 \cdot 10^6$.

5.1.2.2 Frequency Modulation

The modulation of the blowing frequency along the leading edge implies operating individual slot pairs with a decreasing blowing frequency in downstream direction. As the vortex inherent instabilities wave number increase downstream, the dominant frequency decreases downstream as a function of $(x/c_r)^{-1}$, as demonstrated in [12]. Therefore, a blowing strategy with a local actuation frequency adapted to the dominant frequency of these instabilities is investigated in this section. The frequency variation implies a variation of the phase, for which the high frequency blowing in the apex region ejects air prior to the slot pairs downstream. Hence, a phase lead is generated additionally. Two frequency variation strategies for each of the three cases are investigated in this work: segmentwise (FV1) and quasi-continuous (FV2) frequency variation. These actuation strategies do not improve the aerodynamic performance compared to synchronous blowing, but offer a minor benefit compared to phase-modulated pulsed blowing (see also [17]). The downstream frequency distributions and the resulting coefficients are presented in Figures B.2, B.4 and B.4 in Appendix B.

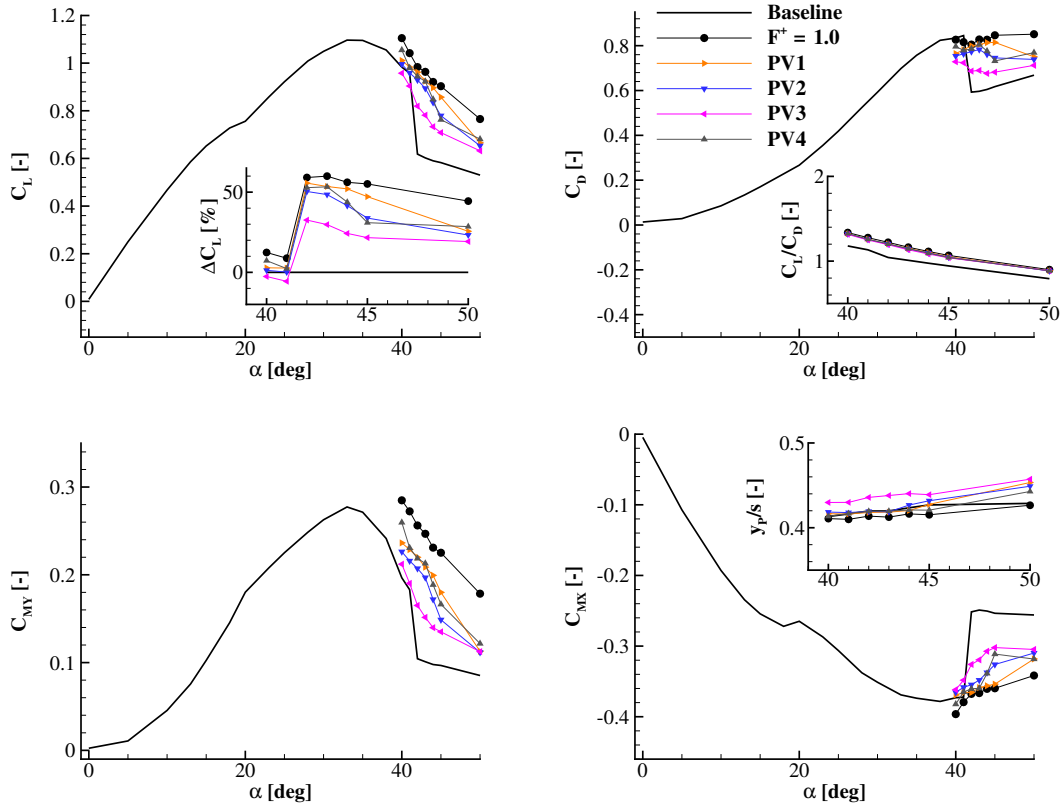

Figure 5.6: Aerodynamic coefficients with phase variation along the leading-edge. Post-stall (23°–38°) at $Re = 0.5 \cdot 10^6$.

5.1.3 Synthesis

The Reynolds number has a negligible effect on the aerodynamic coefficients of the baseline delta-wing flow. This allows a variation of the freestream velocity in order to investigate the influence of the momentum coefficient c_μ on the aerodynamic performance. This actuation coefficient correlates positively with the increase in magnitude of all investigated aerodynamic coefficients.

Furthermore, different blowing strategies are assessed: synchronised, phase-increasing and frequency-decreasing blowing sequences. The results consistent for both stall and post-stall flight regimes: a unison blowing, which is equivalent to a two dimensional manipulation of the separated shear layer, has the highest impact on the aerodynamic performance (lift and lift-to-drag ratio increase).

The stabilising effect on the flow field is attenuated when non-synchronised pulsed blowing is used. Therefore, two additional desynchronised blowing strategies are assessed: phase variation ($\theta \sim x$) and frequency variation ($f \sim 1/x$). Increasing the phase delay along the leading edge and keeping the frequency constant reduces the coefficient increase with respect to synchronised actuators.

The frequency decrease of the periodic actuators downstream results in a phase decrease, which is superior to positive phase variation, but slightly inferior to synchronised leading edge actuators. For the subsequent flow field analysis, the most promising strategies are further investigated in order to explain the obtained coefficients.

5.2 Flow Field Analysis

In this section the mean and transient flow field are described. The first part, in Section 5.2.1, focuses on the three dimensional mean flow velocity field based on PIV measurements, as it includes averaged data over larger time span ($> 30\,s$) than the numerically simulated time ($< 1\,s$). Therefore, the instant flow field is analysed based on DES results following the numerical validation in Section 5.3.

5.2.1 Time-Averaged Flow Field

The baseline flow field is compared with the perturbed flow field (synchronous blowing and frequency/phase-modulated blowing, FV and PV) for three angles of attack, $\alpha = 23°, 35°$ and $45°$, representing three high-incidence flight regimes: pre-stall, stall and post-stall. From the different actuation modes in Section 5.1, only the most promising blowing configurations representing FV and PV are investigated via PIV. Section 3.4 describes in detail the actuation modes measured and discussed subsequently.

5.2.1.1 Pre Stall

Figure 5.7 shows the baseline flow features at $\alpha = 23°, Re = 1.0 \cdot 10^6$. Isosurfaces coloured by the axial velocity related to the freestream velocity magnitude of $U_\infty = 24\,m/s$ are displayed: $u/U_\infty = 1.5$ (green), 0.5 (blue) and 0.2 (violet). Additionally, Figure 5.7 illustrates crossflow slices colour mapping the helicity, which is the scalar product of velocity and vorticity vectors:

$$H = u_i \omega_i \tag{5.2}$$

High values of relative helicity $H(l_\mu/U_\infty^2)$, where both $\boldsymbol{u}$ and $\boldsymbol{\omega}$ are parallel, confirms the existence of a jet type vortex. As soon as the vortex breaks down, moderate helicity values are present only in the separated shear layer that rolls around the low energy core. For a better graphical visualisation, two streamlines represent the mean path of fluid elements inside and outside the vortex core.

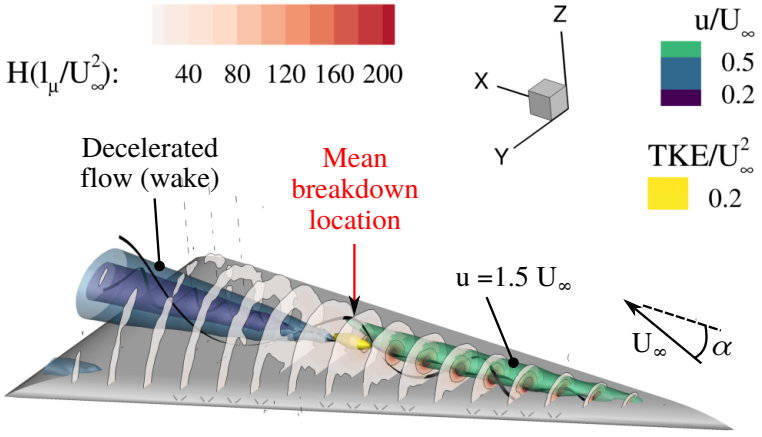

Figure 5.7: Baseline flow field of the VFE-2 delta wing at $\alpha = 23°$, $Re = 1.0 \cdot 10^6$.

The investigated mean flow field shows the breakdown of the leading edge vortex and constitutes of three flow regions: accelerated flow, breakdown and retarded flow region. Starting

from the apex, the separated shear layer (moderate helicity) rolls up into the primary vortex. In its core, fluid accelerates and exceeds $u/U_\infty = 1.5$. The cross sectional velocity distribution describes a jet-type flow up to $x/c_r = 0.55$, in which u/U_∞ increases towards the mean vortex core. The wing's proximity and the secondary separation[1] cause a displacement effect on the primary vortex structure. Thus, the vortex axis and the peak core velocity are not coaxial.

The vortex breakdown causes flow deceleration and abrupt TKE increase caused by the fluctuations of the breakdown location. More specifically, the fluctuations of the stagnation point(s) present in the instant flow field (see Section 5.4). The highly fluctuating region is highlighted by the yellow isosurface ($TKE/U_\infty^2 = 0.2$). Its center (maximum TKE) represents the mean breakdown location, where:

$$TKE = \frac{1}{2}\left(\overline{(u')^2} + \overline{(v')^2} + \overline{(w')^2}\right) \tag{5.3}$$

with:

$$u_{\mathrm{rms}} = \sqrt{\overline{(u')^2}}, \tag{5.4}$$

Equation 5.3 is expressed dimensionless according to the following equation: [2]

$$\frac{TKE}{U_\infty^2} = \frac{1}{2}\left(\left(\frac{u_{\mathrm{rms}}}{U_\infty}\right)^2 + \left(\frac{v_{\mathrm{rms}}}{U_\infty}\right)^2 + \left(\frac{w_{\mathrm{rms}}}{U_\infty}\right)^2\right) \tag{5.5}$$

As the breakdown transitions the flow from jet-type to wake-type, the post-breakdown core shows reduced axial velocity decreasing below $0.2U_\infty$. The mean velocity field does not reach negative values in x direction, indicating no flow reversal. Contrarily, instant velocity fields during breakdown are dominated by stagnating and reversed local flow regions (see Section 5.4). Downstream, the breakdown wake increases in diameter describing a cone (blue and violet isosurfaces). Crossflow distributions of u/U_∞ and $\omega_x \cdot l_\mu/U_\infty$ of the baseline flow are additionally presented in Figure C.2 and C.3.

The mean distributions of relative axial velocity and TKE in the longitudinal PIV plane along the vortex core are displayed in Figure 5.8. The core plane presented intersects the wing plane (xy-plane) in the y-axis at an angle of 6.8°, as described in detail in Section 3.3.2.1. The colour map scales with the dimensionless mean axial velocity in the range $0 \leq u/U_\infty \leq 1.8$. The plots contain additional isolines of constant TKE/U_∞^2 values and marking the mean breakdown location.

Farther away from the vortex axis, u/U_∞ converges outboards to unity and inboard to a slightly higher value. The shear layer protrudes the investigated plane identified by a strip of moderate turbulence, $0.05 < TKE/U_\infty^2 < 0.10$. Prior to breakdown, the velocity fluctuations are concentrated in the vortex core. Breakdown leads to an increase in TKE above $0.3 \cdot U_\infty^2$. From the peak value, two branches of high turbulence extend downstream around the decelerated velocity region (post-breakdown). The strong dissipation caused by the breakdown process reduces the kinetic energy in the core flow and increases the pressure, which is preventing the roll-up of the shear layer and thus energy transport towards the rotation center.

The perturbations generated and injected at the leading edge enhances the turbulent mixing between the freestream flow and the retarded core flow. However, this leads to a minor reduction of the low-energy volume and a breakdown delay of $3\% \cdot c_r$ [17]. The synchronous blowing with the reduced frequency in the range of the helical mode instability, $F^+ = 2.6$, as investigated also in

[1] Vorticity region between LEV and LE in Figure C.3 in Appendix C

[2] In this thesis, turbulent kinetic energy is expressed as TKE for the measured values and as k for the transport variable in CFD (modelling), but represent the same physical variable.

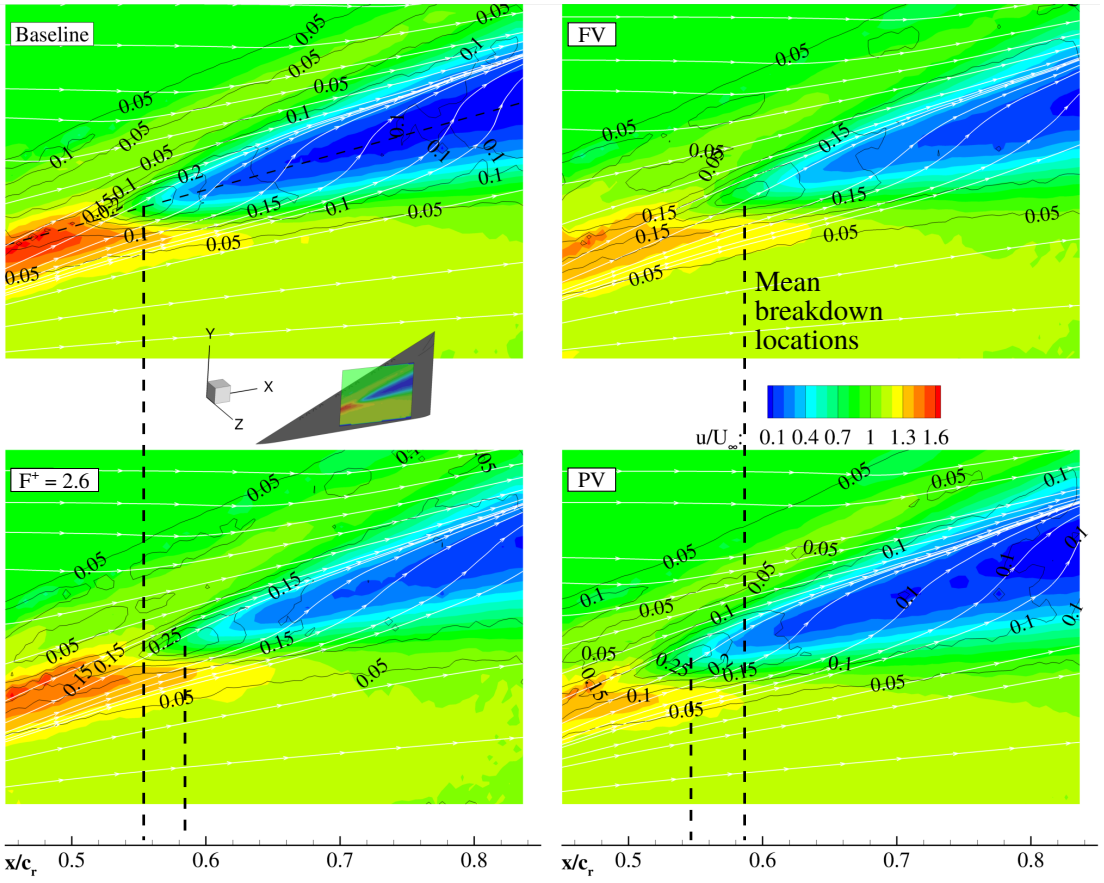

Figure 5.8: Relative longitudinal velocity and TKE during breakdown; $\alpha = 23°$, $Re = 1.0 \cdot 10^6$, all four actuation modes.

[82], leads to the highest reduction of the low-energy region size compared to the frequency/phase modulated blowing. Blowing with downstream phase delay has the least impact on the flow field compared to all investigated blowing strategies. The effect of frequency variation lies in between the other actuated cases.

As expected from the detected insensitivity of the aerodynamic characteristics towards blowing at this angle of attack, minor alterations to the flow field are observed with respect to the actuation modes presented in Figure 5.8. These differences are highlighted in a 1D extraction from the longitudinal PIV plane following the vortex core in Figure 5.9. Continuous lines represent the relative x-velocity and dashed lines the relative TKE at colour-differentiated actuation modes.

Prior to breakdown the axial velocity is highest in the natural flow. Both, the flow deceleration and the TKE peak correlate with the mean breakdown location. The unperturbed flow (baseline) demonstrates the highest deceleration rate. The peaks of the baseline and synchronous-blowing cases measure the equal magnitudes of $TKE/U_\infty^2 \approx 2.2$. The TKE peaks of the modulated cases are flatter and measure lower maxima of $TKE/U_\infty^2 \approx 1.9$ compared to the other two cases, baseline and synchronous blowing.

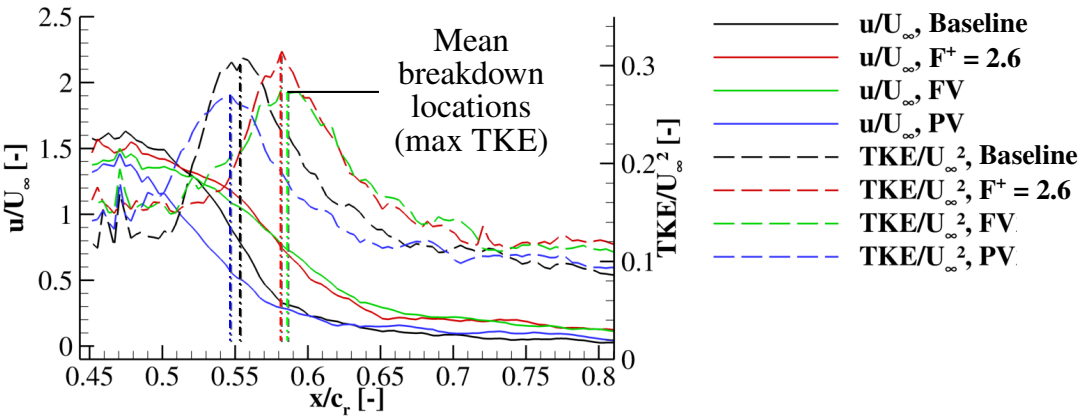

Figure 5.9: Distribution of relative x-velocity and TKE along the core. $\alpha = 23°$, at four actuation modes.

Flatter TKE peaks and smoother axial flow deceleration reveal that the modulated AFC produces breakdown oscillations over a wider chord range. Interestingly, the frequency modulated case shows a higher breakdown-delay effectiveness than the case with phase modulation. The degradation of the aerodynamic coefficients around stall as a result the phase modulated flow manipulation is the result of a premature triggering of the breakdown instability (Figure 5.4). However, at this angle of attack, breakdown reaches the apex and the effect is amplified (cf. the following subsection).

The injection of fluid with constant and downstream decreasing pulse frequency (red and green) leads to a stabilising effect on the vortex. The additional circumferential momentum in combination with the instability-targeted actuation frequency enhances the turbulent mixing and thus the kinetic energy transport in radial direction. This effect leads to a delay in vortex breakdown, though by around $\Delta x/c_r = 3\%$. The measured breakdown location for each case is listed in Table 5.2.

Figure 5.10 shows the cross-sectional distribution of the relative rms value of the axial velocity $u_{\mathrm{rms}}/U_\infty$. The statistics have been computed over all 400 samples for each plane investigated. The crossflow planes shown are located prior to breakdown ($x/c_r = 0.50$) at the mean breakdown location ($x/c_r = 0.55$) and in the breakdown wake ($x/c_r = 0.70$ and 0.85). Within the shear layer, moderate fluctuations ($0.15 \leq u_{\mathrm{rms}}/U_\infty \leq 0.20$) are present. Relative to the shear layer, in the core, higher fluctuations are concentrated in a singular peak prior to breakdown (Figure 5.10a). Approaching breakdown, the core fluctuations increase abruptly as does the core cross section (cf. Figures 5.10b and 5.9).

Table 5.2: Case dependent chordwise breakdown location at $\alpha = 23°$, $Re = 1.0 \cdot 10^6$.

Case	x/c_r
Baseline	0.55
Unison blowing	0.58
Frequency var.	0.58
Phase var.	0.55

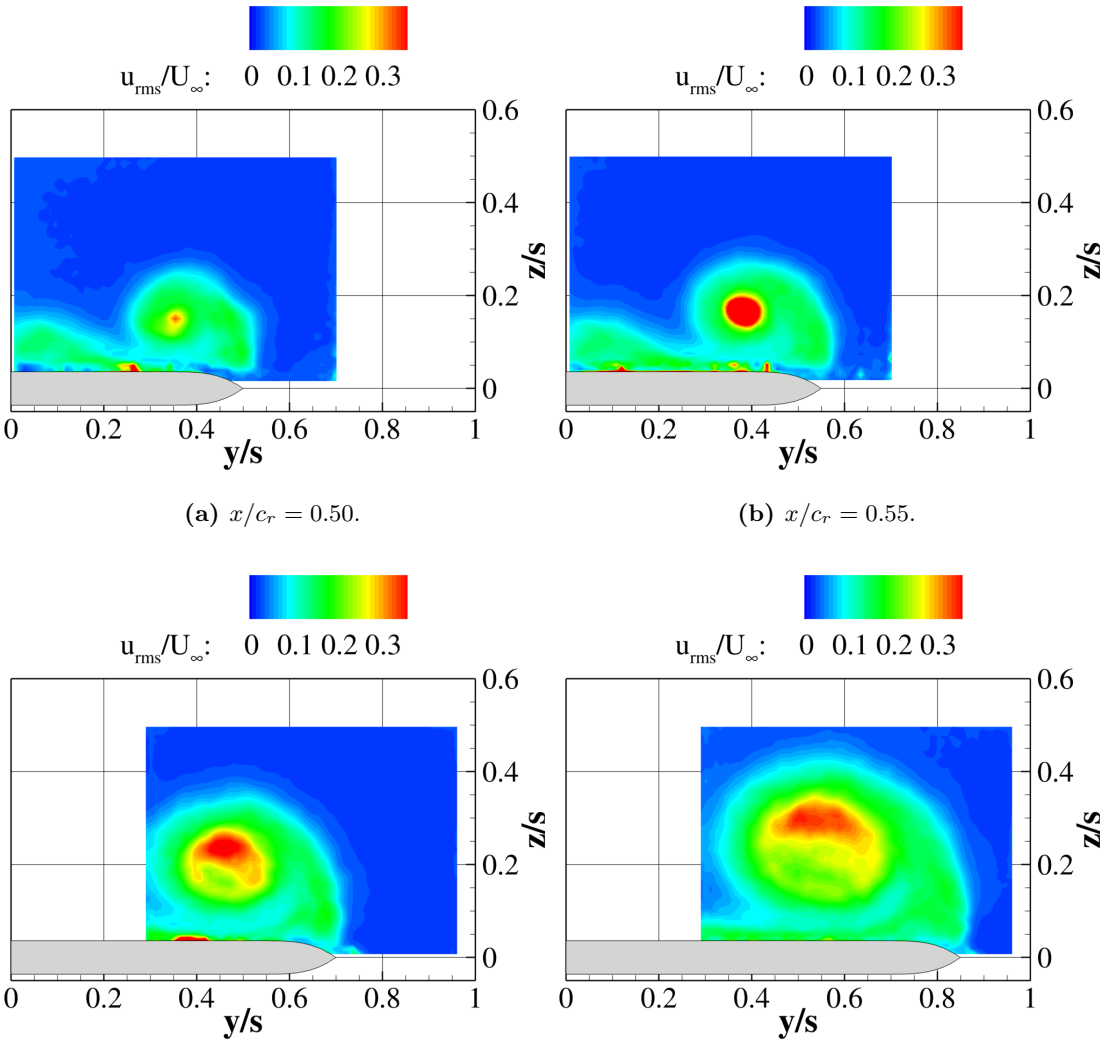

(a) $x/c_r = 0.50$.

(b) $x/c_r = 0.55$.

(c) $x/c_r = 0.70$.

(d) $x/c_r = 0.85$.

Figure 5.10: Rms of the x-velocity distributed in PIV crossflow planes at $\alpha = 23°$.

The wake type flow expands downstream of the breakdown location ($x/c_r \geq 0.60$). In Figures 5.10c and d, high velocity rms values are distributed annularly with minimum values in the center. The distribution is not axis-symmetric, as increased unsteadiness is present farther from the wing (between 10 and 3 o'clock, maximum at 12). The burst vortex expands in cross-section with dissipating turbulence downstream. The flow field of the actuated cases has a similar distribution of u_{rms}/U_∞ at the same chord distance relative to the mean breakdown location x_{bd}.

The vortex detection algorithm described in Section 4.4.2 is applied on the crossflow planes investigated. Figure 5.11 shows the distribution of discrete vortices with axial circulation $\Gamma_x \geq 0.5\,\mathrm{m}^2/\mathrm{s}$. Vortices are represented by circles concentric with their λ_2 minima and the radius scaled to the vortex radius. The determination of the core radius is based on the region decomposition and filtering of the λ_2 field. The colour mapping represents the axial circulation of each vortex. Generally, strong vortices have also a high diameter. The scatter plots presented in Figure 5.11 can be regarded as a long time exposure camera pictures that register discrete vortex events in time and space accumulated from 200 equally spaced samples. However, the analysis of each measruement plane is based on all 400 sampled records.

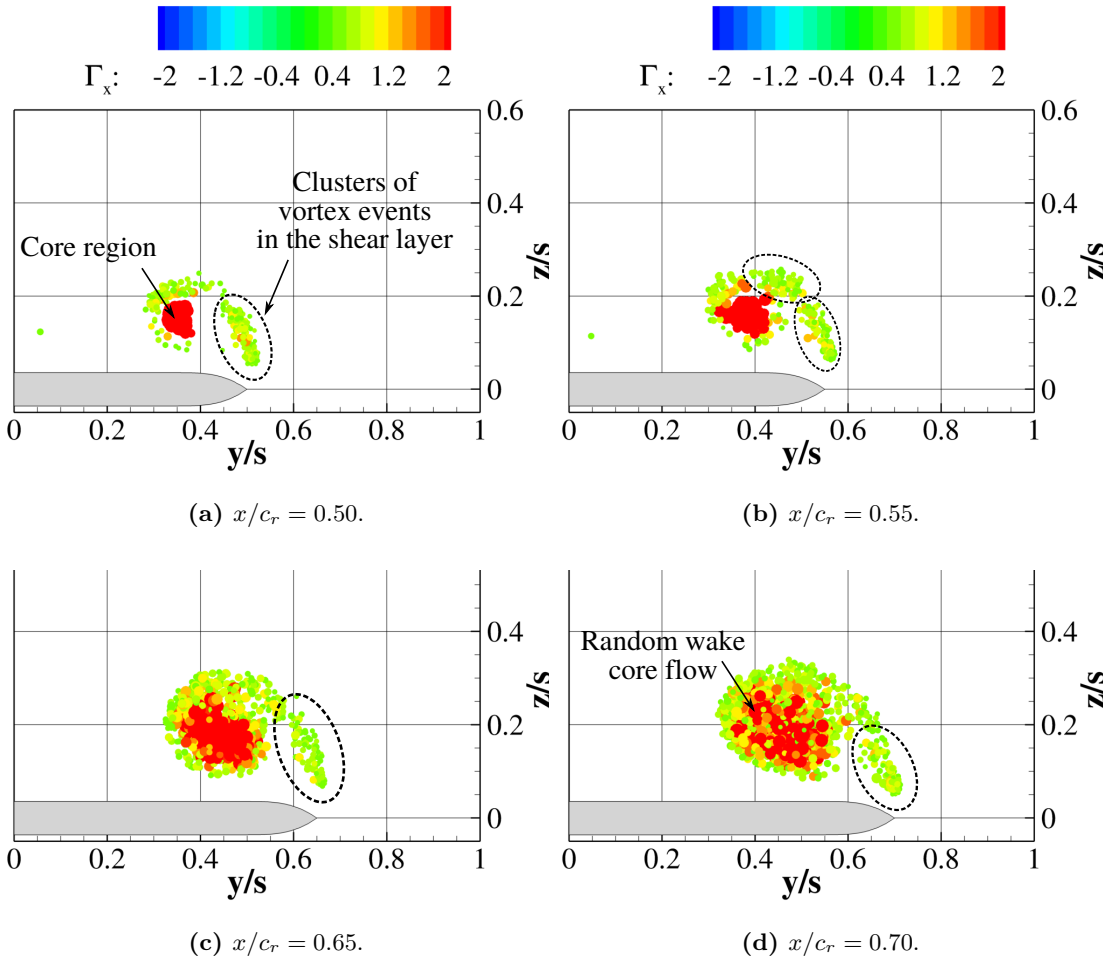

(a) $x/c_r = 0.50$.

(b) $x/c_r = 0.55$.

(c) $x/c_r = 0.65$.

(d) $x/c_r = 0.70$.

Figure 5.11: Discrete vortices from PIV crossflow planes at $\alpha = 23°$, baseline.

Prior to breakdown, at $0.45 \leq x/c_r \leq 0.55$, the primary vortex core is clearly distinguishable from the discrete vortices within the shear layer based on the circulation. The vortex core changes its lateral and vertical position throughout the PIV sampling. This is caused by the wandering of the vortex core due to interaction with the shear layer [50]. The heterogeneous distribution or clustering of relatively strong vortices within the shear-layer can assert the existence of quasi-stationary vortices, also reported in [103, 104]. These clusters spiral downstream with the same

sense of rotation as the leading-edge vortex. The complementary CFD simulations discussed in Section 5.4 predict similar stationary discrete flow features.

As the vortex breaks down, the vortex core compresses and starts to fluctuate in all three directions. The vortex events registered on the crossflow plane represent a quasi-random distribution, as shown in Figure 5.12b. Regarding the unsteady region in this cross section at $0.2 \leq z/s \leq 0.3$ and shown above in Figure 5.10c, there is no evident correlation between the eddy strength or radius and the unsteady region. Not the high concentrations of strong vortex events, but the high shear between the inner, low-energy and the outer, high-energy flow produce high fluctuations distributed asymetrically around the mean rotation axis. The region is located away from the wall, which dampens the flow oscillations.

Comparing the above scatter plots of the baseline case with equivalent representations of the forced flow in Figure 5.12, pulsed blowing affects the discrete vortex distribution by strengthening the shear layer vortices and delaying breakdown. Therefore, this is clear evidence that the vortex-generating shear-layer instability is manipulated. Similar distribution of vortex events, but at different chordwise positions demonstrate that blowing delays breakdown and reduces the wake-type region.

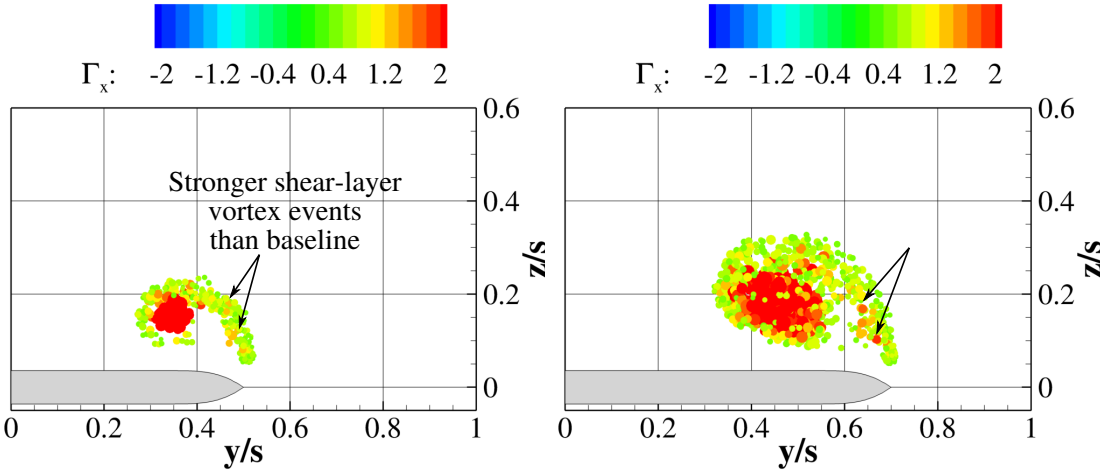

(a) $x/c_r = 0.50$. **(b)** $x/c_r = 0.70$.

Figure 5.12: Discrete vortices from PIV crossflow planes at $\alpha = 23°$, $F^+ = 2.6$

The statistics of the vortex detection algorithm are shown in Figure 5.13 along the relative chord station x/c_r: the mean values of the positive axial circulation $\Gamma_{x,\mathrm{pos}}$, the maximum circulation $\Gamma_{x,\mathrm{max}}$, the ratio of vortex core radius to grid spacing $r_c/\Delta_{\mathrm{PIV}}$ (Table 3.2), and the number of detected vortices with positive circulation $N_{v,\mathrm{pos}}$. The hollow black circles represent the baseline case, the black circles the synchronous blowing ($F^+ = 2.6$), the green diamonds the frequency modulated blowing (FV) and the left-pointing magenta triangles the blowing with downstream phase increase (PV).

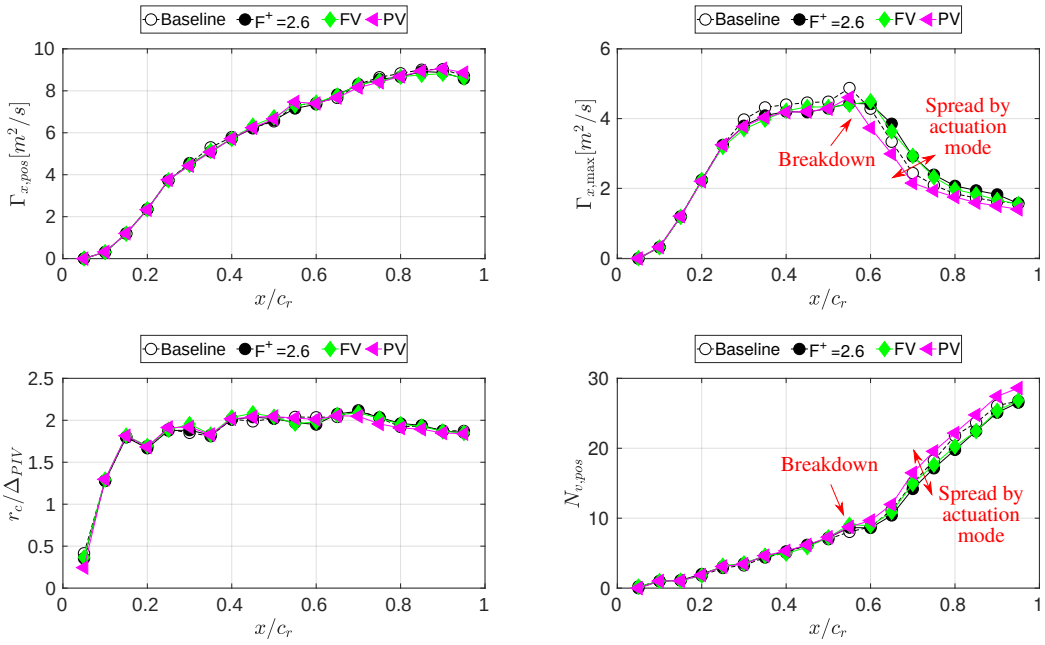

Figure 5.13: Statistics of the vortex detection algorithm from all PIV crossflow planes at $\alpha = 23°$.

The following observations result from analysing Figure 5.13:

- The average radius of the vortices and axial circulation are rather universal. As the average vortex radius remains constant along the chord ($r_c \approx 2\Delta_{\mathrm{PIV}}$), the average circulation of positive rotating vortices increases steadily downstream. At the trailing edge the $\Gamma_{x,\mathrm{pos}}$-curve flattens.
- The maximum circulation is extracted from each sample and averaged. The graphs increase rapidly up to $x/c_r = 0.3$. Downstream, the curve flattens with baseline values slightly higher than the forced cases. The breakdown causes a reduction of the maximum circulation per vortex.
- The reduction of the maximum circulation downstream of $x/c_r \approx 0.60$ correlates with an increasing number of vortices.
- Also in the breakdown wake, phase modulation, which has the least effect on the averaged flow field, generates the lowest maximum circulation and the most vortices.
- Consistent with the aerodynamic coefficients analysis and with the flow-field visualisation, the vortex-statistics are similare for the synchronised and the frequency-modulated blowing. The curve representing the baseline case lies in between phase-delayed and the frequency-modulated blowing.

5.2.1.2 Near Stall

The 3D flow field at $\alpha = 35°$ is shown in Figure 5.14 and constitutes of spiralling wake-type flow above the entire wing. Accelerated flow is present in a small region at the apex inboard of the vortex core and is generated by the displacement effect of the vortex and the test section's boundary layer. This region is designated by a green surface with a constant axial velocity of $u/U_\infty = 1.5$. Immediately downstream, the flow decelerates (blue isosurface: $u/U_\infty = 0.5$) and stagnates (violet isosurface: $u/U_\infty = 0.0$). The decelerated and stagnating surfaces describe a 3D cone, each, axis-symmetric with the vortex axis.

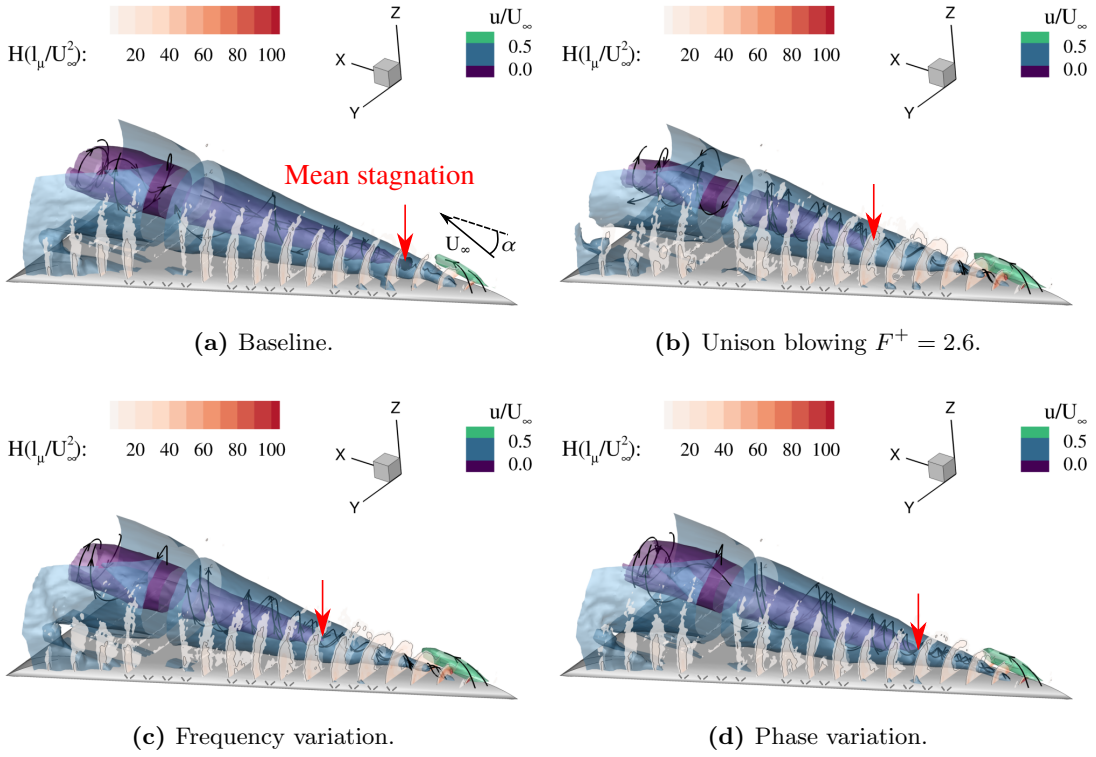

(a) Baseline. **(b)** Unison blowing $F^+ = 2.6$.

(c) Frequency variation. **(d)** Phase variation.

Figure 5.14: Flow field of the VFE-2 delta wing at $\alpha = 35°$, $Re = 0.5 \cdot 10^6$.

Reconsidering the pre-stall case, pulsed blowing has an increased effect rather on the post-breakdown region, as the inherent helical mode instability is addressed. At stall, the effect is similar and more pronounced as the complete flow field constitutes of a post-breakdown flow. Analogue to the previous case, at a lower angle of attack, the impact on flow field with respect to the baseline case (a) decreases in the same order: unison blowing (b), frequency variation (c) and phase variation (d). Simultaneously, the stagnation point (tip of the violet conical surface) is shifted downstream depending on the active flow control strategy, see Table 5.3. Although the momentum coefficient is constant at $c_\mu = 5.5{\cdot}10^{-3}$, the investigated jet-triggering sequence affects the flow field and, consistently, the global aerodynamic coefficients (compare Section 5.1.2).

The apex region is greatly influenced by the jet sequencing, as observed in the assessment of the helicity distribution. Blowing strengthens the vortex region at the apex, generating a more clear helicity peak in the vortex axis. The vortex is very unstable and breaks down at $x/c_r \approx 0.2$, in each investigated case. Towards the trailing edge, the "dissipated" helicity distribution is rather

Table 5.3: Case dependent chordwise location of the mean stagnation point at $\alpha = 35°$, $Re = 0.5 \cdot 10^6$.

Case	x/c_r
Baseline	0.24
Unison blowing	0.43
Frequency variation	0.42
Phase variation	0.34

unaffected. This demonstrates that periodic jets have a strong upstream effect, increasing the pitch-up tendency.

The apex region is further analysed in Figure 5.15 for each investigated case (baseline (a), unison (b), frequency-modulated (c) and phase-modulated blowing (d)). Colour mapping and isolines correlate with non-dimensional axial velocity and TKE distribution, respectively. The investigated plane is co-linear with the vortex axis and is angled at 11° with the wing around the y-axis. By increasing the angle of attack from $\alpha = 23°$ to 35°, the unstable breakdown region shifts upstream, reaching the apex and, here, the flow unsteadiness increases.

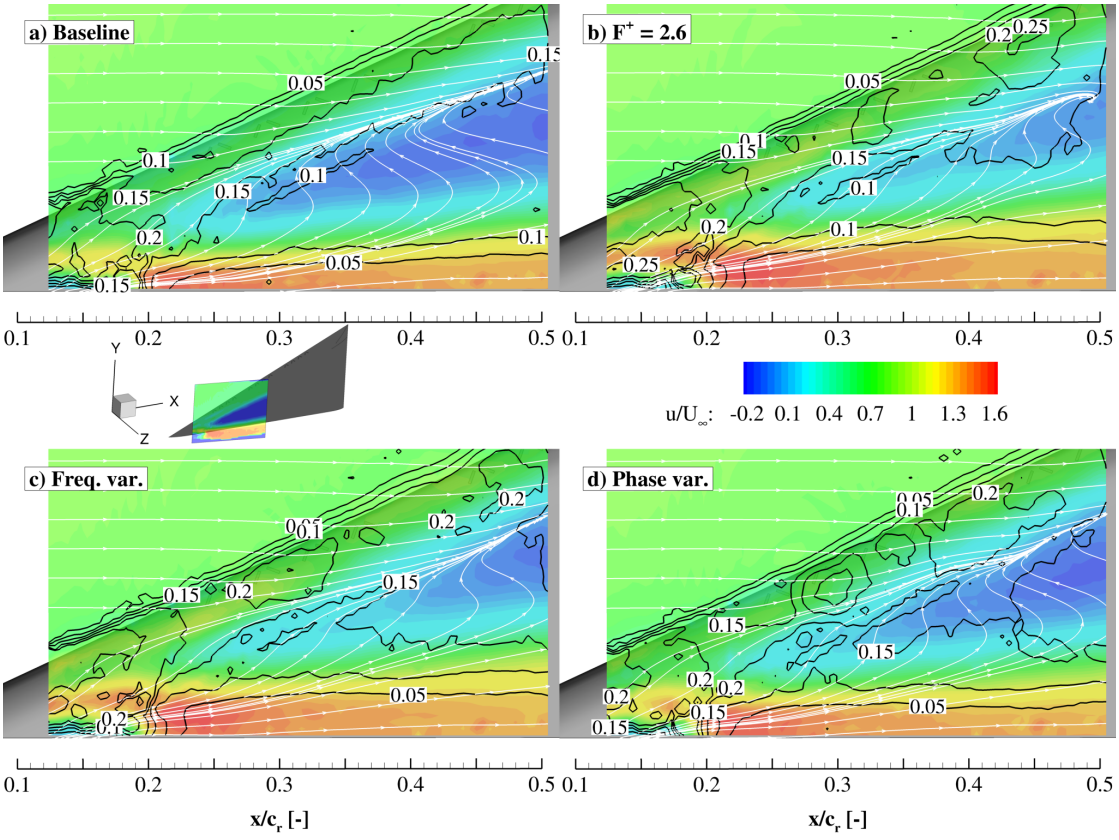

Figure 5.15: Relative longitudinal velocity and TKE along the vortex axis; $\alpha = 35°$, $Re = 0.5 \cdot 10^6$.

The breakdown flow reveals high TKE distributed around the low energy core (see also Figure C.4). A strip with values above $TKE/U_\infty^2 = 0.15$, which is located between the low energy core and the separated shear layer, extends downstream along the leading edge. The cause of this unsteady region is the increased shear forces generating discrete vortices, which spiral around the retarded core flow. Local TKE peaks above the slot-pair result due to flow disturbance.

Figure 5.16 illustrates the distribution of measured TKE in two crossflow planes distanced at $\Delta x/c_r = 0.20$. Similar to the finding above, the wake-type flow-field dominates the post-breakdown region. All measured cross-flow planes with the TKE distribution are presented in Figure C.4. The diameter of the high velocity rms annulus increases downstream. The wall effect is reduced as the primary vortex is farther from the wing.

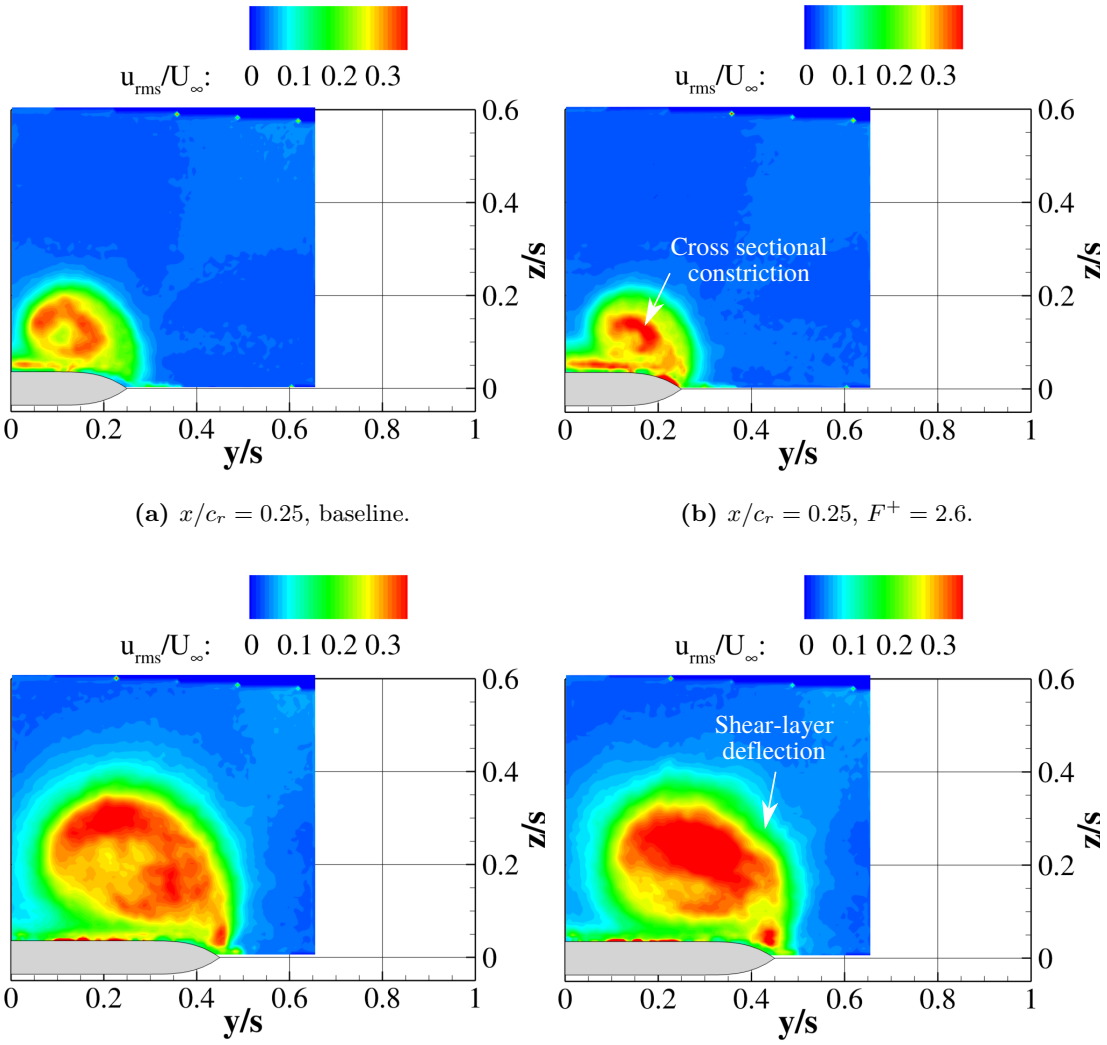

(a) $x/c_r = 0.25$, baseline.

(b) $x/c_r = 0.25$, $F^+ = 2.6$.

(c) $x/c_r = 0.45$, baseline.

(d) $x/c_r = 0.45$, $F^+ = 2.6$.

Figure 5.16: Rms of the x-velocity distributed in PIV crossflow planes at $\alpha = 35°$. Baseline vs. actuated case.

The stall angle of attack case confirms that pulsed blowing reduces the wake region. However, it is not clear if the wake reduction is caused by the delay of breakdown or by the enhanced turbulent mixing. Therefore, the information can be retrieved from CFD data.

The increase of the longitudinal aerodynamic coefficients generated by blowing synchronously with $F^+ = 2.6$ is explained subsequently referring to Figure 5.17. The graphs show the vertical distribution of nondimensional axial and circumferential velocities. The reduction of the low-energy region clearly decreases the wake and increases the angular velocity around the vortex axis. This effect decreases downstream (see dashed lines, representing $x/c_r = 0.5$). This leads to increased induced near-wall velocities in spanwise direction, decreasing pressure and, eventually increasing lift, drag and pitching moment. As discussed in Section 5.2.1.4, the mean rotation axis is independent on the applied actuation.

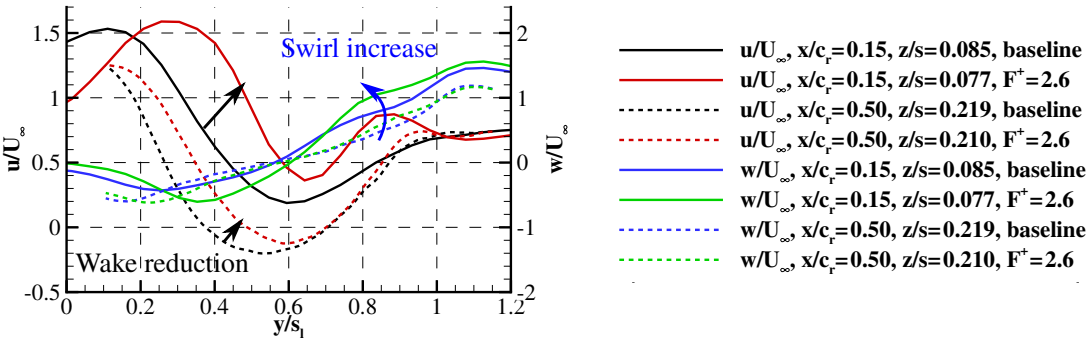

Figure 5.17: Circumferential and axial velocity distribution across the vortex core at $x/c_r = 0.6$, $\alpha = 35°$, $Re = 0.5 \cdot 10^6$.

In Figure 5.18, the crossflow planes are post-processed to show the location, the cross-section and the strength of the discrete vortices at $x/c_r = 0.25$ and 0.45. This analysis confirms the observations on the mean flow field. In the baseline case at $x/c_r = 0.25$, the wake-type flow is already developed (Figure 5.16a) and constitutes of vortices of moderate strength reside mostly in and around the core. Downstream, the structure grows and the vortices are transported around the low energy core. The vortex event density is higher closer to the wing than farther away and opposite to the velocity rms crossflow distribution.

The primary structure responds to actuation by a reduction in diameter/downstream displacement of the breakdown wake. Blowing redistributes the vortices more uniformly (Figure 5.18d) and increases the unsteadiness (Figure 5.16d).

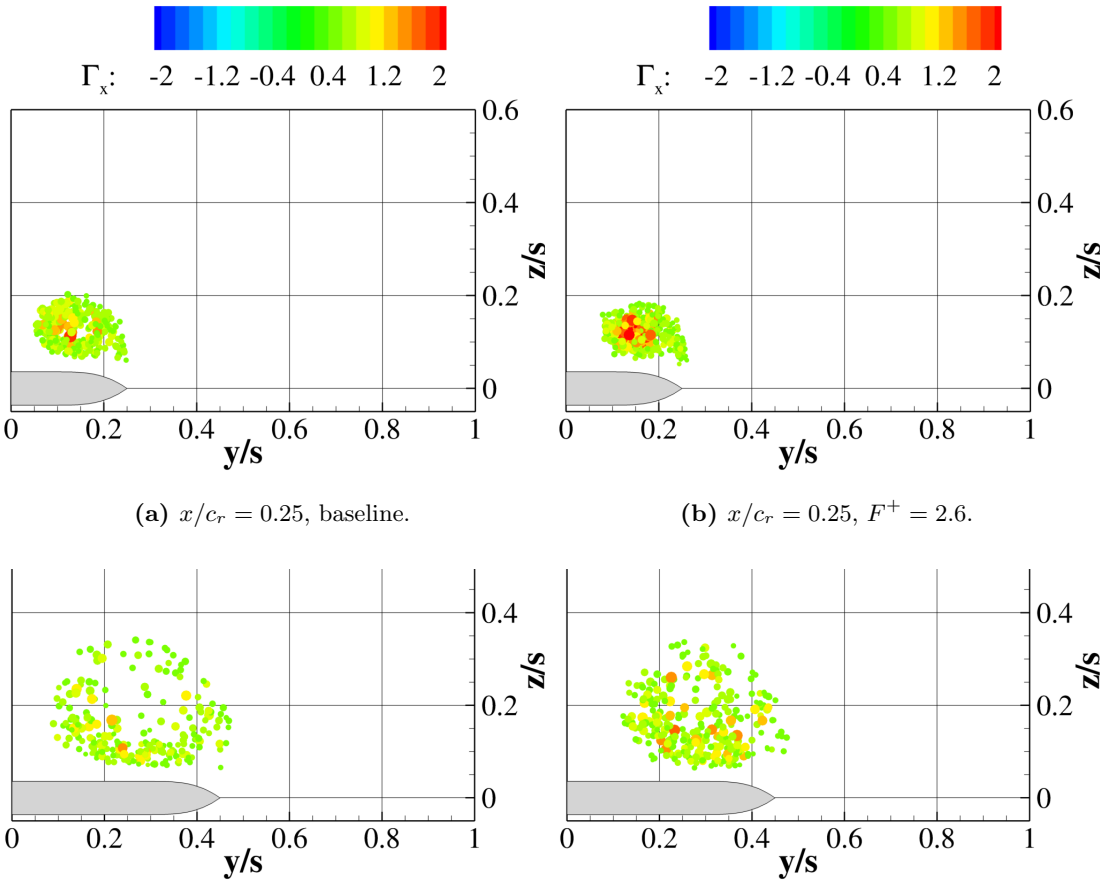

(a) $x/c_r = 0.25$, baseline.

(b) $x/c_r = 0.25$, $F^+ = 2.6$.

(c) $x/c_r = 0.45$, baseline.

(d) $x/c_r = 0.45$, $F^+ = 2.6$.

Figure 5.18: Discrete vortices from PIV crossflow planes at $\alpha = 35°$. Baseline vs. actuated.

The discrete vortex statistics are shown in Figure 5.19 and discussed below:

- The average measured circulation per vortex is lower at $\alpha = 35°$ than at 23°, as the freestream velocity magnitude can introduce a bias. Nonetheless, at this angle of attack, the positive circulation is independent on the actuation mode over a major part of the wing. Towards the trailing edge a low spread is present.
- The average relative radius shows the same independency as seen at $\alpha = 23°$ towards the mode of actuation. In longitudinal direction, it decreases constantly from $r_c/\Delta_{\mathrm{PIV}} = 2.2$ to 1.8[3].
- Maximum circulation per vortex considerably decreases (by a factor of approximately 4) compared to the $\alpha = 23°$ case. At both angles of attack, the breakdown position is designated by the averaged maximum vortex circulation.

[3]Because the vortex detection algorithm increases the resolution by three times, detecting vortices smaller than two cells is possible

- The number of vortices detected is doubled compared to $\alpha = 23°$. The downstream increase in number of vortices is representative for the stall flight regime as well.

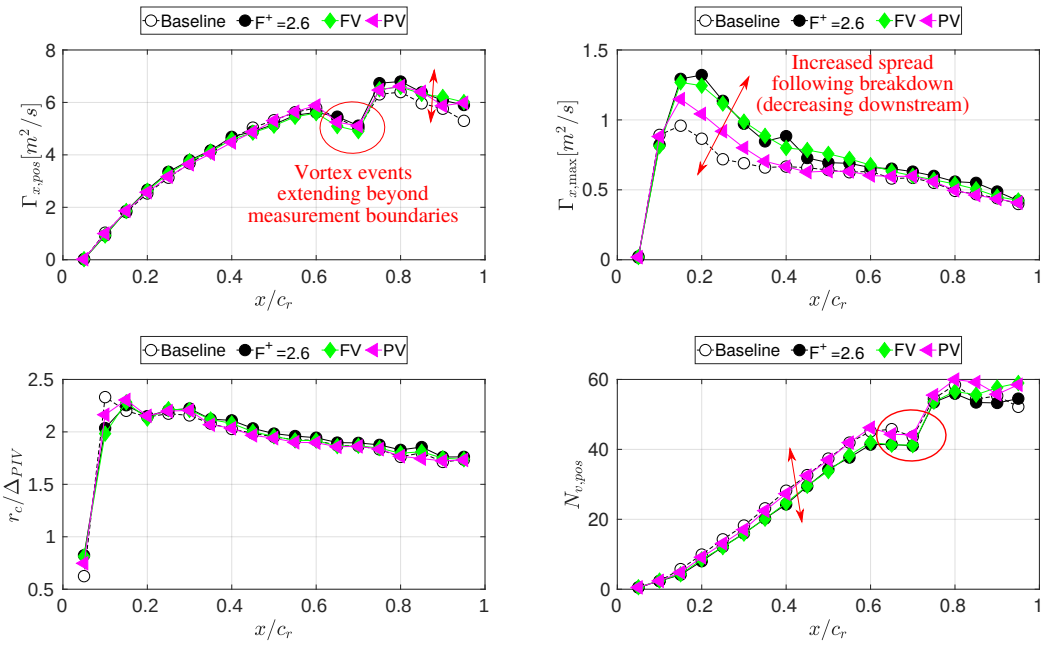

Figure 5.19: Statistics of the vortex detection algorithm from all PIV crossflow planes at $\alpha = 35°$.

5.2.1.3 Post Stall

Figure 5.20 depicts characteristic flow features at post-stall, $\alpha = 45°$. The interpolated isosurface represents zero axial velocity ($u/U_\infty = 0$). At this extremely high angle of attack, the baseline flow field constitutes solely of a wake flow topology (Figure 5.20a). The separated shear layer does not reattach on the wing's upper surface. Flow streamlines describe the recirculatory mean path of fluid elements. With active blowing, the periodic momentum injection leads to a reattachment of the shear layer and, thus, to the generation of a sustained burst vortex (Figures 5.20b–d). The stabilization of the vortex at high angles of attack eliminates the sharp drop of the aerodynamic coefficients caused by the vortex collapse. The additional suction by vortex induced near-wall velocity contributes to the considerable lift, drag and pitching moment increase (Figure 5.6). Table 5.4 lists the case dependent lift increase related to the baseline lift: $\Delta C_L/C_{L,\text{Baseline}}$. The yellow isosurface envelopes the region of high spanwise velocity $v/U_\infty \geq 0.7$ induced by the manipulated vortex. Its volume correlates with the suction force above the wing.

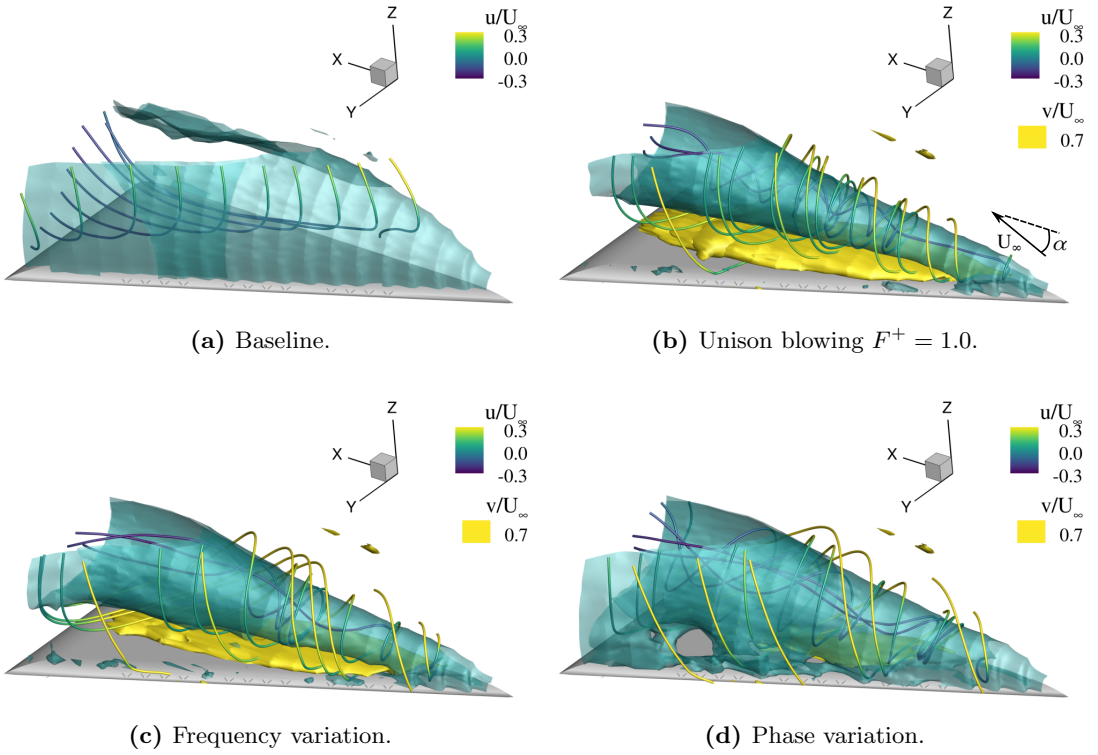

(a) Baseline.

(b) Unison blowing $F^+ = 1.0$.

(c) Frequency variation.

(d) Phase variation.

Figure 5.20: Flow field of the VFE-2 delta wing at $\alpha = 45°$, $Re = 0.5 \cdot 10^6$.

Table 5.4: Lift increase related to baseline lift for three actuation strategies at three post-stall angles of attack $\Delta C_L / C_{L,\text{Baseline}}$.

α	42°	45°	50°
Unison blowing	59.1%	55.1%	44.4%
Frequency var.	66.3%	53.3%	20.7%
Phase var.	55.6%	47.2%	25.6%

The jet synchronisation affects the vortex structure with a different intensity. As demonstrated for both lower investigated angles of attack ($\alpha = 23°$ and $35°$), the actuation strategy with synchronised blowing (cf. Figure 5.20b) is the most effective compared to the modulated strategies (cf. Figures 5.20c,d), as it generates highest cross-section reduction of the reversed flow region. The separated shear layer spirals around the reversed core flow. There is fluid transport from the enclosed reversed flow across the $u/U_\infty = 0$ surface into the shear layer. Increased flow interaction and turbulence dominates this circular region, which is discussed below.

With frequency variation, the flow topology looks similar to the unison blowing, though has a slightly wider reversed-flow core and lower swirl (compare Figure 5.20c and b, respectively). The vortex intensity correlates with a slightly lower lift coefficient than the synchronised blowing. Phase variation generates the least additional lift and shows a rather heterogeneous flow-field (Figure 5.20d).

A detailed analysis of the PIV plane along the vortex core is presented in Figure 5.21. The measurement plane is angled at 11° relative to the wing's xy-plane and translated 10 mm away from the apex. The distribution of axial velocity is colour mapped in the range $-0.25 \leq u/U_\infty \leq 0.65$. Isolines of constant TKE for values of $TKE/U_\infty^2 = 0.05, 0.10, 0.15, 0.20, 0.25$ complement the plots. In the baseline case (Figure 5.21a), the flow is reversed above the wing. The outer flow converges with the upstream flow in the inner part of the shear layer, where $TKE/U_\infty^2 = 0.05$. See also Figure C.5.

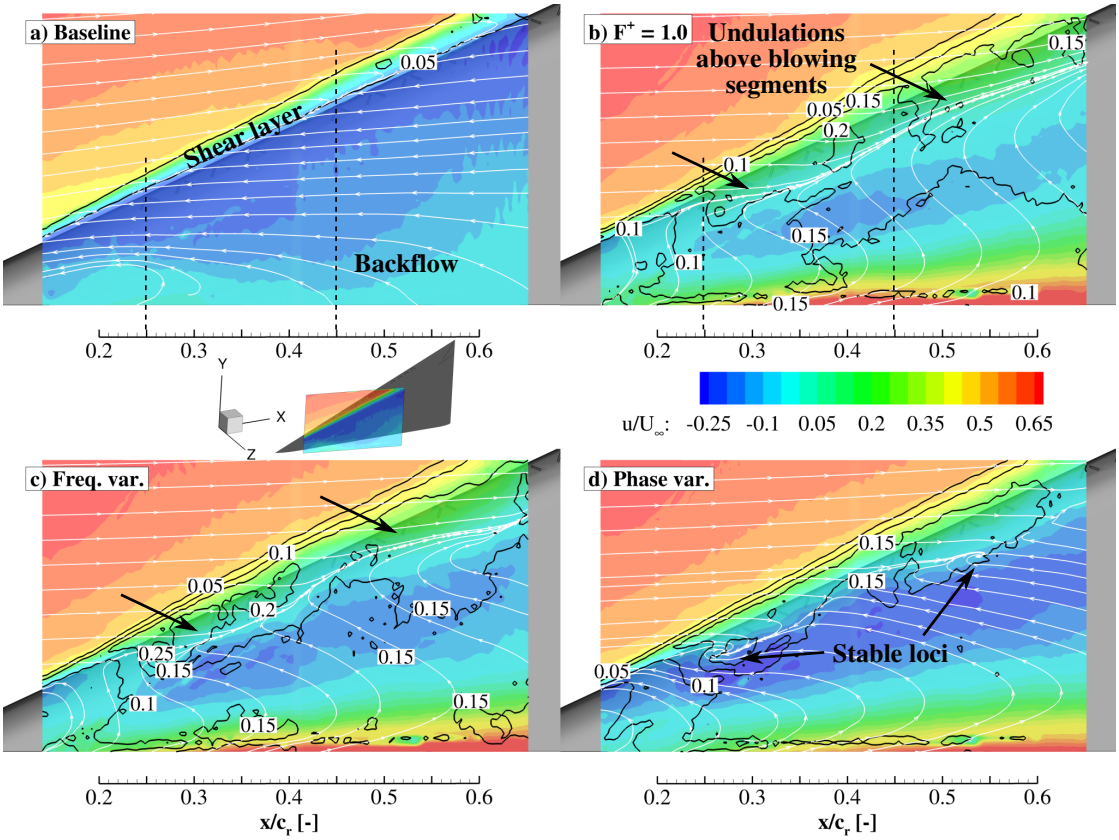

Figure 5.21: Relative longitudinal velocity and TKE along the vortex axis; $\alpha = 45°$, $Re = 0.5 \cdot 10^6$.

The actuated cases (Figure 5.21b–d) show the quasi conical distribution of longitudinal velocity and TKE. From the vortex axis in radial direction, the velocity increases. TKE increases inboard of the leading edge above $TKE/U_\infty^2 = 0.15$. Locally above the slot pairs, axial velocity and fluctuations show increased values relative to the surrounding, demonstrating a rather heterogeneous distribution. The unsteady region of $TKE/U_\infty^2 \geq 0.15$ decreases in size starting with the unison blowing case, followed by frequency variation case and ending with the phase variation case.

White stream tracers designate the mean flow direction in the investigated plane. The convection line is situated in the perturbed cases farther inboard. It shows undulations in its path along the leading edge, with inboard tendencies at jet injection locations (above the blowing segments). The applied flow control has also a noticeable upstream effect, aligning the outer flow

in freestream direction. The phase-modulated case demonstrates stable loci above the blowing segments. Hence, the flow field is strongly three dimensional and inhomogeneous for this case.

Figure 5.22 shows the cross flow distribution of $u_{\mathrm{rms}}/U_\infty$ in the planes designated by dashed lines in Figure 5.21. A separated shear layer with moderate fluctuations constitutes the baseline flow field at $\alpha = 45°$ (cf. Figure 5.22a and c). Synchronised burst mode blowing proves the greatest wake reduction at same actuation amplitude. The shear layer reattaches on the wing surface following the red annular region. In its center, the flow is unsteady, reversed and with low-energy. Obviously, a strong interaction of the periodically released jets into the shear-layer and the vortex generating instability exists. The mean dynamics are investigated via phase-locked investigations in Section 5.2.2 and via transient CFD in 5.4 and 5.5.

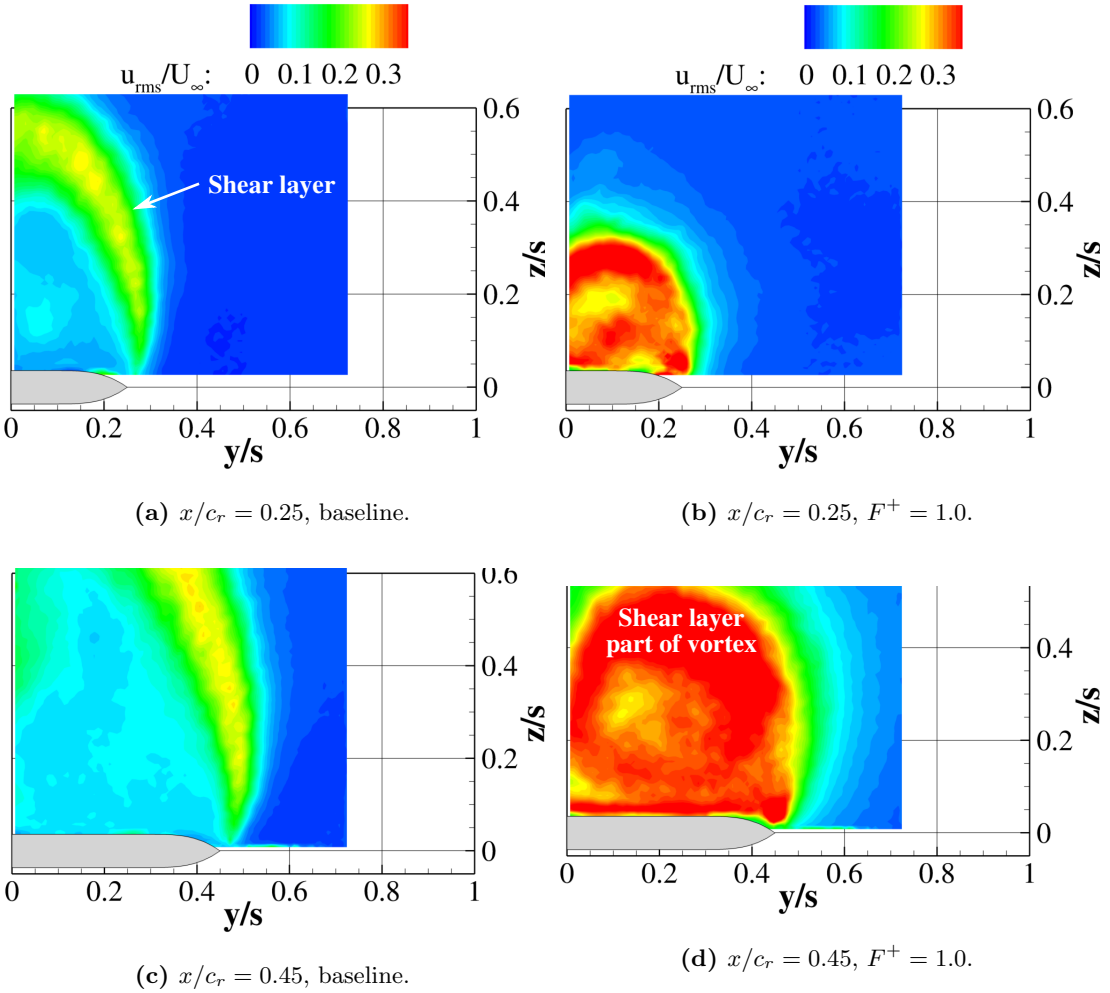

(a) $x/c_r = 0.25$, baseline.

(b) $x/c_r = 0.25$, $F^+ = 1.0$.

(c) $x/c_r = 0.45$, baseline.

(d) $x/c_r = 0.45$, $F^+ = 1.0$.

Figure 5.22: Rms of the x-velocity distributed in PIV crossflow planes at $\alpha = 45°$. Baseline vs. actuated case.

Few vortex events are are recorded in 200 samples from the baseline flow located above the leading edge(cf. Figure 5.23a and c). The vortex generation rate is low, however, increases with actuation (cf. Figure 5.23b and d). The forced flow field resembles to a burst vortex structure, consisting of discrete vortices distributed annularly. Approaching reattachment on the inboard side of the wing, the vortices tend to grow, leading to more intense vortex events near the upper wing surface.

The above assessment of actuation modes is supplemented by the chordwise statistics of discrete vortices in Figure 5.24. The forced flow field constitutes of vortices with reduced circulation, radius and number compared to the flow field at $\alpha = 35°$. Nonetheless, the universal trend concerning the actuation effect is mirrored as well in the vortex event statistics at $\alpha = 45°$.

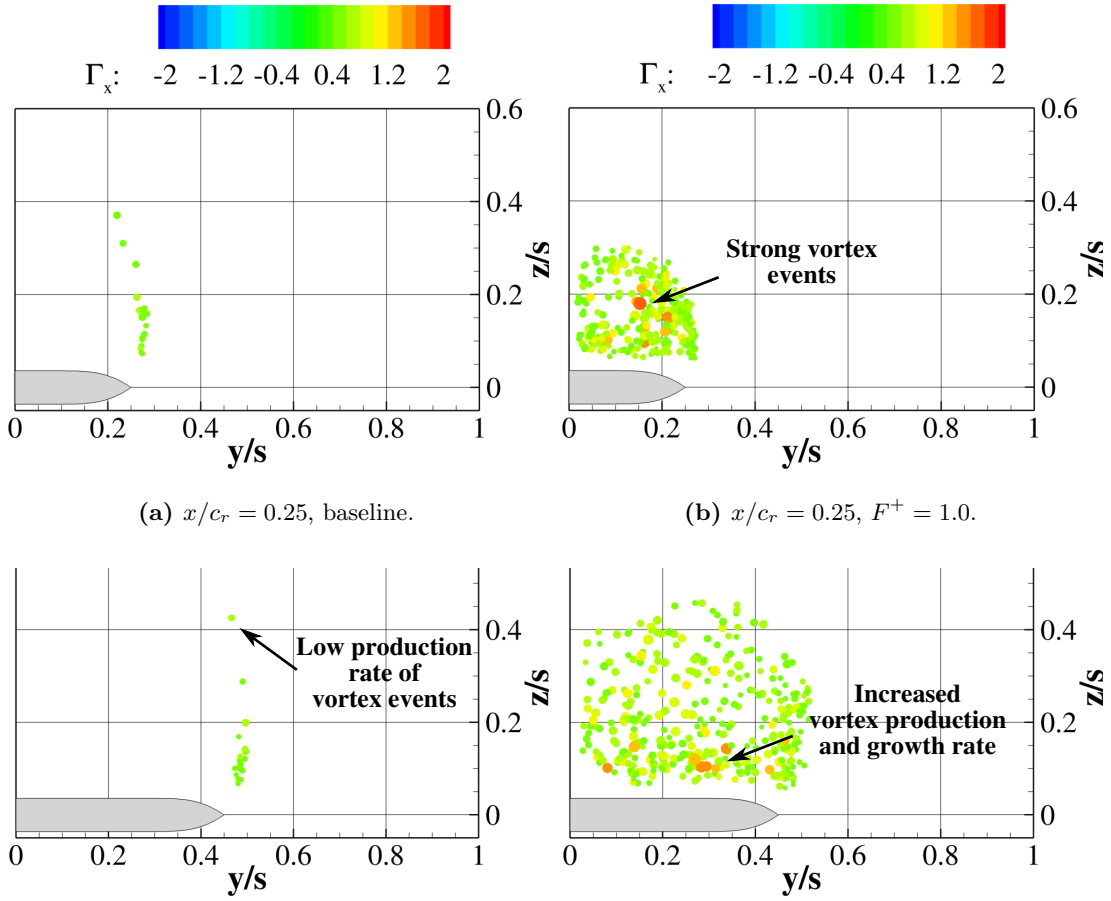

(a) $x/c_r = 0.25$, baseline.

(b) $x/c_r = 0.25$, $F^+ = 1.0$.

(c) $x/c_r = 0.45$, baseline.

(d) $x/c_r = 0.45$, $F^+ = 1.0$.

Figure 5.23: Discrete vortices from PIV crossflow planes at $\alpha = 45°$. Baseline vs. actuated case.

The detection algorithm is dependent on the input data. Especially the PIV grid spacing Δ_{PIV} affects the number, radius and circulation of each detected vortex event [7]. Here, only the fine grid spacing of $\Delta_{\mathrm{PIV}} = 3.7\,\mathrm{mm}$ is considered for the analysis, i.e. crossflow planes $x/c_r = 0.55$. The baseline flow field constitutes of large separation and the only vortex dynamics taking place is within the shear layer. Therefore, the corresponding curve has the lowest values of vortex circulation, radius and number.

The application of AFC transforms the flow field and enhances greatly the production and development of vortices across the flow field. Therefore the curves of the actuated cases tend towards the values of the burst vortex at $\alpha = 35°$. In contrast to the low angles of attack discussed previously, the radius shows a clear dependency on the actuation mode. On average, the largest vortices are generated with pulsed blowing, followed by FV and PV.

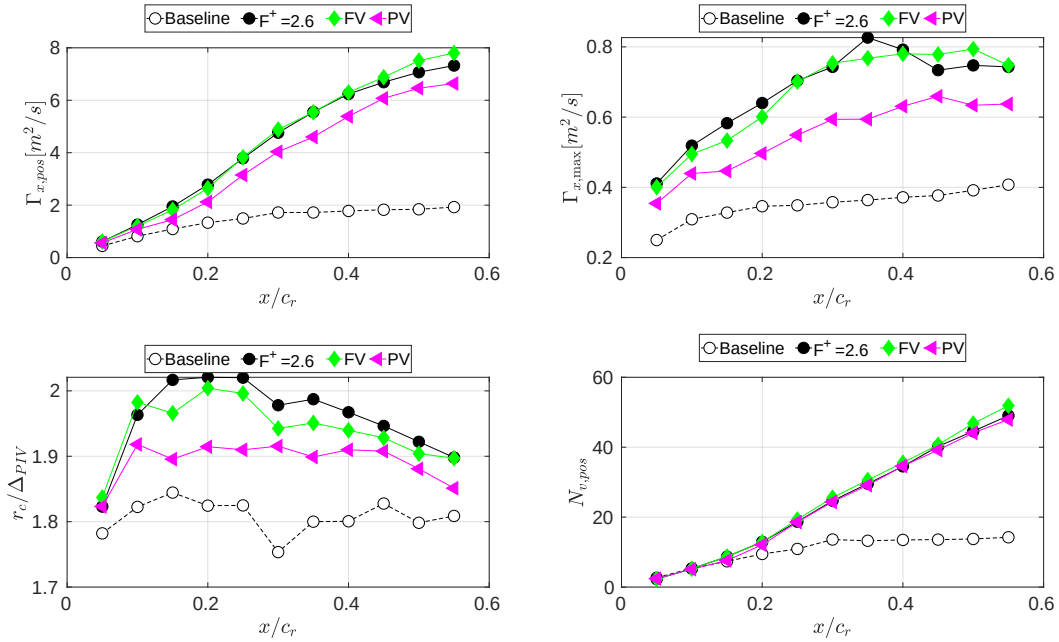

Figure 5.24: Statistics of the vortex detection algorithm from all PIV crossflow planes at $\alpha = 45°$.

5.2.1.4 Mean Rotation Axis

This section analyses the location of the mean rotational axis in dependency on the freestream conditions and actuation modes. The post-stall baseline flow does not include swirling motion and is excluded from the comparison. The rotational axis is determined in equally spaced cross sections and defines the location, where the circumferential velocity reaches zero ($v = w = 0$). The mean flow rotates around this point and coincides with the axis of the mean primary vortex.

Figure 5.25 shows the relative vortex core position in lateral (y/s) and vertical (z/s) direction along the root chord. The position depends greatly on the investigated case and less on the perturbation method. By increasing the angle of attack from $\alpha = 23°$ to $35°$ (compare red with blue symbols), the vortex core departs from the wing's upper surface and moves inboard. This vortex displacement is caused on the one hand by the vortex cross sectional expansion and on the other hand by the strong influence of the freestream direction.

With a further incidence increase from $\alpha = 35°$ to 45° (blue and green symbols, respectively), the vortex lateral motion is constricted. As a result, the vortex can move only in positive z-direction.

The actuation has no considerable effect on the vortex position at pre-stall and stall. The green symbols designating the actuated post-stall flow field show minor but clear differences between actuation modes. The unison blowing, as the most effective blowing sequence, displaces the vortex inboard and away from the wing. Undulations of the vortex core, correlated with the position of the blowing segments, are stronger for this case. Modulated blowing manipulates the vortex with a less pronounced effect.

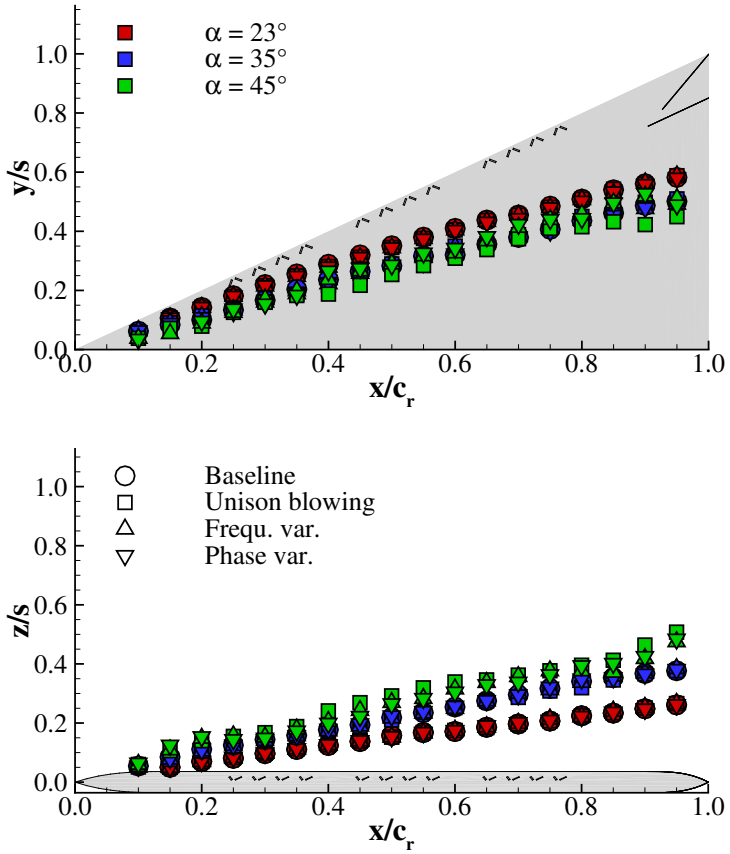

Figure 5.25: Lateral and vertical location of mean vortex rotation axis at three angles of attack and four cases.

5.2.1.5 Reversed Flow

In the same order of AFC modes, the negative velocity peaks and the reversed flow region increase, as seen in Figure 5.26, for both angles of attack $\alpha = 35°$ and $45°$ (represented by red and green symbols, respectively). Considering the stalled flight condition, the reverse flow region extends downstream from $x/c_r \approx 0.2$.

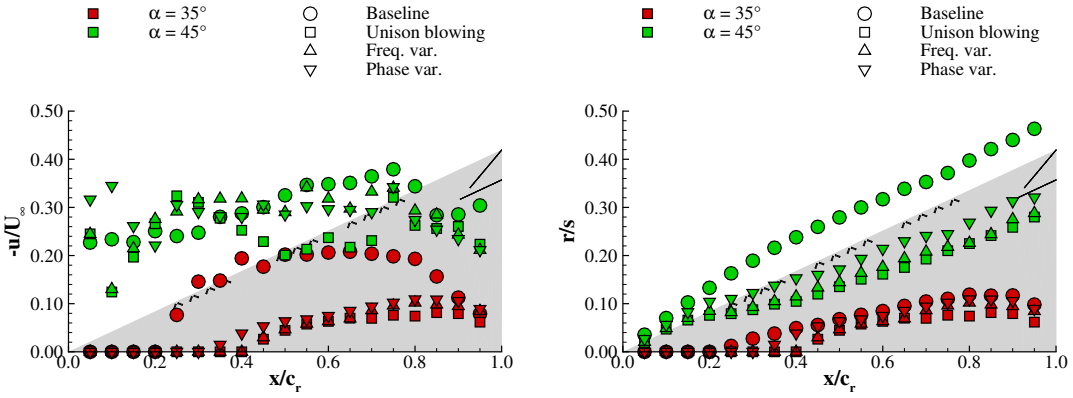

(a) negative axial velocity peaks. **(b)** negative axial velocity radius.

Figure 5.26: Parameters of reversed flow at $\alpha = 35°$ and $45°$, $Re = 0.5 \cdot 10^6$.

For the baseline flow at $\alpha = 35°$, high negative acceleration is present (from $u/U_\infty = 0.0$ to -0.2 at $0.2 \leq x/c_r \leq 0.4$). In this range, the radius of the region with negative axial velocities increases quasi linearly. As presented above the backflow region is shifted downstream and its radius decreases with active blowing. There is a strong correlation between the longitudinal distribution of $\min(u)$ and r, confirming the energy transport in the vortex core.

For the post-stall case, the minimum velocity shows no monotony in x-direction. In the baseline case, the velocity decreases mildly up to $x/c_r = 0.75$, after which it increases again. The negative velocity peak is located in each section close to the leading edge, inboard of the shear layer. In the most aft 10% portion of the root chord, the peak of $-u/U_\infty$ is located farther from the wing. As in the previous case, blowing reduces the backflow in magnitude and cross section. This occurs only locally, i.e. at slot positions (Figure 5.26a: green squares at $x/c_r = 0.5$–0.7). The correlation between both investigated backflow variables is not valid for $\alpha = 45°$. Above the actuation segments, r/s- curves of the actuated cases deviate to lower values compared to the unperturbed case.

5.2.1.6 Longitudinal Circulation

The chordwise circulation distribution is shown in Figure 5.27. The circulation discussed here results from cross sectional integration of positive axial vorticity. Hence, the voticity production can be quantified and assessed. The angle of attack correlates positively with the circulation per unit length $\Gamma_x/(U_\infty l_\mu)$. Despite the increased (actively manipulated) circulation above the wing at $\alpha = 45°$, this does not contribute to the lift increase compared to 35° (Figure 5.6). The vortex is to far from the wing surface, hence, the induction effect decreases.

The actuation does not contribute to a circulation increase at $\alpha = 23°$ (red symbols in Figure 5.27). In comparison, the phase-modulated blowing in the stall case (blue simbols) has less circulation towards the trailing edge ($x/c_r \geq 0.8$). The post-stall case presents a more obvious effect of blowing sequence on the circulation distribution (green symbols). In the baseline flow field at $\alpha = 45°$, the circulation is generated solely by the shear layer detaching from the leading edge. Synchronised blowing with $F^+ = 1.0$ demonstrates a small but more noticeable increase in circulation compared to the modulated cases. The phase modulated case has the least circulation values along the chord length. This trend is correlated with the lift coefficient increase (see Table 5.4).

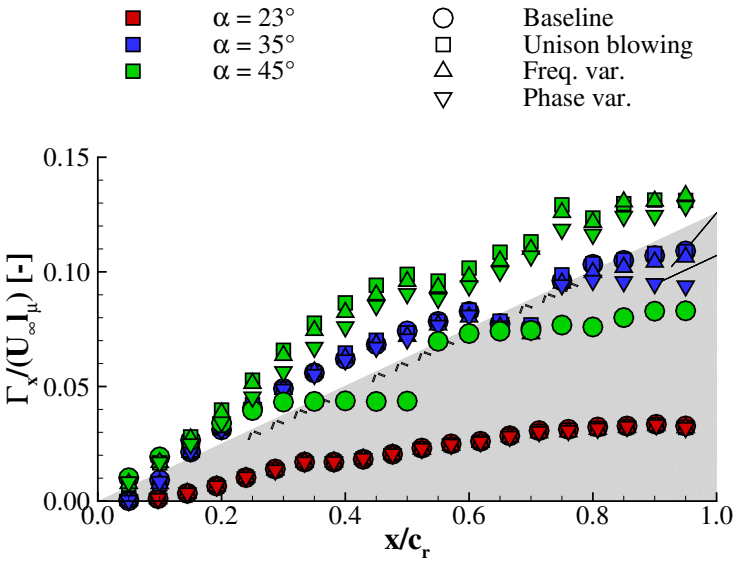

Figure 5.27: Circulation per chord length for three angles of attack and four cases.

5.2.1.7 Synthesis

The flow-field data confirms the aerodynamic characteristics effect towards different blowing strategies. Across all three angles of attack investigated, the highest flow field alteration (breakdown delay, wake/revered flow reduction, shear-layer reattachment) is achieved with the methods ranked below based on their effect on the flow field and aerodynamic characteristics:

1. Synchronised blowing
2. Frequency variation
3. Phase variation

At $\alpha = 23°$, synchronised and frequency-modulated blowing shifts the mean breakdown location downstream and reduces the wake region, whereas blowing with chordwise increasing phase does not.

At $\alpha = 35°$, breakdown occurs near the apex. A measurement of a relatively small structure near the wall was not possible due to reflections. However, because the flow reverses in the wake, a mean stagnation point is detected. Delay of the stagnation point and wake cross-sectional reduction follow the universal trend when applying the above listed AFC modes.

At $\alpha = 45°$, the baseline flow constitutes of massive separation with no flow reattachment on the upper surface. All AFC strategies investigated reattached the shear layer above the wing generating a burst vortex structure expanding over the entire wing.

Investigating the distribution and chrodwise statistics of detected vortex events revealed that small vortices, which are discrete in time and space, are present within and influence the macroscopic vortex system. The analysis confirms the above ranking of the actuation effect on the flow field. This additional investigation tool highlights that pulsed blowing increases discrete vortex production and growth rate.

In conclusion, the quasi-2D disturbance affects the flow field the most compared to phase-delayed blowing or blowing with frequency variation. Hence, deviating from the synchronisation of the leading-edge jets reduces the effect on the flow field. When blowing is operated with decreasing frequency, a negative phase delay is introduced. Based on the present experimental investigations, it can be presumed that, the negative phase delay is superior to its positive counterpart.

The subsequent subsection analyses in detail the phase-averaged flow-field response to synchronised blowing (quasi 2D disturbance). The objective of the analysis is to understand precisely the jet-flow interaction and why synchronised blowing is the best option for pulsed blowing.

5.2.2 Phase-Averaged Flow Field

The current subsection presents the phase-averaged distribution of relative flow field quantities in 5 wing cross sections for all three investigated angles of attack. The investigated planes are located at each 20% root chord length, $x/c_r = 0.20, 0.40, 0.60, 0.80$, and above the actuator pair located at $x/c_r = 0.65$. At each phase ($\theta = 45°$, $90°$, $135°$, $180°$, $225°$, $270°$, $315°$, $360°$), 400 snapshots were taken and averaged, contributing to the analysis of the mean vorticity motion (in the dominant direction: x-axis).

The methodology is described in detail in Section 3.3.2.2. Figure C.1 shows the tuft displacement at each phase angle during one actuation cycle, in which the first 25% represent the blowing phase. The figure demonstrates that independent of the angle of attack, the first phase angle ($\theta = 45°$) includes jet injection.

Besides increasing momentum coefficient, the reduced blowing period is increased from $1/F^+ = 0.4$ at pre-stall and stall to 1.0 at post-stall. With increasing angle of attack the vorticity is distributed on a wider cross section and the peak values decrease (Figures 5.28– 5.36), but the circulation per chord length increases (see Section 5.2.1.6).

As synchronised blowing jets with defined reduced frequencies ($F^+ = 1.0$, 2.6) generate the highest vortex intensification, the investigation of the phase-averaged vorticity field elucidates the dynamics of the vortex subjected to periodic quasi-2D disruption.

5.2.2.1 Pre Stall

Figure 5.28 shows the relative axial vorticity in the range $\omega_x(l_\mu/U_\infty) = \pm 200$ in the chord sections measured. Prior to breakdown, the vorticity peak in the vortex core is stable. In the second plane, $x/c_r = 0.4$ instabilities occur after jet insertion, $\theta \geq 135°$. These propagate downstream, leading to a rotating and spiralling vorticity cluster in the post-breakdown region. The enforced frequency, being in the range of the helical mode instability, generates on average a strong vortex. Vorticity peaks at the leading edge and extending downstream designates a vorticity cluster that rotates around and merges finally into the primary vortical structure.

Important flow features of the phase-averaged PIV investigations:

$\theta = 45°$–$90°$: Small vortex pair in the 4th plane above the slot pair is generated due to active jets.

$\theta = 135°$: The sudden stopping of the jets generates counter rotating vortices. This is seen in the interruption of the shear layer. The alternating opening and closing of the valves reorders vortex shedding at the leading edge. After jet induction, the shedding mechanism starts at the leading edge

$\theta = 180°$: Discrete vortices grow in intensity sustained by the vorticity transport from the shear layer.

$\theta = 225°$–$270°$: Discrete vortices spiral along the shear layer.

$\theta = 315°$–$360°$: Discrete vortices merge into the primary structure, after which the process repeats itself.

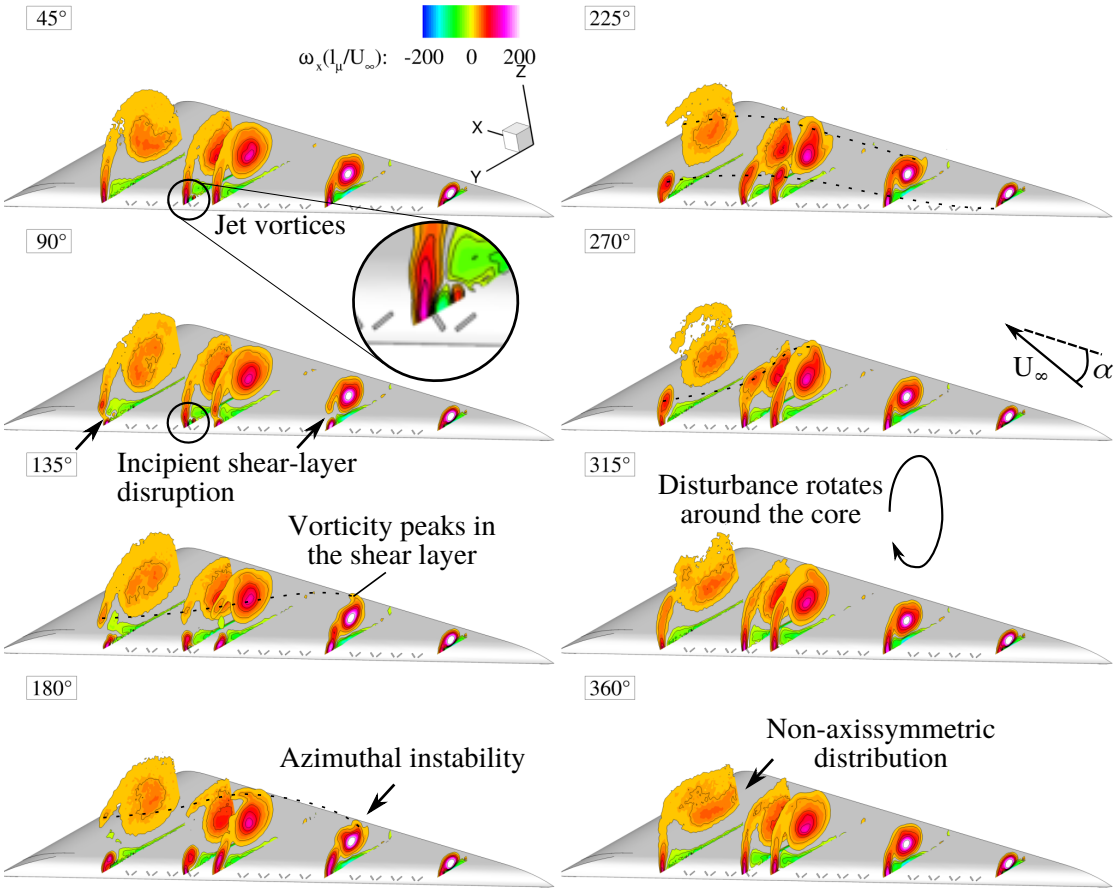

Figure 5.28: Phase-averaged vorticity distribution, $\alpha = 23°$, $Re = 1.0 \cdot 10^6$, $F^+ = 2.6$.

Figure 5.29 captures the vortices detected in 200 samples at three phases in the range $\theta = 135° - 225°$. The examination of two crossflow planes at $x/c_r = 0.60$ and 0.80 brings additional information about the evolution of vortices in longitudinal direction. Prior to $\theta = 135°$, the distribution of vortices is undisturbed, although the jet was injected and ceased at $\theta = 90°$. The subfigures a–c reveal the shear layer disruption and the clustering of vortices above the leading edge. With time passing, the cluster grows and eventually confluences with the primary structure, thereby converging to the initial, natural state.

Velocity profiles across the vortex core in vertical direction of the phase-averaged data are extracted from the mid three crossflow planes and plotted in Figure 5.30. Colour and symbols distinct the phases of one blowing cycle. Upstream of breakdown ($x/c_r = 0.40$), the x-velocity component is distributed with a crest in the core (jet-type flow). At $\theta = 90°$, the core flow has the highest maxima of $u/U_\infty = 3.1$. Within the breakdown wake ($x/c_r = 0.60$, 0.65), the distribution has, instead, a valley with minimum in the rotation axis $v = 0$.

The lateral velocity distribution across the vortex is described by a point-symmetric polynomial curve with respect to the vortex rotation axis. Throughout one blowing cycle, the flow is rather inert with small fluctuations. The rotation axis does not vary much (towards the trailing edge moderate fluctuations occur, see Figure C.6). At $\theta = 180°$ the wake deficit and y-velocity peaks near the wall are reduced. This shows the response time is about a quarter of one blowing cycle, or the same amount of time that the jets were active after they were switched off.

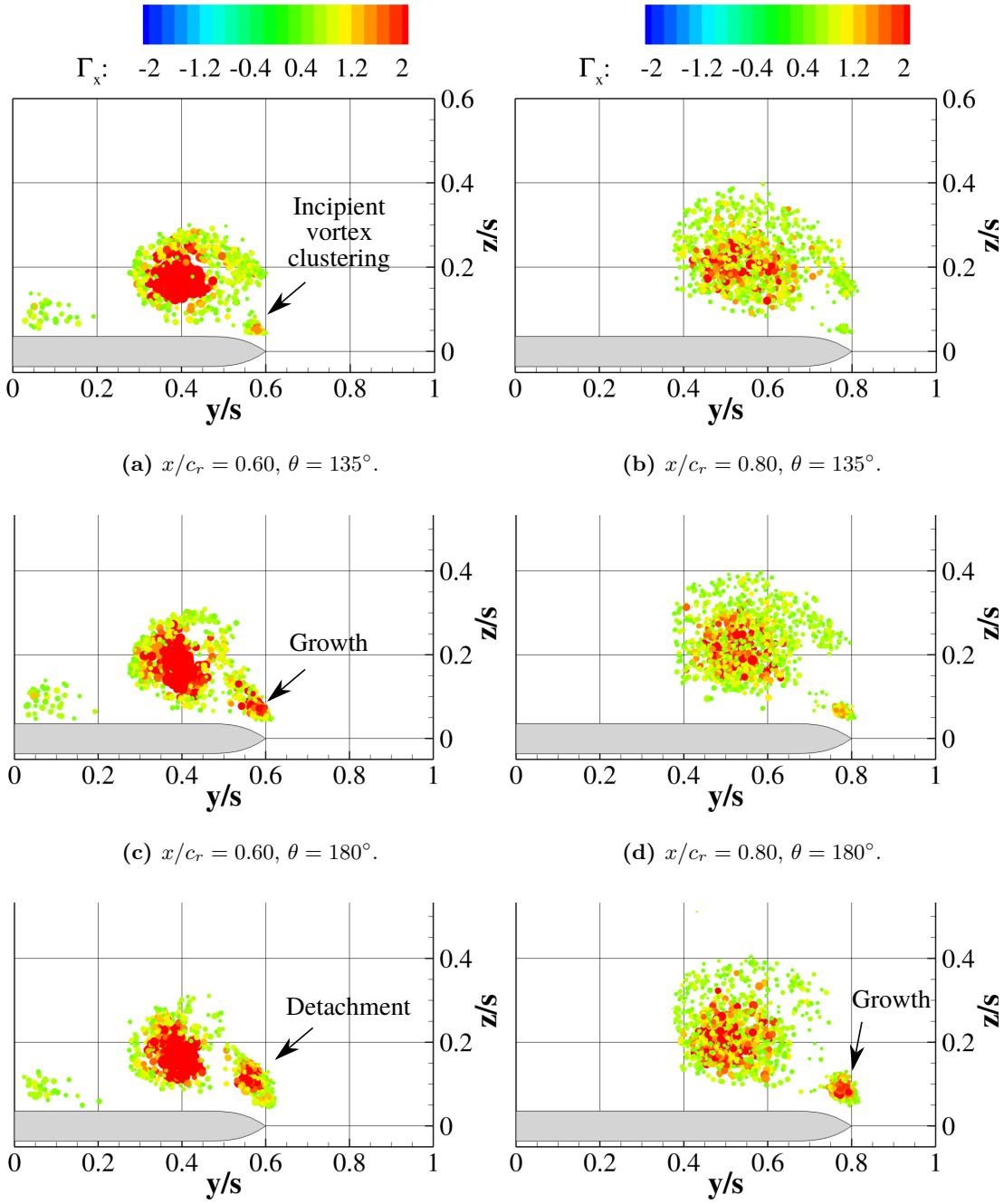

(a) $x/c_r = 0.60$, $\theta = 135°$.

(b) $x/c_r = 0.80$, $\theta = 135°$.

(c) $x/c_r = 0.60$, $\theta = 180°$.

(d) $x/c_r = 0.80$, $\theta = 180°$.

(e) $x/c_r = 0.60$, $\theta = 225°$.

(f) $x/c_r = 0.80$, $\theta = 225°$.

Figure 5.29: Phase-dependent distribution of discrete vortices at $x/c_r = 0.60$ (left) and 0.80 (right). $\alpha = 23°$ and $F^+ = 2.6$.

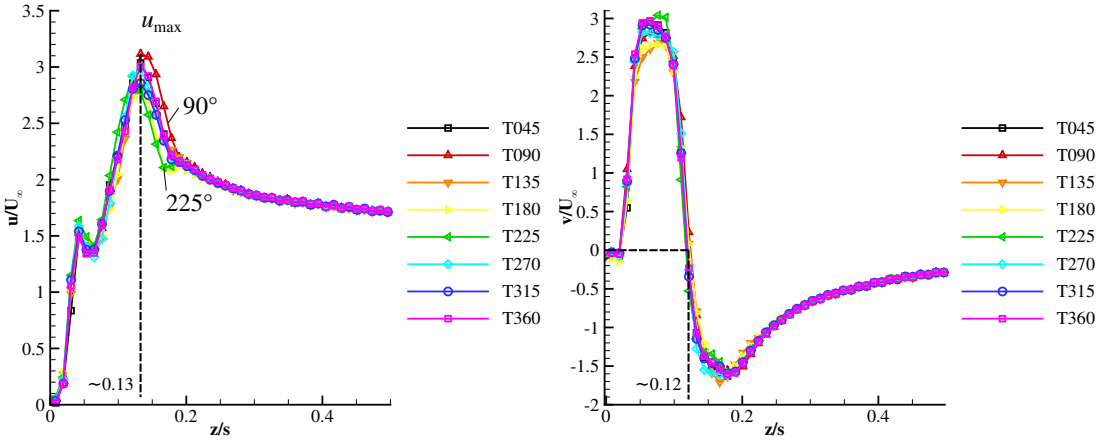

(a) x-velocity at $x/c_r = 0.40$.

(b) y-velocity at $x/c_r = 0.40$.

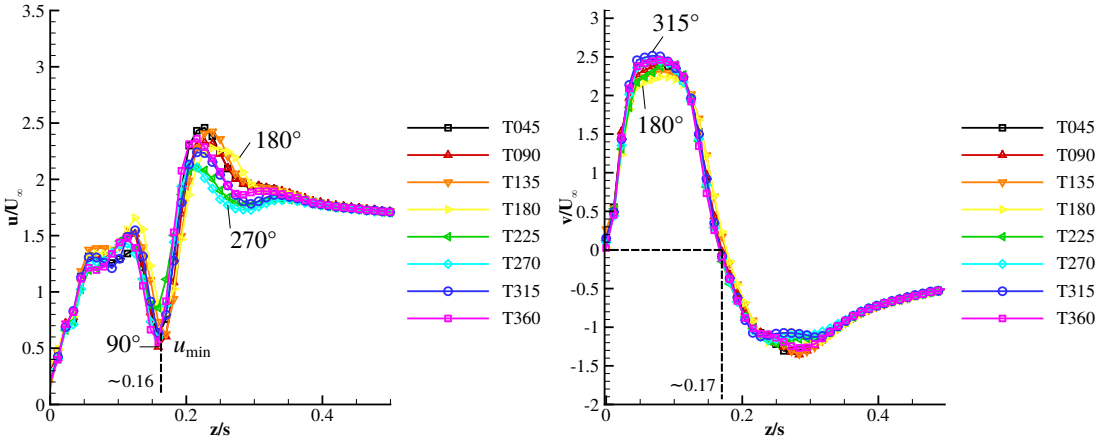

(c) x-velocity at $x/c_r = 0.60$.

(d) y-velocity at $x/c_r = 0.60$.

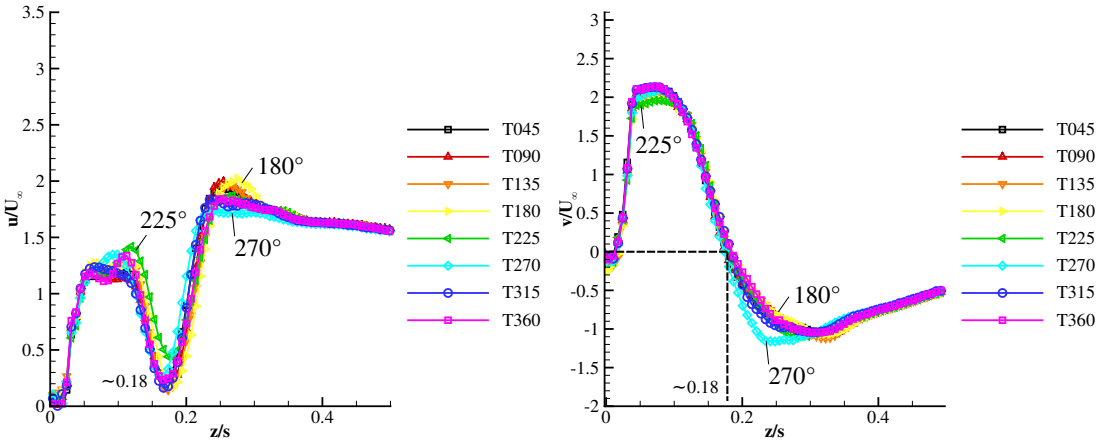

(e) x-velocity at $x/c_r = 0.65$.

(f) y-velocity at $x/c_r = 0.65$.

Figure 5.30: Phase-dependent distribution of axial and lateral velocity at $x/c_r = 0.65$ and 0.80. $\alpha = 23°$ and $F^+ = 2.6$

Throughout one blowing cycle, the vortex wanders in lateral direction with small fluctuations as the curves representing different phases are not quite on top of each other. The curves with highest amplitudes are marked in Figure 5.30. There is a time delay of approximately 25% of one blowing cycle after jet injection. The lag propagates downstream, as the flow near the trailing edge responds later than the upstream region. Increasing the angle of attack amplifies this periodic motion.

5.2.2.2 Near Stall

Figure 5.31 presents the non-dimensional phase-averaged vorticity distribution of the perturbed flow field with $F^+ = 2.6$ measured at $\alpha = 35°$ and $Re = 0.5 \cdot 10^6$, in the range $|\omega_x(l_\mu/U_\infty)| \leq \pm 100$. It demonstrates the same disturbance–vortex interaction and a stronger phase dependency compared to pre-stall. Peaks of increased vorticity emerge at the leading edge and grow with time passing. This translates to a higher accumulation of discrete vortices above the leading edge. After the leading-edge detachment, these vortices spiral downstream. At the end of the blowing cycle and prior to jet injection, the structures merge into the primary structure.

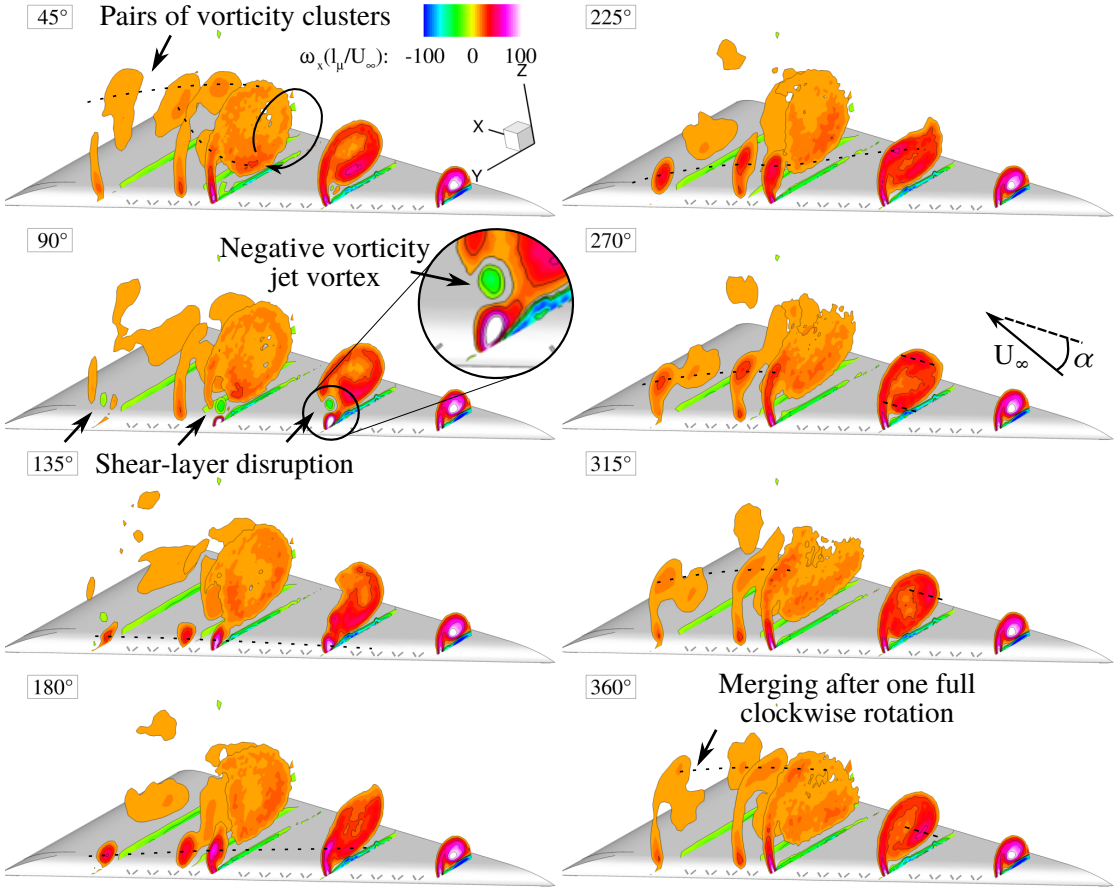

Figure 5.31: Phase-averaged vorticity distribution, $\alpha = 35°$, $Re = 0.5 \cdot 10^6$, $F^+ = 2.6$.

Upstream of breakdown ($x/c_r = 0.2$), the apex vortical flow is steady and stable, as the vorticity distribution represents the jet-type flow. Downstream, the primary structure breaks down and the flow becomes highly transient. Two vortex clusters rotate around each other in a clockwise positive x-direction (cf. Figure 5.18), reducing the wake-type flow region. The motion describes a full rotation during one blowing period, thus, the flow responds to the periodically injected disturbance better than the lower angle of attack $\alpha = 23°$, at which the natural flow is rather too stable.

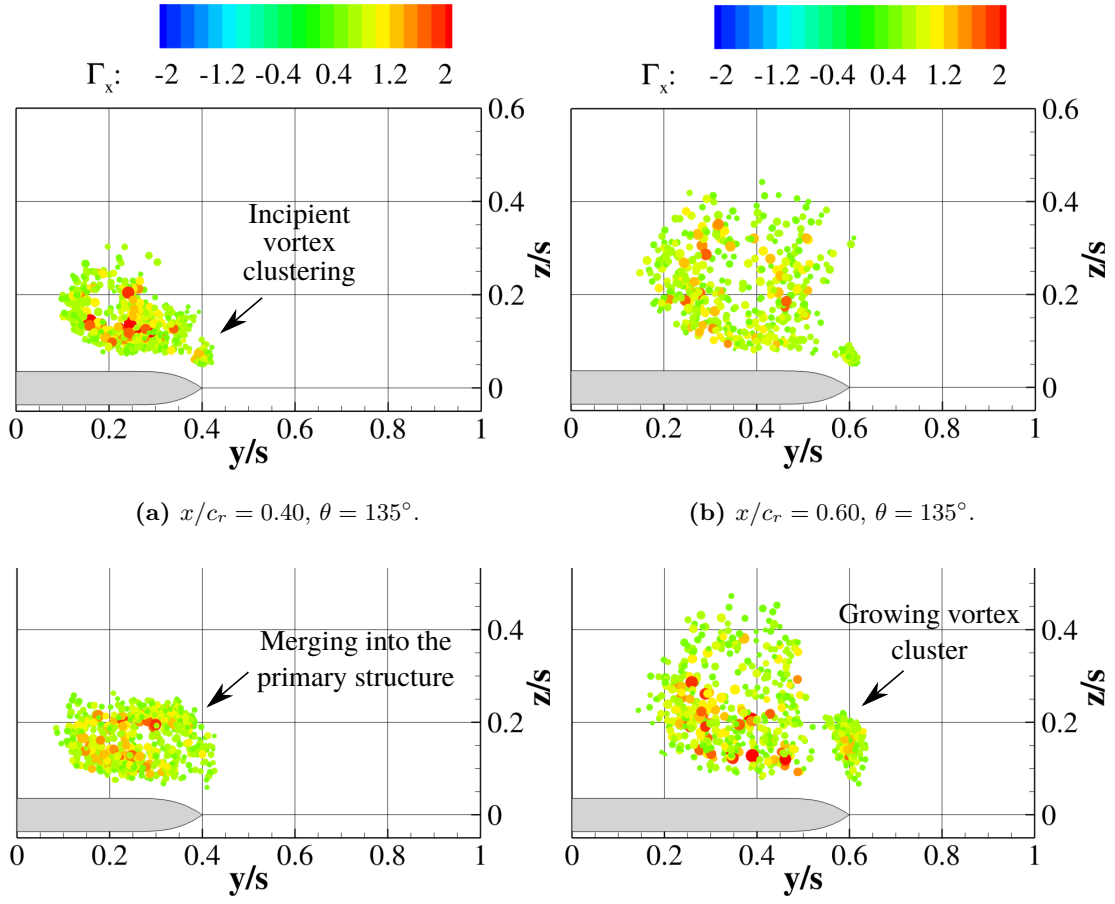

(a) $x/c_r = 0.40$, $\theta = 135°$.

(b) $x/c_r = 0.60$, $\theta = 135°$.

(c) $x/c_r = 0.40$, $\theta = 225°$.

(d) $x/c_r = 0.60$, $\theta = 225°$.

Figure 5.32: Phase-dependent distribution of discrete vortices at $x/c_r = 0.40$ and 0.60. $\alpha = 35°$ and $F^+ = 2.6$.

From the above analysis of the mean flow field data resulted that the synchronised pulsed blowing strategy has the biggest impact on the flow field regardless of the flow field type. Hence, the phase-averaged data revealed that periodic forcing at $\alpha = 23°$ and 35° produces rotating structures, which delay the mean breakdown location. However, the PIV data was not sufficient to find the exact mechanism, for which the DES results are necessary (Section 5.5).

The time dependent reverse flow is quantified by minimum axial velocity and reverse-flow cross sectional radius in Figures 5.33a and b, respectively. The reverse flow is rather steady up to 180°, indicating a response to fluid injection with a delay of at least 90°. The response is a decrease in minimum longitudinal velocity at $x/c_r = 0.6$, which is downstream of the first blowing segment. At $\theta = 225°$ the disturbance reaches the entire wing, after which it converges to the initial state.

From this representation the following conclusions can be drawn: within one blowing cycle the vortex pulsates in longitudinal direction with local contraction/expansion and rotates in the mean vorticity direction.

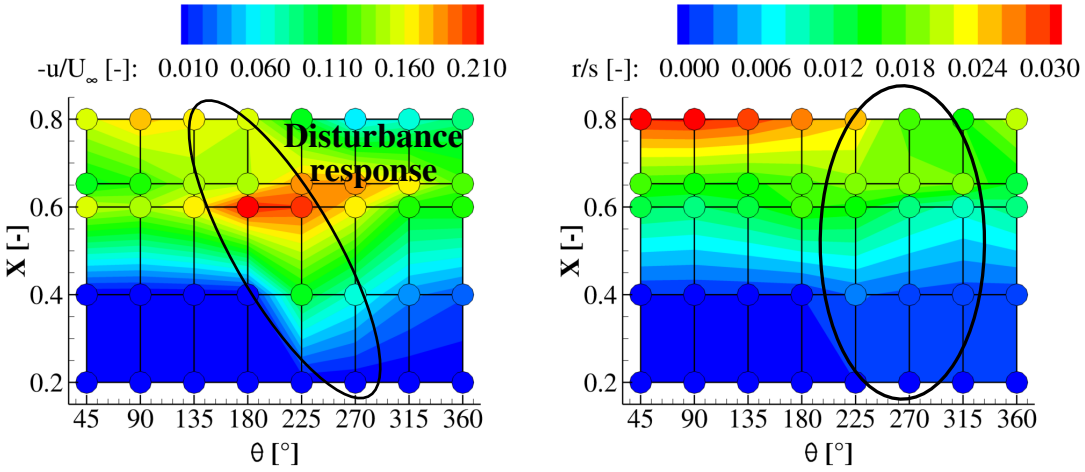

(a) Minimum velocity.

(b) Minimum velocity.

Figure 5.33: Negative axial velocity and backflow radius as function of chord section and phase angle, $\alpha = 35°$, $Re = 0.5 \cdot 10^6$, $F^+ = 2.6$.

Figure 5.34 comprises of u/U_∞ and v/U_∞ profiles across the vortex core in z-direction at $x/c_r = 0.40$ (a,b), 0.65 (c,d) and 0.80 (e,f). Along the chord, the wake increases in diameter and the swirl angle decreases ($\partial v/\partial z$). The maximum-lift flow field is more unsteady than at lower incidences, and responds to periodic forcing with higher amplitudes. However, the lowest angle was investigated at twice the freestream velocity of the stall and post-stall cases. Which can have a stabilising effect on the vortex system.

The near-wall region around $z/s = 0.1$ is dominated by high velocity values that decrease from $(u/U_\infty, v/U_\infty) \approx (1.3, 1.7)$ to $(0.8, 1.1)$ within the chord station range $x/c_r = 0.40 - 0.80$. The phase-dependent velocity distributions are not synchronised along the wing root: minimum u/U_∞ in the wake at $\theta = 225°$, 270° and 90°, for $x/c_r = 0.40$, 0.65 and 0.80, respectively. Reversed flow protrudes the plane at $x/c_r = 0.40$ at $\theta = 225°$. Along the regarded average cycle, the wake cross section increases in response to the discrete jets in the aft half part of the wing. The opposite effect is observed upstream: the wake cross section is reduced and the minima decrease (the valley becomes pointier).

The v/U_∞ distributions describe slight undulation and inflections in time, suggesting a periodic variation of local swirl angle. In conclusion, the average flow dynamics are complex. The primary structure reveals a system of vortex cluster pairs rotating around the global rotation axis. In longitudinal direction, the vortex wake-type flow experiences dilatation and contraction with a approximately $T/2$ delay after jet injection.

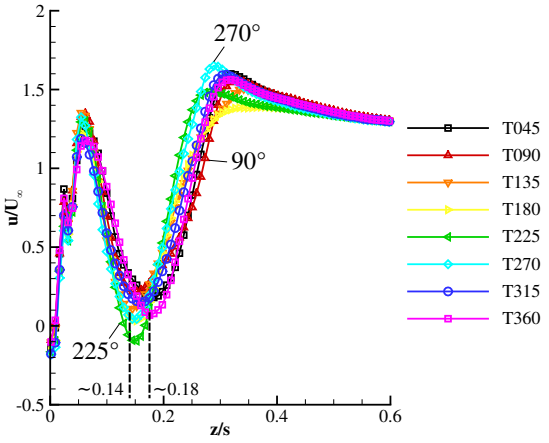

(a) x-velocity at $x/c_r = 0.40$.

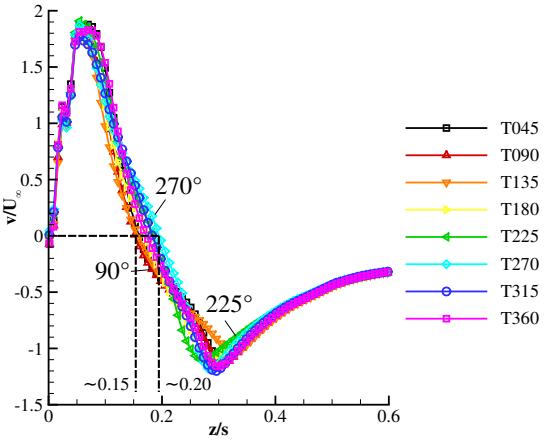

(b) y-velocity at $x/c_r = 0.40$.

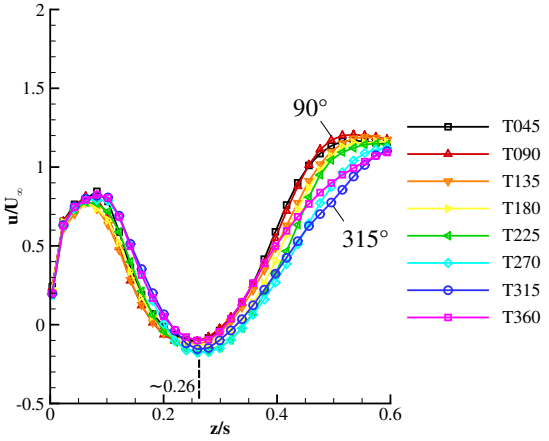

(c) x-velocity at $x/c_r = 0.65$.

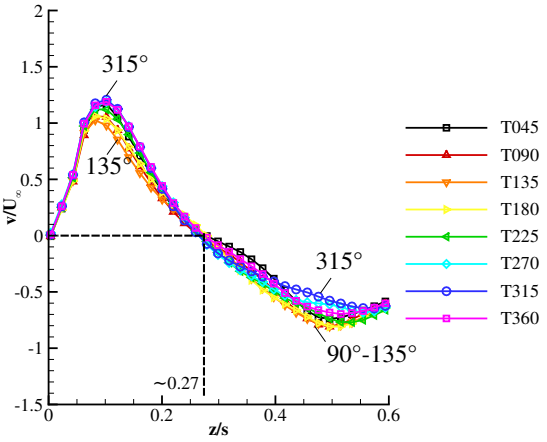

(d) y-velocity at $x/c_r = 0.65$.

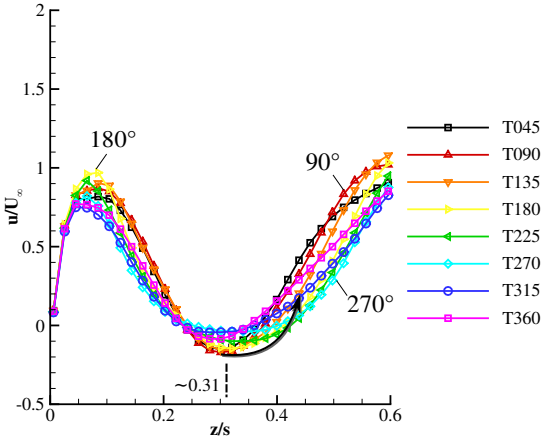

(e) x-velocity at $x/c_r = 0.80$.

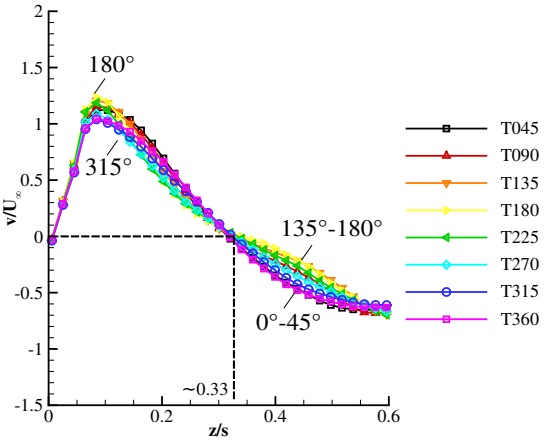

(f) y-velocity at $x/c_r = 0.80$.

Figure 5.34: Phase-dependent distribution of axial and lateral velocity at $x/c_r = 0.65$ and 0.80. $\alpha = 35°$ and $F^+ = 2.6$.

The above investigation of flow field response established a periodic motion of the primary structure. The extracted curves above suggest a phase-averaged motion of the rotation axis ($v = w = 0$) correlated with minimum velocity (see also Figure 5.33). Figure 5.35a shows the phase-averaged location of the rotation axis along the chord. The vortex mean axis undulates downstream with dominant amplitudes in the yz-plane. Vertical fluctuations are rather small.

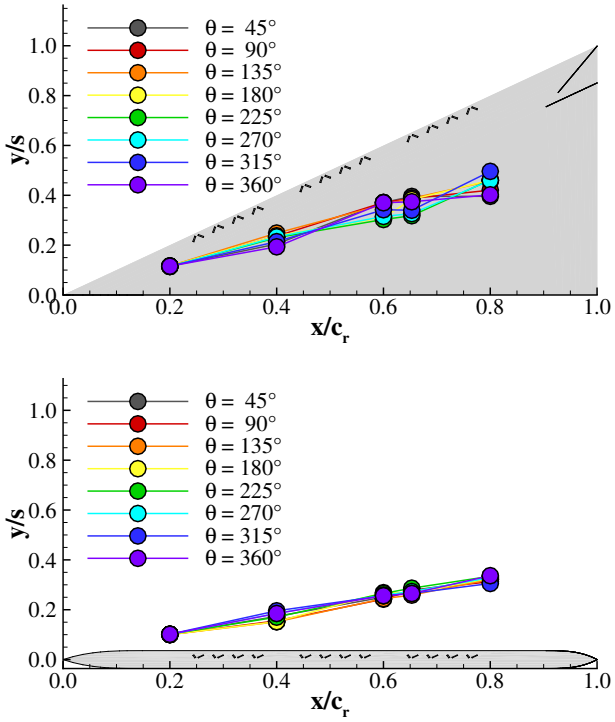

(a) Chordwise location.

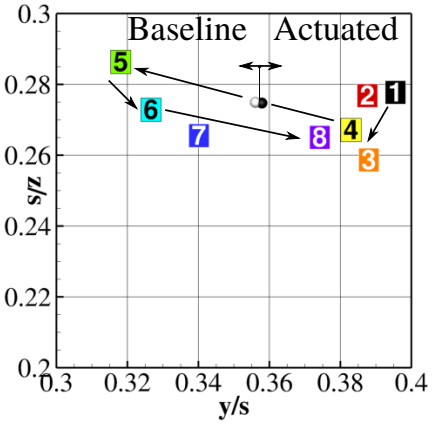

(b) Location in the 4^{th} chord station $x/c_r = 0.65$.

Figure 5.35: Phase-dependent vortex axis location at $\alpha = 35°$.

In Figure 5.35b the coloured and numbered squares represent the location of rotation axis in the crossflow plane at $x/c_r = 0.65$ for each phase. At the start of the blowing cycle ($\theta = 0°/360°$), blowing is initiated and continues during the first phase investigated $\theta = 45°$ and ceases at the second phase $\theta = 90°$.

The largest displacement of the axis occurs during the first and fifth phase investigated. Hence, throughout the blowing phases, the vortex positions most outboard at $y/s = 0.4$ and resides up to the fourth phase ($\theta = 180°$). The largest lateral shift is between the fourth and fifth phase, during which it moves from $y/s = 0.39$ to 0.32. Figure 5.35b also displays the mean location of the baseline and actuated vortex axis designated by a white and black sphere, respectively. Although the vortex fluctuates and undulates under periodic forcing, its mean location is slightly outboards with respect to the location of the unforced rotation axis.

5.2.2.3 Post Stall

As demonstrated in Section 5.2.1, the synchronised pulsating fluid injection with non-dimensional frequency at unity produces the highest constriction of the reverse flow region and the highest induced near-wall velocities. This is valid for all angles of attack. At $\alpha = 45°$, the best lift increase is achieved with synchronised blowing (Figure 5.6). The mechanism that reattaches the shear layer is discussed in this subsection. The analysis of phase-averaged flow response to pulsed blowing brings light upon the question why synchronised blowing or quasi-2D disturbance injection (considering the shear layer flow) has the biggest impact on the flow rearrangement.

Figure 5.36 shows the normalised, axial vorticity distribution in the crossflow planes investigated. High vorticity values are concentrated in the shear layer and in the large vortex-wake structure consisting of two regions that rotate pairwise and spiral around the low energy core. These mean "vorticity events" extend in chordwise direction with a counter-clockwise twisting and a clockwise rotation around the core.

Similar to the above discussed cases at $\alpha = 23°$ and $35°$, AFC manipulates the generation of vortices subsequent to the shear-layer separation. The jet-flow interactions and the response of the flow to actuation at $\alpha = 45°$ based on consecutive phase instances shown in Figure 5.36 are described below:

$\theta = 45°$–$90°$: The jets are active during the first quarter period and generate small localised vortex events that disrupt the shear layer immediately after detachment at $x/c_r > 0.20$. Phase-averaged TKE distribution (Figure C.7) shows local increased activity during blowing $\theta = 0° - 90°$, owed to jet-vortex interactions.

$\theta = 90°$–$135°$: After blowing cessation, the small vortex events interact with the shear layer increasing its inboard deflection.

$\theta = 180°$–$315°$: Within the shear layer, the jet-vortex interaction stimulates shear layer instabilities. As a result vortex events detach from the shear layer and are traced in multiple chord stations. The events spiral (downstream) and rotate (in time) unidirectionally around the low energy core.

$\theta = 180°$–$360°$: The 3D vortex events persist during the inactive part of one period, proving their stabilising effect of the periodic flow excitation.

$\theta = 225°$–$360°$: The rotation of the vortex event pair continues with time passing, completing its rotation around the x-axis at the fin of one cycle. With this process, the wake increases in cross-section as the vortex event pair departs from the center (see below).

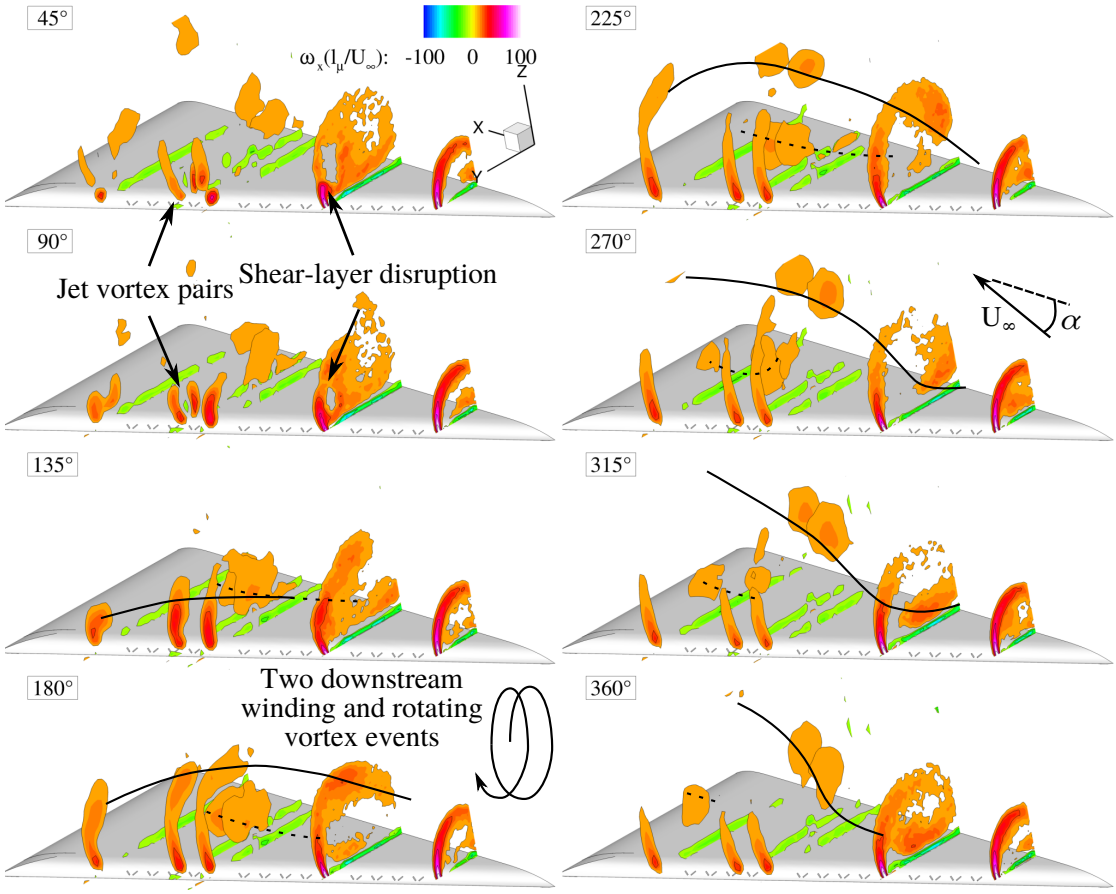

Figure 5.36: Phase-averaged vorticity distribution, $\alpha = 45°$, $Re = 0.5 \cdot 10^6$, $F^+ = 1.0$.

As in the previous cases, the phase dependent distribution of discrete vortices is analysed subsequently for $\alpha = 45°$. Figure 5.37 shows the distribution of the vortex events at the chord station $x/c_r = 0.40$ (second most upstream plane in Figure 5.36) during the inactive-jet phases. The disruption of the shear layer generates a cluster of vortices that rotate around the leading-edge vortex axis.

Throughout this process, strong interactions lead to merging and growth of discrete vortex events. Prior to the next jet injection, at $\theta = 315°$, relatively intense vortex events populate the near wall region. This leads to an increased inboard deflection of the shear layer. At the start of the blowing sequence, the vortex cluster makes a full rotation while transported downstream and the upstream vortex events begin to merge with the shear layer before the additional momentum is injected, reinitiating the entire periodic process.

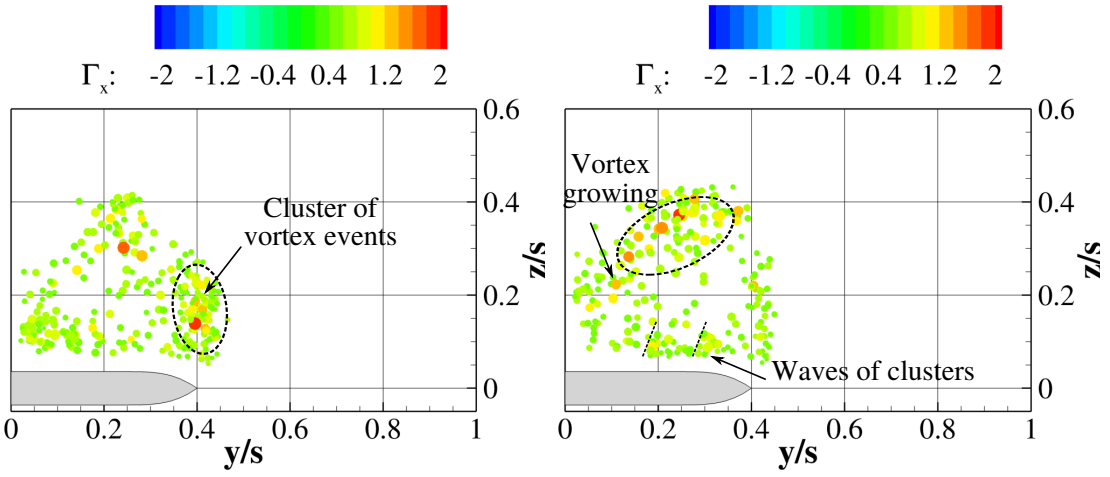

(a) $\theta = 135°$.

(b) $\theta = 180°$.

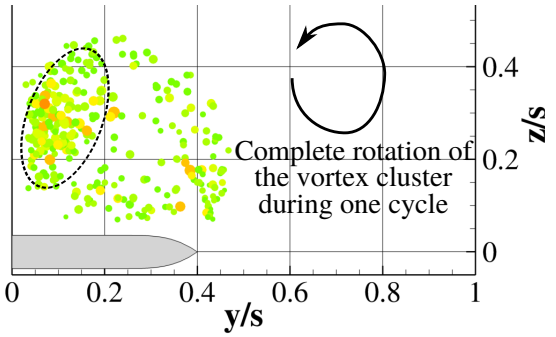

(c) $\theta = 225°$.

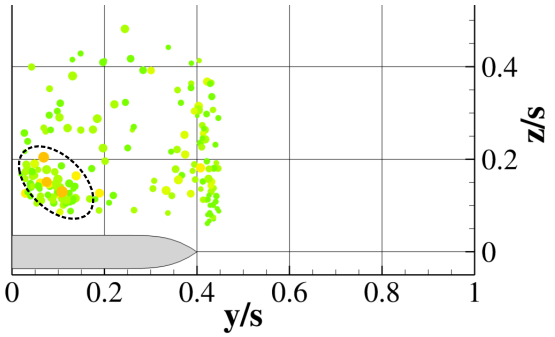

(d) $\theta = 270°$.

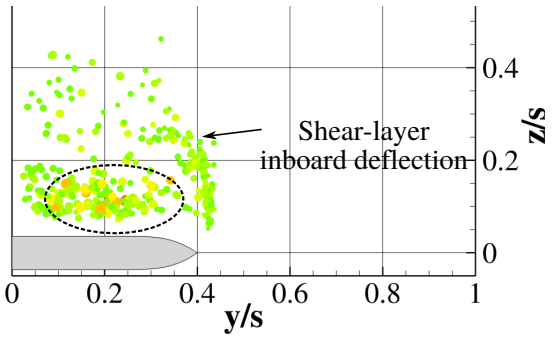

(e) $\theta = 315°$.

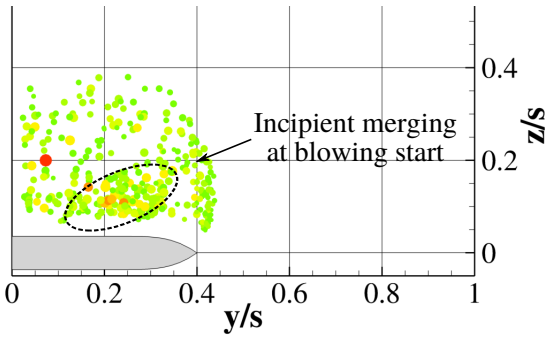

(f) $\theta = 360°$.

Figure 5.37: Phase-dependent distribution of discrete vortices at $x/c_r = 0.40$. $\alpha = 45°$ and $F^+ = 1.0$.

Figure 5.38 presents the peak negative axial velocity and cross section of backflow for the actuated post-stall case. At this angle of attack the reversed flow in the core is more unsteady and more heterogeneous than at 35° (Figure 5.33). With time passing, regions in the θ-x/c_r-space of low minimum and high minimum $-u/U_\infty$ (blue and red) alternate downstream. The radius of reversed flow is rather steady at $x/c_r \leq 0.6$. Downstream, the actuation induces oscillations of backflow cross section.

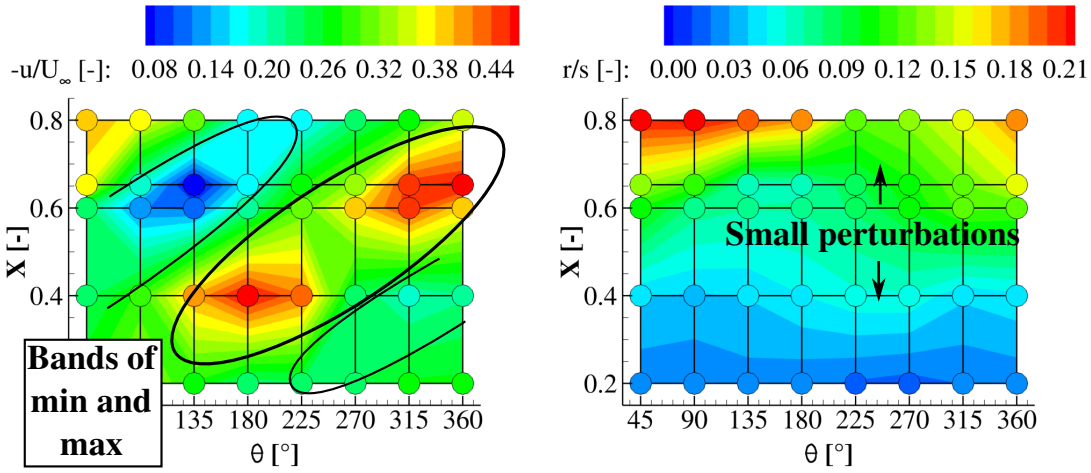

(a) Minimum velocity.

(b) Minimum velocity.

Figure 5.38: Negative axial velocity and backflow radius as function of chord section and phase angle, $\alpha = 45°$, $Re = 0.5 \cdot 10^6$, $F^+ = 1.0$.

Figure 5.39 presents the vertical distribution of u/U_∞ and v/U_∞ across the mean vortex core at $x/c_r = 0.40$, 0.65 and 0.80. Analogue to the lower angles of attack investigated, the flow field constitutes of a swirling wake/reversed flow with periodic motion in all directions. In contrast to $\alpha = 35°$, at the highest angle, the fluctuations are higher and reveal a more clear rotational motion.

At $x/c_r = 0.40$, there is a phase dependent offset of u/U_∞ and v/U_∞ curves (Figure 5.39a and b). In the downstream investigated plane, at $x/c_r = 0.60$, axial and spanwise momentum near the wall increases steadily up to $\theta = 180°$ (Figure 5.39c and d). Progressing in phase, both velocity components decrease and the velocity deficit closer to the wing increases. Minimum axial velocity is highest during the final quarter period, $\theta = 315° - 360°$.

The blowing phase leads to a rapid increase in axial velocity. The highest values corresponds to $\theta = 135°$, at which the wake-type distributions show the appearance of an inflection. The spanwise velocity component demonstrates an inflection, as well at 135°, which remains up to 315°. The inflection propagates downstream at $x/c_r = 0.80$ (Figure 5.39e and f) with a phase delay of $\Delta\theta \approx 45°$. This delay in phase is included in Figure C.8 in Appendix C.

The fluctuation of the velocity field across the vortex suggests that the vortex undergoes a certain periodic motion. Figure 5.40 shows the phase dependent location of the rotation axis. In the first plane upstream of the blowing segments, the rotation axis describes rather random location fluctuations. Downstream the axis rotates around the mean axis in clockwise direction. In addition, the phase-averaged core winds downstream in counter-clockwise direction (Figure 5.40a).

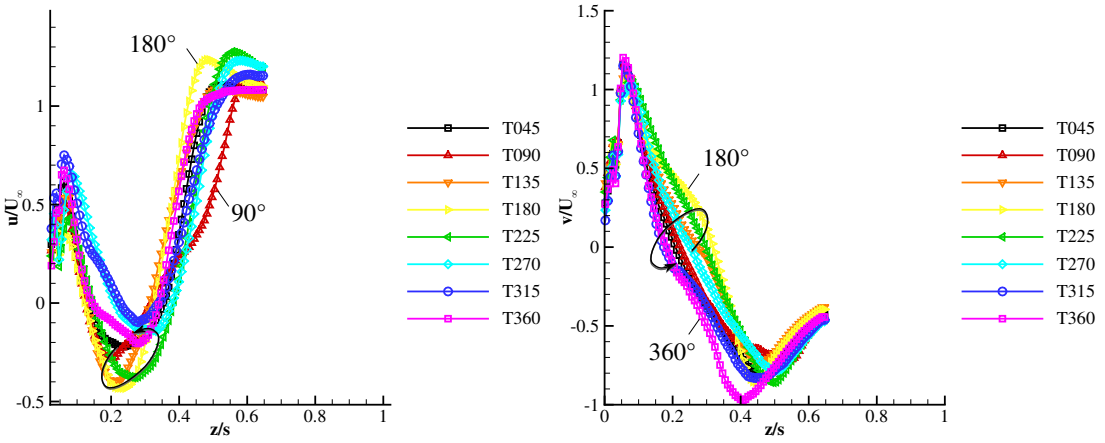

(a) x-velocity at $x/c_r = 0.40$.

(b) y-velocity at $x/c_r = 0.40$.

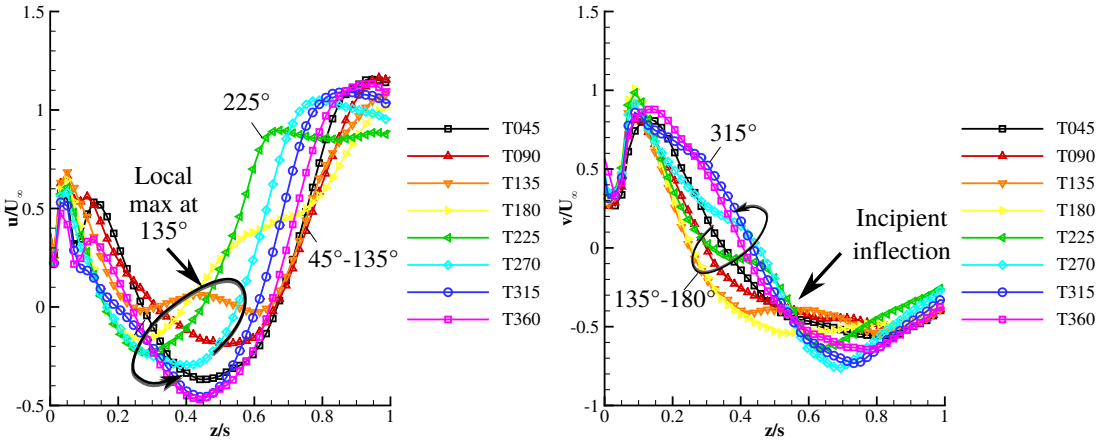

(c) x-velocity at $x/c_r = 0.65$.

(d) y-velocity at $x/c_r = 0.65$.

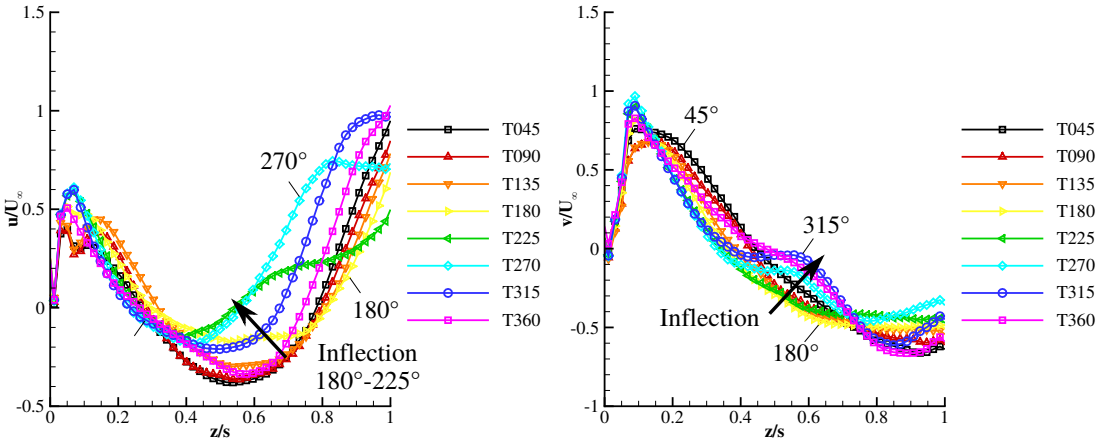

(e) x-velocity at $x/c_r = 0.80$.

(f) y-velocity at $x/c_r = 0.80$.

Figure 5.39: Phase-dependent distribution of axial and lateral velocity at $x/c_r = 0.65$ and 0.80. $\alpha = 45°$ and $F^+ = 1.0$.

At $x/c_r = 0.65$, the phase averaged rotation axis describes an ellipse. Up to $\theta = 135°$, the vortex axis shifts closer to the wing. Subsequently, the axis follows the vorticity direction. Half a period after fluid injection, the vortex is located farthest outboard.

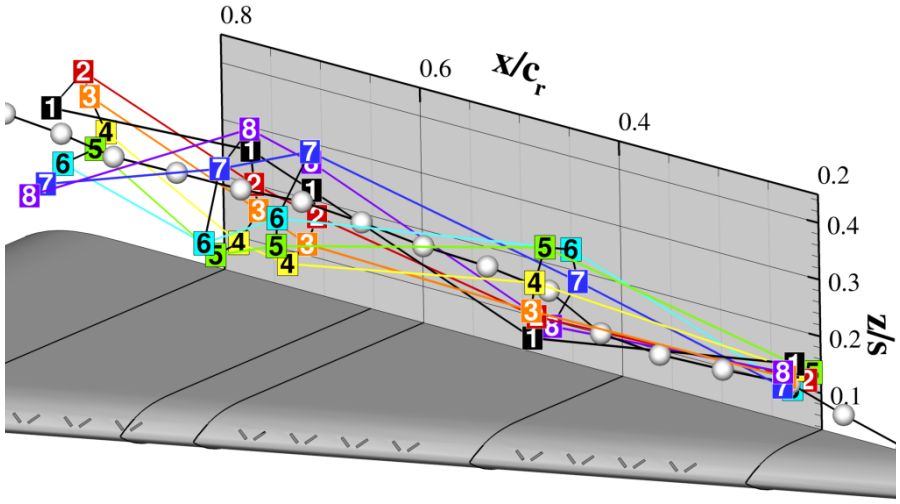

(a) Isometric view. White spheres represent mean locations.

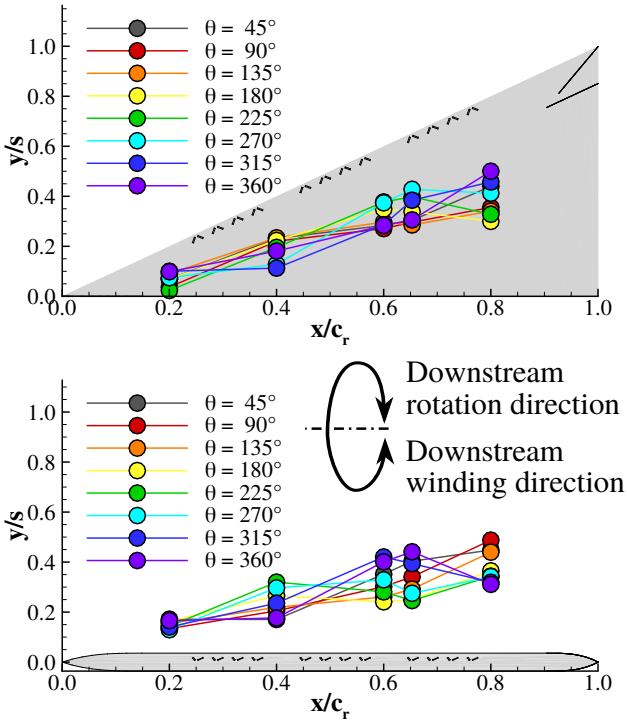

(b) Chordwise location.

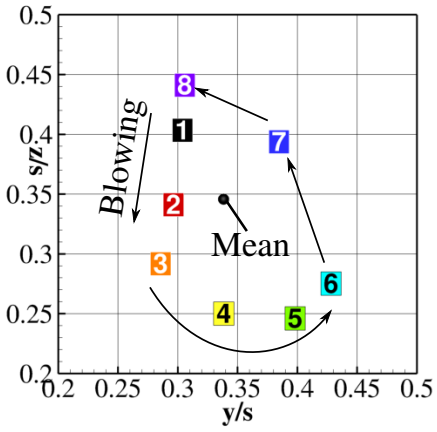

(c) Location in the 4^{th} chord station $x/c_r = 0.65$.

Figure 5.40: Phase-dependent vortex axis location at $\alpha = 45°$.

5.2.2.4 Synthesis

The phase-averaged investigations revealed the mean flow field response towards periodic blowing. Especially in the breakdown wake flow, clusters of vorticity traced along nearly the entire leading edge rotate around a phase dependent rotational axis.

The 3D vortex events emerge subsequently to the jets disturbing the shear layer. These structures show a detachement at the leading edge commencing at the apex and progressing downstream and resulting in a downstream winding contrary to the main vorticity direction.

Although the disturbance is injected in a 2D manner, the winding of the phase dependent vortex axis suggests a downstream lag in response to the actuation. Along the chord, the disturbances propagate phase delayed forming the above described temporal and spatial helical structure sustained by periodic blowing.

Naturally, vortex shedding process works by the same mechanisms. As a result, synchronised blowing generates the strongest vortices with average distribution describing a downstream winding with rotation in time, as seen in the baseline flow. This sustained periodic motion has a stabilising effect on the mean vortex structure, which translates to wake reduction and stagnation delay with respect to axial core velocity and, consequently, to the enhancement of lift coefficient and the aerodynamic efficiency. Desynchronising the jets causes an alternate vortex evolution pattern that departs from the natural pattern with a reduced effect on the mean global structure.

The phase-averaged PIV investigations revealed as well, that the primary structure consists of multiple small vortical structures, whose dynamics describe an ordered periodic motion. Influenced by the rotating mean vortex events (clustering), the axis winds with a full rotation along the wing, coinciding with the enforced frequency at unity ($F^+ = 1.0$). Even though the disturbance is injected simultaneously (in a 2D manner), the flow field response is three dimensional, as investigated here by phase-averaged PIV. The instantaneous 3D structures are investigated in Section 5.5 based on CFD analysis.

5.3 Comparison of Numerical and Experimental Data

This section assesses the computational results (DES) with the experimental results (WTT). Hereby, the discussion focuses on the flow field variables, the pressure distribution and aerodynamic coefficients, noting that the averaging time is reduced in the CFD investigation ($\approx 1\,\mathrm{s}$) compared to PIV and balance measurements ($\approx 30\,\mathrm{s}$ and $20\,\mathrm{s}$, respectively). Still, the CFD averaging time is large enough to cover all occurring flow instabilities.

5.3.1 Flow Field at Pre Stall

The 3D surfaces described by $u_{\mathrm{avg}}/U_\infty = 0.2$, 0.5 and 1.5 and the cross sectional helicity distribution are presented in Figure 5.41 for the pre-stall flow field. The computations (cf. Figure 5.41b and d) overestimate the TKE during breakdown. In addition, the breakdown location is situated farther downstream than in the measured flow field (see Table 5.5). This leads to the underestimation of the pitching moment coefficients in both cases (see Figure 5.55). In addition, the breakdown process is more sudden, i.e. the core cross section grows more abruptly in the computational environment. Despite a delayed breakdown, both computed flow fields predict the the correct flow behaviour.

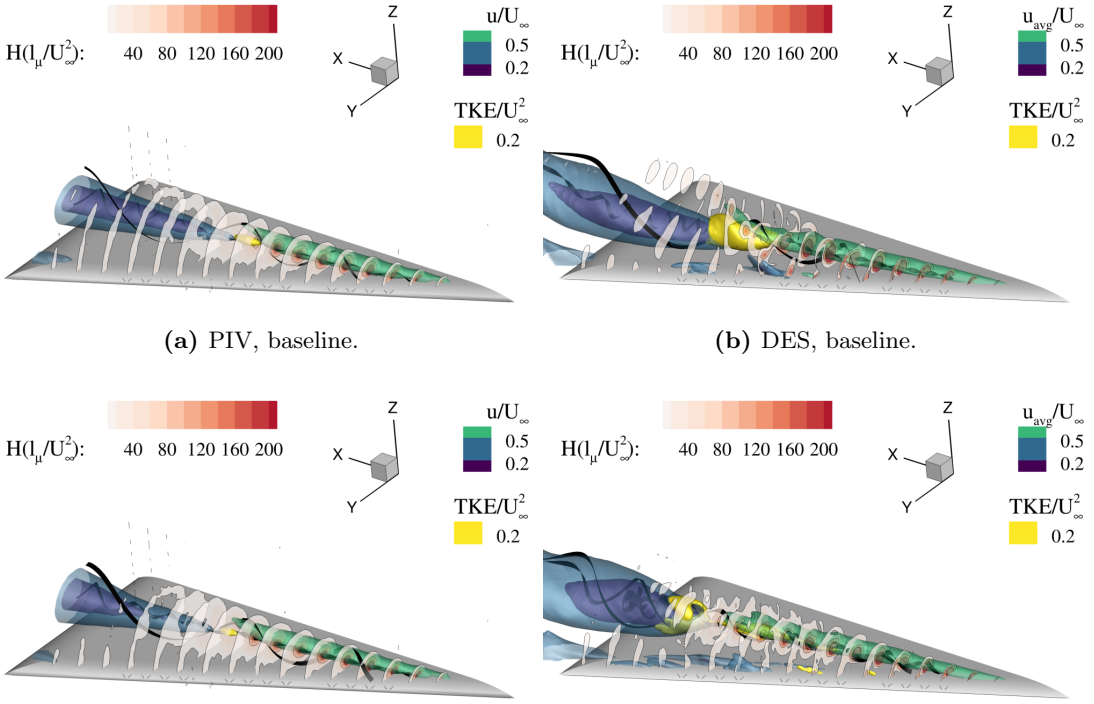

(a) PIV, baseline. **(b)** DES, baseline.

(c) PIV, $F^+ = 2.6$. **(d)** DES, $F^+ = 2.6$..

Figure 5.41: Flow field of the VFE-2 delta wing at $\alpha = 35°$, $Re = 0.5 \cdot 10^6$.

Table 5.5: Method dependent chordwise breakdown location at $\alpha = 23°$, $Re = 1.0 \cdot 10^6$.

x/c_r	Baseline	Actuated
PIV	0.55	0.58
DES	0.66	0.76

The computations show even in the averaged field a transient character, which is attributed to a significantly shorter averaging period of the field quantities than in the experimental approach. This leads to detection of secondary structures, like quasi-stationary discrete vortices, that spiral around the vortex, visible only in the baseline case (Figure 5.41b). This steady vortex' origin coincides with the longitudinal breakdown position, where the axial pressure gradient increases locally and causes vortex wall detachment. The perturbations in the actuated case destabilize steady shear-layer vortices (Figure 5.41d).

In Figure 5.42, smoke visualisations of the vortex core at two random camera recordings indicates breakdown by abrupt core expansion. Between these recordings the breakdown location deviates by roughly $0.1c_r$. This deviation is observed, as well, by comparing computations and experiments at $\alpha = 23°$, which is consistent in both cases, baseline and actuated. Because DES solves one time frame of the transient flow, a more downstream breakdown with respect to the mean measured breakdown location is very likely to occur.

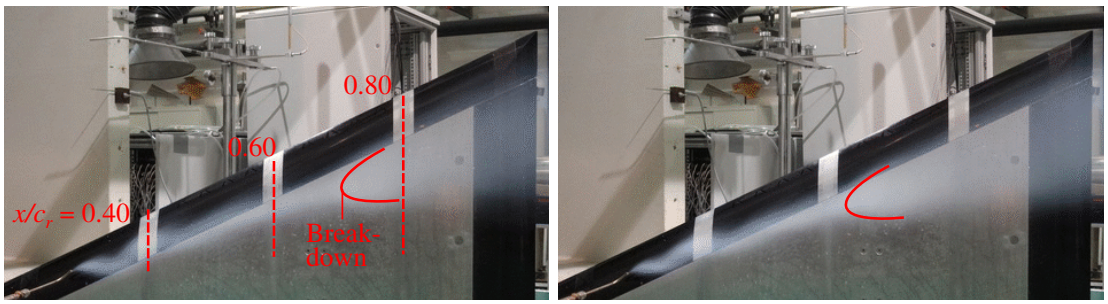

Figure 5.42: Breakdown at $\alpha = 23°$ visualised by smoke.

Figure 5.43 shows the measurement plane cutting horizontally along the vortex core capturing the breakdown phenomenon. Instantaneous out-of-plane vorticity distributions are compared between PIV (Figure 5.43a) and DES (Figure 5.43b). Because, breakdown is predicted farther downstream, the DES plane investigated is shifted by $\Delta x/c_r = \Delta y/s = 0.1$ in positive direction with respect to the presented PIV planes.

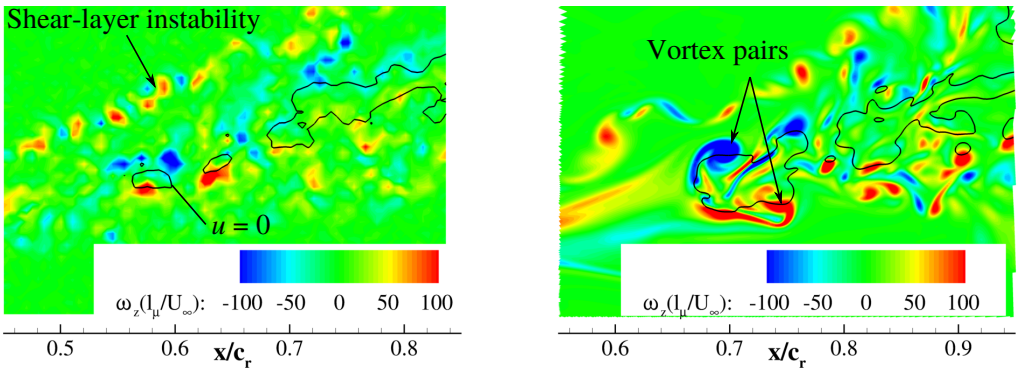

(a) PIV. **(b)** DES.

Figure 5.43: Z-vorticity distribution in axial plane along the vortex core at $\alpha = 23°$, baseline.

The distributions of $\omega_z(l_\mu/U_\infty)$ depict increased number of azimuthal vorticity peaks in the breakdown wake. Hence, breakdown deflects the vorticity vector from axial to azimuthal direction. The wake flow contains random reversed flow regions, enclosed by $u = 0$ isolines in Figure 5.43 between two pairs of counter-rotating fluid regions (vortices) inducing local flow reversal. The wake vortices describe a certain pairing and downstream convection along a conical path. The shear layer is as well dominated by alternating peaks and valleys of ω_z, suggesting discrete vortex generation through shear-layer instabilities, i.e. Kelvin–Helmholtz instability.

The numerical results depict a more abrupt breakdown. Within this process regions of positive and negative out-of-plane vorticity evolve around the primary stagnation point. Downstream, flow asymmetries indicate the precsence of a quasi-helical structure that dissipates downstream.

5.3.2 Flow Field near Stall

The comparison of DES and PIV results regarding the stall flight condition ($\alpha = 35°$) is presented in Figure 5.44. The separated shear layer, designated by increased helicity, rolls up around the vortex without mass transport into its core. On the contrary, due to the reversed flow in the core, the fluid has to exit the region in radial direction. Important flow regions are designated by couloured isosurfaces: accelerated flow (green, $u_{\text{avg}}/U_\infty = 1.5$), decelerated flow (blue, $u_{\text{avg}}/U_\infty = 0.5$) and reversed flow (violet, $u_{\text{avg}}/U_\infty = 0.0$). The flow accelerates above 1.5 of the freestream velocity in the apex region. Due to a relatively upstream breakdown, the flow decelerates abruptly and changes direction mainly in the core region. The typical conical post breakdown flow dominates the flow field.

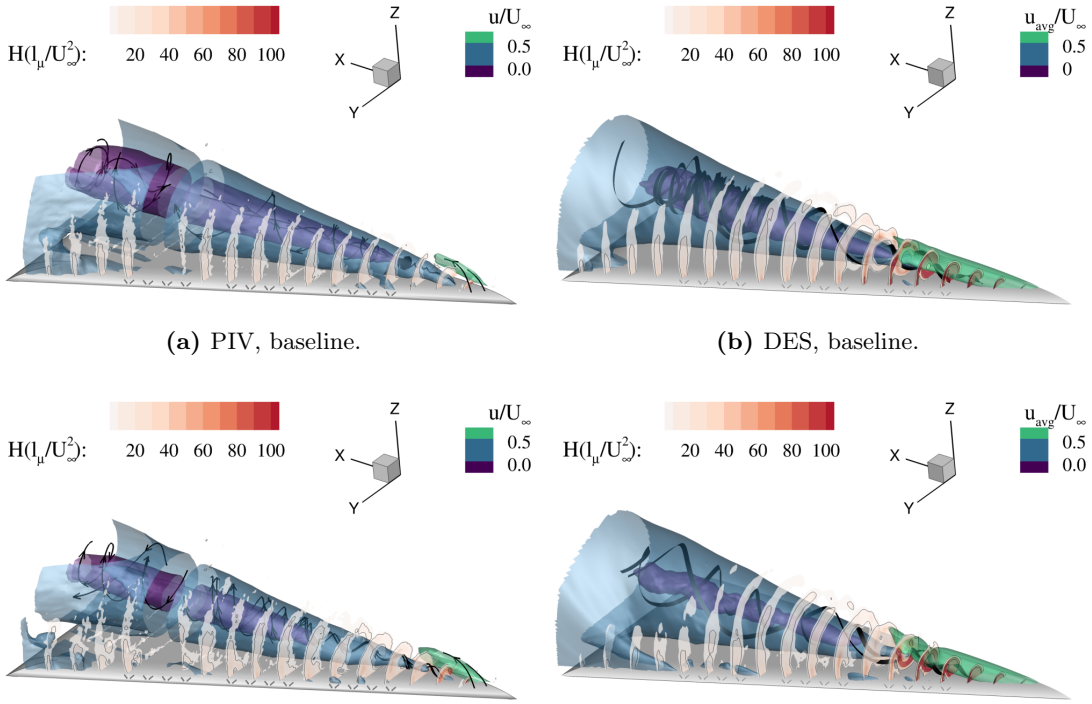

(a) PIV, baseline. **(b)** DES, baseline.

(c) PIV, $F^+ = 2.6$. **(d)** DES, $F^+ = 2.6$..

Figure 5.44: Flow field of the VFE-2 delta wing at $\alpha = 35°$, $Re = 0.5 \cdot 10^6$.

Both analysis methods (experimental and numerical) show the described flow structure, despite the position deviations of breakdown and of the upstream stagnation point (Table. 5.6). The numerical analysis predicts an accelerated flow region at the apex, delaying breakdown and incipient flow reversal with respect to the baseline. Consequently, the apex region, on which the symmetry constriction is dominant, shows main deviations between DES and PIV, which causes the overprediction of aerodynamic coefficients (Figure 5.55) for the unperturbed flow.

Table 5.6: Method dependent location of mean stagnation point at $\alpha = 35°$, $Re = 0.5 \cdot 10^6$.

x/c_r	Baseline	Actuated
PIV	0.24	0.43
DES	0.32	0.45

Around $\alpha_{\max}$, vortex breakdown near the apex distributes the vertical/out-of-plane vorticity along the vortex core according to Figure 5.45. The breakdown region is dominated by dipoles of vertical vorticity along the vortex core upstream of $x/c_r = 0.2$. Under these conditions, the primary vortex and the feeding layer cross-interact ($TKE/U_\infty^2 > 0.15$ in Figure 5.45a and b), clusters of positive vorticity and negative vorticity depart in a conical path around the reversed flow regions, suggesting the formation of the helical-mode instability (c and d).

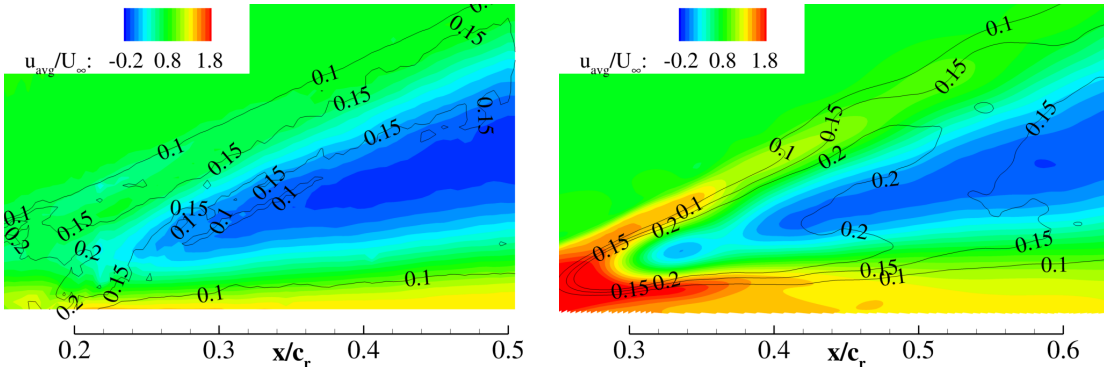

(a) PIV, mean x-velocity.

(b) DES, mean x-velocity.

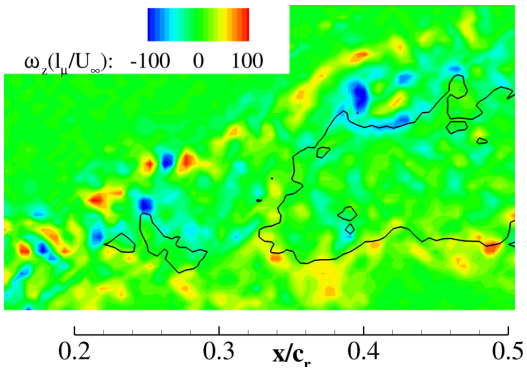

(c) PIV, instant z-vorticity.

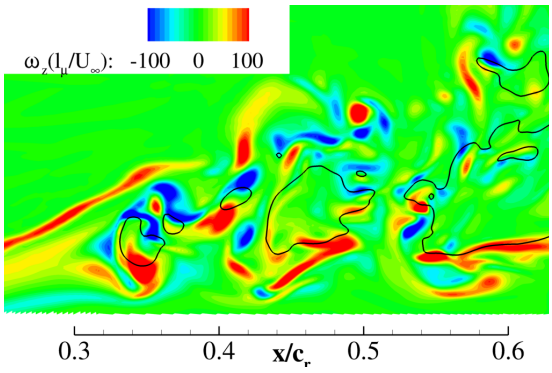

(d) DES, instant z-vorticity.

Figure 5.45: x-velocity and z-vorticity distribution in axial plane along the vortex core at $\alpha = 35°$, baseline.

At both angles of attack $\alpha = 23°$ and 35°, the numerical method predicts a delayed ($\Delta x/c_r = 0.1$) and more sudden breakdown. Prior to breakdown, the computations predict a more stable vortex compared to the measured flow field (i.e. increased core velocities), which explain the delay in breakdown. Downstream, the core flow in both methods decelerate towards similar mean values of u/U_∞, and dimensionless TKE levels in the range $0.10 < TKE/U_\infty^2 < 0.15$ predominate the wake.

Comparing the instantaneous distribution of out-of-plane vorticity between PIV and DES, the numerically predicted breakdown causes a higher core dilatation and wider stagnation regions. In contrast to DES, the core flow in the measurements is unsteady prior to breakdown with low fluctuations along the core with amplitudes of $|\omega_z(l_\mu/U_\infty)| < 50$. DES predicts instead a steady core. Despite the observed differences between experiments and computations that may be due to apex resolution and flow constriction by the symmetric boundary condition in CFD, the vortical unsteady flow field is well predicted.

5.3.3 Flow Field at Post Stall

Figure 5.46 presents the flow field at the highest investigated angle of attack ($\alpha = 45°$), at which wake flow (Figure 5.46a,b) and sustained burst vortex (Figure 5.46c,d) dominate the flow field. The simulations accurately predict the flow structures in both cases, despite the overprediction in aerodynamic coefficients (Fig 5.55).

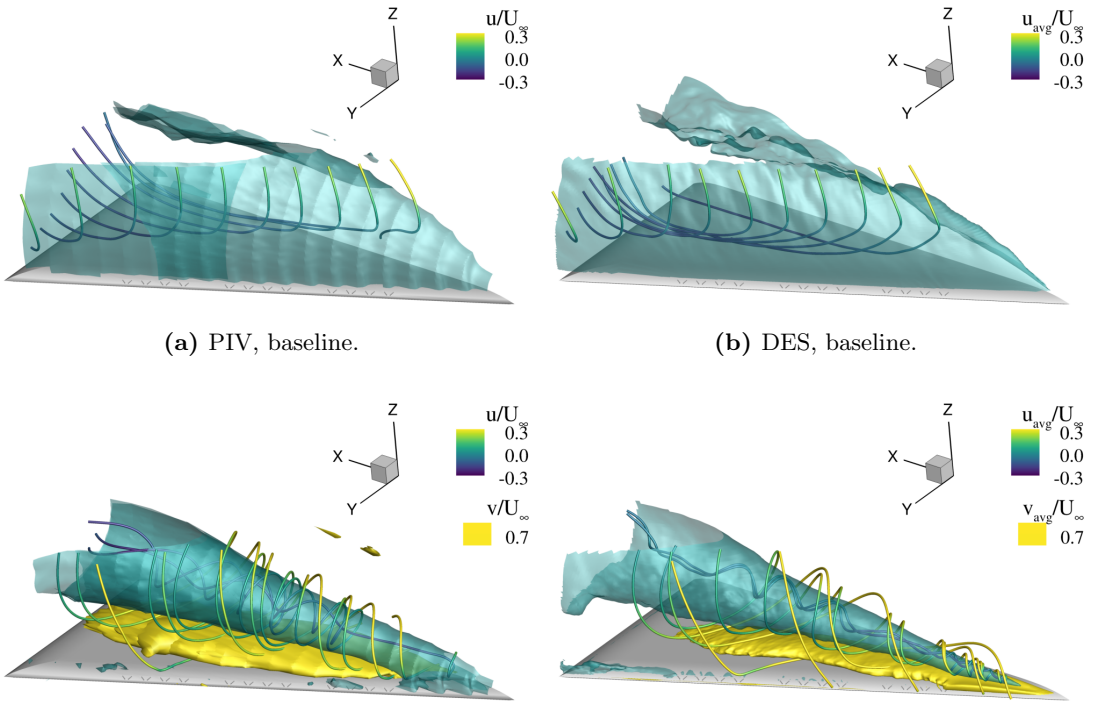

(a) PIV, baseline.

(b) DES, baseline.

(c) PIV, $F^+ = 1.0$.

(d) DES, $F^+ = 1.0$.

Figure 5.46: Flow field of the VFE-2 delta wing at $\alpha = 35°$, $Re = 0.5 \cdot 10^6$.

Figure 5.47 presents the wake-type flow field at $\alpha = 45°$, in which the shear layer is not able to reattach on the wing's upper surface. $TKE/U_\infty^2 > 0.05$ dominates the shear layer, the confluence of the freestream flow, and the reversed low energy flow above the wing. From comparing Figures 5.47a and b, the simulated shear layer requires a longer distance in order to become unstable and initiate discrete vortices generation. The view on the longitudinal plane is shifted relative to the PIV plane by $\Delta x/c_r = \Delta y/s = 0.3$.

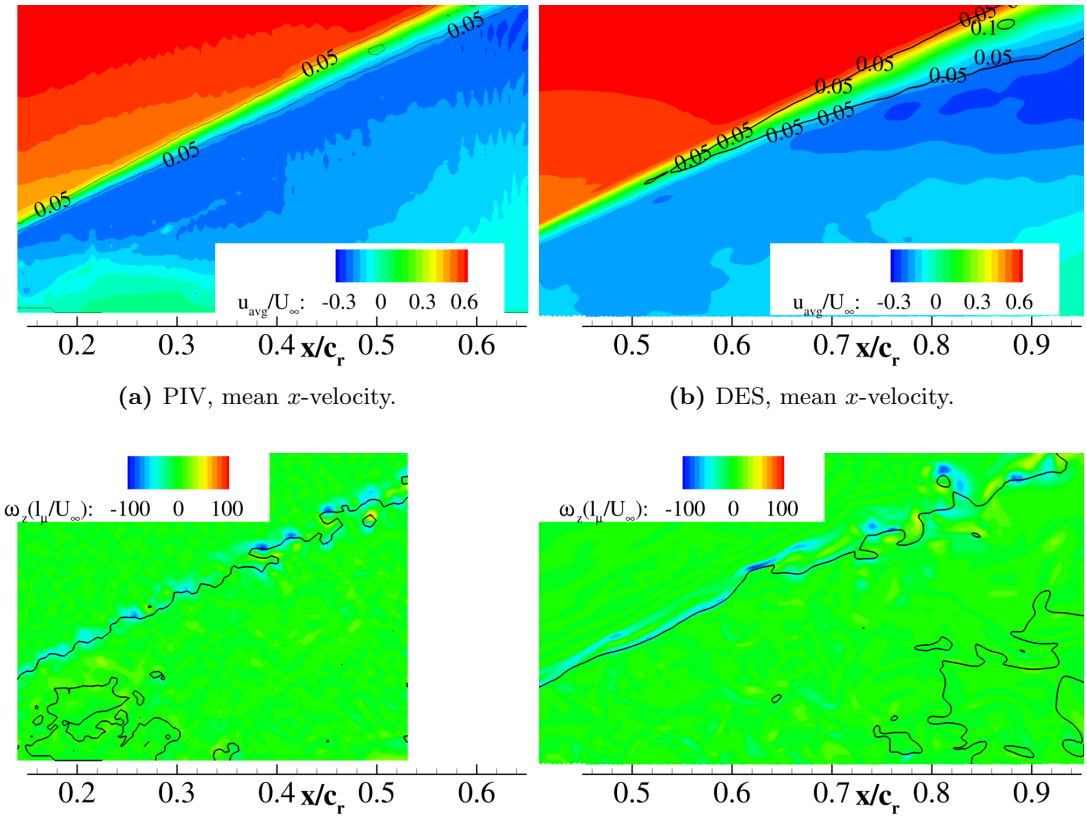

(a) PIV, mean x-velocity.

(b) DES, mean x-velocity.

(c) PIV, instant z-vorticity.

(d) DES, instant z-vorticity.

Figure 5.47: x-velocity and z-vorticity distribution in axial plane along the vortex core at $\alpha = 45°$, baseline.

Due to the shear layer instability, evidenced by the downstream increasing curliness of the isoline $u = 0$ (c and d), discrete vortices with negative vertical vorticity emerge. Similar to the cases discussed previously, the computational baseline flow field at $\alpha = 45°$ describes a more downstream and more accelerated development of shear layer instability compared to the measurements.

5.3.4 Vortex Rotation Axis

As in Section 5.2.1.4, the rotational axis position is presented in Figure 5.48. It compares the numerical with the experimental results, which lie with minor deviations in very good agreement. For all angles of attack investigated, the mentioned deviations refer to a slightly more outboard located primary vortex in the computational environment than the measured position. Furthermore, the computations predict a vortex positioned closer to the wing and also a similar negligible influence of the AFC on its axis position.

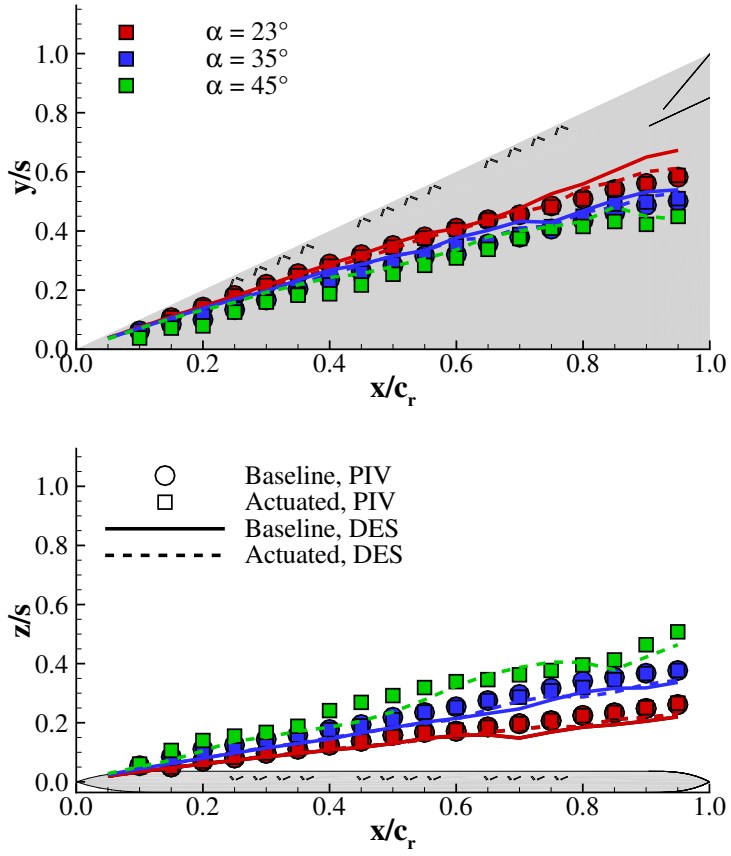

Figure 5.48: Numerical validation of mean vortex axis position.

5.3.5 Pressure Distribution

This section discusses the surface distribution of the computed pressure coefficient in all investigated cases. Figures 5.49– 5.51 compare the experimental average and rms pressure coefficient distributions obtained from steady and usteady pressure ports with the numerical distribution in three chordwise positions $x/c_r = 0.4, 0.6$ and 0.8. The pressure measurement results are obtained from [83].

For all angles of attack investigated and in both baseline and actuated cases, the mean c_p is predicted well. The suction peak in the spanwise distribution correlates with the vortex axis. In the first investigated chord station $x/c_r = 0.40$, computations of the baseline flow slightly overpredict the suction contribution of the secondary vortex (Figures 5.49a and 5.50a). The local difference is that the slots are modelled by wall boundary condition in the computational domain, whereas during the experiments the slots are open. In addition, the influence of the symmetric boundary condition leads to a slight vortex constriction at the apex for stall and post-stall.

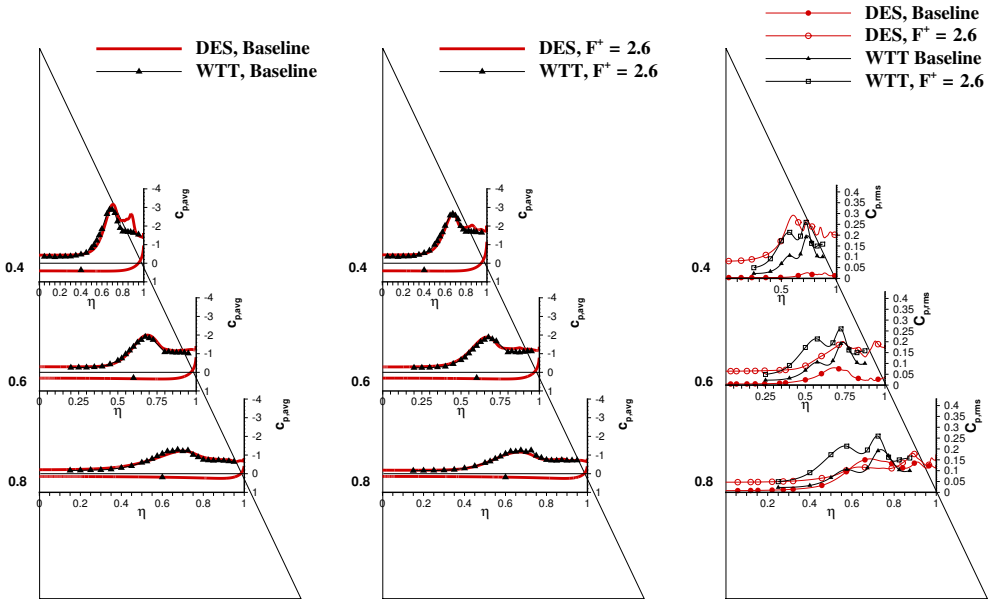

(a) Baseline. **(b)** Actuated. **(c)** RMS.

Figure 5.49: Pressure coefficient distribution in three chord sections at $\alpha = 23°$, $Re = 1.0 \cdot 10^6$.

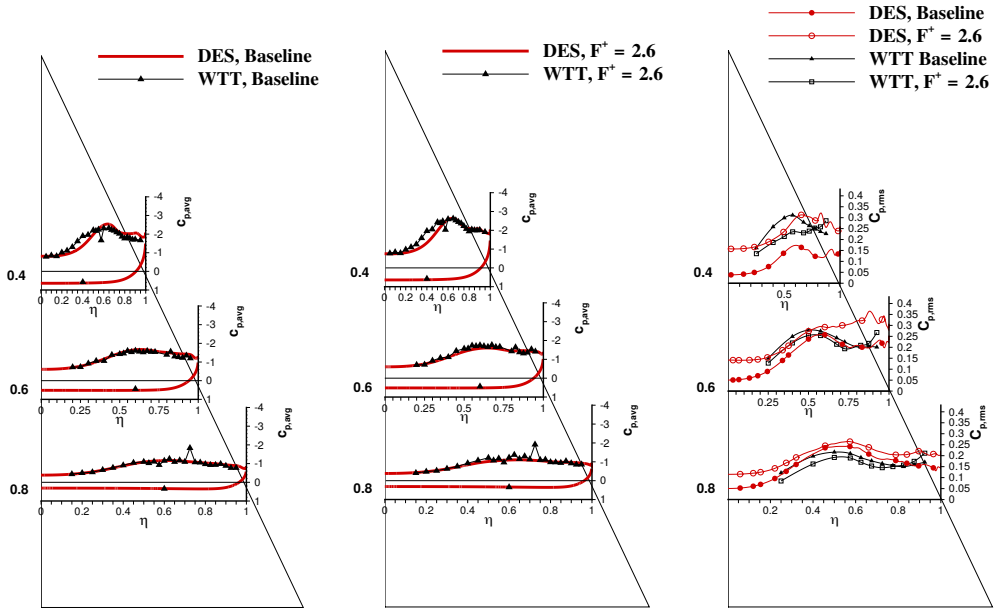

(a) Baseline. **(b)** Actuated. **(c)** RMS.

Figure 5.50: Pressure coefficient distribution in three chord sections at $\alpha = 35°$, $Re = 0.5 \cdot 10^6$.

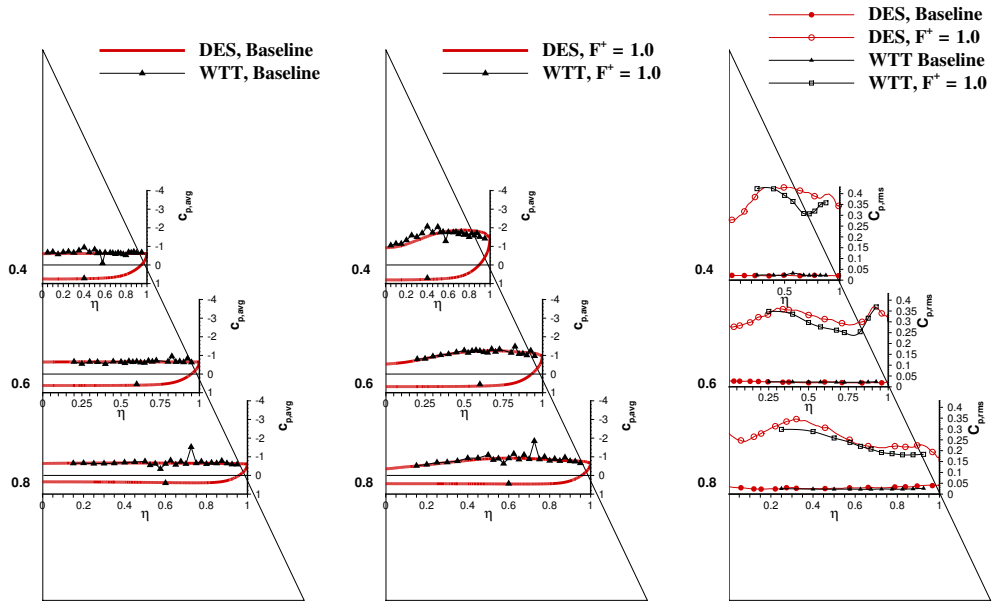

(a) Baseline. **(b)** Actuated. **(c)** RMS.

Figure 5.51: Pressure coefficient distribution in three chord sections at $\alpha = 45°$, $Re = 0.5 \cdot 10^6$.

The time-accurate surface pressure measurements with a sampling rate of 3 kHz and a cut-off frequency of 1 kHz) were post-processed to obtain $c_{p,\mathrm{rms}}$. The measurements where conducted over a 10 s period [82, 83]. Highest deviations between the DES and WTT rms pressure distribution are observed in the pre-stall case (Figure 5.49c). The natural vortex generates no significant fluctuating load at $x/c_r = 0.4$. Downstream pressure rms increases, as the vortex bursts, and converges to the measured values.

In the computational environment, AFC increases the pressure fluctuations. At the apex region computational surface pressure fluctuations are greater than experimental. However, the computations predict a faster downstream $c_{p,\mathrm{rms}}$ decay, and the vanishing of the second inboard rms maximum.

In Figure 5.50c, the measured pressure fluctuations recorded at $\alpha = 35°$ diminish with blowing. However, higher fluctuations reign in the vicinity of the blowing segments. At $x/c_r = 0.40$, the baseline $c_{p,\mathrm{rms}}$-distribution shows a distinct peak, which almost disappears when blowing is active. In contrast to the measurements, the computations at $\alpha = 35°$ predict little increase of pressure fluctuations with active blowing.

A constant mean suction level and low fluctuations represent the completely separated flow at $\alpha = 45°$ (cf. Figure 5.51). Shear-layer reattachment and, thus, the presence of a sustained vortex by the pulsating leading-edge jets causes an increase in suction with flat peaks at a local span of $s(x) \approx 60\%$ (Figure 5.51b). The pressure coefficient rms increases by approximately one order of magnitude (Figure 5.51c). Its spanwise distribution has peaks farther inboard, at around $s(x) = 30\%$, close to the reattachment line. Both mean and rms values of the pressure coefficient decrease chordwise, related to the vortex expansion. At the leading edge, local rms peaks are present in the first two investigated chord stations.

Figures 5.52–5.54 show the upper surface distributions of the baseline average pressure coefficient $c_{p,\mathrm{avg}}$ and the difference due to blowing $\Delta c_{p,\mathrm{avg}}$. The pressure difference due to blowing is expressed as:

$$\Delta c_p = c_{p,\mathrm{Actuated}} - c_{p,\mathrm{Baseline}}. \tag{5.6}$$

At $\alpha = 23°$, the pressure coefficient distribution with additional mean wall friction lines identify the primary reattachment line and the secondary separation line, leading to the secondary vortex with opposite rotation direction (cf. Figure 5.52a). A tertiary structure is also observed, though with a very small diameter, as discussed also in [10].

According to the differential plot in Figure 5.52b, leading-edge pulsed blowing reduces suction close to the secondary and tertiary separation lines with respect to the baseline case. The red regions reveal increased pressure zones relative to baseline. Along the vortex core at the chord station ranges, where blowing segments are located, the overpressure reveals oscillations or local peaks.

Inboard, the actuated case has regions of higher suction than the the baseline case. The pressure alteration described, demonstrates that both marked lines are shifted slightly inboard as effect of blowing. Despite this observation, the primary vortex core is stationary (cf. Figure 5.48). Furthermore, the mean pressure rises upstream of the segments and decreases downstream. Jet activity correlate with high suction around the blowing slots and degradation of the secondary structure (cf. Section 5.4).

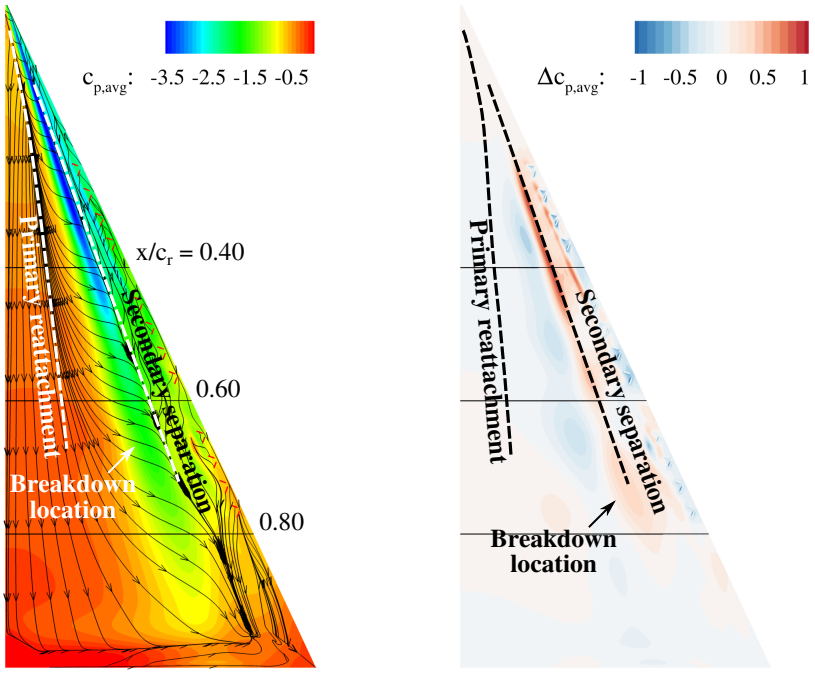

(a) Baseline. **(b)** Difference.

Figure 5.52: Average pressure coefficient distribution on the upper surface at $\alpha = 23°$.

Vortex breakdown at the apex generates the average pressure distribution as shown in Figure 5.53a. The highest rear loading of the wing compared to other angles of attack is evident: high suction at the apex followed by breakdown, which increases the pressure downstream. At this incidence, the computations predict increased pressure below the core followed by pressure decreasing downstream and increasing again (cf. Figure 5.53b). This indicates that breakdown is delayed, however, less suction is produced than the baseline case, accountable for the reduced aerodynamic coefficients (Figure 5.55). The pressure increase below the vortex core indicates local flow deceleration caused by pulsed blowing disturbing locally the flow. The contrary is observed from the experimental investigations on the distributed and integrated mean loading, in which the suction increases slightly in the forward wing half owed to pulsed blowing [83].

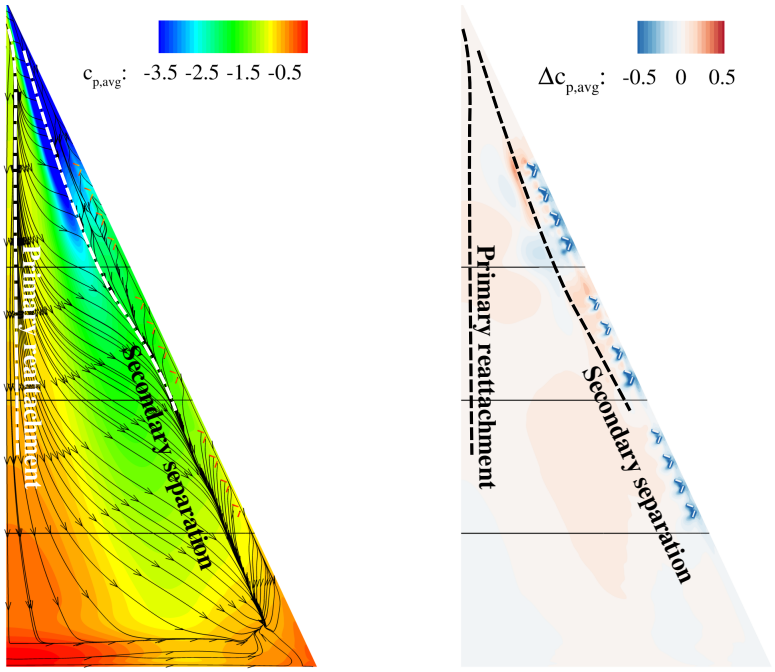

(a) Baseline, average. **(b)** Difference.

Figure 5.53: Average pressure coefficient distribution on the upper surface at $\alpha = 35°$.

At post-stall, pulsed blowing changes the flow field from a wake flow (Figure 5.54a) to a sustained large scale vortex, as suggested by the differential pressure distribution (Figure 5.54b). The periodic blowing triggers discrete vortices that enhances the mixing of the outer flow with the recirculation region. The additional impulse through fluid injection increases the circumferential velocity. The region with high pressure fluctuations is located between the reattachment line (which coincides with the symmetry line) and the vortex axis. The transport of discrete structures towards the wing's surface is responsible for this increase, which describes the typical pressure distribution of a burst vortex.

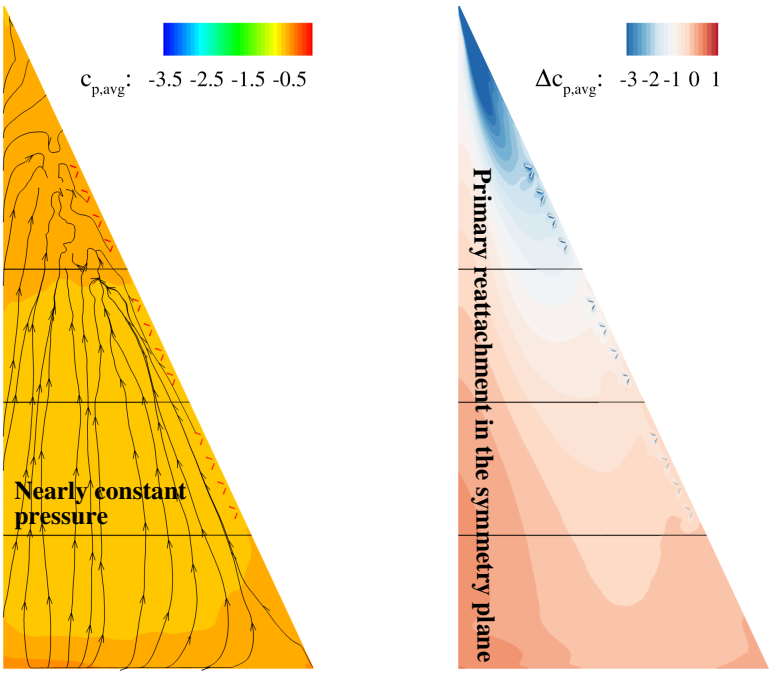

(a) Baseline, average. **(b)** Difference.

Figure 5.54: Average pressure coefficient distribution on the upper surface at $\alpha = 45°$.

5.3.6 Aerodynamic Coefficients

For each case, lift/drag and pitching moment coefficients (C_L, C_D and C_{MY}) are discussed. For validation purposes, Figure 5.55 compares the CFD against WTT results. Lift C_L (top graph and symbols) and pitching moment coefficient C_{MY} (middle) share the same axis on the left hand side, and the axis of the drag coefficient C_D (bottom) is positioned on the right hand side. The coefficients are plotted as function of angle of attack in the range around stall $22° \leq \alpha \leq 50°$.

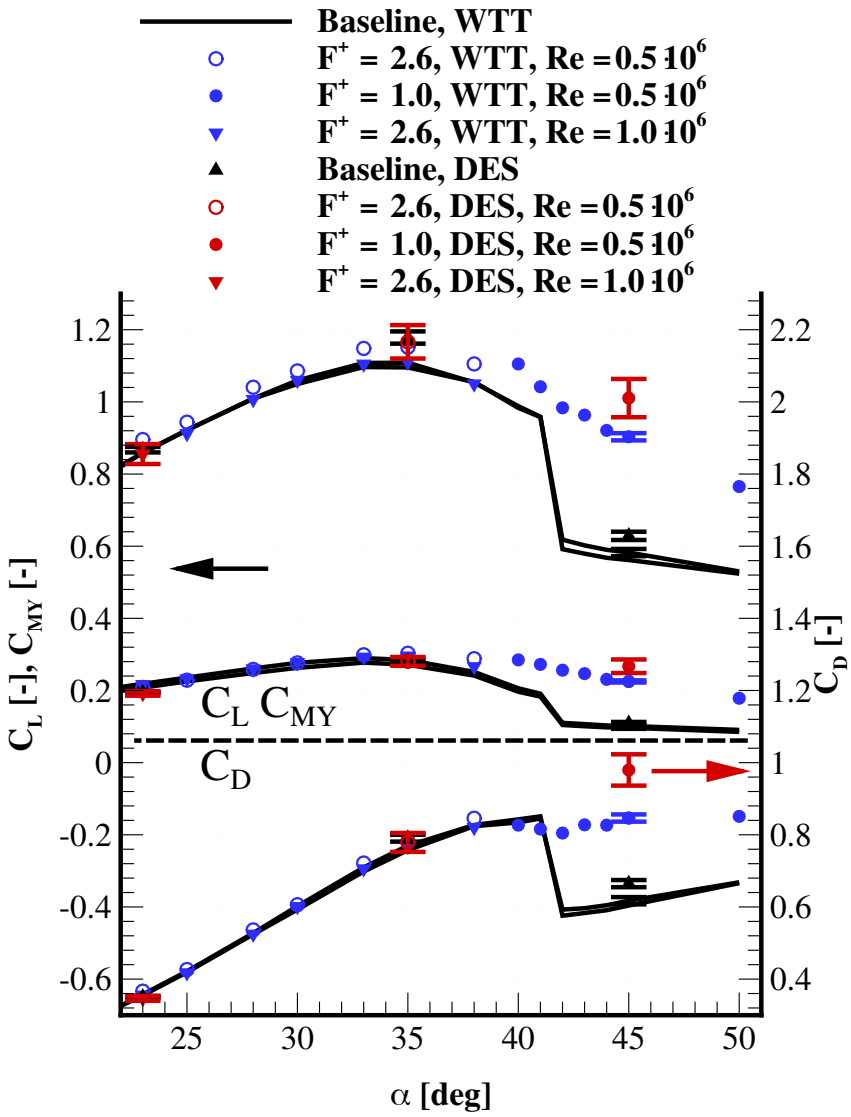

Figure 5.55: Lift, drag and pitching moment coefficients as function of angle of attack, actuation mode and method DES/WTT.

Measurement data for other angles of attack than those investigated numerically are included in the graphs, represented by black lines (baseline) and blue symbols (actuated). For the entire α range investigated, the measurement accuracy is within the error bars plotted at $\alpha = 45°$ (see Section 3.3.1).

The computed aerodynamic coefficients of the baseline and the actuated cases are represented by black delta symbols and red symbols, respectively. The bars of the computed coefficients indicate the rms values of each coefficient, resulting from the statistics over the total simulated time (Table 4.5).

Without actuation, discontinuities in all three measured polars (black lines) are present beyond stall, at $\alpha = 41° - 42°$, which are caused by the vortex collapse. Both investigation methods, DES and WTT, demonstrate that pulsed blowing has a relative minor effect on the coefficients prior to stall $22 \leq \alpha \leq 35°$, but a significant one at post-stall $\alpha > 35°$.

DES predicts well the aerodynamic coefficients at $\alpha = 23°$ but overestimates those at $\alpha = 35°$ and 45°. Pulsed blowing does not affect the coefficients at the lowest incidence investigated, at which the computations and measurements are in good agreement. However, at the highest angles of attack investigated, the simulations overpredict the aerodynamic coefficients. Contrary to the WTT, in which an increase in C_L, C_D and C_{MY} is measured at $\alpha = 35°$ as an effect of pulsed blowing, DES predicts the inverse effect, a minor degradation of the coefficients.

5.3.7 Synthesis

The current section offeres a comparison between the numerical and experimental investigation methods with the scope of cross-validation. Despite the differences highlighted below, both methods agree quite well. The DES is able to predict also the AFC effects on the flow field. Therefore, the subsequent transient analysis is based mainly on the DES results.

The computations predict a delayed breakdown location compared to the PIV results and a too stable pre-breakdown vortex core followed by a high-TKE region, which is overpredicted in the computational environment.

Modelling a symmetrical boundary condition reduced significantly the computational effort, however, constricted the apex flow (secondary importance in this analysis and reduced measurement data/spacing), where the deviations between DES and PIV are greater than in the rest of the domain.

The location of the vortex axis correlates with minima in the spanwise distribution of surface pressure minima. This is in good agreement for all investigated cases. Pressure fluctuations and downstream decay are higher in DES.

The spread between measured and computed coefficients of lift, drag and pitching moment increases with the angle of attack. As a result, the coefficients at the highest angle of attack are overpredicted. The deviations between WTT and DES can be related to: disconsideration of the influence of the model on the wind-tunnel open-test-section conditions and the increase of unsteadiness with the angle of attack.

5.4 Transient Flow Field

After discussing the averaged and phase-averaged 3D flow field, this section provides the discussion of the instant flow field based on DES results. Equal attention is given to all cases: $\alpha = 23°$, 35° and 45°, with inactive and active blowing. For the actuated cases, the presented time steps represent the end of a blowing period. The following discussion is based on instantaneous 3D flow visualisation. For this purpose, instant streamlines and vortex cores (see Section 4.4.2) are extracted and analysed.

5.4.1 Pre Stall

Figure 5.56 shows the breakdown flow field: high velocity swirling flow, which breaks down, expands and reverses locally. In the vortex core, high suction is generated. Breakdown causes pressure increase downstream and, consequently, core expansion. The isosurfaces, in Figure 5.56b, reveal the existence of a stable and unstable region, separated by the breakdown. Above the front wing part, the core of the primary structure with high suction and swirling around it, are two smaller stable vortices. The breakdown instability causes the core to wind downstream and increases the number of quasi random vortices responsible for the high turbulence values in the wake.

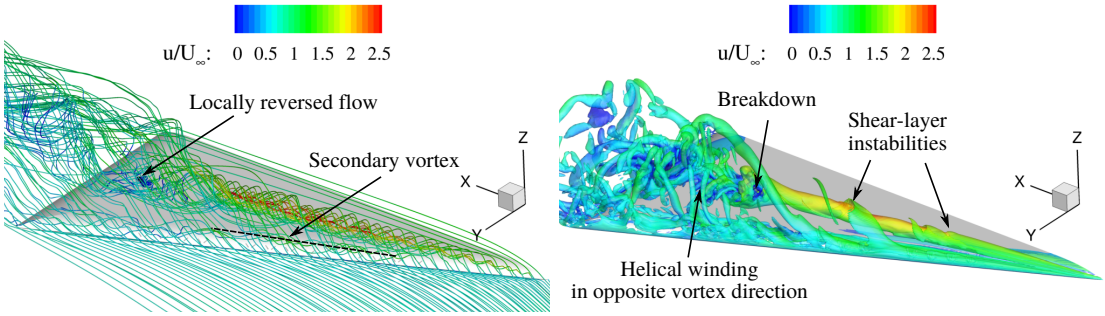

(a) Streamlines. **(b)** Q-criterion of $Q = 10^6\,\mathrm{s}^{-2}$.

Figure 5.56: DES instantaneous baseline flow field at $\alpha = 23°$.

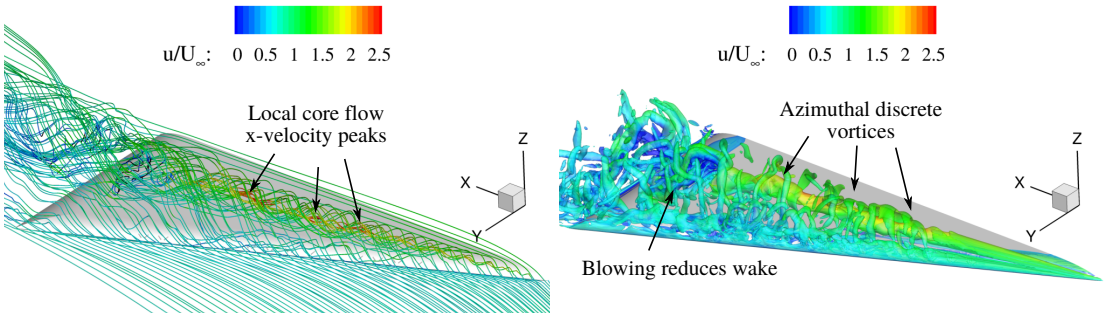

(a) Volume streamlines. **(b)** Q-criterion of $Q = 10^6\,\mathrm{s}^{-2}$.

Figure 5.57: DES instantaneous actuated flow field at $\alpha = 23°$.

As demonstrated on the averaged flow field, the periodic blowing has relative minor effects on the instant flow field. Streamlines in Figure 5.57a reveal the destabilisation of the secondary vortex, breakdown delay and heterogeneous axial velocity maxima along the primary vortex core.

The unsteady jets generate discrete vortices oriented in azimuthal direction. In Figure 5.57b, these small structures are wrapped around the primary vortex, even at the end of the blowing cycle, stabilising the primary vortex.

5.4.2 Near Stall

At $\alpha = 35°$, breakdown at the apex constitutes the baseline flow field, as indicated by the instantaneous flow field in Figure 5.58. Accelerated flow is dominant in the apex region. Streamlines released from the leading edge are entrained by the vortex and accelerate around the reversed core flow (Figure 5.58a). The isosurfaces defined by $Q = 10^6\,\mathrm{s}^{-2}$ reveal the core of the primary structure and secondary structures, shed from the leading edge and in the wake of breakdown (Figure 5.58b). Downstream of the breakdown point, the primary vortex develops downstream in a helical path with opposite winding compared to the main vorticity direction. Farther downstream, turbulence increases and the core dissipates in small quasi-random structures. There is no evidence of a stable secondary structure.

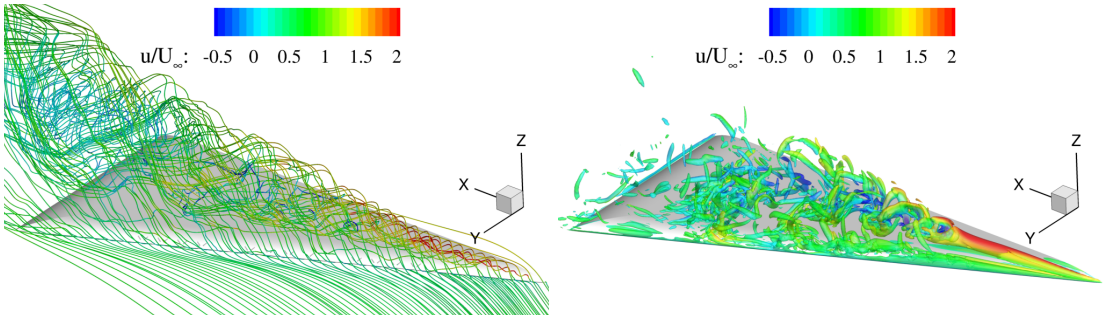

(a) Instant stream lines. **(b)** Q-criterion of $Q = 10^5\,\mathrm{s}^{-2}$.

Figure 5.58: DES instant baseline flow field at $\alpha = 35°$, $Re = 0.5 \cdot 10^6$.

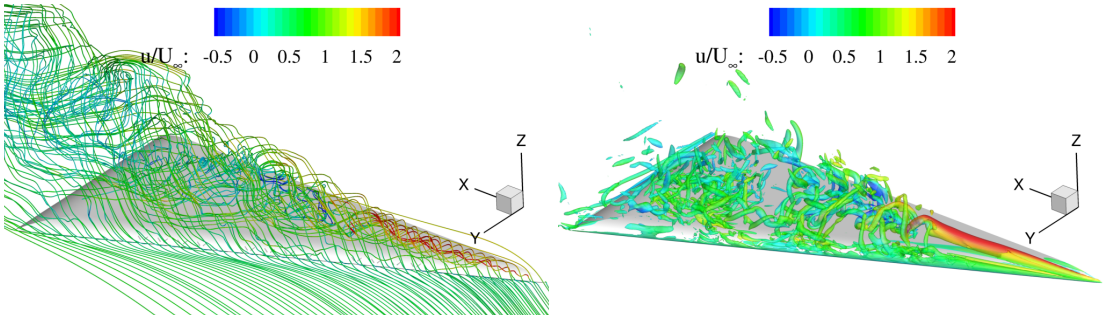

(a) Instant stream lines. **(b)** Q-criterion of $Q = 10^6\,\mathrm{s}^{-2}$.

Figure 5.59: DES instantaneous actuated flow field at $\alpha = 35°$.

Streamlines in Figure 5.59a reveal a more increased swirling motion as opposed to the unperturbed flow. As the time step shown is the final time step during the final blowing cycle, the blowing effect is still present. The reordering of the flow and the stabilising effect comes from vortices circling around the primary vortex core, as concluded as well at $\alpha = 23°$.

As presented in Figure 5.59b, pulsed blowing has a strong upstream effect, which shifts the breakdown location farther downstream compared to the baseline case. The helical structure in the wake is maintained. In contrast to the baseline flow, the shear-layer vortices tilt in the circumferential direction due to the induced disturbances.

Figure 5.60 presents vortex cores of the equal time steps shown above by alternative methods: the λ_2-criterion and the relative total-pressure loss (caused by increased dissipation in the vortex core). The stable core breaks down causing the helix shape twisting in opposite direction of the flow. After two twist, the core dissipates into turbulence. The total pressure loss shows a same twisting of the core. However, for the baseline flow, total pressure loss shows a combination of bubble and helix type breakdown.

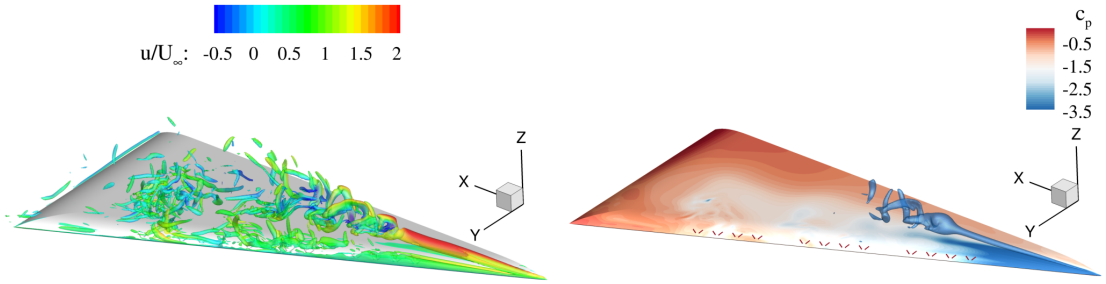

(a) Baseline, $\lambda_2 = -10^6$ 1/s^2. **(b)** Baseline, $\frac{p_{t,\infty} - p_t}{p_{t,\infty}} = 99.6\%$.

Figure 5.60: DES instantaneous vortex cores at $\alpha = 35°$, $Re = 0.5 \cdot 10^6$. Baseline.

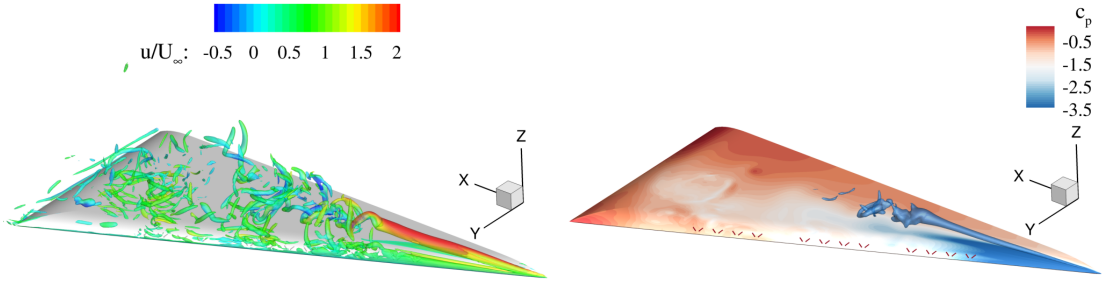

(a) $F^+ = 2.6$, $\lambda_2 = -10^6$ 1/s^2. **(b)** $F^+ = 2.6$, $\frac{p_{t,\infty} - p_t}{p_{t,\infty}} = 99.6\%$.

Figure 5.61: DES instantaneous vortex cores at $\alpha = 35°$, $Re = 0.5 \cdot 10^6$. $F^+ = 2.6$.

In contrast to the baseline flow, the perturbed flow reveals a pure spiral-type breakdown (cf. Figure 5.61). Additionally, the blowing affects the leading-edge shedding process. Above the blowing segments, cross flow ring shaped vortices rotate around the primary vortex. These transport free stream flow into low energy core, increasing axial velocity.

5.4.3 Post Stall

Figure 5.62 presents the wake flow during post-stall at the final time step. The flow from the lower side separates without reattachment above the wing. Instead, massive recirculating flow predominates. The shear layer is unstable and sheds vortices that are transported downstream. Isotropic turbulence is present above the upper wing side.

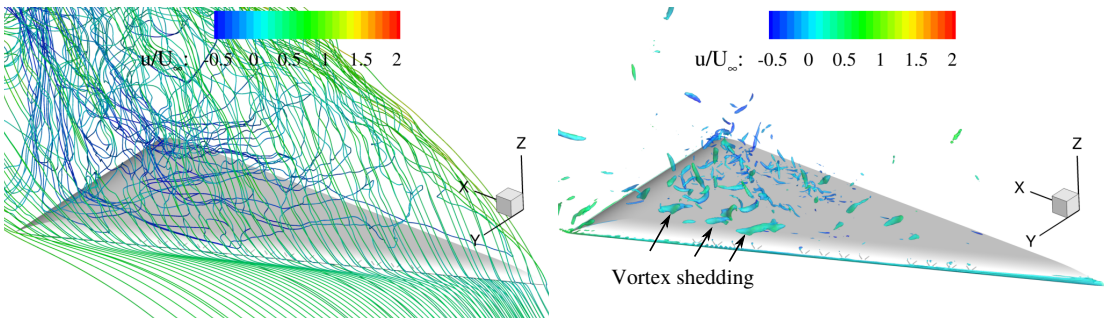

(a) Streamlines. **(b)** Q-criterion of $Q = 10^6\,\mathrm{s}^{-2}$.

Figure 5.62: DES instantaneous baseline flow field at $\alpha = 45°$.

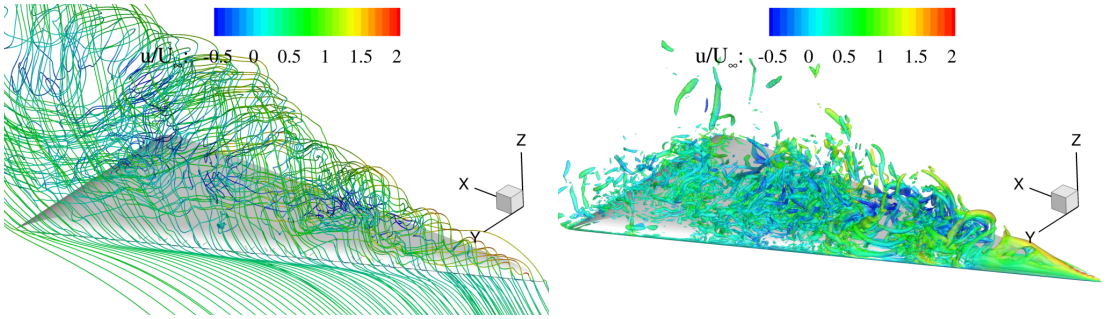

(a) Instant stream lines. **(b)** Q-criterion of $Q = 10^5\,\mathrm{s}^{-2}$.

Figure 5.63: DES instantaneous actuated flow field at $\alpha = 45°$.

The blowing shows its biggest effect at this extremely high angle of attack by reattaching the shear layer on the wing's upper surface. This contributes to the elimination of the post-stall lift drop. The final time step reveals a burst vortex, sustained by pulsating short jet bursts. Instantaneous stream lines and random vortical structures reveal the highly turbulent nature of the flow, as the jets interact with the flow, speeding up the vortex interactions. Similar to the actuated flow field at $\alpha = 35°$ (cf. Figure 5.59), the disturbed core at $\alpha = 45°$ describes a helix with two twists at the breakdown occurring very close to the apex. Both cases also reveal the same orientation of the rotating flow feature.

5.4.4 Synthesis

This subsection complements the investigation by discussing the instantaneous flow field computed by DES at the final computational time step for all cases investigated. For the computations with no blowing (baseline), the presented time step is a priori, while, for the cases with AFC, the time step represents the end of one blowing cycle ($3T/4$ after blowing).

The flow analysis was based on flow streamlines and isosurfaces of the Q-criterion, coloured by the axial velocity. At the lowest angle of attack investigated ($\alpha = 23°$), shear-layer vortices spiral around the unforced primary vortex. At $\alpha = 35°$, the flow field becomes more unsteady, which is related to the increased breakdown wake. At both lower angles of attack, the breakdown type apears to be a combination of bubble and spiral type. Complete separation at post-stall ($45°$) dominates the natural flow field above the wing. Unsteady activity is observed mainly in the shear layer.

Applying pulsed blowing reorders the shear layer vortices, such that ring vortices wrap around the primary vortex core stabilising it and delaying breakdown. At $\alpha = 35°$, the numerical results show no effect of the blowing in the mean pressure distribution (pressure increase). The experiments suggest otherwise. However, both PIV and DES results show the same AFC effect on the flow field, wake reduction and breakdown delay.

At $\alpha = 35°$ and $45°$, each respective final time step of one blowing cycle reveals a pure helix structure with approximately two twists with a universal angular position. Blowing has a strong upstream effect on this flow feature. Its rotation in the main vorticity direction is synchronised with the blowing frequency.

5.5 Disturbance-Flow Interaction

The investigations on the averaged flow-field revealed that there are two distinct AFC effects, the delay of breakdown (at $\alpha = 23°$ and 35°) and the reattachment of the shear layer (45°). For all three angles of attack, subsequent phase-locked investigations concluded that the flow field responds to synchronised pulsed blowing in a similar process, which includes:

1. Shear-layer disruption
2. Generation and growth of shear-layer vortices
3. Vortex clusters spiral in time and space
4. Flow stabilisation and wake/backflow reduction

The vortex detection algorithm and the visualisation of DES results demonstrated, that the macroscopic 3D structure contains discrete small vortices, which influence the vortex-system dynamics by their complex interactions. Based on the above investigations, the current section targets the analysis of the interaction between the disturbance and the flow field by investigating the flow response to blowing within one computed blowing cycle.

5.5.1 Breakdown Delay

When pulsed blowing is applied on the flow field dominated by vortex breakdown with the frequency of the helical mode instability ($F^+ = 2.6$), the average breakdown location shifts downstream and the wake volume is reduced. This section analyses the manipulation of the vortex breakdown at two angles of attack $\alpha = 23°$ and 35°, representing breakdown near the trailing edge and near the apex, respectively.

Figure 5.64 presents phase-averaged velocity records over two blowing cycles. The colour-marked monitor points are located along a ray above the leading edge starting at the origin: $y/s(x) = 1.06$ and $z/s(x) = 0.55$ (cf. Figure 5.64a). The presented graphs of axial and vertical velocities are reduced by the freestream velocity magnitude (which is twice as high for the lowest angle of attack, $U_\infty = 24\,\mathrm{m/s}$).

Despite the difference in freestream velocity, the phase-averaged local response is qualitatively similar for both velocity components investigated. In the most upstream location, at $x/c_r = 0.4$, the highest mean value and fluctuations are present. These decrease steadily downstream above the leading edge as the vortex expands. Vertical velocity at $\alpha = 35°$ is scaled by a factor of two with respect to the 23° case as a consequence of the reduced U_∞ (cf. Figure 5.64b,c).

Throughout one blowing cycle, the upstream monitor point records two distinct peaks (see black curves). Conclusively, the flow responds on average with a second harmonic of the actuation frequency. Downstream, the second peak fades out and a certain phase delay is observed. This demonstrates once again the highly 3D response to a 2D (planar) disruption.

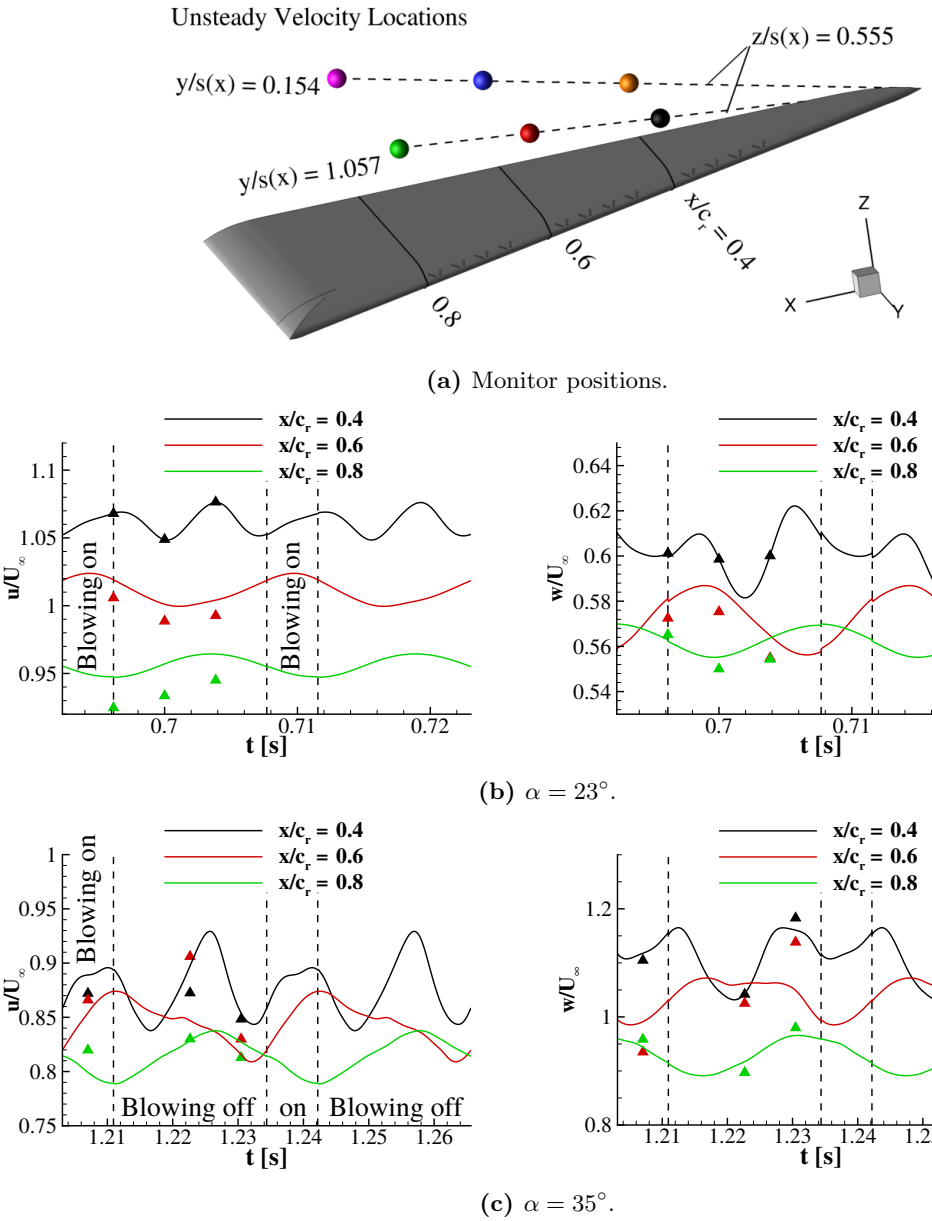

(a) Monitor positions.

(b) $\alpha = 23°$.

(c) $\alpha = 35°$.

Figure 5.64: Phase-averaged recordings of axial/vertical velocity at local coordinates above the leading edge (x/c_r = 0.4 0.6 and 0.8, $z/s(x) = 0.55$, $y/s(x) = 1.06$). Symbols represent the instantaneous values. $F^+ = 2.6$.

The delta symbols in Figure 5.64b represent instantaneous values at the corresponding simulated time steps, which deviate by a small amount from the phase-average trend. In Figure 5.65, the axial velocity distribution in the vortex core plane angled at 6.8° with respect to the wing and the axial vorticity distribution in the crossflow plane at $x/c_r = 0.65$ capture the breakdown flow field corresponding to $\alpha = 23°$.

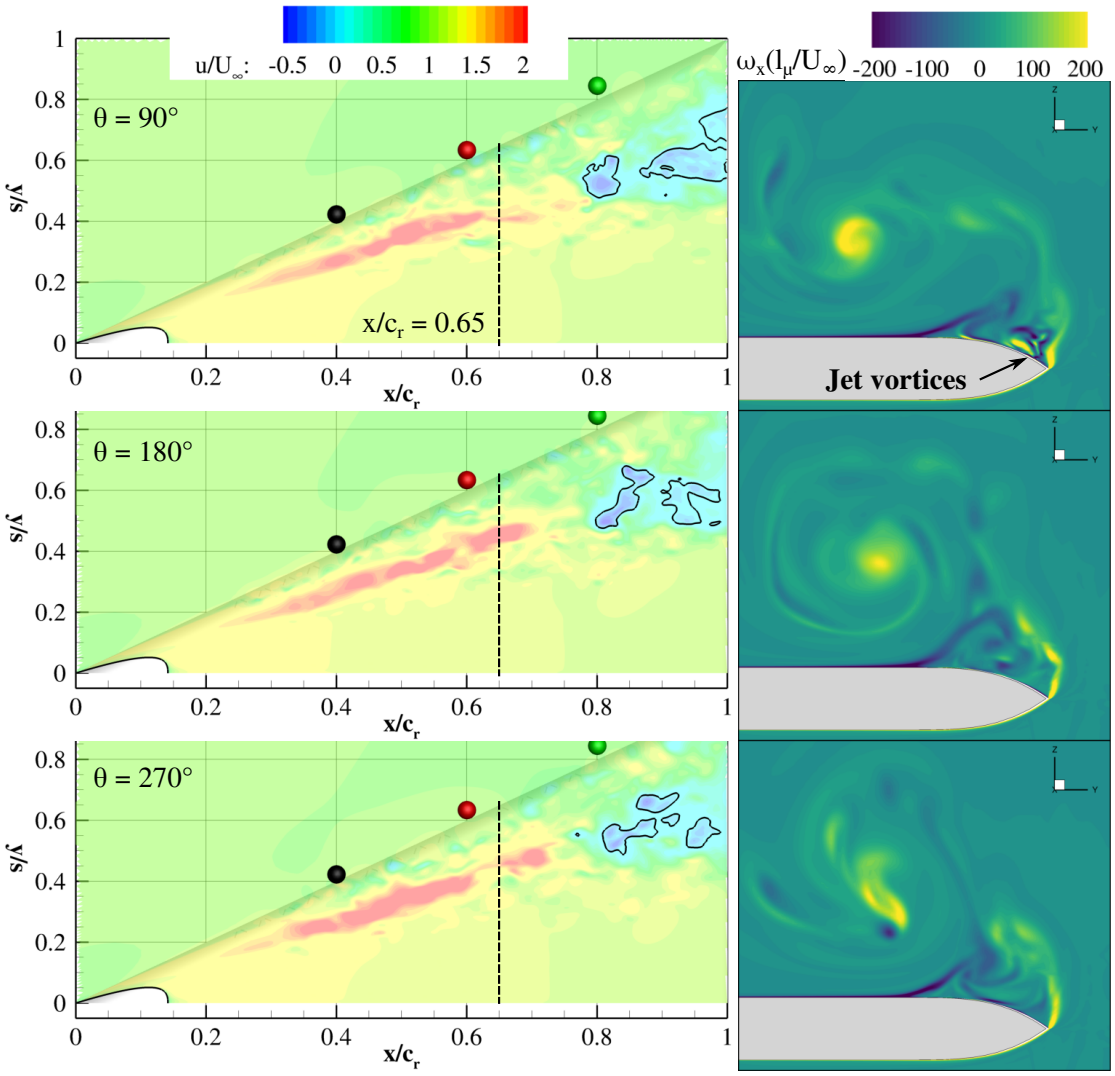

Figure 5.65: Distribution of axial velocity in the core plane (left) and axial vorticity at $x/c_r = 0.65$ at the phases selected ($\theta = 90°$, 180°, 270°). $\alpha = 23°$ and $F^+ = 2.6$.

After 1/4 of the blowing cycle considered (T/4), the jets are switched off and the recuperation phase commences. This moment is captured in the top contour plots (at phase $\theta = 90°$). The vortex core, designated by maximum axial velocity and vorticity, is deflected most inboard. Above the slots, jet vortices are present. The inboard directed jet generates a strong boundary layer vortex that induces the inboard shift of the vortex core.

In the most upstream monitor point, the axial velocity reaches a local peak, while, at $x/c_r = 0.6$, u/U_∞ decreases and at 0.80 reaches a minimum (cf. Figure 5.64b). At blowing cessation, the local vertical component reaches a minimum at $x/c_r = 0.4$, a decreasing trend at 0.6 and increasing trend at 0.8.

The axial distribution in the core plane at the time steps representing phases $\theta = 180°$ and $270°$ reveal a vortex core at its initial position. As demonstrated by the phase-averaged PIV investigations, the vortex flow at this angle of attack is stable enough to quickly converge to the initial state subsequent to the disturbance injection. At $\theta = 270°$ a region of maximum u/U_∞ is detaching from the core. Vorticity contours reveal the same shear layer disruption and rotation in form of vorticity clusters as measured by PIV in Section 5.2.2.

Figure 5.66 shows three time instances designated in the time records of Figure 5.64c by filled delta symbols. The plots at the top represent an instance during the blowing phase, at $\theta = 45°$, while the instances below correspond to the recuperation phase, corresponding to $\theta = 225°$ and $315°$. The view shows a horizontal cut through the vortex core, colour mapping the relative axial velocity distribution and the crossflow vorticity distribution. Black isolines designate $u = 0$.

The pulsating momentum induced in the shear layer is transported around the vortex low energy core. However, an influence of it is visible. Within one blowing period, the core is energized and the stagnation point is shifted downstream. In addition to the downstream displacement of the stagnation point, the jets displace the vortex core in inboard direction. Within the shear layer, regions of alternating velocities are convected downstream along the leading edge. The passing of these high velocity waves are recorded as peaks in Figure 5.64c.

The cross-sectional vorticity distribution for each corresponding phase reveals a strong interaction when the jets are introduced into the flow (right hand side of Figure 5.66). Jets generate waves of vortex pairs above the wing surfaces. Induced by the global structure, these follow the mean flow path outboard. Near the leading edge these vortices disrupt the shear layer, thus generating strong shear layer vortices, measured as well by phase averaged PIV (cf. Section 5.2.2). The vortices spiral downstream and around the core before the subsequent blowing cycle is initiated.

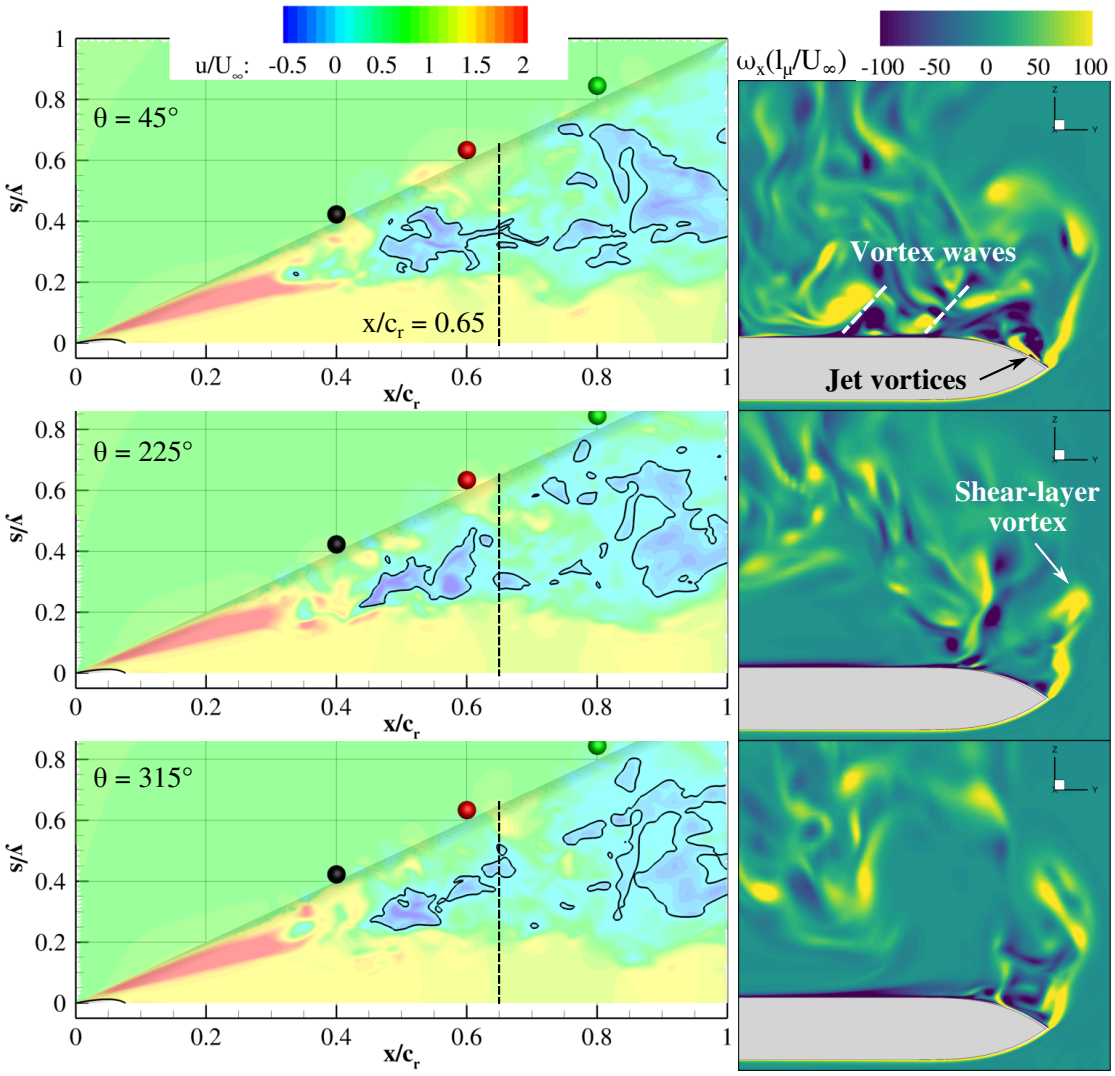

Figure 5.66: Distribution of axial velocity in the core plane (left) and axial vorticity at $x/c_r = 0.65$ at the phases selected ($\theta = 45°$, 225°, 315°). $\alpha = 35°$ and $F^+ = 2.6$.

Figure 5.67 presents the Q-criterion of $Q = 10^5\,\mathrm{s}^{-2}$ coloured by the relative axial velocity in the range $-0.5 \leq u/U_\infty \leq 1.5$ at two instances separated in time by $T/2$. In contrast to the section above, the isosurfaces represent instantaneous cores of weaker vortices, where the Q-criterion is one order of magnitude lower. Hence, the shear-layer vortices appear as well. Both in the baseline (a) and actuated (b) cases, shear-layer vortices detach from the leading edge starting upstream and reveal an orientation opposite to the primary core winding.

As demonstrated above, periodic forcing has little effect on the vortex flow field: delay of the mean stagnation point by about x/c_r and wake reduction. The disturbances interact with the flow field by generating disturbances in form of vortices that enhance the mixing between the shear-layer and the primary structure. Blowing excited merely the shear layer, but affected the whole vortex system with a time delay of $T/2$.

In the left plots of Figure 5.67b, shear-layer vortices spiral around the unsteady primary vortex core. Downstream, waves of vortices designated by dashed lines wind up in the opposite direction compared to the shear layer vortices upstream of breakdown. The disruptions of the shear layer are caused by the discrete jets of the first actuation segment being switched on/off.

The flow field evolves $T/2$ after the perturbation of the shear layer according to the right hand side of Figure 5.67b. At $\theta = 225°$, the perturbations lead to ring vortices around the leading-edge vortex core. This phenomenon stabilises the vortex core and delays breakdown (cf. Figure 5.66).

The numbered vortex clusters are located farther downstream with an increased tilting towards the freestream direction. Consequently, synchronising the jets at the leading-edge generates vortex clusters transporting high axial momentum $u/U_\infty > 1.0$ towards the core in a periodic manner.

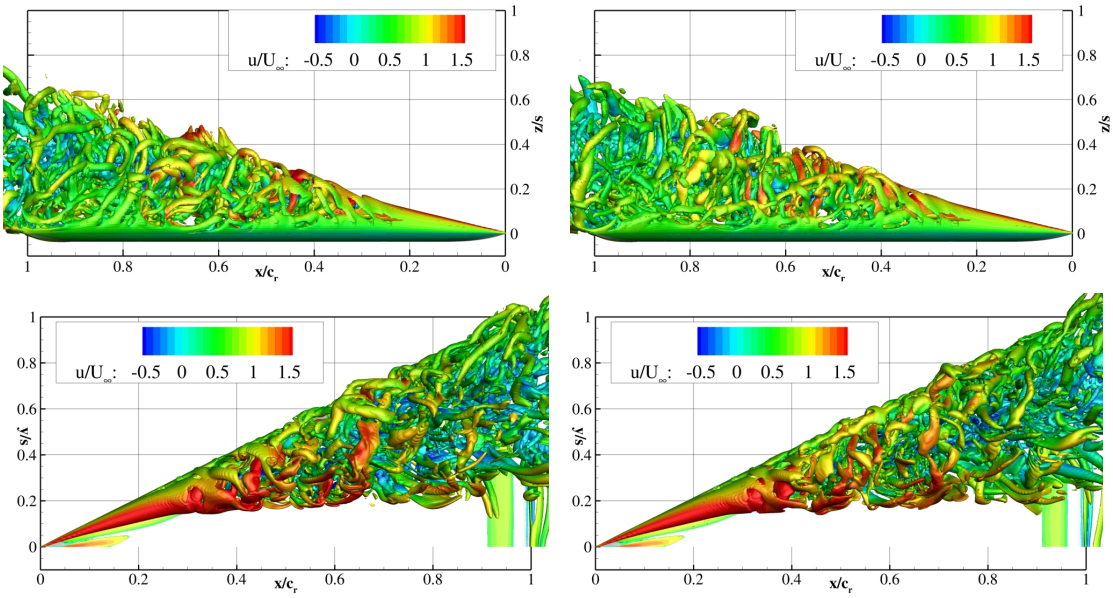

(a) Baseline.

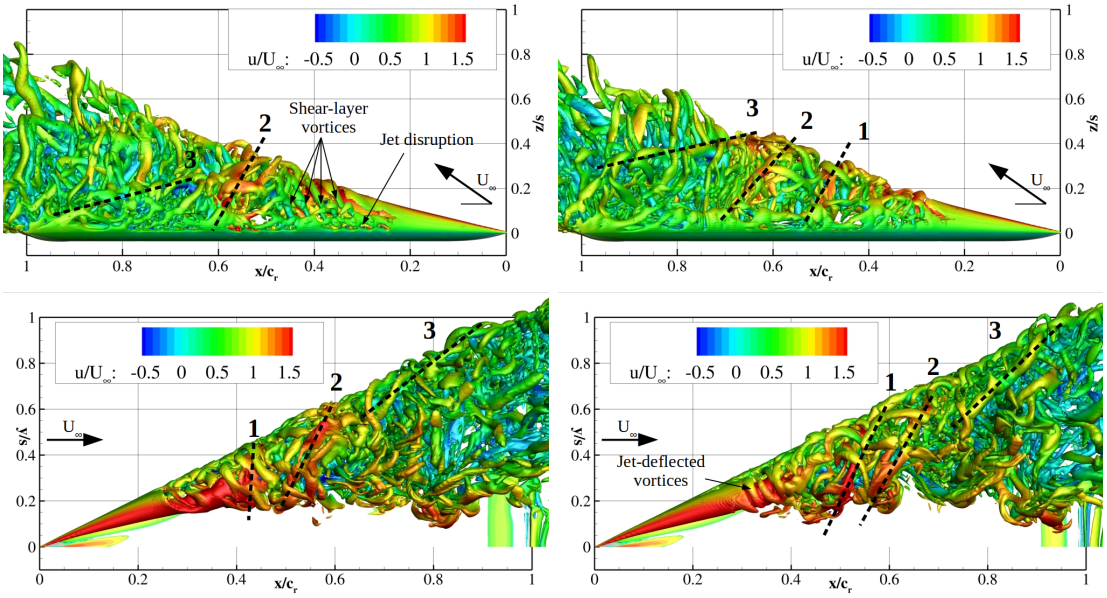

(b) $F^+ = 2.6$, during blowing ($\theta = 45°$, left) and $T/2$ after ($\theta = 225°$, right).

Figure 5.67: Q-criterion $Q = 10^5\,\mathrm{s}^{-2}$, representing two instances separated in by $T/2$. Baseline vs. actuated at $\alpha = 35°$

5.5.2 Shear-Layer Reattachment

Pulsed blowing from the same location has an increased effect on the flow-field at $\alpha = 45°$, demonstrating the high versatility of the applied AFC method. As seen above, the shear layer reattaches, when pulsed blowing is applied. However, as the conditions and baseline flow state changes by increasing the angle of attack from $\alpha = 35°$ (stall) to 45° (post-stall), the optimum frequency decreases from $F^+ = 2.6$ to unity, $F^+ = 1.0$. Gursul reported in Ref. [50], that instabilities are interconnected and their specific dominant spectral range fade at their borders . The mechanism leading to the reattachment is analysed in this section by corresponding time accurate DES results, which were also reported in Refs. [18, 21].

Analogous to the analysis of breakdown delay, the velocity component time records u/U_∞ and v/U_∞ at selected positions are phase averaged and plotted for two blowing cycles in Figure 5.68. The monitor points are located along two rays within the shear layer: above the leading edge ($y/s(x) = 1.06$) subsequent to leading edge detachment and close to the symmetry plane ($y/s(x) = 0.15$) prior to wall reattachment (Figure 5.68a). The vertical dashed lines in the velocity plots (Figures 5.68b and c) delimit the blowing phase in the first quarter ($1/4T$) of each cycle.

Although the jets are synchronised, the conical flow field reacts with a downstream phase delayed velocity magnitude increase (both components) above the leading edge, as the graphs on the left hand side demonstrate. Within the recuperation phase, a large phase-averaged spread is present that does not correlate with the chord position: In the second half of the blowing cycle, both u/U_∞ and w/U_∞ are highest at $x/c_r = 0.4$, the lowest at 0.6 and in between at 0.8.

At the inboard positions ($y/s(x) = 0.15$), the axial velocity reaches values around the free stream magnitude, however with high amplitudes. A downstream correlation is evident designated by the arrow in Figure 5.68b. The vertical component is negative and shows no such effect as for the axial component. On the contrary, a certain negative phase phase shift can be observed (leading phase in upstream direction: from $x/c_r = 0.8$, pink, to 0.4, orange).

Figure 5.69 analyses the crossflow plane at $x/c_r = 0.4$. The orange and black curves represent the phase averaged relative axial velocities supplemented by time-step-specific values as delta symbols. Corresponding crossflow distribution of λ_2 criterion multiplied by the vorticity sign are shown below. The blue colour represents counter-clockwise rotating vortices. At the blowing cessation ($T/4$) jet vortices are present that have an opposed rotation sign as the shear layer. Subsequently, strong discrete vortices are generated and cluster in the shear layer above the leading edge. These enhance the momentum transport across the sheet, leading to an increase in local axial velocity. Inboard, the velocity decreases. The vortex activity region follows the path described by the phase averaged PIV measurements in Section 5.2.2. The graphs in Figure 5.69 show a clear phase delay of 180° consolidating the helical form of discrete vortices and their counter directional helical path.

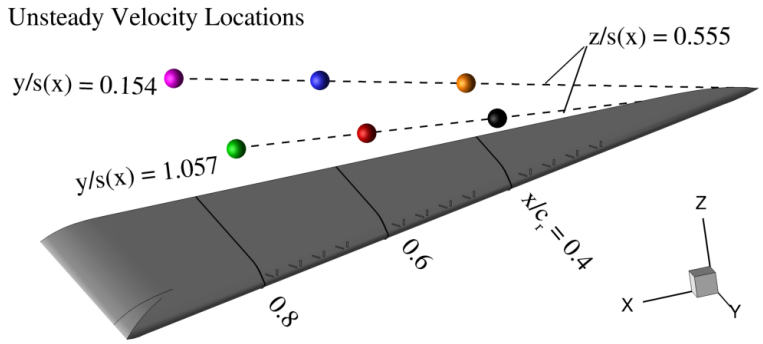

(a) Monitor positions.

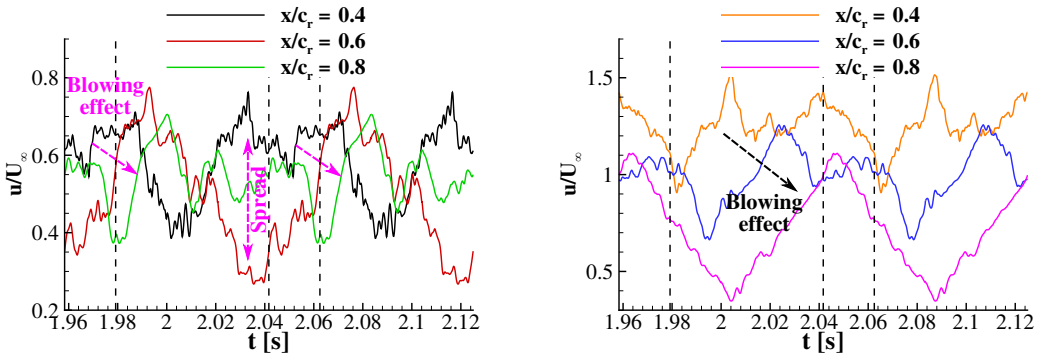

(b) Axial velocity.

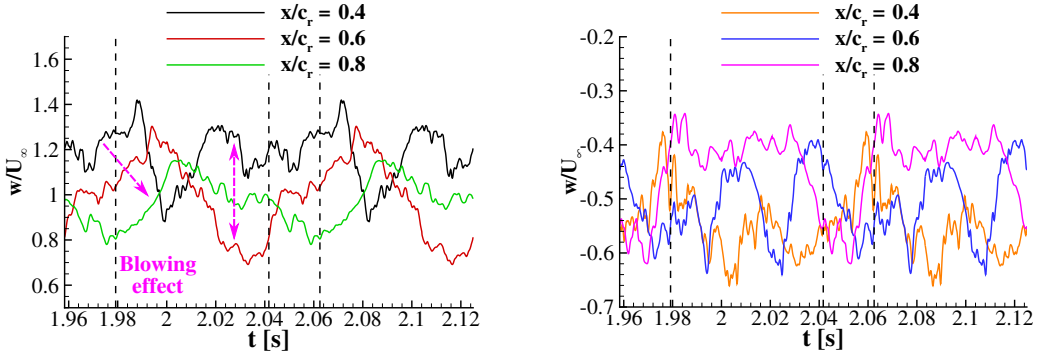

(c) Vertical velocity.

Figure 5.68: Phase-averaged recordings of axial/vertical velocity at $x/c_r = 0.4$ 0.6 and 0.8, $z/s(x) = 0.55$. Outboard ($y/s(x) = 1.06$, left) and inboard ($y/s = 0.15$, right). $\alpha = 45°$ and $F^+ = 1.0$.

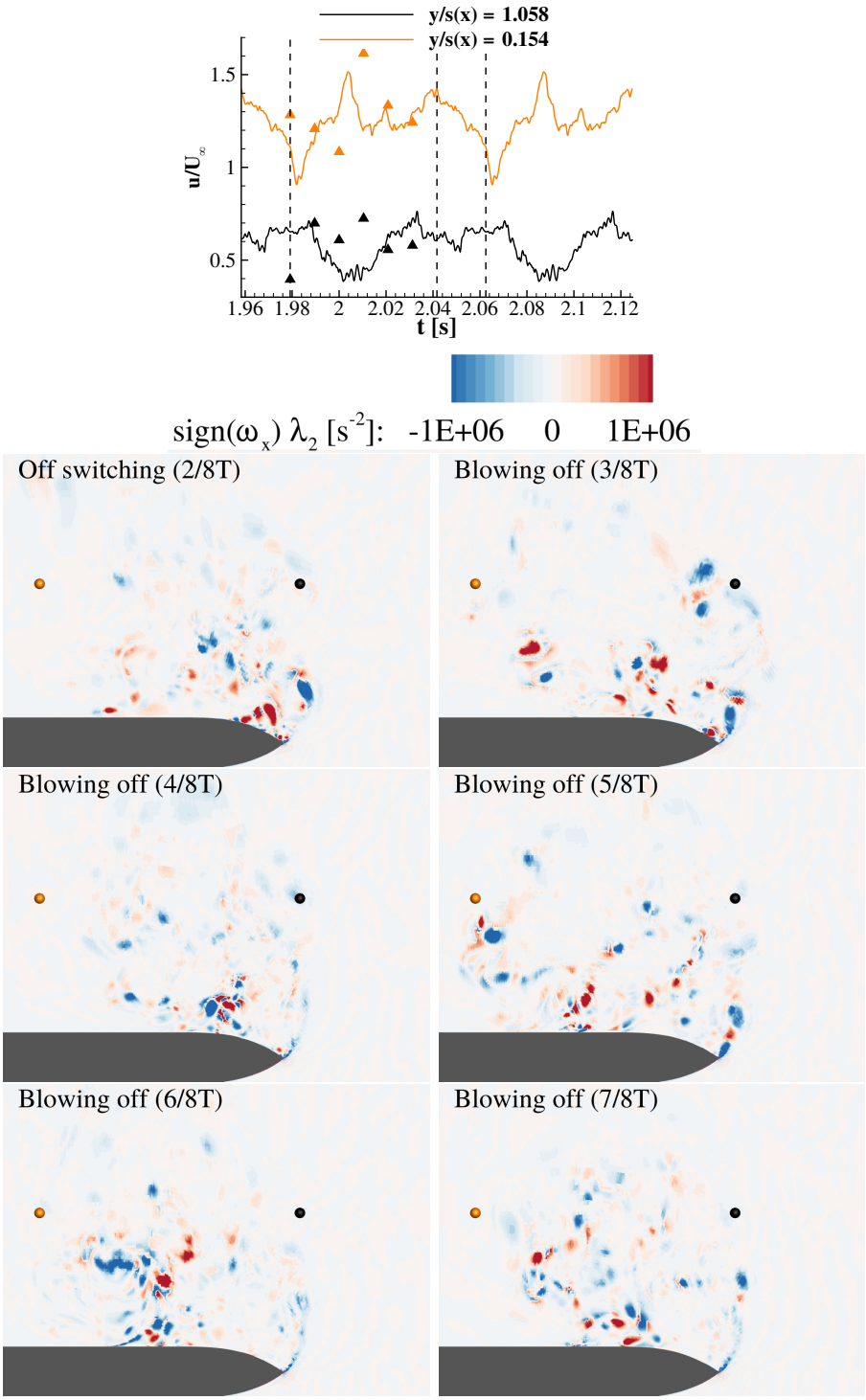

Figure 5.69: Phase-averaged axial velocity at local coordinates, $x/c_r = 0.4$, $z/s(x) = 0.55$, $y/s(x) = 0.15, 1.06$ (above) and instant λ_2-criterion multiplied by the sign of axial vorticity ω_x distributed in $x/c_r = 0.4$. Blue represents counter-clockwise rotation. $\alpha = 45°$ and $F^+ = 1.0$.

Figure 5.70 shows the 3D flow fields at two discrete instances separated in time by $\Delta t = 1/4T$. The visualisations include isosurfaces of the Q-criterion ($Q = 10^5\,\mathrm{s}^{-2}$) coloured with the relative axial velocity in the range $-0.5 \leq u/U_\infty \leq 1.5$. The baseline flow field in Figure 5.70a constitutes of leading-edge shedding of coherent structures (discrete vortices). The shedding process starts at the apex and advances along the leading edge resulting in a rather 3D detachment as the axis of the vortices reveal a downstream and downward inclination. Throughout the downstream transport process, the vortices become unstable along their axis and cant in the freestream direction as a product of secondary 3D instabilities and complex vortex interactions. The flow inboard of the shear layer represents the dead-water region with low negative axial velocities and low turbulence (low energy).

The flow field is completely altered when blowing is applied, leading to shear-layer reattachment and complex vortex activities throughout this process, as presented in Figure 5.70b based on two time steps of the final computed blowing cycle. The reattachment of the shear layer generates a flow field resembling the stalled flow field. On a big scale, AFC generates a leading-edge vortex extending over the entire wing (from the symmetry plane to the leading-edge). On a smaller scale, the shedding mechanism presented in Figure 5.70a is altered when the flow field is perturbed.

AFC increases the circumferential momentum, on the one hand, and enforces a frequency dependent vortex shedding, on the other. As a result, the shear layer consists of unsteady discrete vortices spiralling and winding around the reversed flow region. The leading-edge shedding occurs in a three-dimensional manner as in the baseline case. However, with forcing, the vortices are subjected to jet interaction and increase in intensity downstream with specific curling around the wake relative to the natural flow. The perturbations have a significant, upstream effect, especially on the apex region, where the quasi-steady shear layer is reattached and becomes unstable further downstream, eventually shedding vortices that twist counter clockwise around the low energy core, where $u/U_\infty < 0$.

Dashed lines in Figure 5.70b designate vortex fronts that demonstrate a certain periodicity. When the blowing ceases, the vortex fronts are ordered circumferentially and convect downstream. These waves originate from the manipulated shear layer instability initiated at the apex. Inboard, the flow constriction leads to high axial velocities. $T/4$, after blowing cessation, waves of shear-layer vortices nearly parallel to the leading-edge are present in the flow field, disturbing the annular structures. Advancing within the blowing period, the discrete vortices are transported downstream on a spiralling path, recovering to the initial state. Throughout this process, mixing between the inner wake region and the outer region is sustained.

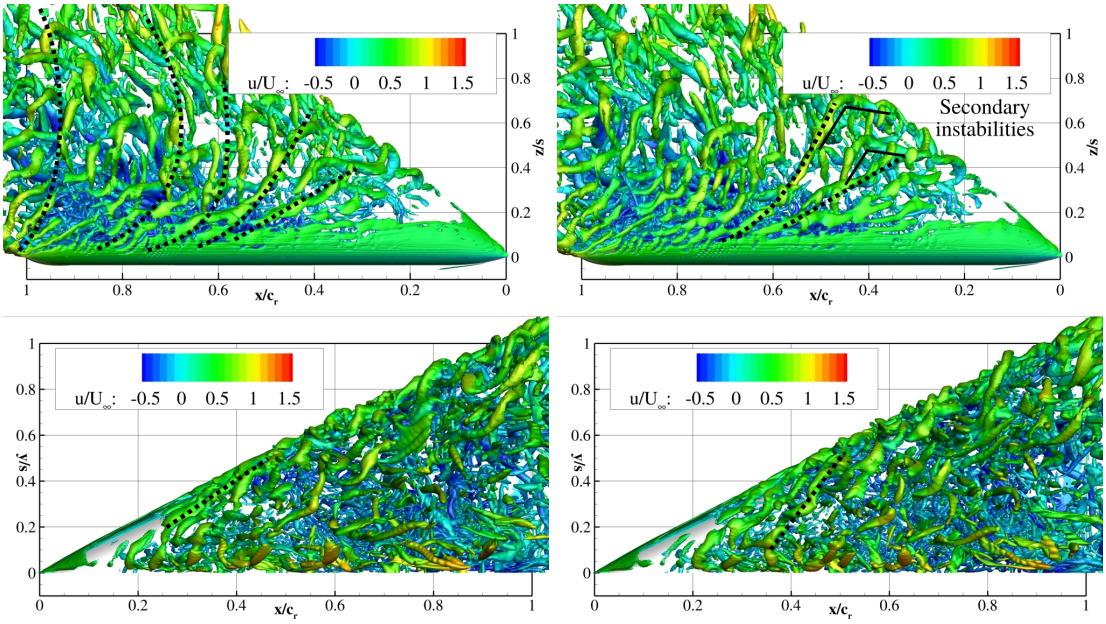

(a) Baseline.

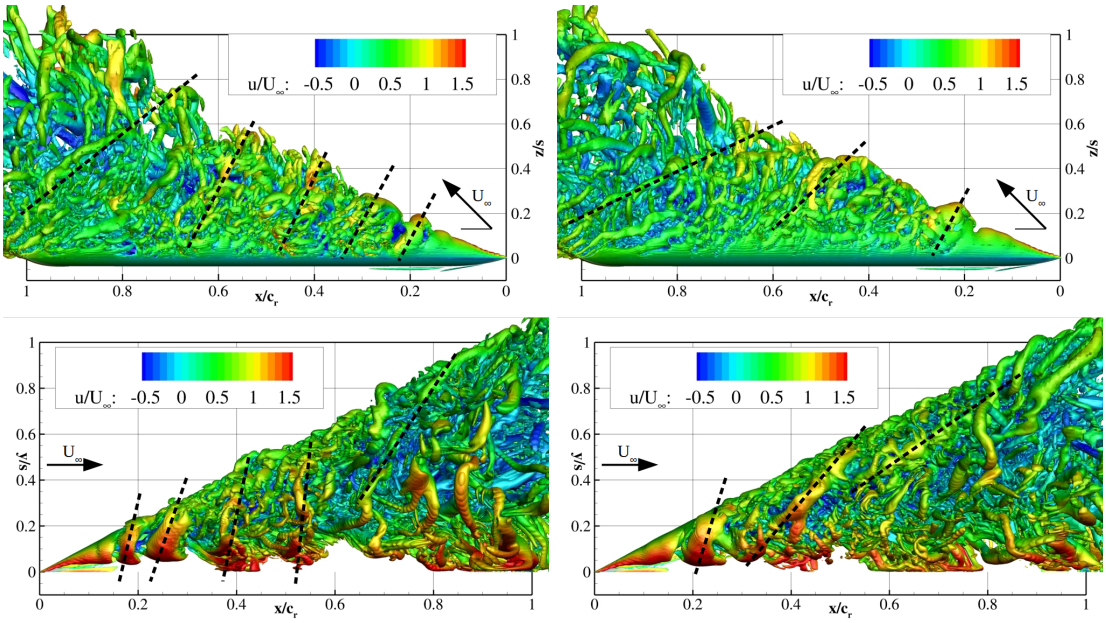

(b) $F^+ = 1.0$, at blowing cessation ($\theta = 90°$, left) and $T/4$ after ($\theta = 180°$, right).

Figure 5.70: Q-criterion $Q = 10^5\,\mathrm{s}^{-2}$, representing two instances separated in by $T/4$. Baseline vs. actuated at $\alpha = 45°$.

5.5.3 Frequency Shift

Figure 5.71 shows the power spectral density (PSD) in dimensionless form of the relative axial velocity signal, monitored above the leading edge at the following relative wing coordinates: $x/c_r = 0.6$, $y/s(x) = 1.06$, $z/s(x) = 0.55$ plotted against the reduced frequency $k_{\mathrm{red}} = f \cdot c_r/U_\infty$ in double logarithmic representations.

The Fourier transform is obtained from a measured/monitored time signal of $u(x,t)$ according to expression:

$$X_u = \int_{t_1}^{t_N} \frac{u'}{U_\infty} e^{-i\omega t} dt, \tag{5.7}$$

where $t_N - t_1$ is the total time of the record and ω the angular frequency. Consequently, using the complex conjugate of the Fourier transform X_u^*, the dimensionless PSD is defined as:

$$PSD = \frac{U_\infty}{c_r} \frac{2}{t_N - t_1} X_u^* X_u. \tag{5.8}$$

In Figure 5.71, the graphs reveals power concentrations at distinct reduced frequency ranges. The measurements were conducted at $\alpha = 35°$ and $45°$, sampling within the shear layer near mid chord above the leading edge ($x/c_r = 0.60$, $y/s = 0.63$, $z/s = 0.33$, red mark in Figure 5.71a). The graphs show the numerical (in black) and the experimental (red) results on a double logarithmic plane, for the baseline case (left) and for the actuated case (right).

Considering the baseline case at $\alpha = 35°$, the dominant frequency ranges differ slightly between measurement and computation. The latter predicts a lower dominant reduced frequency range of $k_{\mathrm{red}} = 0.7{-}1.2$ and an additional peak at $k_{\mathrm{red}} = 2.0$ (DES), compared to the WTT measurements, $k_{\mathrm{red}} = 1.3{-}1.7$ (cf. Figure 5.71b). However, distinct higher frequency peaks at $k_{\mathrm{red}} \approx 3.0, 4.1, 5.0$ and 6.0/6.5 (WTT/DES) are in agreement for both experimental and numerical results.

The unsteady shear layer responds to the periodic actuation of $F^+(= k_{\mathrm{red}}) = 2.6$ with a frequency increase of the spectral peaks: $k_{\mathrm{red}} = 1.0, 1.4, 2.6, 5.2$ (DES); $k = 1.4, 2.6, 5.2, 7.8, 10.4$ (WTT). In both graphs, also secondary peaks at $k_{\mathrm{red}} = 1.7$ and 3.9 are present, which are marked by round brackets in Figure 5.71c.

The spectra of the baseline case at post-stall ($\alpha = 45°$ in Figure 5.71d) show nearly constant PSD levels up to $k_{\mathrm{red}} \approx 3.5$, after which the values drop. This flat distribution demonstrates that the local flow field oscillates randomly, with no unique frequency. The shedding of the vortices is, hence, not ordered. Distinguishable peaks are observed at $k \approx 4.2$, in the experiments conducted in [84], and at $k_{\mathrm{red}} \approx 3.4$, in the flow simulations. The hot wire apparatus records the typical turbulence scale decay with the exponent of $-5/3$ (also known as the Kolmogorov law). In the numerical investigations however, the slope differs from that distribution. The PSD values drop with a steeper slope in the range $3.5 \leq_{\mathrm{red}} \leq 20.0$ and the Kolmogorov decay is observed at higher frequencies. Hence, the spectral distribution of the energy contained in the turbulent scales is well predicted by DES at low frequencies and underpredicted at higher. This is traced back to the scale resolving capabilities of LES. This method resolves the scales larger than the grid spacing and models the subgrid scales. In other words, the grid "filters" the resolved flow field. A finer grid would resolve finer scales but with a considerably higher computational cost. For the current investigations the selected grid is fine enough in order to resolve the relevant, geometry-dependent flow structures.

With blowing, the spectral content changes (Figure 5.71e). A clear peak associated with the blowing frequency is detected in both numerical and experimental investigations. The hotwire anemometry detects in addition to the DES two higher harmonic peaks ($k_{\mathrm{red}} = 2.0, 3.0$). The PSD levels of the DES computation with blowing matches the measured ones.

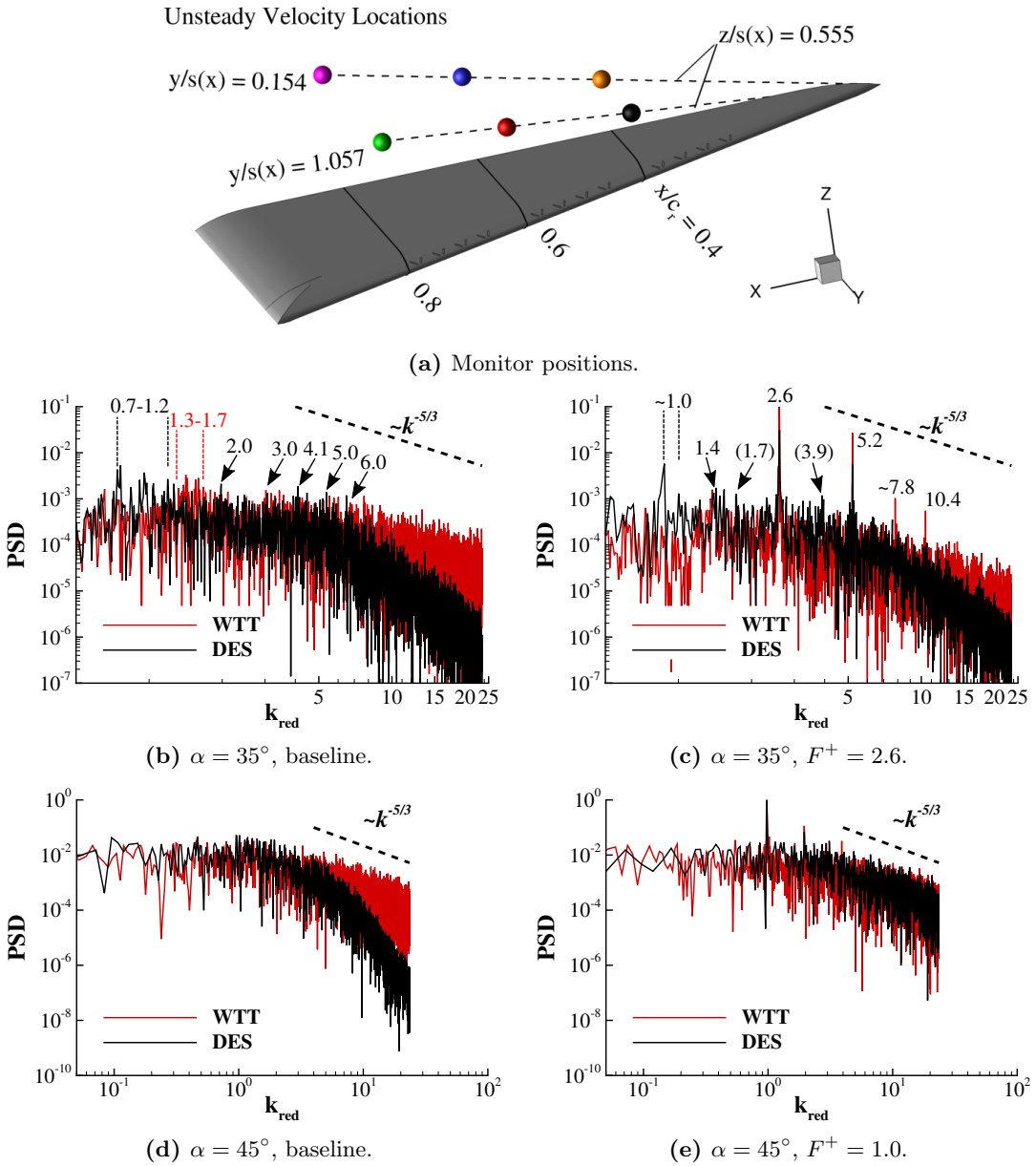

(a) Monitor positions.

(b) $\alpha = 35°$, baseline.

(c) $\alpha = 35°$, $F^+ = 2.6$.

(d) $\alpha = 45°$, baseline.

(e) $\alpha = 45°$, $F^+ = 1.0$.

Figure 5.71: PSD of measured and simulated the relative axial velocity against the reduced frequency k_{red} at position: $x/c_r = 0.60$, $y/s(x) = 1.06$ and $z/s(x) = 0.55$. $\alpha = 35°$ and 45°; baseline and actuated; DES and WTT.

5.5.4 Synthesis

The effect of blowing was investigated based on transient data as planar velocity and vorticity distributions and Q-criterion maxima. The jets interact with the boundary layer directed in spanwise direction. Additional negative vorticity is, thus, injected into the boundary layer, which detaches from the surface and disrupts the shear layer. The effect ripples throughout the flow field by altering the dominant frequency range of shear-layer instabilities.

The additional unsteady momentum and the synchronised actuation lead to the generation of stronger shear-layer vortices, which enhances the energy transport across the mixing sheet. Vortex waves as effect of the disruption are connected downstream in a spiralling path and tilting in freestream direction. In addition to inducing axial velocity into the vortex core, the shear layer vortices induce also longitudinal instability into the primary core. This leads to periodic detachment and downstream transport of high core velocity regions.

The biggest AFC effect was the shear layer reattachment at $\alpha = 45°$. For this a lower frequency and higher unsteady momentum was used. However, the unsteady flow phenomena in response to blowing are similar to the manipulation of the flow field at $\alpha = 35°$: waves of vortices with a dominant orientation in azimuthal direction transported in a spiral path downstream. Regarding the spectral domain, a frequency shift occurs which influences the shear layer instabilities propagating in the flow field.

The most significant effects of the AFC devices on the flow field are:

- Increase of turbulent mixing between the outer, high-energy flow and the low-energy, core flow,
- Kinetic energy increase in the shear layer, especially in circumferential direction leading to reattachment and
- Ordering the vortex shedding, such that when a wave of disturbances exits the flow field above the wing the next disturbance is induced at the leading edge.

5.6 Dynamic Mode Decomposition

Snapshots of the numerical, time-dependent flow-field data were analysed with the method described in Section 4.4.1 and formulated in [124]. The DMD spectra and the most dominant modes are presented and discussed in this section. For computational reasons, only data from selected planes are considered. Two planes are investigated: cross flow planes ($x/c_r = 0.4$ and 0.6) and a plane positioned longitudinally along the vortex core and parallel to the wing's y-axis. For each case investigated, table 5.7 summarises the DES transient input data for the DMD analysis.

Table 5.7: DMD input.

Angle of attack α	**Case**	**No. of snapshots** N	**Time sampling** $\Delta t = t_{i+1} - t_i$	**Total time** $t_N - t_1$
35°	Baseline	2000	$3.9 \cdot 10^{-4}$ s	0.78 s
	Actuated	2000	$3.9 \cdot 10^{-4}$ s	0.78 s
45°	Baseline	2060	$1.0 \cdot 10^{-3}$ s	2.15 s
	Actuated	1400	$1.0 \cdot 10^{-3}$ s	1.46 s

5.6.1 Breakdown Delay

The delay of vortex breakdown is the effect of pulsating blowing at the leading edge with the frequency matching the helical mode instability ($F^+ = 2.6$). AFC interacts and manipulates inherent flow instabilities (e.g. KH, breakdown, vortex meandering, oscillation of breakdown location, etc.). These transient phenomena are unique in frequency ranges and structures. Therefore, the subsequent investigation identifies these instabilities by regarding dominant DMD modes from subsets of the flow field data (i.e. x-velocity in crossflow and core-flow planes).

5.6.1.1 Cross Flow

Figure 5.72 compares the PSD of the axial velocity in six locations with the DMD spectra in the crossflow plane $x/c_r = 0.60$ as function of reduced frequency. The red and blue curves (b) represent the PSD in the investigated chord station and show similar dominant frequencies as the DMD spectra (c). The following conclusions are drawn from comparing the natural flow spectra on the left hand side with the actuated ones on the right hand side:

- The flow responds to periodic actuation by a shift towards higher frequencies.
- More dominant frequencies are present with actuation.
- Baseline shear layer is dominated by periodic motion with distinct frequency ranges: $k_{\text{red}} =$ 1, 4–8 and around 11. These periodicity is transported within the shear layer and recorded in all monitored points.
- The unsteady energy injected enhances the periodic activity in the shear layer, such that the PSD increases and DMD modes with higher frequencies appear in the range $0.9 \leq k_{\text{red}} \leq 8.1$ and around higher values as 12.0 and 24.0.

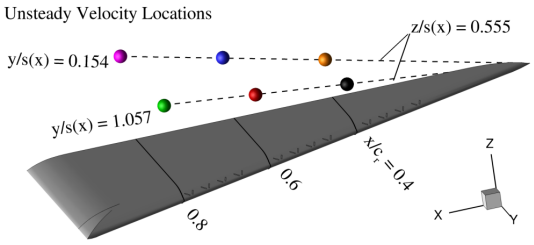

(a) Monitor positions.

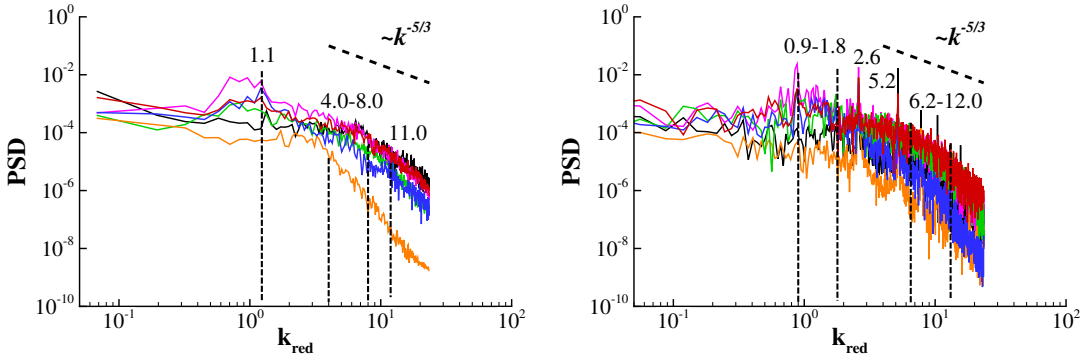

(b) x-velocity PSD.

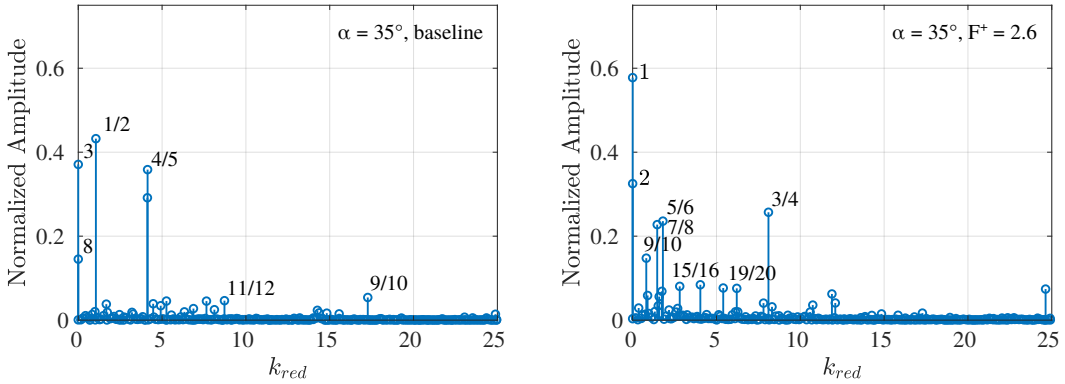

(c) DMD spectrum.

Figure 5.72: Comparison of PSD and DMD spectra of the axial velocity in the crossflow plane. $\alpha = 35°$. Left–baseline, right–$F^+ = 2.6$.

Dominant DMD mode pairs designated in the spectra by the mode number ranked by the normalised amplitudes are plotted in Figures 5.73 and 5.74, for the baseline and actuated cases, respectively. The points on the y-axis represent steady modes. The baseline steady modes (3 and 8) are shown in Figure 5.73a and b. The 8th mode represents the mean flow field.

The most dominant unsteady modes demonstrate a velocity distribution with alternating negative and positive axial velocity regions axis-symmetric with the vortex axis. In Figure 5.73c, these structures oscillate with a low frequency ($k_{\text{red}} = 1.1$) and has velocity regions distributed as the first steady mode (reversed sign). This means that the flow is distributed rather heterogeneously and has a low frequent displacement in lateral and vertical direction. The PSD curves

in Figure 5.72b (left) show the first dominant peak converging downstream towards this value. The conical flow leads to a decrease of the frequencies downstream with the relation $f \sim 1/x$.

At $k_{\mathrm{red}} = 4.1$, modes 4/5 show as well an axis-symmetric distribution, however, with an X-shaped distribution of negative/positive velocity peaks (referred hereafter as "structures"). Larger structures are present between the shear layer and the reverse flow region (compare Figure 5.73b and d) and smaller structures in the central, reverse-flow region. Hence, mode 4/5 represents the first mode of azimuthal periodic motion, which is the most unstable polar coordinate responsible for the breakdown process.

At the upper end of the range of dominant DMD modes (or PSD peaks) related to shear-layer instabilities, $4 \leq k_{\mathrm{red}} \leq 8$, Figure 5.74f shows high amplitudes above the leading edge, where discrete vortices grow and pair along their helical path. Mode 9/10 is high frequent, i.e. $k_{\mathrm{red}} = 17.3$ (Figure 5.73e), with large amplitudes between the reattached shear layer and the reverse flow region and also above the leading edge, capturing the leading-edge shedding process.

The most dominant DMD modes corresponding to the manipulated flow field are arranged rather uniformly in the spectra up to $k_{\mathrm{red}} \approx 12$. PSD peaks at 0.9, 2.6, 5.2 and smaller peaks within frequency ranges $0.9 \leq k_{\mathrm{red}} \leq 1.8$ and $6.2 \leq k_{\mathrm{red}} \leq 12.0$ exist in the spectra. The low frequent mode pairs show unique distribution of dynamic structures with increased amplitudes above the leading edge. The dynamics are complex and require multiple modes for accurate dynamics modelling.

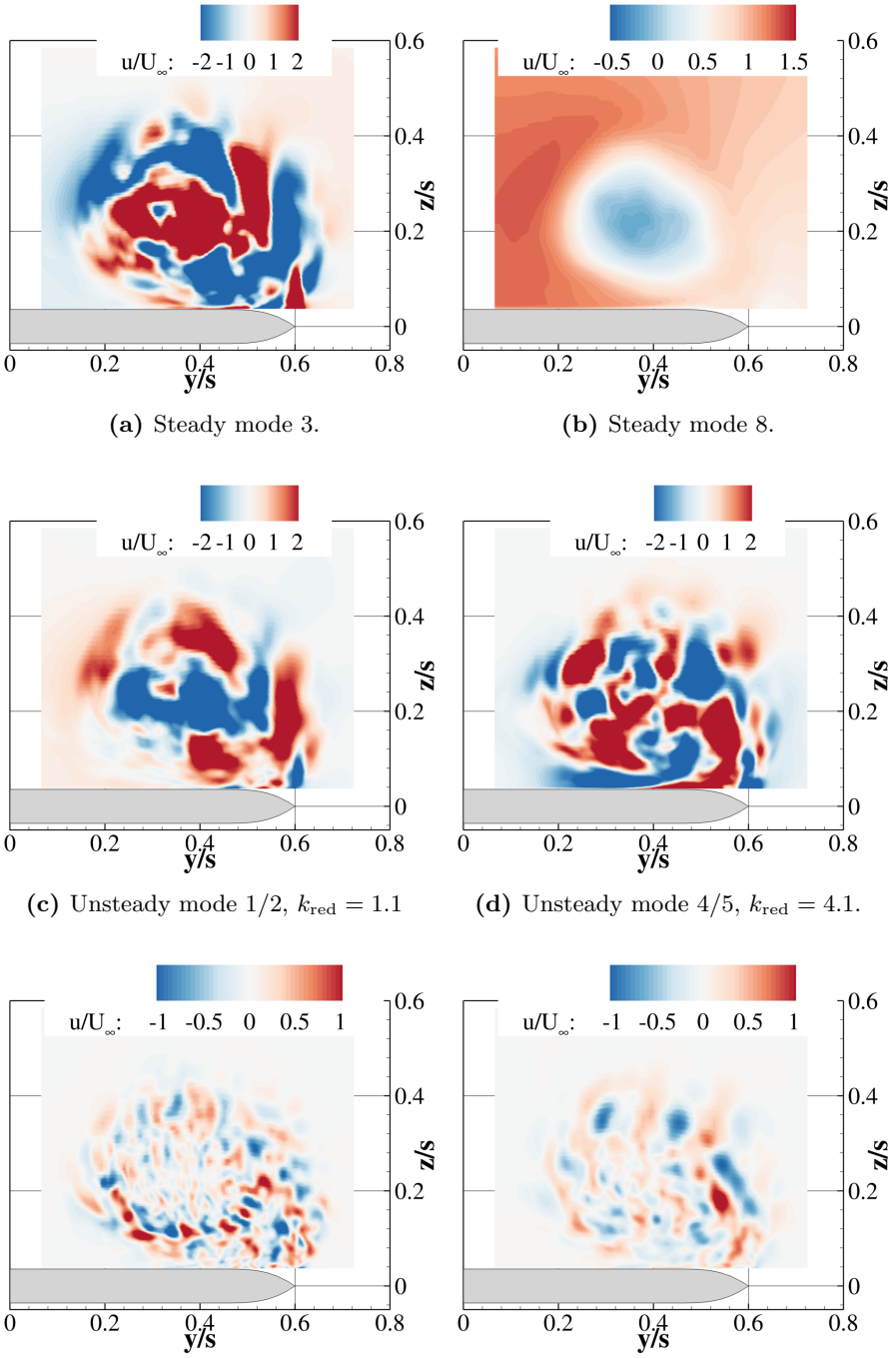

(a) Steady mode 3.

(b) Steady mode 8.

(c) Unsteady mode 1/2, $k_{\mathrm{red}} = 1.1$

(d) Unsteady mode 4/5, $k_{\mathrm{red}} = 4.1$.

(e) Unsteady mode 9/10, $k_{\mathrm{red}} = 17.3$.

(f) Unsteady mode 11/12, $k_{\mathrm{red}} = 8.7$.

Figure 5.73: DMD modes of the velocity field in the vortex crossflow plane $x/c_r = 0.6$, $\alpha = 35°$, baseline.

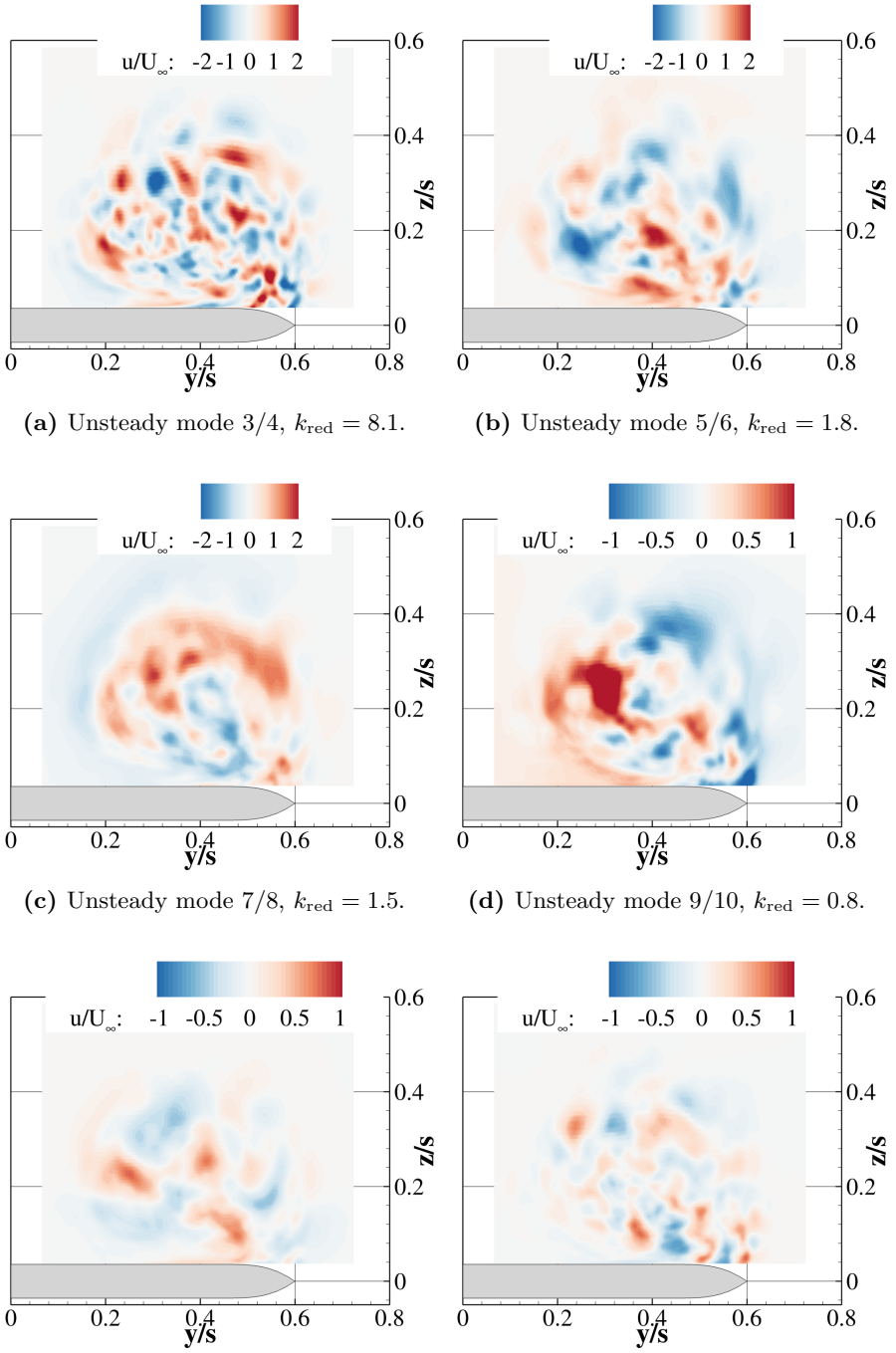

(a) Unsteady mode 3/4, $k_{\mathrm{red}} = 8.1$.

(b) Unsteady mode 5/6, $k_{\mathrm{red}} = 1.8$.

(c) Unsteady mode 7/8, $k_{\mathrm{red}} = 1.5$.

(d) Unsteady mode 9/10, $k_{\mathrm{red}} = 0.8$.

(e) Unsteady mode 15/16, $k_{\mathrm{red}} = 2.8$.

(f) Unsteady mode 19/20, $k_{\mathrm{red}} = 6.2$.

Figure 5.74: DMD modes of the velocity field in the vortex crossflow plane $x/c_r = 0.6$, $\alpha = 35°$, $F^+ = 2.6$.

5.6.1.2 Core Flow

Data from the plane along the vortex core (core flow) is investigated with the same method for extraction of dominant harmonic modes. Because of different input data with different dynamics in longitudinal direction, the spectra differentiate from the cross flow but have common frequency ranges as shown in Figure 5.75.

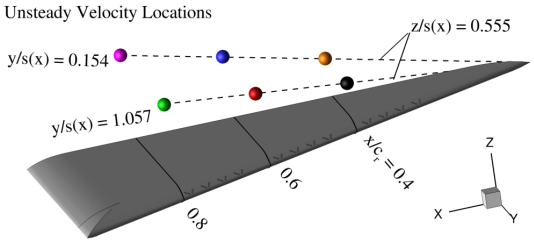

(a) Monitor positions.

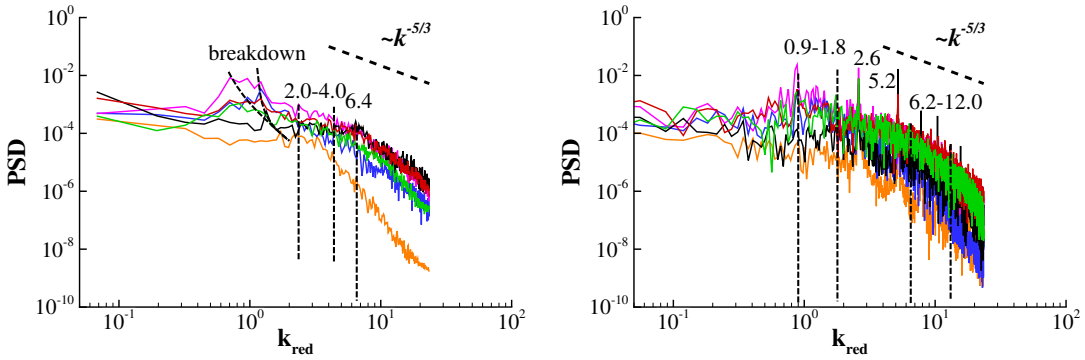

(b) x-velocity PSD.

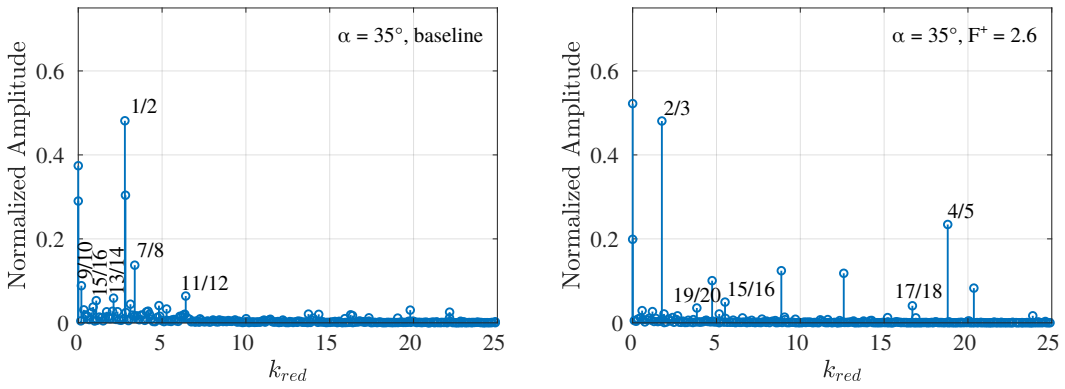

(c) Core-flow plane.

Figure 5.75: Comparison of PSD and DMD spectra of the axial velocity in the core-flow plane. $\alpha = 35°$. Left–baseline, right–$F^+ = 2.6$.

Modes 1/2 represent wake structures that are most dominant at $k_{\mathrm{red}} = 2.8$, see Figure 5.76. As in the crossflow investigation the first unsteady mode includes large structures in the shear layer and smaller structures in the reverse flow. At the same frequency, mode pair 15/16 reveals low-frequency structures in the reversed flow with alternating peaks at the breakdown location. This process corresponds to the first PSD peak in Figure 5.75.

The lateral oscillation of the breakdown is captured by modes 7/8 and the longitudinal oscillation of the breakdown location by 9/10 in Figure 5.76b and c. Smaller dominant structures are distributed in the region where the breakdown wake interacts with the shear layer with frequencies in the range of the KH instability, see Figure 5.76a. Mode 13/14 in (Figure 5.76b) is an asymmetric mode of the reversed wake, while 15/16 is symmetric (Figure 5.76c).

The response to actuation changes the dominant modes and the spatial structures also in the longitudinal plane. The modes with normalised amplitudes above 0.2 are shown in Figure 5.78. Modes 2/3 reveal structures with opposed sign symmetric to the vortex center line (Figure 5.78a). The structures increase in size. Added to the low-frequent motion is the second dominant pair involving high frequent dynamics at the interaction of the wake and the shear layer (Figure 5.78b).

The subsequent dominant modes investigated in Figure 5.79 represent several dominant modes with highest amplitudes in regions of the breakdown wake. Mode 15/16 has high amplitudes above the slot segments (Figure 5.79a). Mode 17/18 represents the high-frequent motion of the V-shaped disturbed wake (Figure 5.79b). As for mode 19/20, the asymmetric dominant mode of the wake field is contained (Figure 5.79c).

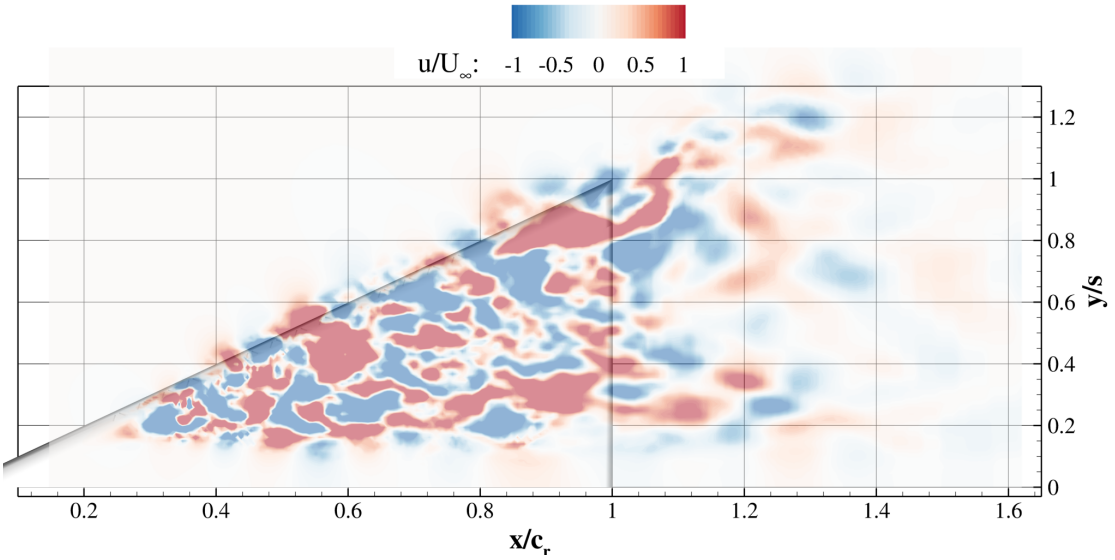

(a) Unsteady mode 1/2, $k_{\mathrm{red}} = 2.8$

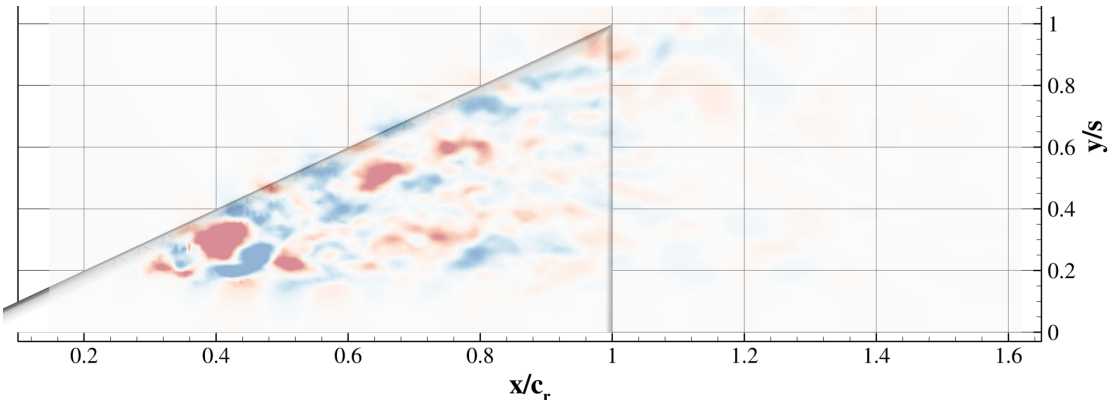

(b) Unsteady mode 7/8, $k_{\mathrm{red}} = 3.4$.

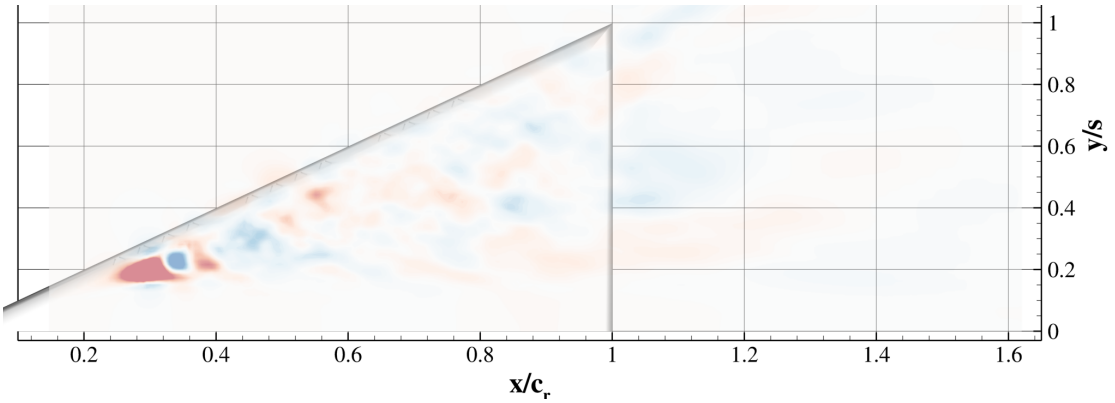

(c) Unsteady mode 9/10, $k_{\mathrm{red}} = 0.2$.

Figure 5.76: DMD modes of the velocity field in the vortex core plane, $\alpha = 35°$, baseline.

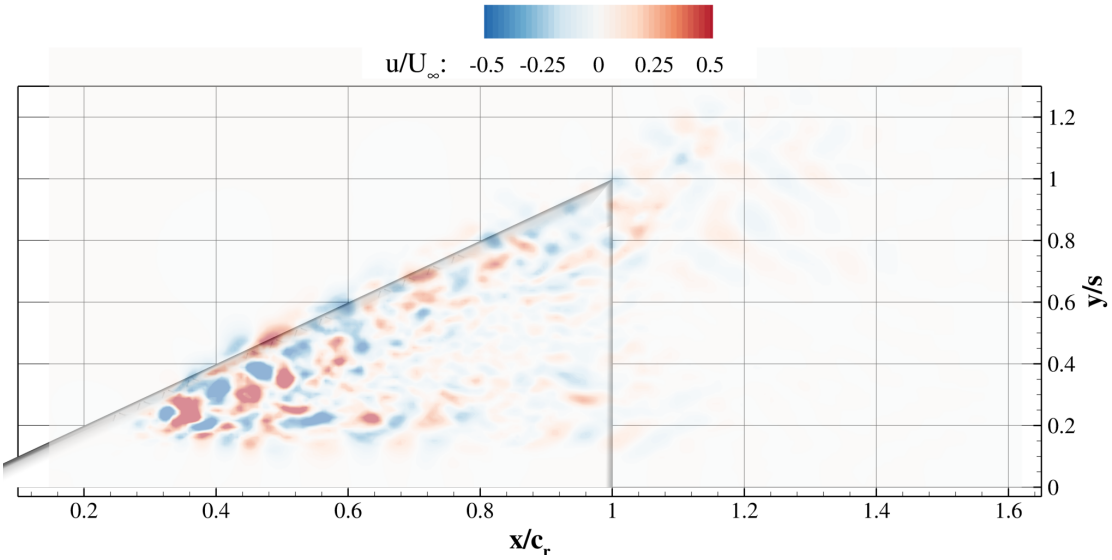

(a) Unsteady mode 11/12, $k_{\mathrm{red}} = 6.4$.

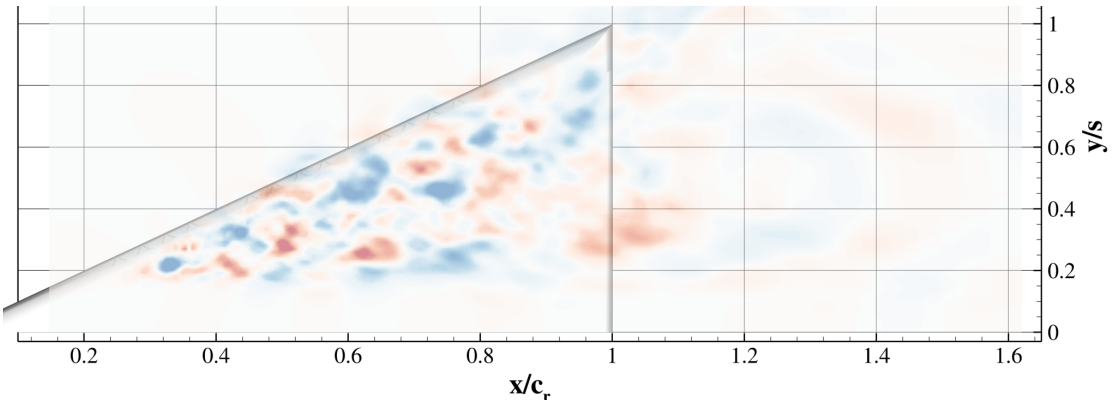

(b) Unsteady mode 13/14, $k_{\mathrm{red}} = 2.1$.

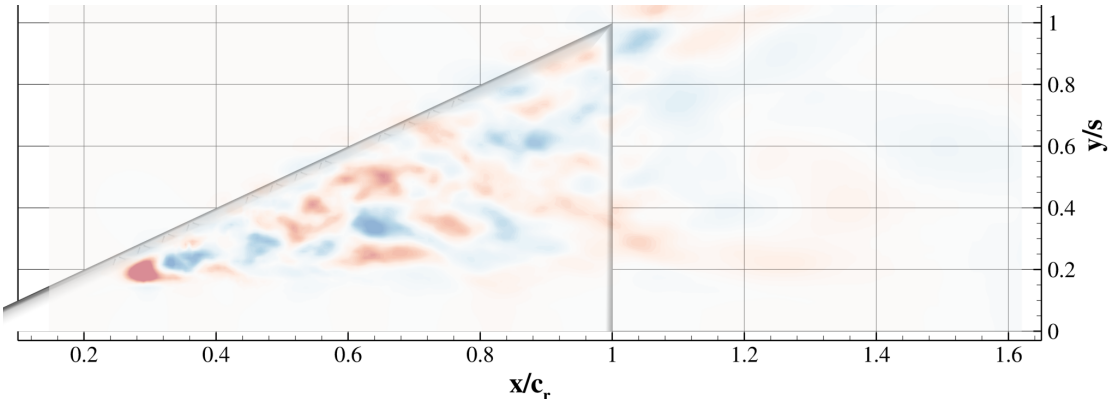

(c) Unsteady mode 15/16, $k_{\mathrm{red}} = 1.1$.

Figure 5.77: DMD modes of the velocity field in the vortex core plane, $\alpha = 35°$, baseline.

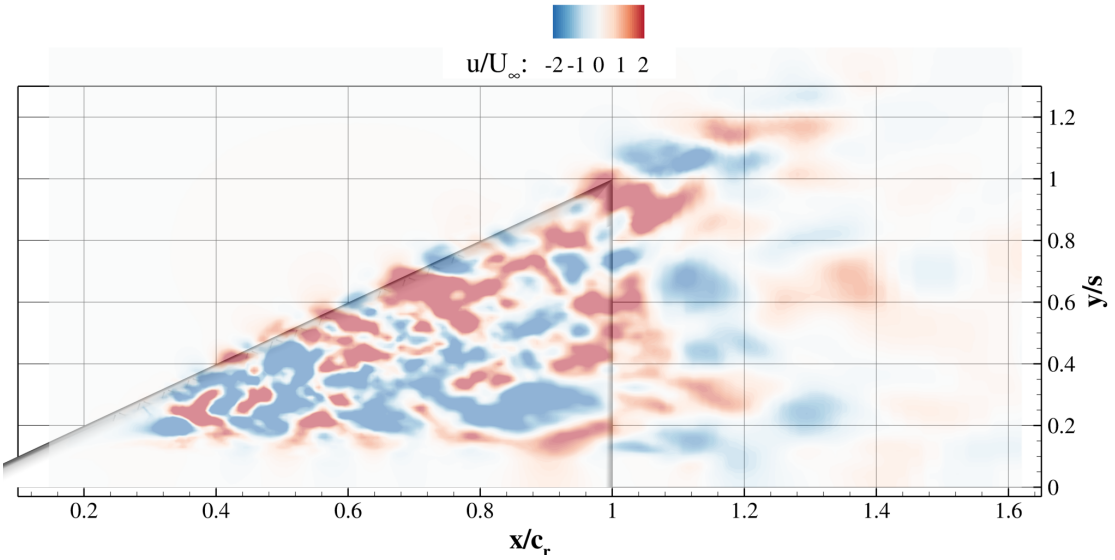

(a) Unsteady mode 2/3, $k_{\mathrm{red}} = 1.7$.

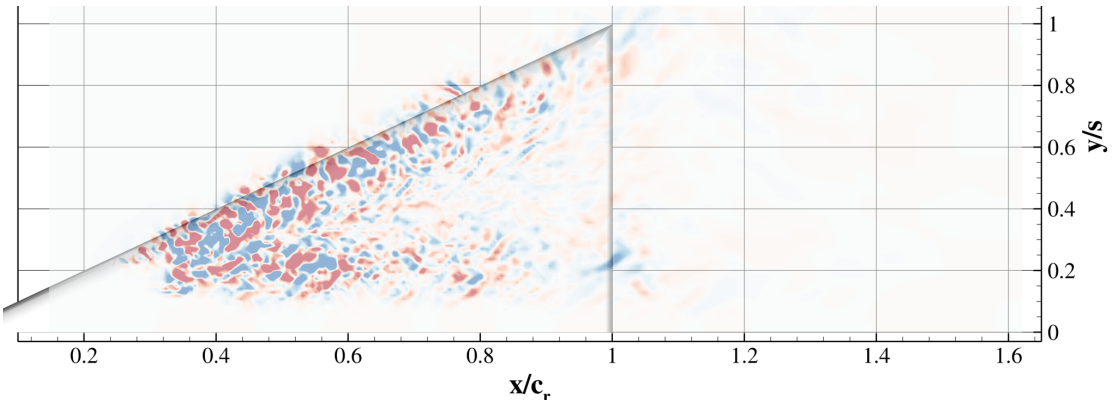

(b) Unsteady mode 4/5, $k_{\mathrm{red}} = 18.8$.

Figure 5.78: DMD modes of the velocity field in the vortex core plane, $\alpha = 35°$, $F^{+} = 2.6$.

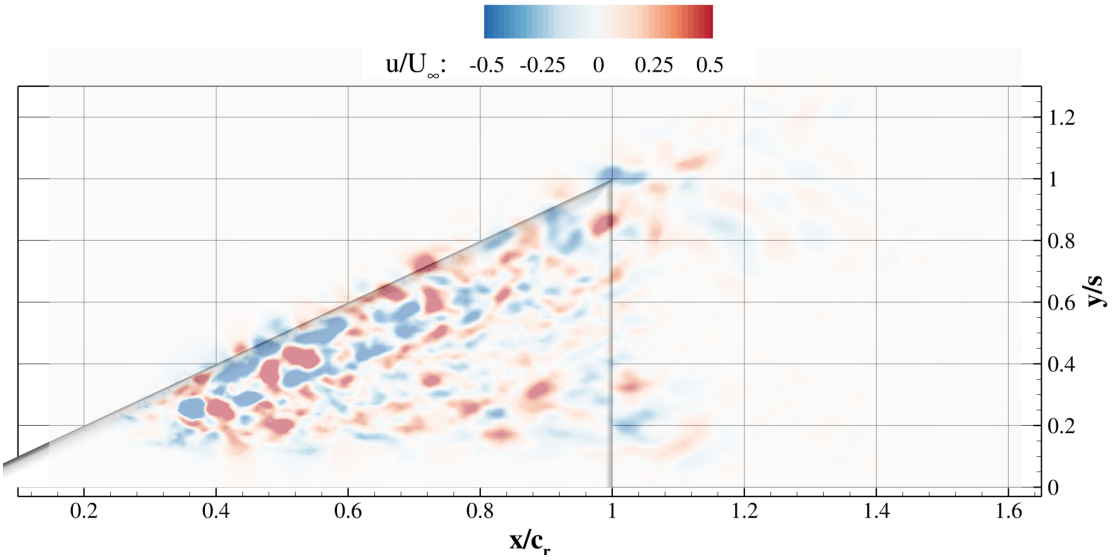

(a) Unsteady mode 15/16, $k_{\mathrm{red}} = 5.5$.

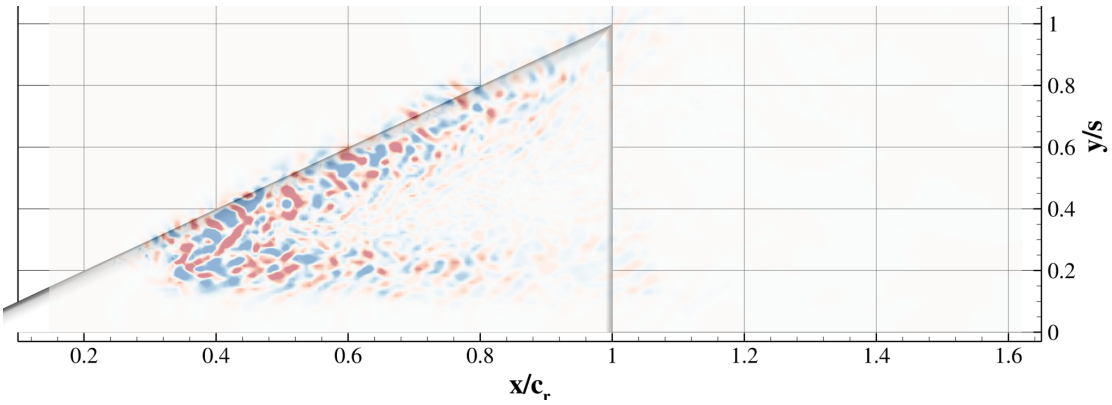

(b) Unsteady mode 17/18, $k_{\mathrm{red}} = 16.7$.

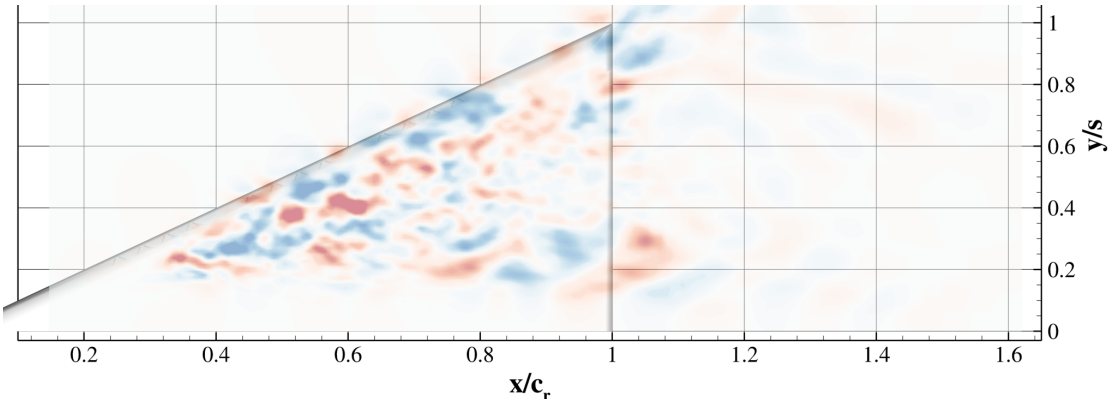

(c) Unsteady mode 19/20, $k_{\mathrm{red}} = 3.8$.

Figure 5.79: DMD modes of the velocity field in the vortex core plane, $\alpha = 35°$, $F^+ = 2.6$.

5.6.2 Flow Reattachment

Figure 5.80 shows the PSD and DMD spectra of the flow field at $\alpha = 45°$. The spectral peaks of the natural flow (left graphs)correspond to vortex shedding at low reduced frequencies up to unity, shear layer instabilities and secondary instabilities (only dominant above the leading edge) in the range $k_{\mathrm{red}} = 2 - 5$. Additional instabilities of the mixing sheet as KH instabilities occur at a reduced frequency of $k_{\mathrm{red}} \approx 8$.

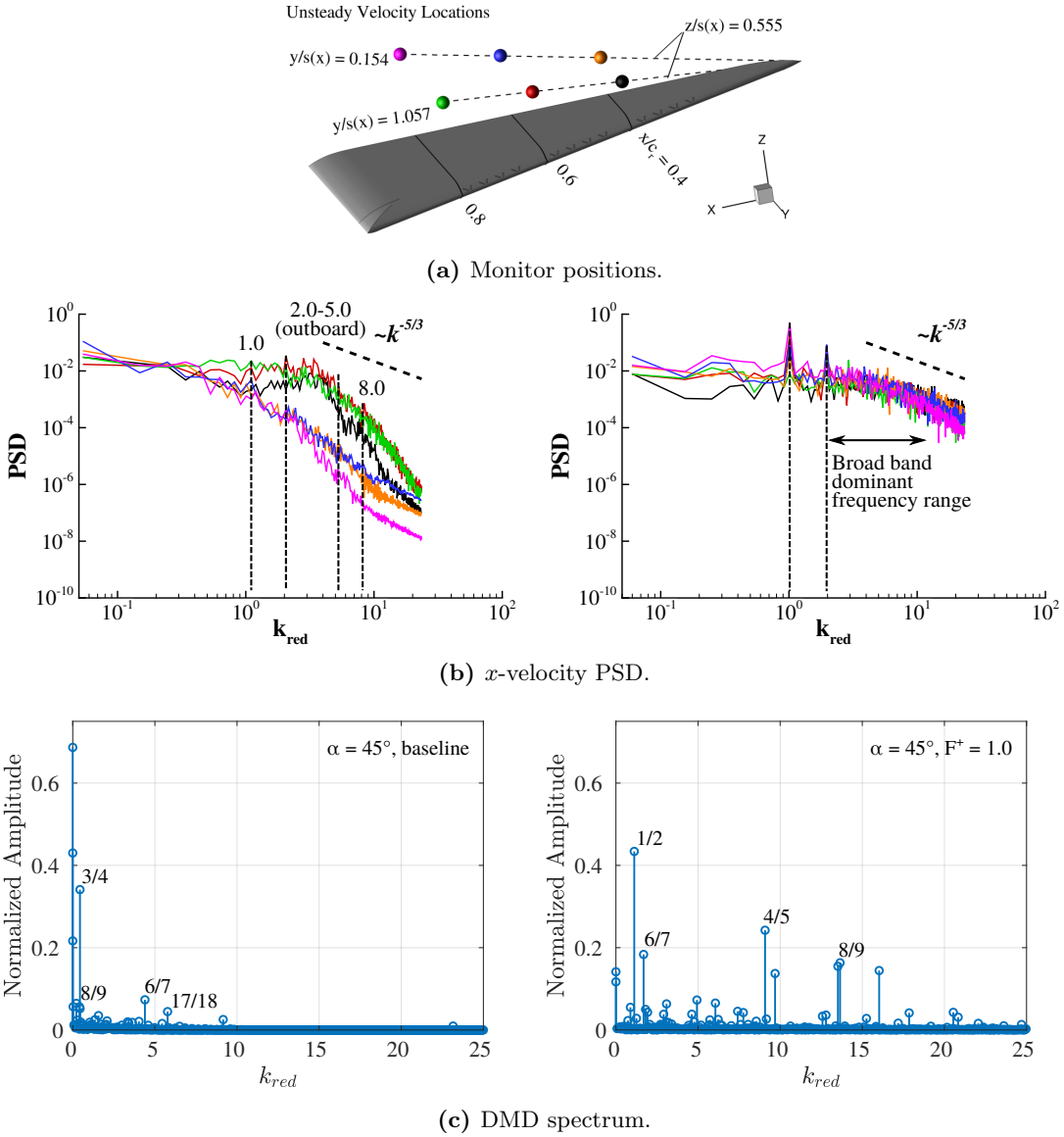

(a) Monitor positions.

(b) x-velocity PSD.

(c) DMD spectrum.

Figure 5.80: Comparison of PSD and DMD spectra of the axial velocity in the core-flow plane. $\alpha = 45°$. Left–baseline, right–$F^+ = 1.0$.

The baseline flow shows the typical dynamics of a 2D separated shear layer. The DMD investigation reveals two instabilities: vortex shedding (Figure 5.81a,c) and KH instabilities (b,d).

The stabilising effect of pulsed blowing reveals its effectiveness in the dominance of azimuthal instabilities that maintain the transport of momentum across outer and inner layer at relatively high frequencies, $k_{\mathrm{red}} \approx 9.1$, 13.6 (Figure 5.82b and c, respectively). Low frequency oscillation (Figure 5.82a and c) imply periodic motion of the entire structure.

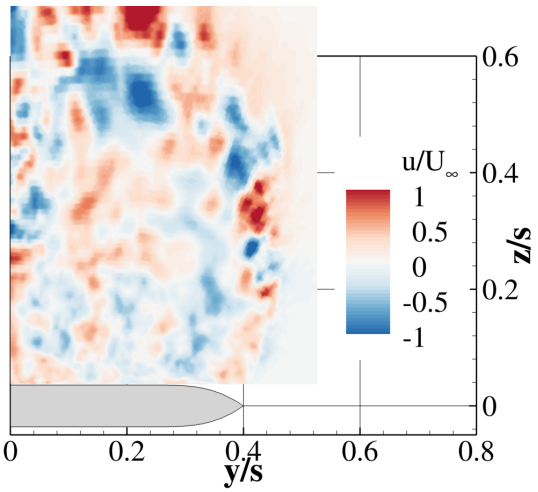

(a) Unsteady mode 3/4, $k_{\mathrm{red}} = 0.4$.

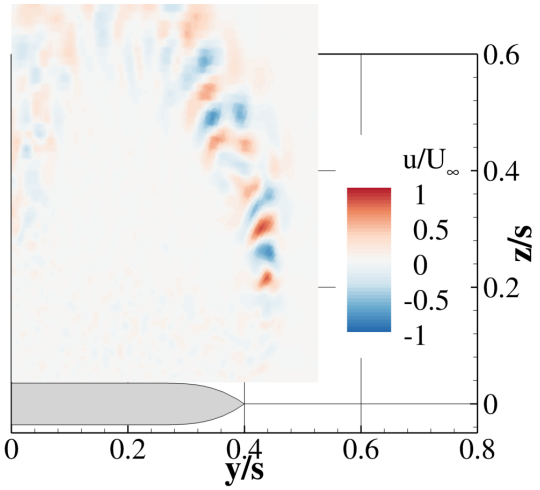

(b) Unsteady mode 6/7, $k_{\mathrm{red}} = 4.4$.

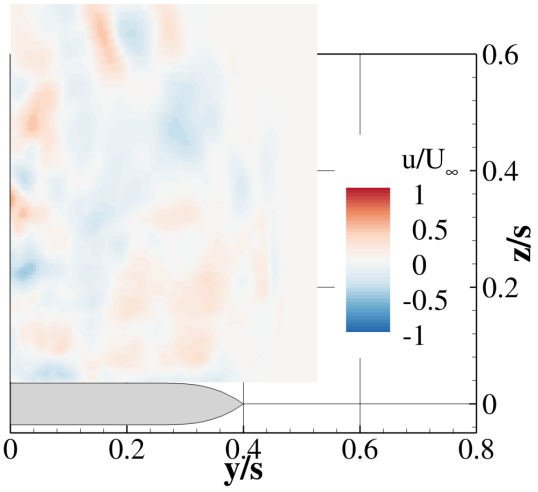

(c) Unsteady mode 8/9, $k_{\mathrm{red}} = 0.2$.

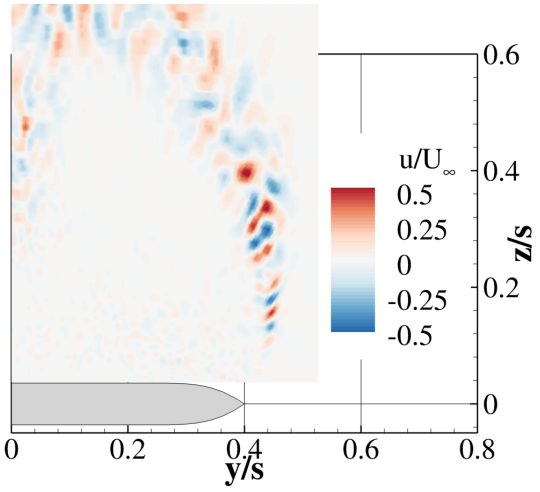

(d) Unsteady mode 17/18, $k_{\mathrm{red}} = 5.8$.

Figure 5.81: DMD modes of the velocity field in the vortex crossflow plane $x/c_r = 0.4$, $\alpha = 45°$, baseline.

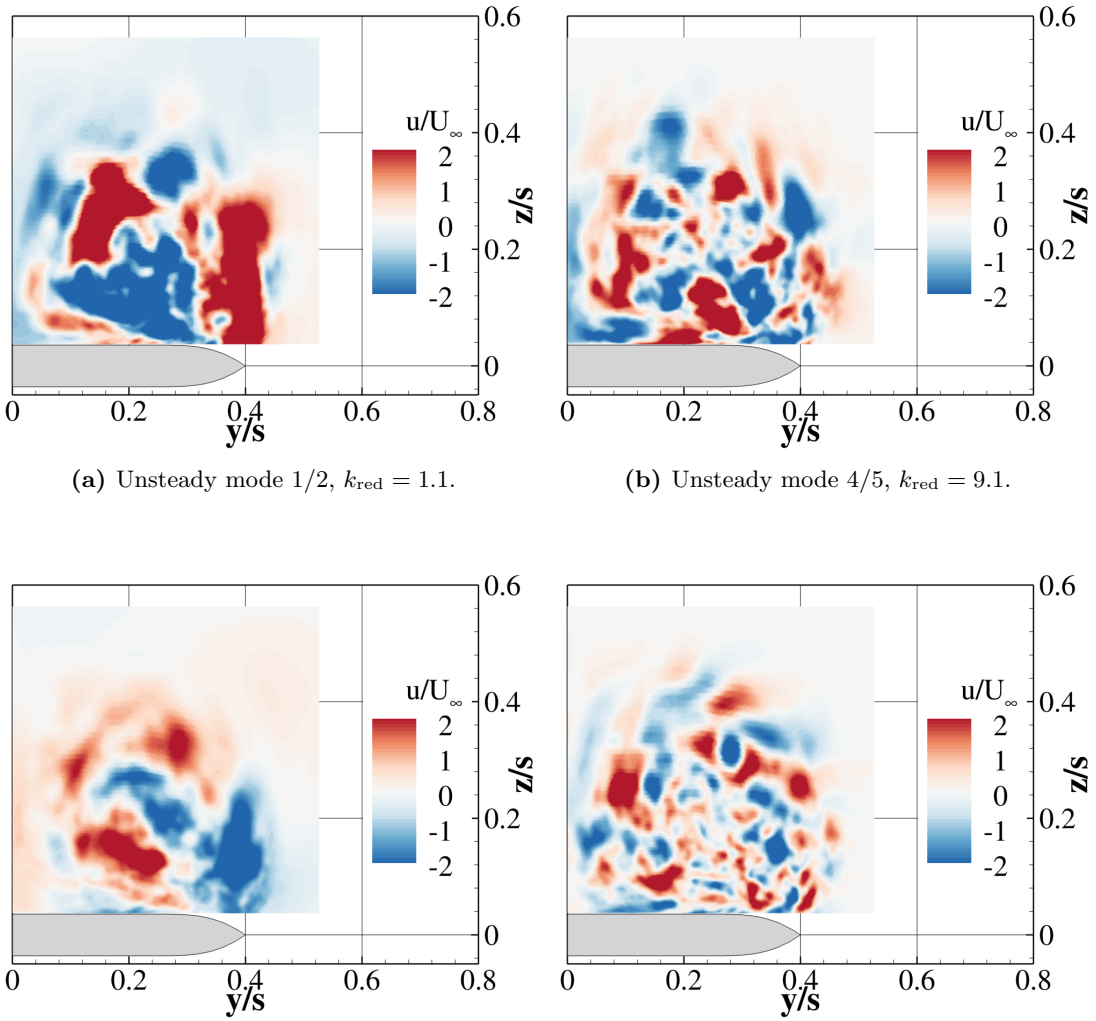

(a) Unsteady mode 1/2, $k_{\mathrm{red}} = 1.1$.

(b) Unsteady mode 4/5, $k_{\mathrm{red}} = 9.1$.

(c) Unsteady mode 6/7, $k_{\mathrm{red}} = 1.7$.

(d) Unsteady mode 8/9, $k_{\mathrm{red}} = 13.6$.

Figure 5.82: DMD modes of the velocity field in the vortex crossflow plane $x/c_r = 0.4$, $\alpha = 45°$, $F^+ = 1.0$.

5.6.3 Synthesis

Dominant dynamic mode spectra are compared to PSD distribution of monitored velocities in the shear layer roll-up path. PSD and DMD frequencies correlate indicating increased periodic activity. Dynamic modes from planar x-velocity distribution reveal structures at corresponding dominant frequency and highlighting different types of instabilities. The dimension of periodic structures correlate with the mode frequency. In crossflow planes based on the frequency and amplitude distributions the following instabilities were identified: vortex shedding, KH instabilities, vortex meandering and unsteady regions at interaction zones. Pulsed blowing increases the energy at discrete frequencies (and higher harmonics) triggering/enhancing/cancelling instabilities.

6 Conclusion and Outlook

Pulsed blowing affecting the delta-wing flow and its potential to stabilise vortex flow around stall was investigated in detail in the current work, which can be broadly separated into two phases. In the first phase, wind-tunnel balance measurements determined the aerodynamic coefficients for various actuation parameters and strategies. Based on the lift increase with respect to baseline, the most efficient of each actuation strategy was subsequently investigated by means of stereoscopic particle image velocimetry (PIV). By adding crossflow and vortex-longitudinal planes, the resolution increased significantly in the third direction. The wind-tunnel testing was performed for combinations of three angles of attack and four actuation modes: baseline, unison blowing, frequency variation and phase variation. Both the flow field and aerodynamic coefficients were most affected when synchronising the unsteady jets. Desynchronised blowing, either by varying the blowing frequency or the phase delay in the longitudinal direction, mitigated the positive effect of the actuators. Therefore, the subsequent investigations focused only on baseline and frequency-conditioned unison blowing for three high-angle-of-attack flow conditions: pre stall, near stall and post stall.

In the second phase, the transient response of the flow field towards pulsed blowing was analysed with phase-locked PIV and transient detached eddy simulations (DES). The phase-averaged investigations were conducted by triggering the PIV sampling sequence using the blowing signal. Data gathered from eight equally spaced phases of one blowing cycle determined a flow-field response to synchronised blowing, which is similar at all three angles of attack investigated. DES were conducted on the SuperMUC high performance computer cluster for each of the six flow cases. The validity of the approach was supported by the good agreement between the numerical and the experimental data. The scale-resolving capability of DES aided in identifying discrete structures and flow-inherent instabilities. Pulsed blowing is able to manipulate instabilities within the shear layer, generating stronger vortices. These vortices are then convected in a spiral downstream, increasing the momentum transport between the outer and the inner flow region. This leads to an average reduction of the wake-type flow region downstream of the vortex breakdown location.

A number of key research questions were posed at the beginning of this work that are now, as a result of experimental and numerical investigations, able to be addressed:

How does the time-averaged 3D flow structure above the wing at high angles of attack respond to pulsed blowing? The time-averaged flow field reveals vortex bursting at $\alpha = 23°$ and $35°$ and stalled flow at $\alpha = 45°$. In the former, pulsed blowing led to postponed breakdown and in the latter to the reattachment of flow to the upper wing surface. Spatially synchronised pulsed blowing outperformed desynchronised blowing, either by downstream decreasing pulse frequency $f \sim 1/x$ or increasing phase delay $\theta \sim x$ as indicated by wake/reversed-flow volume reduction. This correlates with the increase in aerodynamic coefficients.

What is the effect of frequency modulation on the flow field? Downstream decreasing actuation frequency mimics the conical flow, however, it performs second best, with less effect on the flow than synchronised blowing. In addition, when frequency decreases downstream, phase automatically decreases, which reduces the wake-type flow region more than downstream increasing phase.

How does desynchronised jets affect the flow field and the aerodynamic characteristics? Synchronised blowing introduces periodic disturbance in a "two-dimensional" manner. However, the resulting vortex shedding is in fact three-dimensional: it starts at the apex and continuously progresses downstream. As a result, stabilising vortical substructures are generated in the rolled-up shear layer. With spatially modulated blowing, either by phase or frequency, disturbances are introduced within the shear layer in a three-dimensional manner. Compared to synchronous blowing, desynchronised blowing alters the vortex shedding mechanism generating weaker substructures with a less stabilising effect on the macroscopic leading-edge vortex, thus, the aerodynamic performance is reduced. Balance measurements showed that increasing the phase delay downstream further reduces the effect of Active Flow Control (AFC).

What is the fundamental interaction of the periodic jets with the shear layer? Statistically averaged phase-dependent data determines the probability of vortex events occurring at the corresponding phase of blowing. This experimental investigation showed a disruption of the separated shear-layer subsequent to the jet pulse. Despite the fact that the jets were active concomitantly, the disruption propagated downstream with an increasing delay. After the shear-layer disruption, the growth of discrete vortex events is initiated. DES also revealed discrete vortex structures growing and winding downstream in the opposite direction, but rotating in time in the same direction as the resulting vorticity.

What are the mechanisms that lead to breakdown delay and shear-layer reattachment at optimal actuation parameters? Pulsed blowing ordered and enhanced the discrete vortices and in a periodic manner energised the reduced energy wake-type flow region of low velocities. Increasing the momentum coefficient also increases the magnitude of the periodic flow response. In conclusion, momentum injection generates intense vortices that periodically enhance momentum transport across the shear layer, which on average reduces the wake-type flow region downstream of vortex breakdown. Figure 6.1 presents the processes leading to both effects.

What kind of instabilities are manipulated? Dynamic mode decomposition (DMD) applied on the transient DES data revealed different dominant modes at frequencies similar to peaks in the power spectral densities of velocities recorded in unsteady flow regions during wind-tunnel testing. The flow proved to be complex comprising of several instabilities occurring in the vortical flow field. Although AFC is operated at one frequency, the periodic jet injection triggers vortex-flow instabilities coexisting on a broad frequency spectrum, including shear-layer instabilities (Kelvin-Helmholtz), helical-mode instabilities, and periodic flow motion, e.g. vortex core meandering/winding.

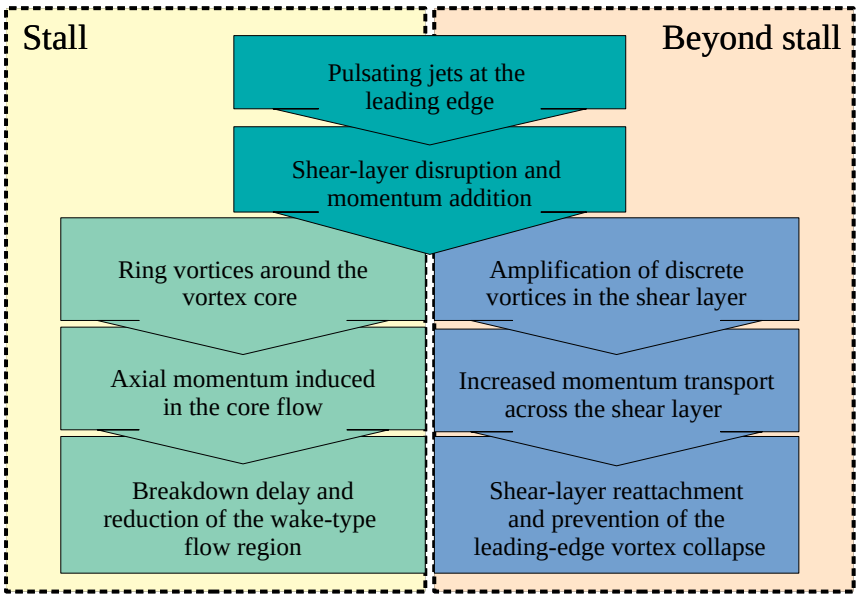

Figure 6.1: The consequences of flow manipulation through pulsed blowing under stall and beyond stall conditions.

Dynamic mode decomposition proves to be useful in identifying periodic dominant modes of the flow, thus, aiding the analysis of the complex vortex system dynamics with and without AFC. Lower dimensional models for robust and fast feedback loop control can be generated from the most dominant DMD modes. Additionally, knowing the location, size and frequency of (un)stable periodic flow features/structures can lead to increasing the efficiency of flow control devices if they are placed in these regions.

It is only a matter of time before AFC of vortex-dominated flows matures into an applied technology. The combination of early design integration and off-design operation of feedback-loop controlled AFC provides a promising increase in performance and efficiency of wing configurations. Additionally, this unlocks the possibility of resigning all moving control surfaces, e.g. ailerons, flaps, rudders, which reduces structural weight and complexity considerably. Rapidly improving machine-learning algorithms and progress in microelectronics can further improve aerodynamic efficiency. These changes will provide attractive and affordable implementations, making air transportation more efficient and sustainable.

Bibliography

[1] ANSYS Academic Research, Release 19.2, *Fluent Theory Guide*, Ansys Inc.

[2] ANSYS Academic Research, Release 19.2, *Fluent User's Guide*, Ansys Inc.

[3] *On the Vortex Breakdown Phenomenon in High Angle of Attack Flows Over Delta Wing Geometries*, volume Volume 1: Advances in Aerospace Technology of *ASME International Mechanical Engineering Congress and Exposition*, 2014.

[4] M. Amitay, A.E. Washburn, S.G. Anders, D.E. Parekh, and A. Glezer. Active Flow Control on the STINGRAY UAV: Transient Behaviour. In *33rd AIAA Fluid Dynamic Conference and Exhibit, AIAA 2003-4001*, Orlando, FL, 2003.

[5] N. Aubry. On the Hidden Beauty of the Proper Orthogonal Decomposition. *Theoretical and Computational Fluid Dynamics*, 2:339–352, 1991.

[6] J. Bartasevicius. Delta Wing Flow Manipulation by Unsteady, Spatially Varying Leading-Edge Blowing. Final Report for Individual Project ENG 5041P, University of Glasgow, 2016.

[7] J. Bartasevicius, A. Buzica, and C. Breitsamter. Discrete Vortices on Delta Wings with Unsteady Leading-Edge Blowing. In *8th AIAA Flow Control Conference, AIAA Paper 2016-3170*, Washington, DC, 2016.

[8] A. Batikh, L. Baldas, and S. Colin. Application of Active Flow Control on Aircrafts - State of the Art. In *International Workshop on Aircraft System Technologies, hal-01820331*, Hamburg, Germany, 2017.

[9] M. Bauer, T. Grund, W. Nitsche, and V. Ciobaca. Wing Tip Drag Reduction at Nominal Take-Off Mach Number: An Approach to Local Active Flow Control with a Highly Robust Actuator System. *Aerospace*, 3(4):1–36, 2016.

[10] M. Biswanger. DES Strömungssimulationen fur hoch anfestellte Deltaflügel und Untersuchung einer rückgekoppelten Strömungsbeeinflussung. Master's thesis, Technische Universität München, 2017.

[11] M. Biswanger. Zeitechte, numerische Strömungssimulationen an einem Deltaflügel mit Ausblasschlitzen im Post-Stall-Bereich. Semesterarbeit, Technische Universität München, 2017.

[12] C. Breitsamter. Unsteady Flow Phenomena Associated with Leading-Edge Vortices. *Progress in Aerospace Sciences*, 44(1):48–65, 2008.

[13] J. Brett and A. Ooi. Effect of Sweep Angle on the Vortical Flow over Delta Wings at an Angle of Attack of 10°. *Journal of Engineering Science and Technology*, 9(6):768–781, 1990.

[14] C.E. Brown and W.H. Michael. On Slender Delta Wings with Leading-Edge Separation. Technical Report 3430, NACA TN, 1955.

[15] G.L. Brown and J.M. Lopez. Axisymmetric Vortex Breakdown Part II: Physical Mechanisms. *Journal of Fluid Mechanics*, 221:553–576, 1990.

[16] A. Buzica, J. Bartasevicius, and C. Breitsamter. Active Vortex Flow Control on a Generic Delta Wing. In *30th Congress of the International Council of the Aeronautical Sciences*, Daejon, Korea, 2016.

[17] A. Buzica, J. Bartasevicius, and C. Breitsamter. Experimental Investigation of High-Incidence Delta-Wing Flow Control. *Experiments in Fluids*, 58:1–16, 2017.

[18] A. Buzica, M. Biswanger, and C. Breitsamter. Detached-Eddy Simulation of Delta-Wing Post-Stall Flow Control. *Transportation Research Procedia*, 9:46–57, 2018.

[19] A. Buzica and C. Breitsamter. Experimental and Numerical Investigation on Delta-Wing Post-stall Flow Control. In A. et al. Dillmann, editor, *New Results in Numerical and Experimental Fluid Mechanics XI*, volume 136 of *Notes on Numerical Fluid Mechanics and Multidisciplinary Design*, pages 167–179. Springer, Cham, 2018.

[20] A. Buzica and C. Breitsamter. Turbulent and Transitional Flow Around the AVT-183 Diamond Wing. *Aerospace Science and Technology*, 92:520–535, 2019.

[21] A. Buzica and C. Breitsamter. Pulsed Blowing Interacting with a Leading-Edge Vortex. *Aerospace*, 7(1), 2020.

[22] A. Buzica and C. Breitsamter. Manipulation of Leading-Edge Vortex Flow. In R. Radespiel and R. Semaan, editors, *Fundamentals of High Lift for Future Civil Aircraft*, volume 145 of *Notes on Numerical Fluid Mechanics and Multidisciplinary Design*. Springer, Cham, 2021.

[23] A. Buzica, L. Debschütz, F. Knoth, and C. Breitsamter. Leading-edge Roughness Affecting Diamond-Wing Aerodynamic Characteristics. *Aerospace*, 5(3), 2018.

[24] L.N. Cattafesta III and M. Sheplak. Actuators for Active Flow Control. *Annual Review of Fluid Mechanics*, 43:247–272, 2011.

[25] C. Çetin, A. Çelik, and M.M. Yavuz. Control of Flow Structure over a Nonslender Delta Wing Using Periodic Blowing. *AIAA Journal*, 56(1):90–99, 2018.

[26] J.J. Charonko and P.P. Vlachos. Estimation of Uncertainty Bounds for Individual Particle Image Velocimetry Measurements from Cross Correlation Peak-Ratio. *Measurements Science and Technology*, 24(6):065301, 2013.

[27] H. Chen and J.-J. Wang. Vortex Structures for Flow over a Delta Wing with Sinusoidal Leading Edge. *Experiments in Fluids*, 55(1761), 2014.

[28] C.F. Chenault, J. Dorris III, D. Smith, and V. Kibens. Active Core Exhaust (ACE) Control of Reduction of Thermal Loading. In *Fluids 2000 Conference and Exhibit, AIAA 2000-2471*, pages 1–11, 2000.

[29] J. Chu and J.M. Luckring. Experimental Surface Pressure Data Obtained on 65° Delta Wing Across Reynolds Number and Mach Number Ranges. Technical Report NASA/TM-4645, NASA Langley Research Center, Hampton, VA, 1996.

[30] S.S. Collis, R.D. Joslin, A. Seifert, and V. Theofilis. Issues in active flow control: theory, control, simulation, and experiment. *Progress in Aerospace Sciences*, 40(4-5):237–289, 2004.

[31] D.A. Compton and J.P. Johnston. Streamwise Vortex Production by Pitched and Skewed Jets in a Turbulent Boundary Layer. *AIAA Journal*, 30(3):640–647, 1992.

[32] W.M. Crowther, M. Jabbal, and S.C. Liddle. Flow Control Fallacies: A Review of Commonpitfalls in Flow Control Research. *Proceedings of the Institution of Mechanical Engineers, Part G: Journal of Aerospace Engineering*, 225(1):1–11, 2011.

[33] R.M. Cummings, S.A Morton, and S.G. Siegel. Computational Simulations and Experimental Measurements for a Delta Wing with Periodic Suction and Blowing. *Journal of Aircraft*, 40(5):923–931, 2003.

[34] P.B. Earnshaw and J.A. Lawford. Low-Speed Wind-Tunnel Experiments on a Series of Sharp-Edged Delta Wings. Technical Report 3424, Aeronautical Research Council. Reports and Memoranda, 1964.

[35] A. Furman and C. Breitsamter. Turbulent and Unsteady Flow Characteristics of Delta Wing Vortex Systems. *Aerospace Science and Technology*, 24:32–44, 2013.

[36] M. Gad-El-Hak. Introduction to Flow Control. In *Flow Control - Fundamentals and Practices*, pages 1–108. Cambridge Univ. Press, 1998.

[37] M. Gad-El-Hak and R.F. Blackwelder. The Discrete Vortices from a Delta Wing. *AIAA Journal*, 23(6):961–962, 1985.

[38] M. Gad-El-Hak and R.F. Blackwelder. Control of the Discrete Vortices from a Delta Wing. *AIAA Journal*, 25(8):1042–1049, 1987.

[39] Q. Gao, C. Ortiz-Dueñas, and E.K. Longmire. Analysis of Vortex Populations in Turbulent Wall-Bounded Flows. *Journal of Fluid Mechanics*, 678:87–123, 2011.

[40] K. Gersten. Calculation of Non-Linear Aerodynamic Stability Derivatives of Aeroplanes. Technical Report 342, AGARD Report, 1961.

[41] R.E. Gordnier and M.R. Visbal. Compact Difference Scheme Applied to Simulation of Low-Sweep Delta Wing Flow. *AIAA Journal*, 43(8):1744–1752, 2005.

[42] D. Greenblatt, B. Nishri, A. Darabi, and I. Wygnanski. Some Factors Affecting Stall Control with Particular Emphasis on Dynamic Stall. In *30th Fluid Dynamics Conference, AIAA 99-3504*, Norfolk, VA, 1999.

[43] D. Greenblatt, K.B. Paschal, C.S. Yao, and J. Harris. Experimental Investigation of Separation Control Part 2: Zero Mass-Flux Oscillatory Blowing. *AIAA journal*, 44(12):2831–2845, 2006.

[44] D. Greenblatt and I. Wygnanski. The Control of Flow Separation by Periodic Excitation. *Progress in aerospace Sciences*, 36(7):487–545, 2000.

[45] W. Gu, O. Robinson, and D. Rockwell. Control of Vortices on a Delta Wing by Leading-Edge Injection. *AIAA Journal*, 31(7):1177–1186, 1993.

[46] Z. Guoqing and Q. Zhao. Parametric Analysis for Synthetic Jet Control on Separation and Stall over Rotor Airfoil. *Chinese Journal of Aeronautics*, 27(5):1051–1061, 2014.

[47] I. Gursul. Effect of Nonaxisymmetric Forcing on a Swirling Jet with Vortex Breakdown. In *3rd Shear Flow Conference*, Orlando, FL, 1993.

[48] I. Gursul. Unsteady Flow Phenomena over Delta Wings at High Angles of Attack. *AIAA Journal*, 32(2):225–231, 1994.

[49] I. Gursul. Recent Developments in Delta Wings Aerodynamics. *The Aeronautical Journal (1968)*, 108:437–452, 2004.

[50] I. Gursul. Review of unsteady vortex flows over delta wings. *Journal of Aircraft*, 42(2):299–319, 2005.

[51] I. Gursul, S. Srinivas, and G. Batta. Active Control of Vortex Breakdown over a Delta Wing. *AIAA Journal*, 33(9):1743–1745, 1995.

[52] I. Gursul, E. Vardaki, and Z. Wang. Active and Passive Control of Reattachment on Various Low-Sweep Wings. In *44th AIAA Aerospace Sciences Meeting and Exhibit, AIAA-2006-506*, Reno, NV, 2005.

[53] I. Gursul and Z. Wang. Flow Control of Tip/Edge Vortices. *AIAA Journal*, 56(5):1731–1749, 2018.

[54] I. Gursul, Z. Wang, and E. Vardaki. Review of Flow Control Mechanisms of Leading-Edge Vortices. *Prog. Aerosp. Sci.*, 43(7-8):246–270, 2007.

[55] Y. Guy, J.A. Morrow, and T.E. McLaughlin. Control of vortex breakdown on a delta wing by periodic blowing and suction. In *37th AIAA Aerospace Sciences Meeting and Exhibit, AIAA 99-0132*, Reno, NV, 1999.

[56] M.G. Hall. A Theory for the Core of a Leading-Edge Vortex. *Journal of Fluid Mechanics*, 11(2):209–228, 1961.

[57] M.G. Hall. Vortex Breakdown. *Annual Review of Fluid Mechanics*, 4:195–218, 1972.

[58] G. Haller. An Objective Definition of a Vortex. *Journal of Fluid Mechanics*, 525:1–26, 2005.

[59] M.S. Hemati, M.O. Williams, and C.W. Rowley. Dynamic Mode Decomposition for Large and Streaming Datasets. *Physics of Fluids*, page 111701, 2014.

[60] P. Hemon and F. Santi. Simulation of a Spatially Correlated Turbulent Velocity Field Using Biorthogonal Decomposition. *Journal of Wind Engineering and Industrial Aerodynamics*, 95:21–29, 2007.

[61] M.J. Hemsch and J.M. Luckring. Connection between Leading-Edge Sweep, Vortex Lift, and Vortex Strength for Delta Wings. *Journal of Aircraft*, 27(5):473–475, 1990.

[62] S.M. Hitzel and R. Osterhuber. Enhanced Maneuverability of a Delta-Canard Combat Aircraft by Vortex Flow Control. *Journal of Aircraft*, 55(3):1090–1102, 2017.

[63] M.A. Hossain, R. Prenter, R.K. Lundgreen, L.M. Agricola, A. Ameri, J.W. Gregory, and J.P. Bons. Investigation of Crossflow Interaction of an Oscillating Jet. In *55th AIAA Aerospace Sciences Meeting, AIAA 2017-1690*, Grapevine, TX, 2017.

[64] A. Hövelmann. *Analysis of Partly-Developed Leading-Edge Vortices.* dissertation, Technische Universität München, 2016.

[65] A. Hövelmann, M. Grawunder, A. Buzica, and C. Breitsamter. AVT-183 Diamond Wing Flow Field Characteristics Part 2: Experimental Analysis of Leading-Edge Vortex Formation and Progression. *Aerospace Science and Technology*, 57:31–42, 2016.

[66] A. Hövelmann, F. Knoth, and C. Breitsamter. AVT-183 Diamond Wing Flow Field Characteristics Part 1: Varying Leading-Edge Roughness and the Effects on Flow Separation Onset. *Aerospace Science and Technology*, 57:18–30, 2016.

[67] A. Huang, J. Lew, Y. Xu, Y.-C. Tai, and C.-M. Ho. Microsensors and Actuators for Macrofluidic Control. *IEEE Sensors Journal*, 4(4):494–502, 2004.

[68] D. Hummel. On The Vortex Formation over a Slender Wing at Large Angles of Incidence. In *High Angles of Attack Aerodynamics*, number AGARD-CP-247, 1978.

[69] D. Hummel and H.-C. Oelker. Vortex Interference Effects on Closecoupled Canard Configuration at Low Speed. In *Aerodynamics of Combat Aircraft Controls and of Ground Effects*, number AGARD-CP-465, 1989.

[70] D.J. Hummel. The International Vortex Flow Experiment 2 (VFE-2): Background, Objectives and Organization. *Aerospace Science and Technology*, 24(1):1–9, 2003.

[71] D.J. Hummel. The Second International Vortex Flow Experiment (VFE-2): Objectives and Present Status. In *25th Applied Aerodynamics Conference, AIAA 2007-4446*, Miami, FL, 2007.

[72] D.J. Hummel. The Second International Vortex Flow Experiment (VFE-2): Results of the First Phase 2003–2008. In *26th Congress of the International Council of Aeronautical Sciences, ICAS 2008-3.3.1 (invited)*, Anchorage, AK, 2008.

[73] J.C.R. Hunt, A.A. Wray, and P. Moin. Eddies, Stream and Convergence Zones in Turbulent Flows. Technical Report CTR-S88, Center for Turbulence Research Report, 1988.

[74] Mark Jabbal and Valerio Tomasso. Sensitivity Analysis of Active Flow Control Systems: Operating Parameters and Configuration Design. *Journal of Aircraft*, 51(1):330–335, 2014.

[75] M. Jentzsch, L. Taubert, and I. Wygnanski. Using Sweeping Jets to Trim and Control a Tailless Aircraft Model. *AIAA Journal*, 57(6):2322–2334, 2019.

[76] J. Jeong and F. Hussain. On the Identification of a Vortex. *Journal of Fluid Mechanics*, 285:69–94, 1995.

[77] R.D. Joslin. Overview of Laminar Flow Control. Technical Report NASA/TP-1998-208705, NASA Langley Research Center, Hampton, VA, 1998.

[78] A. Khodadoust and A Shmilovich. High Reynolds Number Simulation of Distributed Active Flow Control for a High-Lift System. In *25th AIAA Applied Aerodynamics Conference, AIAA 2007-4423*, 2007.

[79] J. Kiedaisch, H. Nagib, and B. Demanett. Active Flow Control Applied to High-Lift Airfoils Utilizing Simple Flaps. In *3rd AIAA Flow Control Conference, AIAA 2006-2865*, 2006.

[80] J.M. Kirshner, editor. *Fluid Amplifiers*. New York: McGraw-Hill, 1966.

[81] V. Kolář. Vortex Identification: New Requirements and Limitations. *International Journal of Heat and Fluid Flow*, 28:638–652, 2007.

[82] A. Kölzsch. *Active Flow Control of Delta Wing Leading-Edge Vortices*. dissertation, Technische Universität München, 2017.

[83] A. Kölzsch, S. Blanchard, and C. Breitsamter. Dynamic Actuation for Delta Wing Post Stall Flow Control. In A. Dillmann, G. Heller, E. Krämer, C. Wagner, and Christian Breitsamter, editors, *New Results in Numerical and Experimental Fluid Mechanics X, Notes on Numerical Fluid Mechanics and Multidisciplinary Design 132*, pages 823–832, Cham, 2016. Springer International Publishing.

[84] A. Kölzsch and C. Breitsamter. Vortex-flow manipulation on a generic delta-wing configuration. *Journal of Aircraft*, 51(5):1380–1390, 2014.

[85] R. Konrath, C. Klein, A. Schröder, and J. Kompenhans. Combined Application of Pressure Sensitive Paint and Particle Image Velocimetry. *Experiments in Fluids*, 44:357–366, 2008.

[86] L.D. Kral, J.F. Donovan, A.B. Cain, and A.W. Cary. Numerical Simulation of Synthetic Jet Actuators. In *4th Shear Flow Control Conference, AIAA*, page 1824, Snowmass Village, CO, 1997.

[87] R.M. Kulfan. Wing Airfoil Shape Effects on the Development of Leading Edge Vortices. In *5th AIAA Atmospheric Flight Mechanics Conference on Future Space Systems*, pages 1–27, 1979.

[88] M. Lee and C.M. Ho. Vortex Dynamics of Delta Wings. In *Frontiers in Experimental Fluid Mechanics, Lecture Notes in Engineering*, volume 46, pages 365–427, Berlin, 1989. Springer-Verlag.

[89] M. Lengers. Industrial Assessment of Overall Aircarft Driven Local Active Flow Control. In *29th Congress of the International Council of the Aeronautical Sciences*, St. Petersburg, Russia, 2014.

[90] J.C. Lin, M.Y. Andine, M.G. Alexander, E.A. Whalen, M.A. Spoor, J.T. Tran, and I.J. Wygnanski. An Overview of Active Flow Control Enhanced Vertical Tail Technology Development. In *54th AIAA Aerospace Sciences Meeting*, San Diego, CA, 2016.

[91] Y. Liu, M. Wu, J.J. Zhu, D.A. Lawrence, E.J. Gutmark, J.H. Myatt, and C.A. May. Reactive Flow Control of Delta-Wing Vortex. *Journal of Aircraft*, 45(3):880–892, 2008.

[92] W.K. Lord, D.G. MacMartin, and T.G. Tillman. Flow Control Oportunities in Gas Turbine Engines. In *Fluids 2000 Conference and Exhibit, AIAA 2000-2234*, pages 1–15, 2000.

[93] R. Lynn and I. Gursul. Vortex Dynamics on a Generic UCAV Configuration. In *44th Aerospace Sciences Meeting and Exhibit, AIAA 2006-0061*, Reno, NV, 2006.

[94] K.W. Mangler and J.H.B. Smith. A Theory of the Flow Past a Slender Delta Wing With Leading Edge Separation. In *Proceedings of the Royal Society*, volume 251, pages 200–217, 1959.

[95] S. Margalit, D. Greenblatt, A. Seifert, and I.J. Wygnanski. Delta wing stall and roll control using segmented piezoelectric fluidic actuators. *Journal of Aircraft*, 42(3):698–709, 2005.

[96] S. Mariappan, A.D. Garder, K. Richter, and M. Raffel. Analysis of Dynamic Stall Using Dynamic Mode Decomposition Technique. *AIAA Journal*, 52(11):2427–2–439, 2014.

[97] D.C. McCormick. Boundary Layer Separation Control with Directed Synthetic Jets. In *38th Aerospace Sciences Meeting & Exhibit, AIAA 2000-0519*, Reno, NV, 2000.

[98] J.M. Mcmichael. Progress and Prospects for Active Flow Control using Microfabricated Electromechanical Systems (MEMS). 1996.

[99] F.R. Menter. Zonal Two Equation $k - \omega$ Turbulence Models for Aerodynamic Flows. In *24th AIAA Fluid Dynamics Conference, AIAA 93-2906*, Orlando, FL, 1993.

[100] F.R. Menter. Best Practice: Scale-Resolving Simulations in Ansys CFD. Technical Report Version 2.0, Ansys Germany GmbH, Otterfing, Germany, 2015.

[101] F.R. Menter and M. Kunz. *Adaption of Eddy-Viscosity Turbulence Models to Unsteady Separated Flow Behind Vehicles*, pages 339–352. Springer, Berlin/Heidelberg, Germany, 2004.

[102] F. Meyer. Topographic Distance and Watershed Lines. *Signal Processing*, 38(1):113–125, 1994.

[103] A.M. Mitchell and J. Delery. Research into Vortex Breakdown Control. *Progress in Aerospace Sciences*, 37(4):385–418, 2001.

[104] A.M. Mitchell, S.A. Morton, J.R. Forsythe, and R.M. Cummings. Analysis of Delta-Wing Vortical Substructures Using Detached-Eddy Simulations. *AIAA Journal*, 44(5):964–973, 2006.

[105] A.M. Mitchell, S.A. Morton, P. Molton, and Y. Guy. Flow Control of Vortical Structures and Vortex Breakdown over Slender Wings. In *RTO Applied Vehicle Technology Panel (AVT) Symposium*, Leon, Norway, 2001.

[106] A.T. Mohan, R. Visbal, and D.V. Gaitonde. Model Reduction and Analysis of Deep Dynamic Stall on a Plunging Airfoil Using Dynamic Mode Decomposition. In *53rd AIAA Aerospace Sciences Meeting, AIAA 2015-1058*, Kissimmee, FL, 2015.

[107] R.C. Nelson and K.D. Visser. Breaking Down the Delta Wing Vortex—The Role of Vorticity in the Breakdown Process. In *Symposium on Vortex Flow Aerodynamics, Paper 21*, number AGARD-CP-494, 1990.

[108] T.T. Ng. On the Leading Edge Vlortex and Its Control. In *16th Atmospheric Flight Mechanics Conference, AIAA 89-3346*, Boston, MA, 1989.

[109] B. Nishri and I. Wygnanski. Efects of Periodic Excitation on Turbulent Separation from a Flap. *AIAA Journal*, 36(4):547–556, 1998.

[110] H.-C. Oelker and D. Hummel. Investigations on the Vorticity Sheets of a Closed Coupled Delta-Canard configuration. In *16th Congress of the International Council of the Aeronautical Sciences*, Jerusalem, Israel, 1988.

[111] M.V. Ol and M. Gharib. Leading-Edge Vortex Structure of Nonslender Delta Wings at Low Reynolds Number. *AIAA Journal*, 41(1):16–26, 2003.

[112] D. Oster, I. Wygnanski, B. Dziomba, and H. Fiedler. *The Effect of Initioal Conditions on the Two-Dimensional, Turbulent Mixing Layer*, volume 75, pages 48–64. Springer, Berlin, 1978.

[113] L.G. Pack and R.D. Joslin. Overview of Active Flow Control at NASA Langley Research Center. Technical Report 20040110283, NASA Langley Research Center, 1998.

[114] E.C. Polhamus. A Concept of the Vortex Lift of Sharp-Edge Delta Wings based on a Leading-Edge-Suction Analogy. Technical Report D-3767, NASA TN, 1966.

[115] E.C. Polhamus. Predictions of vortex-lift characteristics by a leading-edge suctionanalogy. *Journal of Aircraft*, 8(4):193–199, 1971.

[116] S.B. Pope. *Turbulent Flows*. Cambridge University Press, Cambridge, UK, 2000.

[117] L. Prandtl. Über Flüssigkeitsbewegung bei sehr kleiner Reibung. In *Third International Congress of Mathematicians at Heidelberg*, pages 484–491, Heidelberg, Germany, 1904.

[118] O.K. Rediniotis, H. Stapountzis, and D.P. Telionisn. Vortex Shedding over Delta Wings. *AIAA Journal*, 28(5):944–946, 1989.

[119] O.K. Rediniotis, H. Stapountzis, and D.P. Telionisn. Periodic Vortex Shedding over Delta Wings. *AIAA Journal*, 31(9):155–162, 1993.

[120] S. Rieger. Numerische Strömungsfeldanalyse zur rückgekoppelten Strömungsbeeinflussung an einem Deltaflügel. Bachelor's Thesis, Technische Universität München, 2017.

[121] D. Rockwell. Three-Dimensional Flow Structure on Delta Wings at High Angle-of-Attack: Experimental Concepts and Issues. In *31st AIAA Aerospace Sciences Meeting, AIAA 93-0550*, 1993.

[122] N.W. Schaeffler, T.E. Hepner, G.S. Jones, and M.A. Kegerise. Overview of Active Flow Control Actuator Development at NASA Langley Research Center, AIAA 2002-3159. In *1st Flow Control Conference*, pages 1–12, 2002.

[123] L.A. Schiavetta, K.J. Badock, and R.M. Cummings. Comparison of DES and URANS for Unsteady Vortical Flows over Delta Wings. In *45th AIAA Aerospace Science Meeting and Exhibit, AIAA 2007-1085*, Reno, NV, 2007.

[124] P.J. Schmid. Dynamic Mode Decomposition of Numerical and Experimental Data. *Journal of Fluid Mechanics*, 656:5–28, 2010.

[125] P.J. Schmid, K.E. Meyer, and O. Pust. Dynamic Mode Decomposition and Proper Orthogonal Decomposition of Flow in a Lid-Driven Cylindrical Cavity. In *8th International Symposium on Particle Image Velocimetry*, Melbourne, Australia, 2009.

[126] A. Schmücker and K. Gersten. Vortex Breakdown and Its Control on Delta Wings. *Fluid Dynamics Research*, 3:268–272, 1988.

[127] A. Sciacchitano, D.R. Neal, B.L. Smith, S.O. Warner, P.P. Vlachos, B. Wieneke, and F. Scarano. Collaborative framework for PIV Uncertainty Quantification: Comparative Assessment of Methods. *Measurements Science and Technology*, 26(7):074004, 2015.

[128] A. Sciacchitano, B. Wieneke, and F. Scarano. PIV Uncertainty Quantification by Image Matching. *Measurements Science and Technology*, 24(4):045302, 2013.

[129] A. Seifert, A. Darabi, and I. Wygnanski. Delay of Airfoil Stall by Periodic Excitation. *Journal of Aircraft*, 33(4):691–698, 1996.

[130] A. Seifert, S. Eliahu, D. Greenblatt, and I. Wygnanski. Use of Piezoelectric Actuators for Airfoil Separation Control. *AIAA Journal*, 36(8):1535–1537, 1998.

[131] L. Shen, Chen Z.-N., and C. Wen. Experimental Investigation of the Flow Structure over a Delta Wing via Flow Visualization Methods. *Journal of Visualized Experiments*, 134:e57244, 2018.

[132] A. Shmilovich and Y. Yadlin. Flow Control of Airplane Trailing Wakes. In *4th International Conference on Vortex Flows and Models*, Daejon, South Korea, 2008.

[133] A. Shmilovich and Y. Yadlin. Active Flow Control for Practical High-Lift Systems. *Journal of Aircraft*, 46(4):1354–1364, 2009.

[134] A. Shmilovich and Y. Yadlin. Flow Control Techniques for Transport Aircraft. *AIAA Journal*, 49(3):489–502, 2011.

[135] S.G Siegel, T.E. McLaughlin, and J.A. Morrow. PIV Measurements on a Delta Wing with Periodic Blowing and Suction. In *19th Applied Aerodynamics Conference, AIAA 2001-2436*, Anaheim, CA, 2001.

[136] J. Smagorinsky. General Circulation Experiments with the Primitive Equations: I. The Basic Equations. *Monthly Weather Review*, 91:99–164, 1963.

[137] P.R. Spalart and C. Streett. Young Person's Guide to Detached-Eddy Simulation Grids. Technical Report NASA/CR-2001-211032, 2001.

[138] H.B. Squire. On the Stability of Three-Dimensional Distribution of Viscous Fluid Between Parallel Walls. *Proceeding of the Royal Society A*, 142:621–628, 1933.

[139] M. Strelets. Detached Eddy Simulation of Massively Separated Flows. In *39th AIAA Aerospace Sciences Meeting and Exhibit, AIAA 2001-879*, Reno, NV, 2001.

[140] E. Tangermann, A. Furman, and C. Breitsamter. Detached Eddy Simulation Compared with Wind Tunnel Results of a Delta Wing with Sharp Leading Edge and Vortex Breakdown. In *30th AIAA Applied Aerodynamics Conference, AIAA 2012-3329*, New Orleans, LA, 2012.

[141] G. Taylor, Z. Wang, E. Vardaki, and I. Gursul. Lift Enhancement over Flexible Nonslender Delta Wings. *AIAA Journal*, 45(12):2979–2993, 2007.

[142] G.S. Taylor and I. Gursul. Buffeting Flows over a Low-Speed Delta Wing. *AIAA Journal*, 42(9):1737–1745, 2004.

[143] G.S. Taylor, T. Schnorbus, and I. Gursul. An Investigation of Vortex Flows over Low Sweep Delta Wings. In *33rd Fluid Dynamics Conference and Exhibit, Fluid Dynamics and Co-located Conferences, AIAA 2003-4021*, Orlando, FL, 2003.

[144] F. Ternoy, J. Dandois, F. David, and M. Pruvost. Overview of Onera Actuators for Active Flow Control. Technical Report hal-01184470, AerospaceLab, 2013.

[145] V. Theofilis. *Role of Instability Theory in Flow Control*, chapter 4, pages 73–114. AIAA, 2009.

[146] B.H. Timmins, B.W. Wilson, B.L. Smith, and P.P. Vlachos. A Method for Automatic Estimation of Instantaneous Local Uncertainty in Particle Image Velocimetry Measurements. *Experiments in Fluids*, 53(4):1133–1147, 2015.

[147] E. Vardaki, I. Gursul, and G. Taylor. Physical Mechanisms of Lift Enhancement for Flexible Delta Wings. In *43rd AIAA Aerospace Sciences Meeting and Exhibit, AIAA 2005-0867*, Reno, NV, 2005.

[148] N.G. Verhaagen, L.N. Jenkins, S.B. Kern, and A.E. Washburn. A Study of the Vortex Flow over a 76/40-deg Double-Delta Wing. In *33rd Aerospace Sciences Meeting and Exhibit, AIAA 95-0650*, Reno, NV, 1995.

[149] M.R. Visbal and R.E. Gordnier. Origin of Stationary Shear-Layer Sub-Structures above Delta Wings. In *Vortex Breakdown over Slender Delta Wings, RTO Technical Report AVT-080*, 2009.

[150] K.D. Visser and R.C. Nelson. Measurements of Circulation and Vorticity in the Leading-Edge Vortex of a Delta Wing. *Journal of Aircraft*, 31(1):104–111, 1993.

[151] C.Y. Wang, Q. Gao, T. Li, and J.J. Wang. 3D Flow Visualization and Tomographic Particle Image Velocimetry for Vortex Breakdown over a Non-Slender Delta Wing. *Experiments in Fluids*, 57:98, 2016.

[152] A.E. Washburn and M. Amitay. Active Flow Control on the STINGRAY UAV: Physical Mechanisms. In *42nd AIAA Aerospace Sciences Meeting and Exhibit, AIAA 2004-0745*, Reno, NV, 2004.

[153] B. Wieneke. PIV Uncertainty Quantification from Correlation Statistics. *Measurements Science and Technology*, 26(7):074002, 2015.

[154] N. Williams, Z. Wang, and I. Gursul. Active Flow Control on a Nonslender Delta Wing. In *46th AIAA Aerospace Sciences Meeting,AIAA-2008-0740*, Reno, NV, 2008.

[155] R. Wlezien. Micro Adaptive Flow Control. *The Aeronautical Journal (1968)*, 104(1040):453–458, 2000.

[156] B. Wood, E. Loth, and P. Geubelle. Mesoflaps for Aeroelastic Transpiration for SBLI Control. In *37th Aerospace Sciences Meeting & Exhibit, AIAA 99-0614*, pages 1–11, 1999.

[157] H. Yang and I. Gursul. Vortex Breakdown over Unsteady Delta Wings. *AIAA Journal*, 35(3):571–574, 1997.

[158] B. Yaniktepe and D. Rockwell. Flow Structure on a Delta Wing of Low Sweep Angle. *AIAA Journal*, 42(3):513–525, 2004.

[159] S.X. Ying, F.W. Spaid, C.B. McGinley, and C.L. Rumsey. Investigation of Confluent Boundary Layers in High-Lift Flows. *Journal of aircraft*, 36(3):550–562, 1999.

[160] B.Y. Zhou, N.R. Gauger, C. Tsolakis, J. Pardue, A. Chernikov, F. Drakopoulos, N. Chrisochoides, and B. Diskin. Hybrid RANS/LES Simulation of Vortex Breakdown Over a Delta Wing. In *AIAA Aviation 2019 Forum*, Dallas, TX, 2019.

[161] J. Zhou, R.J. Adrian, S. Balachandar, and T.M. Kendall. Mechanisms for Generation Coherent Packets of Hairpin Vortices in Channel Flow. *Journal of Fluid Mechanics*, 387:353–396, 1999.

[162] C. Zwerger. *Numerical Investigation of the Flow Field around a Delta Wing.* dissertation, Technische Universität München, 2016.

A Methodology

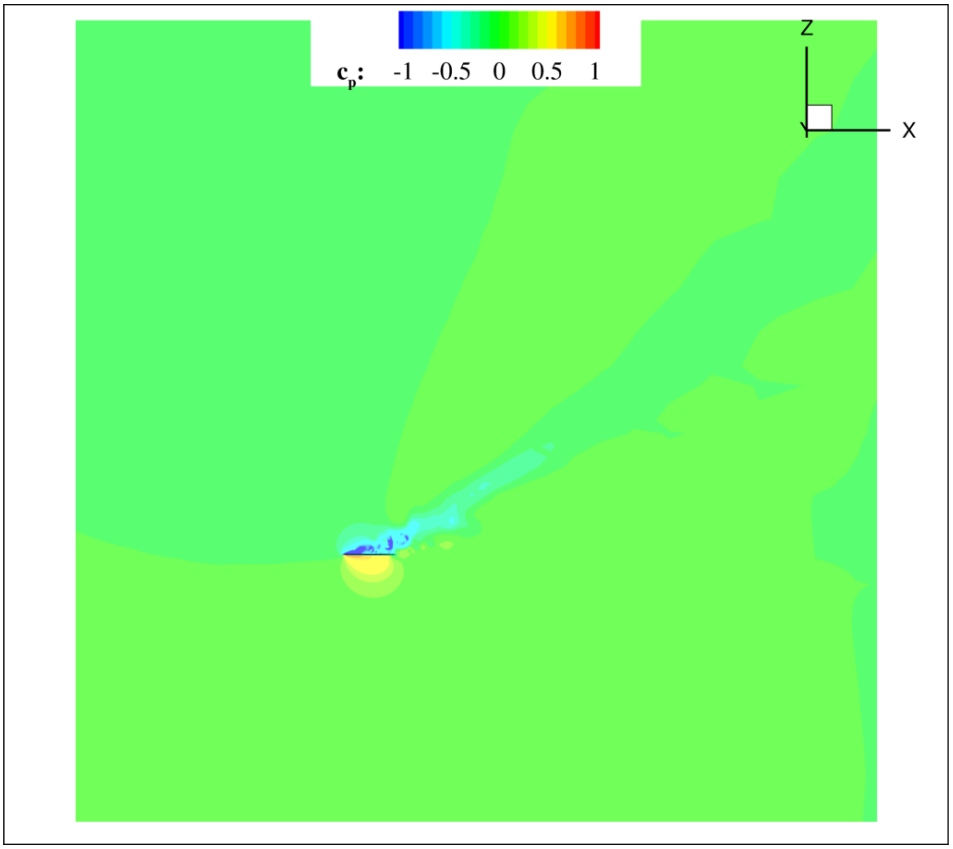

Figure A.1: Pressure coefficient in the symmetry plane. $\alpha = 45°$, $Re = 0.5 \cdot 10^6$, $F^+ = 1.0$.

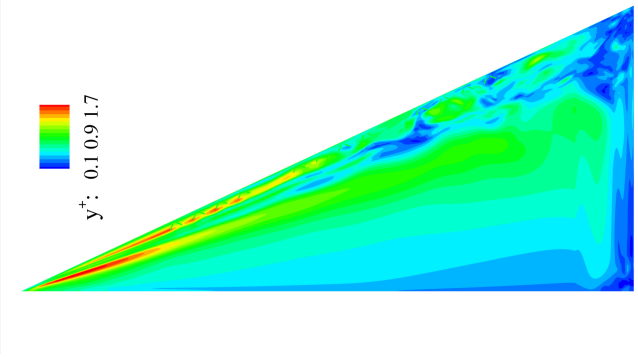

Figure A.2: Distribution of y^+ on the delta wing's upper surface. $\alpha = 23°$, $Re = 1.0 \cdot 10^6$, baseline.

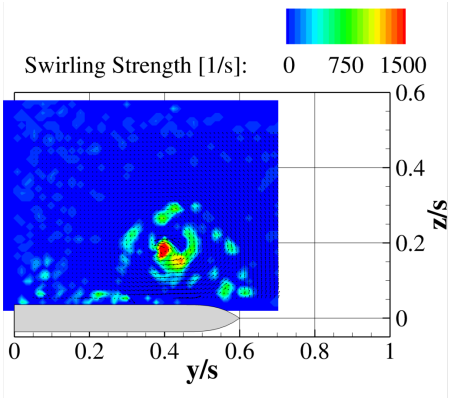

Figure A.3: Swirling strength. PIV Frame 200, $\alpha = 23°$, $x/c_r = 0.6$.

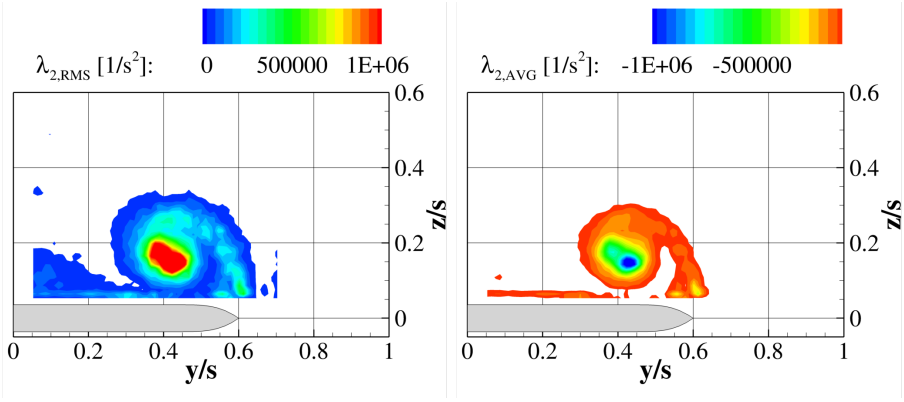

(a) λ_2, with rms Filter. **(b)** λ_2, with avg Filter.

Figure A.4: Filters based on $\lambda_{2,\mathrm{rms}}$ and $\lambda_{2,\mathrm{avg}}$.

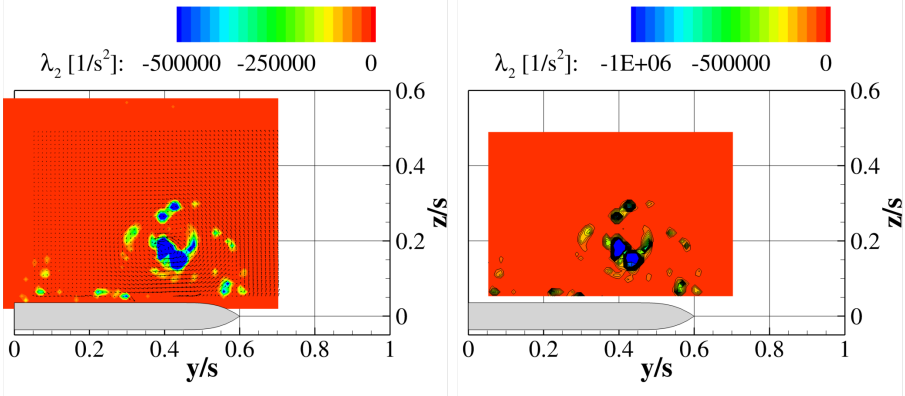

(a) λ_2, after rms-Filter. **(b)** λ_2, after avg-Filter.

Figure A.5: Frame 200, $\alpha = 23°$, $x/c_r = 0.6$, baseline. Vortex detection.

B Aerodynamic Characteristics

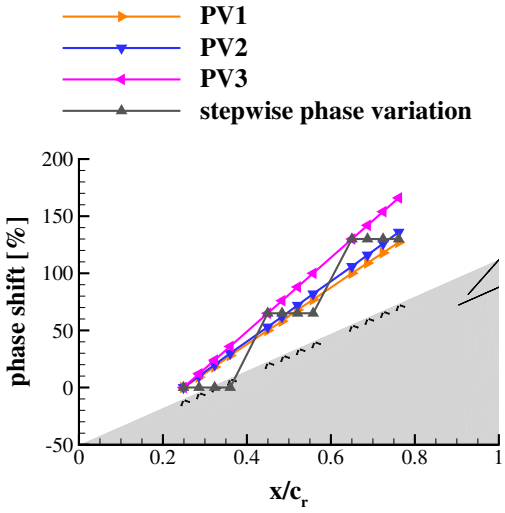

(a) Downstream phase shift.

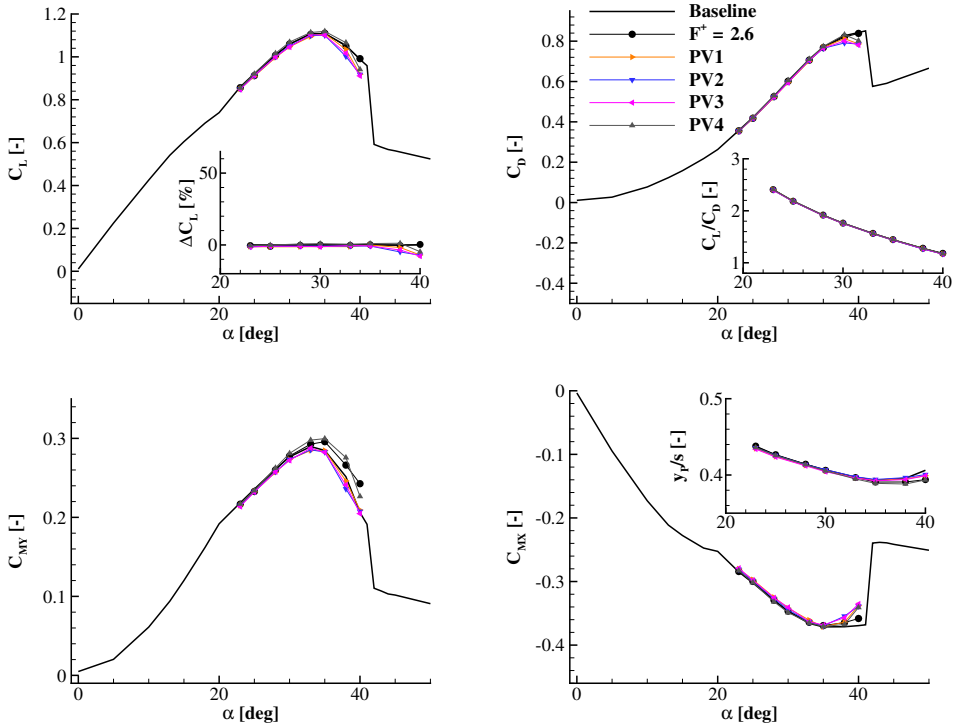

(b) Aerodynamic coefficients and derived variables.

Figure B.1: Effect of phase modulation on stall aerodynamic coefficients; $Re = 1.0 \cdot 10^6$, $F^+ = 2.6$.

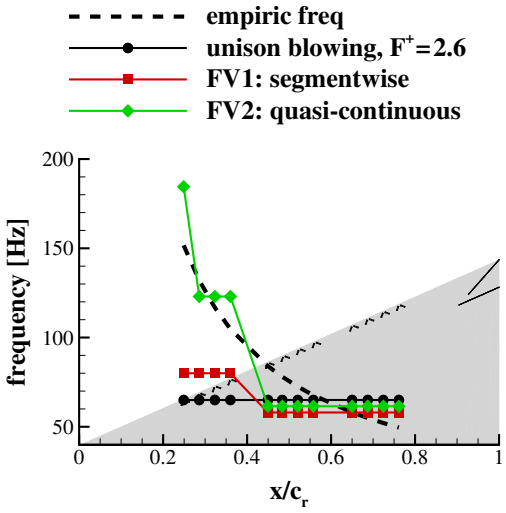

(a) Downstream frequency variation.

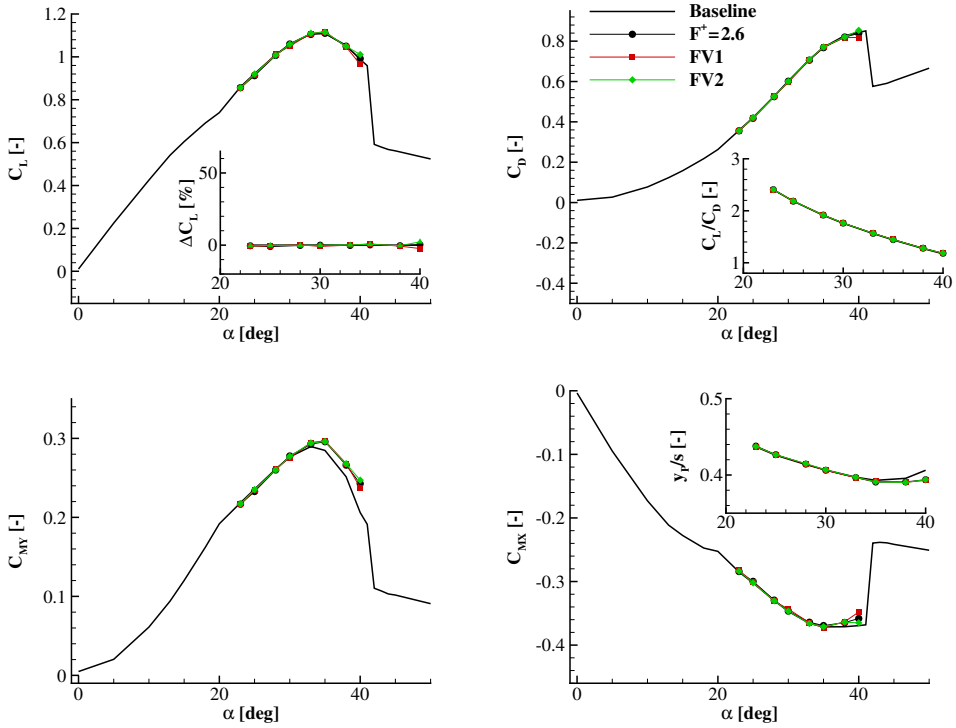

(b) Aerodynamic coefficients and derived variables.

Figure B.2: Effect of frequency variation on stall aerodynamic coefficients; $Re = 1.0 \cdot 10^6$.

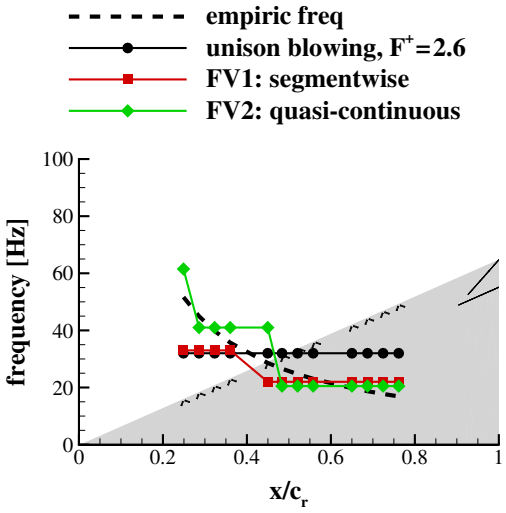

(a) Downstream frequency variation.

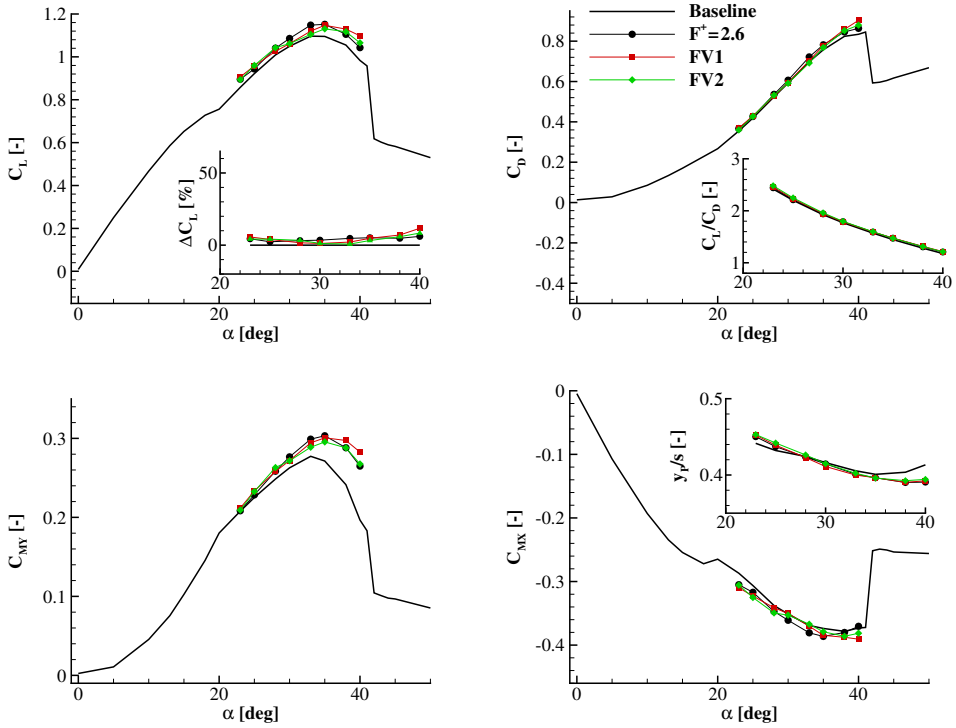

(b) Aerodynamic coefficients and derived variables.

Figure B.3: Effect of frequency variation on stall aerodynamic coefficients; $Re = 0.5 \cdot 10^6$.

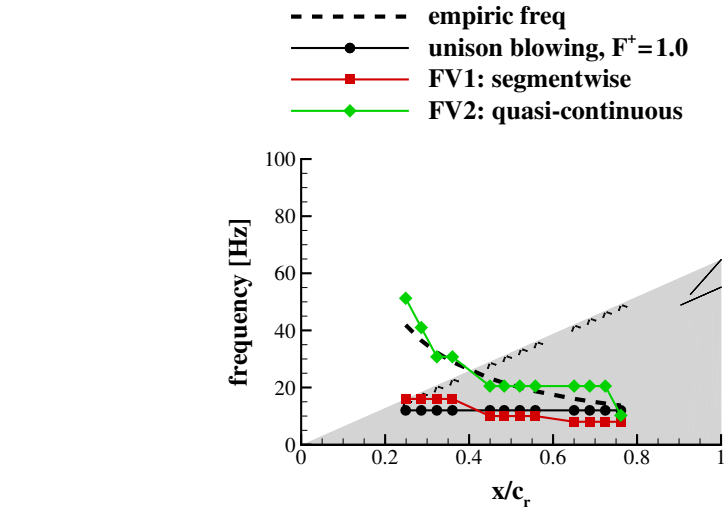

(a) Downstream frequency variation.

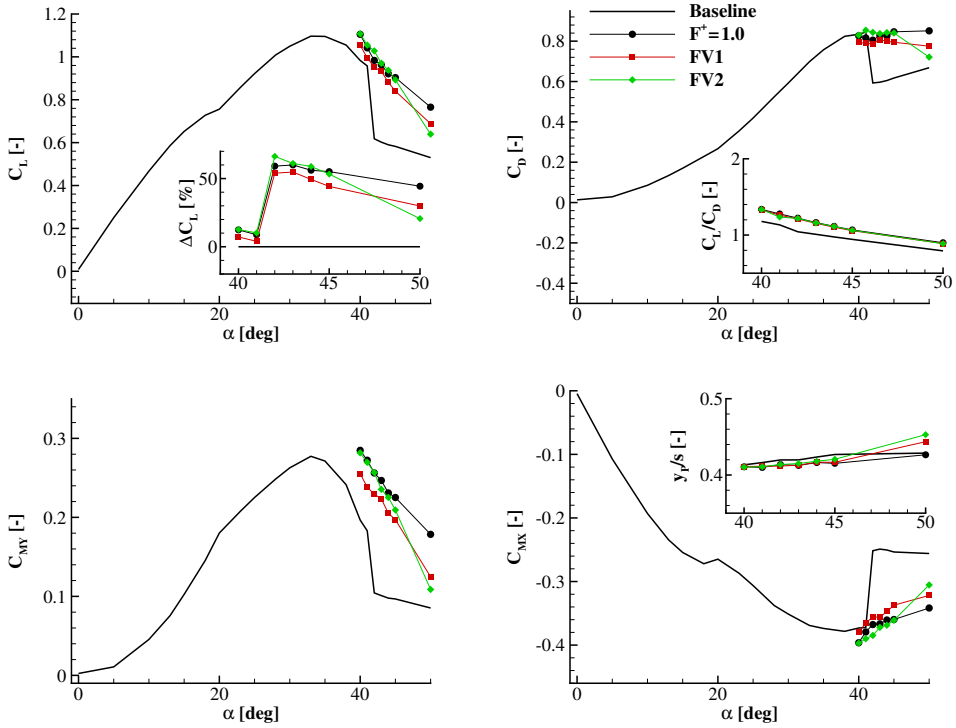

(b) Aerodynamic coefficients and derived variables.

Figure B.4: Effect of frequency variation on post-stall aerodynamic coefficients; $Re = 0.5 \cdot 10^6$.

C Flow Field Manipulation

C.1 Phase Definition

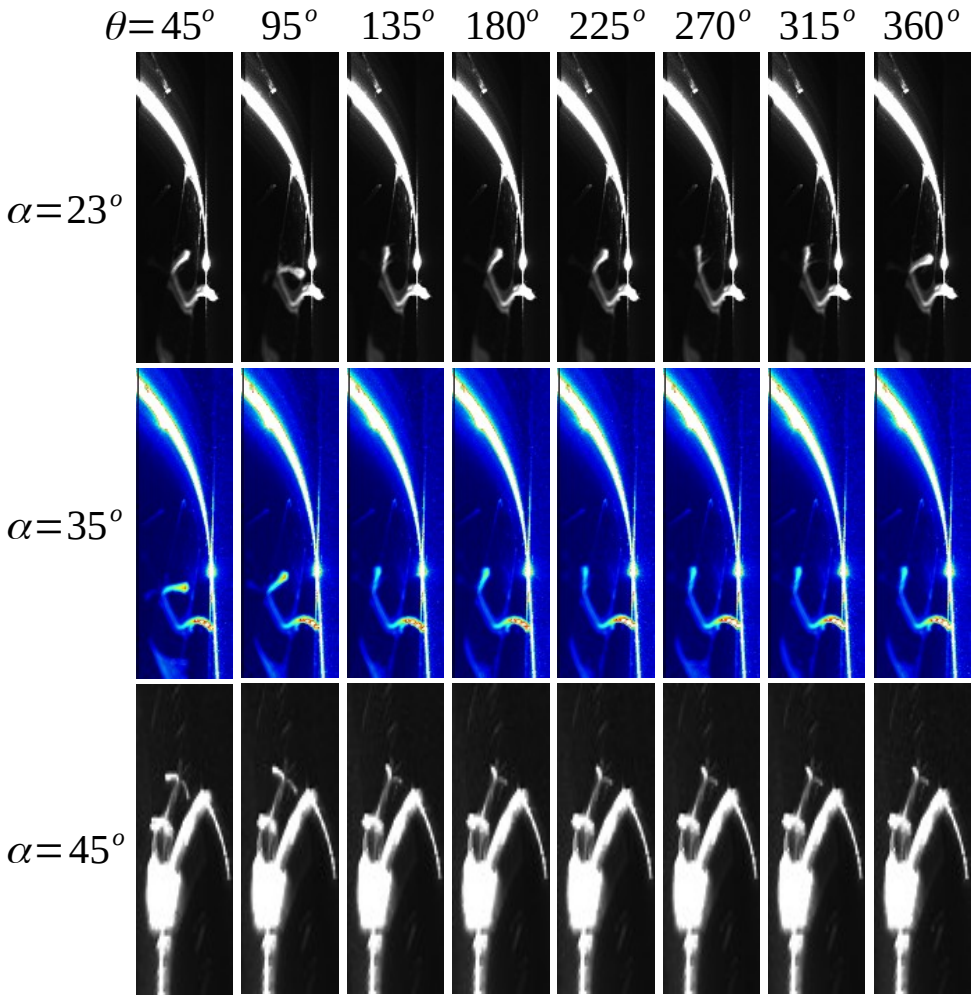

Figure C.1: Tuft displacement due to blowing around $\theta = 45°$ for three cases and 8 phases.

C.2 Pre Stall

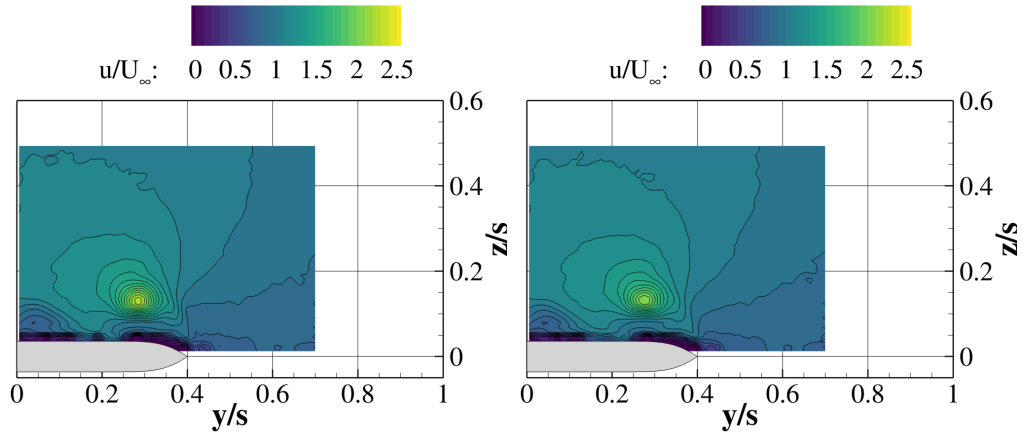

(a) Baseline, $x/c_r = 0.4$.

(b) Actuated, $x/c_r = 0.4$.

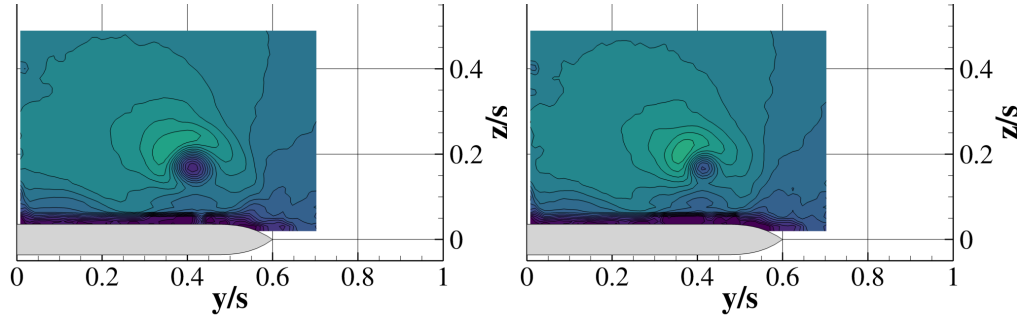

(c) Baseline, $x/c_r = 0.6$.

(d) Actuated, $x/c_r = 0.6$.

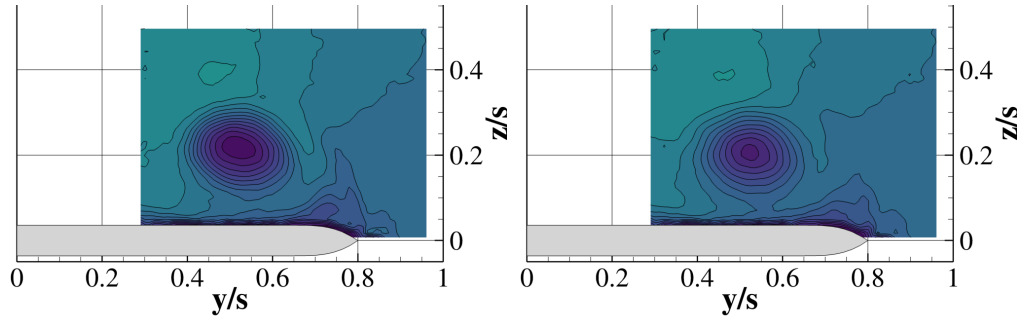

(e) Baseline, $x/c_r = 0.8$.

(f) Actuated, $x/c_r = 0.8$.

Figure C.2: Actuation effect on axial velocity distribution in PIV crossflow planes at $\alpha = 23°$, $Re = 1.0 \cdot 10^6$.

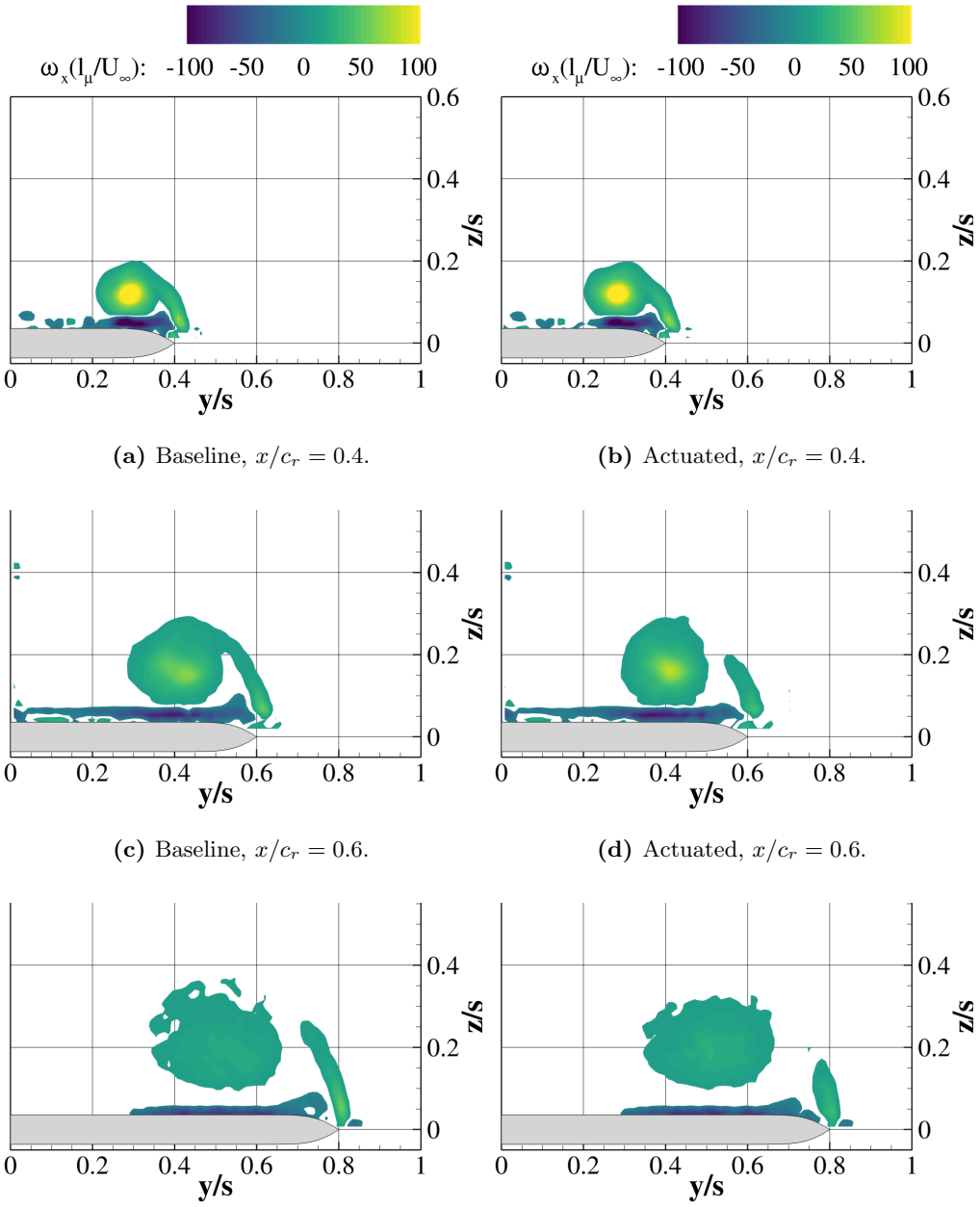

(a) Baseline, $x/c_r = 0.4$.

(b) Actuated, $x/c_r = 0.4$.

(c) Baseline, $x/c_r = 0.6$.

(d) Actuated, $x/c_r = 0.6$.

(e) Baseline, $x/c_r = 0.8$.

(f) Actuated, $x/c_r = 0.8$.

Figure C.3: Actuation effect on axial velocity distribution in PIV crossflow planes at $\alpha = 23°$, $Re = 1.0 \cdot 10^6$.

C.3 Near Stall

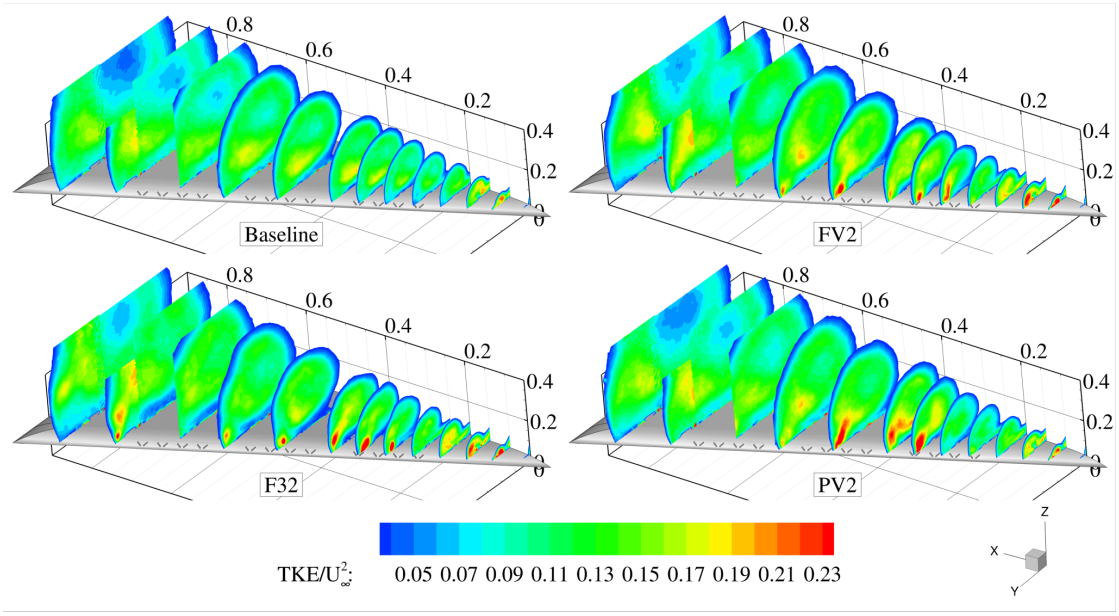

Figure C.4: TKE distribution at $\alpha = 35°$.

C.4 Post Stall

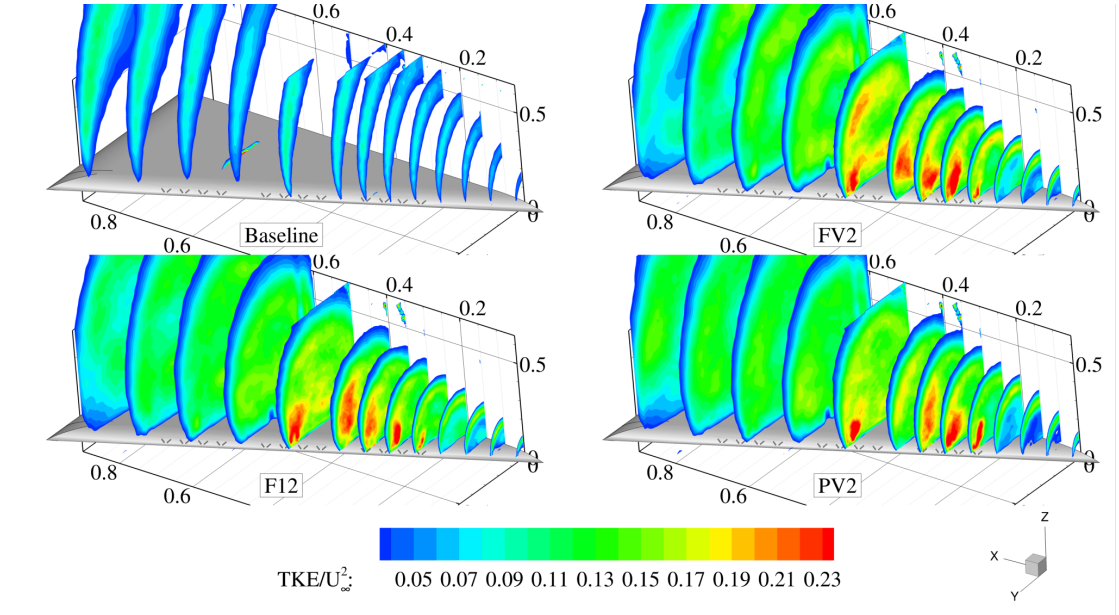

Figure C.5: TKE distribution at $\alpha = 45°$.

C.5 Phase-Averaged Flow Field

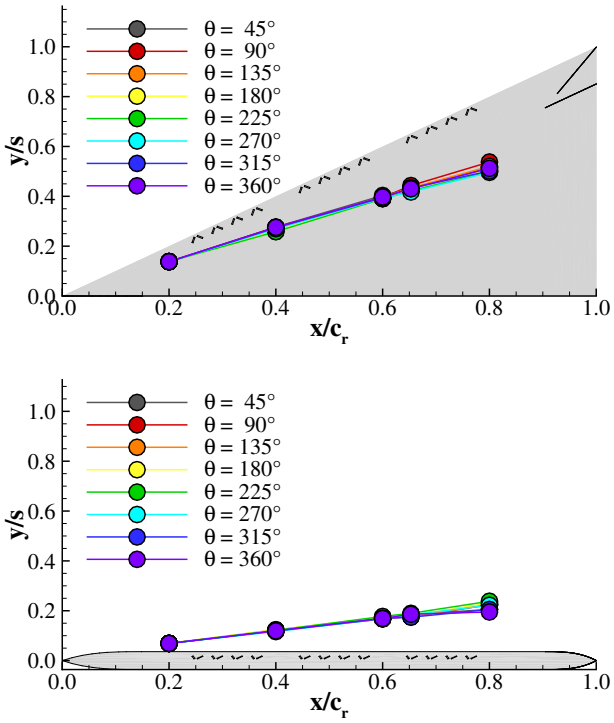

Figure C.6: Phase-dependent lateral and vertical location of vortex rotation axis at $\alpha = 23°$.

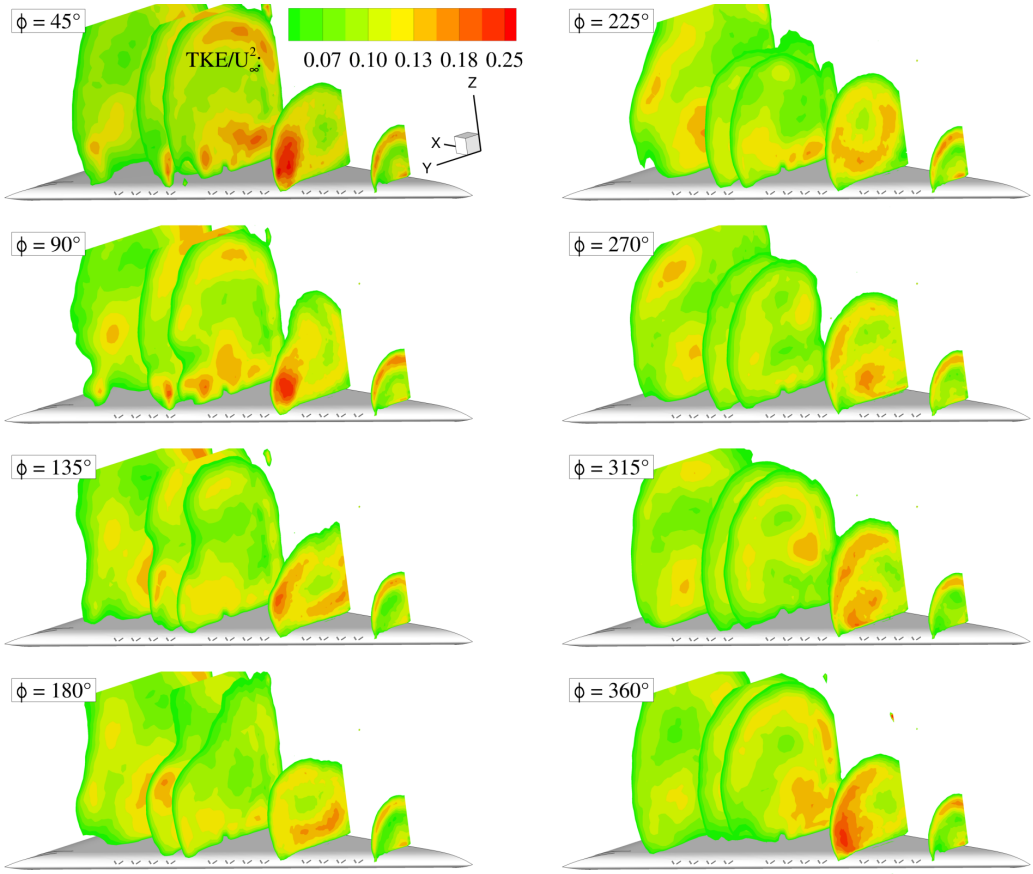

Figure C.7: Phase-averaged TKE, $\alpha = 45°$, $Re = 0.5 \cdot 10^6$, $F^+ = 1.0$.

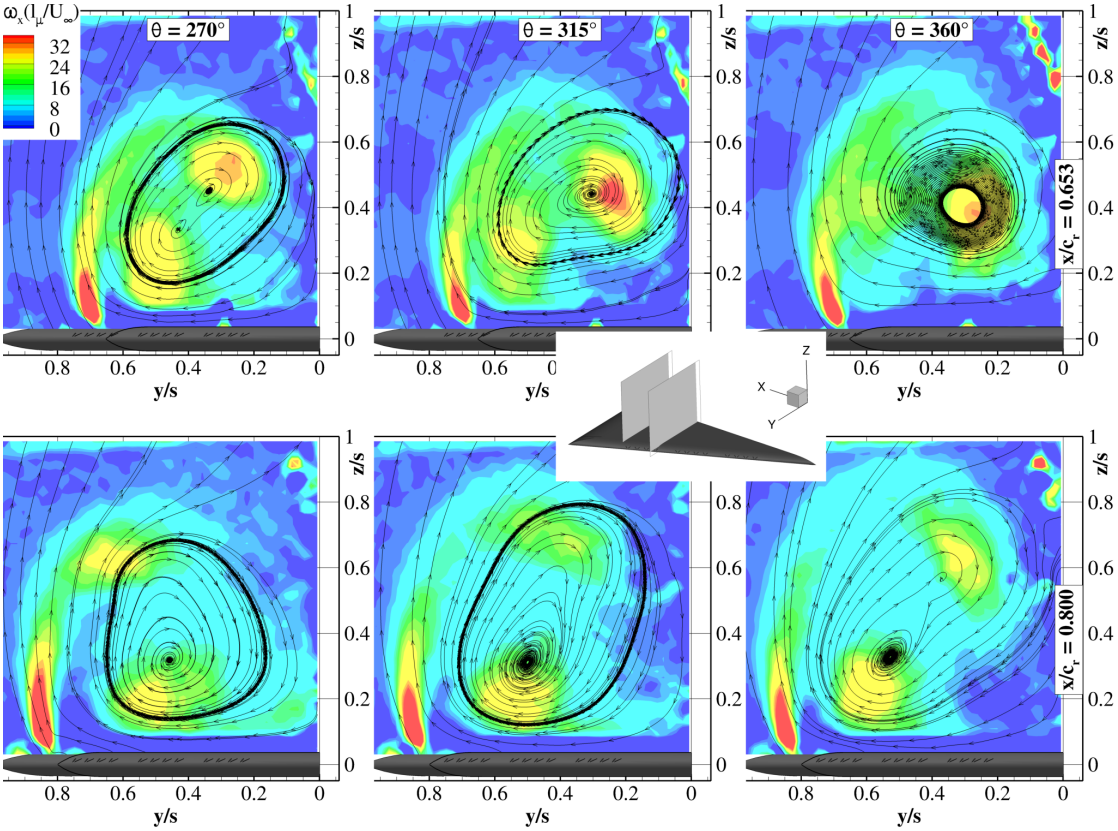

Figure C.8: Phase-averaged vorticity distribution at $x/c_r = 0.65$ and 0.80 during the recuperation phases $\theta = 270°$–$360°$, $\alpha = 45°$, $Re = 0.5 \cdot 10^6$, $F^+ = 1.0$ [17].